MODELING OF BIOMASS STEAM GASIFICATION IN A DUAL FLUIDIZED BED REACTOR WITH/WITHOUT LIME-BASED CO_2 CAPTURE

by

Bijan Hejazi

B.Sc., Sharif University of Technology, Tehran, Iran, 2005
M.A.Sc., Sharif University of Technology, Tehran, Iran, 2009

A THESIS SUBMITTED IN PARTIAL FULFILLMENT OF
THE REQUIREMENTS FOR THE DEGREE OF

DOCTOR OF PHILOSOPHY
in

THE FACULTY OF GRADUATE AND POSTDOCTORAL STUDIES
(Chemical and Biological Engineering)

THE UNIVERSITY OF BRITISH COLUMBIA
(Vancouver)

February 2017

Abstract

Lime-enhanced biomass gasification in a dual fluidized bed (DFB) reactor is a promising technology that allows enhanced hydrogen production from a renewable resource with simultaneous CO_2 capture via calcium looping.

In this thesis, modeling Ca-looping in a DFB biomass gasifier is broken down into different steps. Firstly, a comprehensive single particle model is developed, based on conservation of mass, energy and momentum, with two different biomass pyrolysis kinetic schemes for particles of changing thermo-physical properties. Secondly, a coupled particle and reactor model of biomass drying and pyrolysis in a bubbling fluidized bed reactor is developed to predict the yields of pyrolysis products and composition as a function of process operating parameters. Thirdly, our coupled particle and reactor model is extended to steam gasification of biomass in a bubbling fluidized bed (BFB) gasifier, and its applicability is tested by comparing predictions with independent experimental data from the literature. For steam gasification of pine sawdust at a reactor temperature of 750°C, the H_2 mole fraction in the product gas increases with increasing steam-to-biomass ratio because of the water-gas, steam methane reforming and water-gas shift (WGS) reactions. Elevating the reactor temperature reverses the exothermic WGS reaction towards more CO production and CO_2 consumption. Fourthly, the BFB gasifier model is expanded into a generic two-phase fluidized bed reactor model to evaluate the performance of the UBC dual fluidized bed gasifier under steady-state operating conditions. Finally, integrated biomass gasification with cyclic CO_2 capture in a DFB reactor is simulated by developing a model which takes into account sorbent loss of reactivity due to sintering during cyclic operation.

This comprehensive reactor model is developed and tested based on a stepwise approach. Unlike previous models, this is a predictive model that minimizes reliance on empirical correlations. By coupling single particle and reactor models, biomass drying, pyrolysis and gasification are studied as a continuous process. A gap of knowledge in predicting major compounds composition in pyrolysis gas is addressed. Furthermore, the kinetic model is capable of accommodating *in situ* CO_2 capture during cyclic operation.

Preface

By the time of submitting this thesis, three research papers have been published, the first paper related to Chapters 2 and 3, the second paper related to Chapter 4, and the third paper related to a version of Chapter 6:

I. Hejazi B, Grace JR, Bi X, Mahecha-Botero A. Steam gasification of biomass coupled with lime-based CO_2 capture in a dual fluidized bed reactor: a modeling study. Fuel 2014;117:1256–66.

II. Hejazi B, Grace JR, Bi X, Mahecha-Botero A. Kinetic model of steam gasification of biomass in a bubbling fluidized bed reactor. Energy Fuels 2017; DOI: 10.1021/acs.energyfuels.6b03161.

III. Hejazi B, Grace JR, Bi X, Mahecha-Botero A. Coupled reactor and particle model of biomass drying and pyrolysis in a bubbling fluidized bed reactor. J Anal Appl Pyrol 2016; 121: 213–229.

For both papers, the author carried out all stages of the research described in the paper and submitted it after receiving input from the other authors, prepared responses to the reviewers and handled correspondence with the journal editors.

The author has also had several poster and oral presentations at international, national and local conferences:

Poster presentations:

- Hejazi B, Masnadi MS, Grace JR, Bi X, Lim CJ, Ellis N, Mahecha-Botero A. Steam gasification integrated with CO_2 capture by solid sorbent. 4th Annual Carbon Management Canada Conference (CMC), Alberta, 2014.

- Hejazi B, Grace JR, Bi X, Mahecha-Botero A. Kinetic modeling of biomass pyrolysis in a bubbling fluidized bed reactor. Advanced Biofuels Symposium (ABS), Montreal, 2015.

Oral presentations:

- Hejazi B, Grace JR, Bi X, Mahecha-Botero A. Kinetically-modified equilibrium modeling of steam gasification of biomass with cyclic lime-based CO_2 capture. 3rd Int. Symp. on Gasification and Applications (iSGA-3), Vancouver, 2012.

- Hejazi B, Grace JR, Bi X, Mahecha-Botero A. Kinetic modeling of biomass pyrolysis in a bubbling fluidized bed reactor. 5th International Conference on Biorefinery - towards Bioenergy (ICBB), Vancouver, 2015.

- Hejazi B, Grace JR, Bi X, Mahecha-Botero A. A modeling study on calcium looping for CO_2 capture in a dual fluidized bed biomass gasifier. Carbon Capture Conference (NSERC CREATE annual meeting), Ottawa, 2016.

Table of Contents

List of Tables

List of Figures

List of Symbols

A	Bubbling bed cross-sectional area, m^2
a	Decay constant for voidage profile of riser, -
$a_{I_{L\rightarrow H}}$	Inter-phase transfer area between phases per unit volume, m^{-1}
Ar	Archimedes number, -
A_S	External heat-transfer surface area per unit reactor volume, m^{-1}
C_i	Concentration of species i, mol/m^3
$C_{i\varphi}$	Concentration of species i in phase φ, mol/m^3
C_p	Specific heat capacity, J/kg.K
d_b	Bubble diameter, m
$D_{eff,i}$	Effective diffusivity of i^{th} species, m^2/s
D_i	Molecular diffusivity of i^{th} species, m^2/s
D_{ij}	Binary diffusion coefficient between species i and j, m^2/s
d_p	Particle diameter, m
d_{pore}	Pore diameter, m
D_{riser}	Riser internal diameter, m
E	Activation energy, kJ/mol
E_j	Activation energy of j^{th} reaction, kJ/mol
$E(t)$	Solids residence time distribution function, s^{-1}
$F_{i\varphi}$	Molar flow rate of species i in phase φ, mol/s
Fr	Froude number, -
g	Acceleration of gravity, 9.81 m^2/s
Gr	Grashof number, -
G_S	Solid circulation flux, $kg/m^2.s$
G_S*	Solid circulation flux at saturation carrying capacity of the fluid, $kg/m^2.s$
h	Thickness of $CaCO_3$ product layer, m
h_{air}	Heat transfer coefficient between reactor surface and ambient, $W/m^2.K$
$h_{mass,i}$	Mass transfer coefficient of i^{th} species, m/s
$h_{overall}$	Overall heat transfer coefficient, $W/m^2.K$
H_i^*	Total enthalpy of stream i, J/mol or J/kg
ID	Inside diameter, m
K	Equilibrium constant, -
k	Thermal conductivity, W/m.K
k_{cond}	Thermal conductivity of gas and solid phases, W/m.K
$k_{c_{i,L\rightarrow H}}$	Inter-phase mass transfer coefficient of species i, m/s

k_d	Sorbent deactivation constant, -
k_{eff}	Effective thermal conductivity, W/m.K
$k_{0\,j}$	Pre-exponential factor of j th reaction, s^{-1}
k_j	Kinetic rate constant of j th reaction, s^{-1}
k_{rad}	Radiative conductivity of solid particle, W/m.K
K_S	Intrinsic kinetic rate constant for carbonation reaction, m^4/mol.s
k_{wall}	Reactor wall thermal conductivity, W/m.K
L_{bed}	Dense bubbling bed height, m
L_{riser}	Riser height, m
m	Mass, kg
m	Parameter for modified two-phase theory, -
$\dot{m}$	Mass flow rate, kg/s
M_{Char}	Char hold-up inside reactor, kg
M_{CaO}	Total reacting sorbent hold-up inside reactor, kg
M_P	Biomass particle hold-up inside reactor, kg
MW	Molecular weight, g/mol
n	Particle shape parameter, n=0 for flat, n=1 for cylinder, n=2 for sphere
N	Cycle number, -
N_C	Number of gas components, -
N_{or}	Number of holes in distributor plate, -
N_r	Number of reactions, -
Nu	Nusselt number, -
OD	Outside diameter, m
P	Reactor pressure/Total pressure inside particle, Pa
P_i	Partial pressure of ith species, Pa or bar
P_0	Standard pressure, 1 bar
Pr	Prandtl number, -
Q	Volumetric flow rate, m^3/s or Nm^3/h
$\dot{Q}$	Net heat source/sink, kW
q_{flux}	Source heat flux, W/m^2
Q_{loss}	Heat loss, kW
r	Radial coordinate inside particle, m
r	Reaction rate, s^{-1} or mol/m^3.s
R	Universal ideal gas constant, 8.314 J/mol.K
$Rate_{i,\varphi}$	Net reaction rate of species i in phase φ, mol/m^3_{φ}.s
R_C	Spherical char particle radius, m
R_{core}	Core radius, m

Re	Reynolds number, -
R_p	Spherical biomass particle radius, m
Sc	Schmidt number, -
Sh	Sherwood number, -
S_N	Specific surface area available for carbonation in a particle after N cycles, m^2/m^3
$Split_H$	H-phase flow split factor, -
t	Time, s
T	Temperature, K
u	Gas phase velocity inside pores of particle, m/s
U	Superficial gas velocity, m/s
U_b	Bubble rise velocity, m/s
U_c	Superficial gas velocity at transition from bubbling to turbulent fluidization regime, m/s
U_{mb}	Minimum bubbling velocity, m/s
U_{mf}	Minimum fluidization velocity, m/s
U_{se}	Transition velocity from turbulent to fast fluidization regime/significant entrainment, m/s
U_{gas_φ}	Convective gas velocity of phase φ, m/s
u_φ	Absolute gas velocities in phase φ, m/s
V_{CA}	Transition superficial gas velocity to core-annulus flow regime, m/s
V_{mp}	Transition superficial gas velocity to pneumatic transport, m/s
VM_{CaCO_3}	Molar volume of $CaCO_3$, m^3/mol
w	Mass fraction, -
$W(R_P)$	Weight fraction of biomass particles with radius R_p, -
W_{bed}	Solids bed inventory, kg
X_{ave}	Overall average carbonation conversion of CaO, -
X_B	Dry-ash-free biomass conversion, -
X_C	Char conversion/Overall carbon conversion, -
X_N	Maximum conversion of CaO particles at end of fast carbonation stage after N^{th} cycle, -
$\overline{X}_N$	Average carbonation of N^{th} group of particles, -
$X_N(t)$	Conversion of CaO to $CaCO_3$ as function of reaction time and number of cycles, -
X_P	Moist biomass particle conversion, -
$\bar{X}_P$	Average biomass particle conversion inside fluidized bed, -
X_r	Sorbent residual conversion constant, -
y_i	Mole fraction of i^{th} species, -
Y	Yield, kg/kg dry biomass
$\bar{Y}$	Average yield at reactor exit, kg/kg moist biomass
z	Axial coordinate along reactor height, m

z_0 Height of dense bottom zone of riser, -

Greek

α_N Fraction of sorbent cycled N times, -

β_g Permeability of gas phase, -

γ_i Stoichiometric coefficient of i th species in tar cracking reaction, -

ΔH^o_{rxn} Heat of reaction at standard condition, kJ/kg or kJ/mol

$\Delta H_{rxn,j}$ Heat of j th reaction, kJ/kg

ε Bed voidage at height *z* / particle porosity, -

$\bar{\varepsilon}, \varepsilon_{ave}$ Average bubbling bed voidage, -

ε_a Annulus voidage, -

ε_c Core voidage, -

ε_s Solids holdup, -

ε_{sd} Solids holdup in bottom dense zone of riser, -

ε_s^* Solids holdup at top exit of riser, -

ε_φ Void fraction of phase φ, -

η_{chem} Chemical efficiency, -

η_{CO2} CO_2 capture ratio, -

η_{H2} Hydrogen production efficiency, -

λ Stoichiometric oxygen ratio for combustion, -

μ Viscosity, kg/m.s

ν_φ Volumetric flow rate of phase φ, m^3/s

$\nu'''_{Bulk_{L\to H}}$ Volumetric flow rate convectively transferred from L-phase to H-phase per unit volume of phase, s^{-1}

ρ Density, kg/m^3

ρ_i Density of i^{th} species inside pores of particle, kg/m^3

$\rho_{i,bulk}$ Bulk density of i^{th} species inside reactor, kg/m^3

$\bar{\rho}_P$ Average biomass particle density inside bubbling bed, -

σ Stefan-Boltzmann constant, $5.75x10^{-8}$ $W/m^2.K^4$

τ Tortuosity,-

τ_g Total gas residence time inside reactor, s

τ_N Time required for particle to reach conversion of X_N, s

τ_s Mean solids residence time, s

φ Phase L or H

ψ_{φ}	Volume fraction of phase φ, -
ω	Emissivity, -
Ω	Temperature-dependent collision integral

Subscripts

a	Annulus
b	Bubble
B	Biomass
B0	Virgin biomass
c	Core
C	Char, Carbon
Cf	Final char
comb	Combustor/riser
eq	Equilibrium
f	Film
fb	Freeboard
fuel	Dry-ash-free biomass feed
g	Gas phase
G	Non-condensable gas
G_2	Secondary gas
H	Hydrogen/High density phase (emulsion or annulus)
i	Species number
int	Internal
j	Reaction number, Element number
L	Low density phase (bubble or core)
M	Moisture
M0	Initial moisture
NG	Natural gas
O	Oxygen
ox	Oxidation
P	Particle
PG	Product gas
S	Solid/sand

Surf	Surface
T	Tar
V	Water vapour
w	Reactor wall

List of Abbreviations

AER	Adsorption Enhanced Reforming
BFB (G)	Bubbling Fluidized Bed (Gasifier)
BECCS	Bio-Energy with Carbon Capture and Storage
CCS	Carbon Capture and Storage
CFB (G)	Circulating Fluidized Bed (Gasifier)
CFD	Computational Fluid Dynamics
CSTR	Continuous Stirred Tank Reactor
CHP	Combined Heat and Power
DFB	Dual Fluidized Bed
FC	Fixed Carbon
FICFB	Fast Internally Circulating Fluidized Bed
GHG	Greenhouse Gas
HHV	Higher Heating Value
HyPr-RING	Hydrogen Production by Reaction-Integrated Novel Gasification
IPCC	Intergovernmental Panel on Climate Change
LHV	Lower Heating Value
PCM	Progressive Conversion Model
PFR	Plug Flow Reactor
RTD	Residence Time Distribution
S/B	Steam/Biomass Ratio
SEM	Scanning Electron Microscope
SEWGS	Sorption Enhanced Water Gas Shift
SMR	Steam-Methane Reforming
TGA-MS	Thermogravimetric Analysis/Mass Spectrometry
TRL	Technical Readiness Level
WGS	Water-Gas Shift

Acknowledgements

I am very fortunate to have been a student of an extremely knowledgeable team of supervisors and mentors at one of the world's leading universities.

It is my great pleasure to have had my thesis supervised by Professor John R. Grace. His openness to new ideas, tolerance of mistakes, scrutiny in providing instrumental technical advice and proofreading are among the positive characteristics that make working with him an inspiring experience.

I owe particular thanks to my intellectual co-supervisors, Professor Xiaotao Bi and Doctor Andrés Mahecha-Botero, for their constructive comments and questions that helped improve the quality of the research, and their sharing of professional experience.

My special thanks go to my departmental committee members, Professor Jim Lim and Doctor Xuantian Li, for their contributions in leading the research in the right direction.

I also offer particular thanks to the faculty, staff and my fellow students at UBC, especially the gasification group members at the Chemical & Biological Engineering department.

Financial support from Carbon Management Canada, NSERC and BioFuelNet is gratefully acknowledged.

Last but not least, I owe my enduring gratitude to my family for their caring, moral support and emotional reinforcement.

Dedication

This thesis is dedicated to my parents for their unconditional love and support.

Chapter 1: Introduction

Since approximately 1850, global use of fossil fuels (coal, oil and natural gas) has dominated energy supply, leading to a rapid growth in greenhouse gas (GHG) emissions. According to the Intergovernmental Panel on Climate Change (IPCC) Fourth Assessment Report, "Most of the observed increase in global average temperature since the mid-20th century is very likely due to the observed increase in anthropogenic greenhouse gas concentrations".

Some of the possible options to lower GHG emissions while still satisfying the global demand for energy services are: energy conservation and efficiency, fossil fuel switching, renewable energy, nuclear and carbon capture and storage (CCS). The share of renewable energy in the energy mix has substantially increased in recent years and projected to increase substantially under most ambitious mitigation scenarios [1]. Bioenergy can be produced from a variety of biomass feedstocks, including forest, agricultural and livestock residues, short-rotation forest plantations, energy crops, the organic component of municipal solid waste, and other organic waste streams. Through a variety of processes, these feedstocks can be directly used to produce electricity or heat, or can be used to produce gaseous, liquid, or solid fuels. The range of bioenergy technologies is broad and the technical maturity varies substantially. Bioenergy technologies have applications in centralized and decentralized settings, with the traditional use of biomass in developing countries being the most widespread current application. Bioenergy projects usually depend on local and regional fuel supply availability, but recent developments show that solid biomass and liquid biofuels are increasingly traded internationally [1].

Currently, biomass covers approximately 10% of the global energy supply. Roughly two-thirds of the energy use of biomass take place in developing countries for cooking and heating. The remaining use of biomass is in industrialized countries, where biomass is utilized both in industrial applications within heating, power and road transportation sectors and for heating purposes in the private sector. In 2009, about 13% of biomass use was consumed for heat and power generation, while the industrial sector consumed 15% and the transportation sector 4%. The global consumption of biofuels in transportation accounted to only about 2% of the total fuels consumed in the transportation sector [2].

1.1 Biomass gasification

Moving towards a sustainable energy future is among the top priorities of today's mankind. One cannot talk about sustainability and a sustainable energy future without considering the relationship of humans to the environment. Emission of enormous amounts of greenhouse gases (especially CO_2) to the atmosphere as a byproduct of converting energy from burning fossil fuels has been scientifically proven to contribute considerably to climate change. During the past decade, this has motivated many institutions and organizations throughout the world to invest largely in research and development of new technologies in efforts to address the ever-growing world energy demand in a sustainable manner. Among the options for reducing greenhouse gas emissions is gasification of biomass. Despite its long history, there is renewed interest in gasification, due in part to its ability to produce H_2 as a clean energy carrier [3]. Enhanced hydrogen production from biomass gasification with simultaneous CO_2 capture, when integrated with CO_2 sequestration technologies, could potentially result in net removal of CO_2 from the atmosphere, i.e. "negative emissions".

Gasification is defined as a high-temperature partial oxidation process in which a solid carbonaceous feedstock such as biomass is converted into gaseous products (in particular H_2, CO, CO_2, CH_4, light hydrocarbons), as well as liquid tar[1] and minor contaminants, using gasifying agents such as air, oxygen, steam, carbon dioxide or their mixtures [7]. These gasifying agents produce synthetic gases of different calorific values. Steam gasification of biomass produces a medium heating value gas mixture, i.e. 10–18 MJ/Nm^3, Higher Heating Value (HHV), an attractive choice compared to lower heating value gases generated from air gasification (4–7 MJ/Nm^3, HHV). Gasifying with O_2-enriched air, on the other hand, results in similar product gas heating values to steam gasification at the cost of larger investments required for oxygen separation from air [8]. Gasifying with pure steam produces higher hydrogen content of product gas compared to gasification with a mixture of steam and oxygen, whereas the hydrogen concentration in product gas generated by air gasification is the lowest [9].

[1] Tar is defined as the condensable fraction of the organic gasification products which are largely aromatic hydrocarbons with molecular weights higher than benzene [4]. Although attempts have been made to clarify "tar" such as the EU/IEA/US-DOE meeting on tar measurement protocol in Brussels, 1998, there is still no consensus over the definition, sampling and analytical methods for tars [5, 6].

Figure 1.1 summarizes a complex reaction network occurring during gasification of biomass. The three main steps include [10]:

(i) Devolatilization or pyrolysis at relatively low temperatures, between 300 and 500^{o}C, during which 70-90% by weight of the biomass is converted to volatile matter and tars.

(ii) Cracking and reforming of volatile matter and tars at temperatures > 600^{o}C.

(iii) Gasification of unreacted char at temperatures > 800^{o}C.

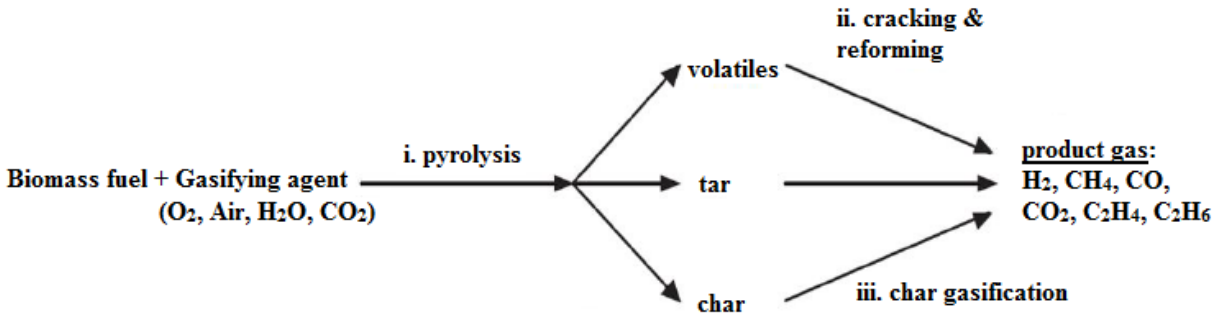

Figure 1.1. General three-step reaction mechanism for gasification of biomass [10]. (i) Devolatilization or pyrolysis occurring at relatively low temperatures between 300-500^{o}C (ii) Cracking and reforming of volatile matter and tars at temperatures > 600^{o}C. (iii) Gasification of unreacted carbon i.e. char, at temperatures > 800^{o}C.

These reactions result in a distribution of products, including tar, char and a product gas composed mainly of H_2, CO, CO_2, CH_4, C_2H_4 and C_2H_6. Step (ii) (cracking and reforming reactions) dominate the final product gas composition during biomass gasification [10].

The endothermic nature of biomass gasification necessitates external energy input. According to the ways to provide this required energy, gasifiers can be grouped into autothermal and allothermal types. For autothermal gasifiers, e.g. air and oxygen gasification, partial oxidation of the biomass in the gasifier provides the necessary heat. However, the exhaust gas generated from *in situ* oxidation dilutes the product gas, reducing its heating value. In contrast, allothermal gasifiers derive energy from external sources; steam and CO_2 gasification are examples of this type. Combustion of residual char (resulting from incomplete gasification) outside the gasifier is another method in which allothermal gasifiers can acquire the required energy. Allothermal gasifiers have the possibility of being integrated with other forms of renewable energies,

including direct solar energy, geothermal energy, and nuclear heat [7]. The main advantage of allothermal gasification systems is their ability to produce significantly higher H_2/CO ratios [7]. When comparing the efficiency of different types of gasifiers, the energy requirements for producing a desired target quantity and quality of gasification product gas should also be taken into account.

Key parameters affecting the thermo-chemical conversion of solid biofuels to gaseous products can be divided into two main categories: fuel-related and process-related. The most important fuel-related parameters include molecular composition (cellulose, hemicellulose and lignin contents) and elemental composition of solid fuel particles, such as ash content and percentage of catalytically active compounds (mostly minerals such as alkali and alkali earth metals). Moisture content and other physical qualities such as size, shape and density of the fuel particles may also be considered in this category. Process-related parameters, on the other hand, include the design and operating conditions (e.g. temperature and pressure) of the gasifier itself.

1.1.1 Dual fluidized bed gasifier

Fluidized beds have a history of proven operability in the field of solid fuel conversion to gaseous products. Good heat and mass transfer, temperature uniformity, superior solid-gas contact, high solids flow rates and great flexibility with regards to handling a variety of fuel quantity and quality relative to fixed-beds are among their characteristics [10, 11].

A fluidized bed is formed when particulate solids are subjected to appropriate conditions to cause the solid/fluid mixture to behave as a fluid. This is usually achieved by upwards flow of pressurized fluid through the particulate medium. This causes the medium to have many properties and characteristics of normal liquids; such as the ability to flow freely under gravity, or to be pumped using fluid type technologies. A fluidized bed may operate in quite distinct flow regimes, depending on its geometry and the particle and gas properties, as well as the fluidizing gas velocity. Figure 1.2 graphically explains the different flow regimes for gas-solid fluidized beds. When the flow is very small, the fluid percolates through the voids within the packed solids without causing any appreciable solids movement (fixed-bed). When upward gas flow increases, the bed reaches or exceeds the minimum fluidization condition ($U \geq U_{mf}$), and for group A

particles in the Geldart classification[2], homogeneous expansion can be observed. If the fluid velocity is further increased beyond minimum bubbling, most excess gas forms bubbles, corresponding to bubbling fluidization. If at some point the bubble size is physically constrained by the reactor diameter (i.e., for tall narrow vessels) the bed operates in the slugging flow regime. When the fluid velocity is further increased, the bubbles disappear, and the turbulent fluidization flow regime is established. As entrainment grows, a solids recirculation system is needed, and the reactor is said to be in the fast fluidization regime, characterized by dilute upward flow in the core and descending streams at the wall (core-annulus). A further flow regime, dense suspension upflow, can be reached at very high solids circulation rates [12].

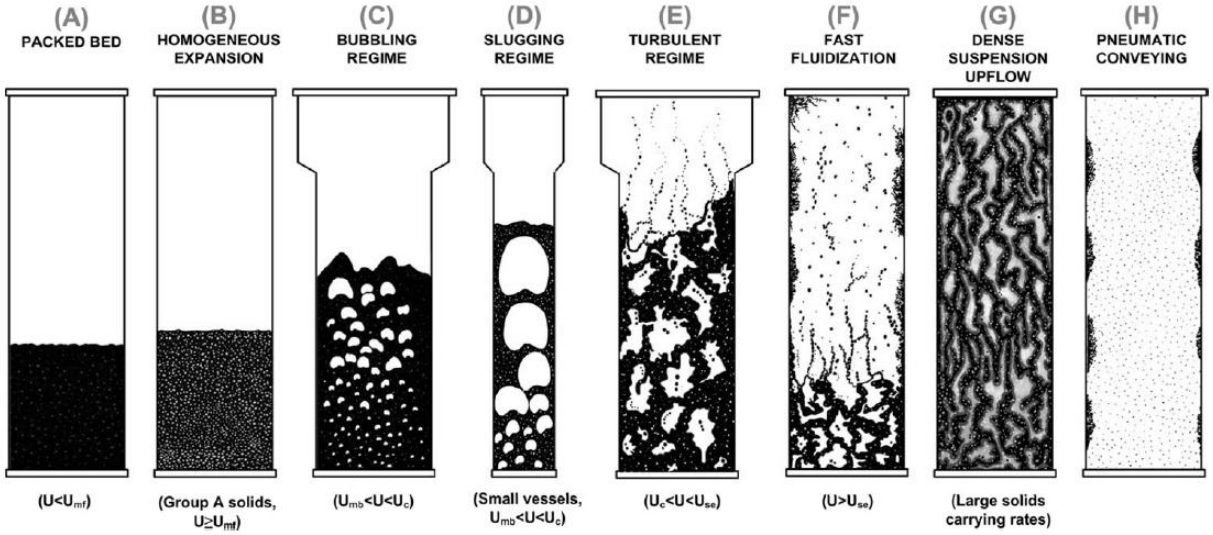

Figure 1.2. Fluidization flow regimes: (A) packed bed; (B) homogeneous/bubble-free expansion (only for group A particles); (C) bubbling fluidization regime; (D) slugging fluidization regime (only in small diameter vessels); (E) turbulent fluidization regime; (F) fast fluidization regime; (G) dense suspension upflow (only for large solids carrying rates); (H) pneumatic conveying. U=superficial gas velocity; U_{mf} =minimum fluidization velocity; U_{mb}=minimum bubbling velocity; U_c=velocity of transition from bubbling to turbulent fluidization regime; U_{se}= velocity of transition from turbulent to fast fluidization regime/significant entrainment [12].

[2] In 1973, Geldart divided powders into four "Groups" defined by their locations on a diagram of solid-fluid density difference and particle size. For Group A: particle size varies between about 20 and 100 μm, particle density less than 1.4 g/cm^3, Group B: particle size between 40 and 500 μm, particle density between 1.4-4 g/cm^3, Group C: particle size less than 20 to 30 μm, and Group D: particles larger than 600 μm and high particle densities.

Based on the major fluidization flow regimes in which fluidized bed gasifiers can operate, they are further categorized as Bubbling Fluidized Bed Gasifiers (BFBG) (operating in the bubbling flow regime) and Circulating Fluidized Bed Gasifiers (CFBG) (operating in the fast fluidization flow regime). The CFBGs require recirculation of particles. Recycling of fines can also be applied to a Bubbling Fluidized Bed Gasifier, leading to a greater efficiency of carbon conversion by increasing the residence time of particles. CFBGs are taller and operate with higher superficial gas velocities, typically in the range of 2-5 m/s, whereas the superficial velocities in BFBGs are only 0.5-2 m/s. Therefore, for equal cross section, CFBGs require higher fuel flow rates than BFBGs [13].

A recent development of fluidized bed gasifiers, integrating BFB and CFB components, is the twin-bed configuration, widely known as Dual Fluidized Bed (DFB) gasifiers. As seen in Figure 1.3, biomass fuel is fed into one fluidized bed (referred to as the gasifier) and fluidized with steam. Since the biomass conversion under gasification conditions is less than unity, there remains a fraction of unconverted carbon (char or coke) resulting from gasification that is circulated to the second fluidized bed (known as the combustor) to be burnt at higher temperatures with introduced air. If necessary, an additional source of fuel or an external heating medium may also be supplied to the combustor. Solid bed materials (e.g. inert silica sand) heated within the combustor are circulated back to the gasifier, providing a source of sensible heat, necessary for the endothermic gasification reactions. By separating the gasification zone from the combustion zone, the Dual Fluidized Bed configuration generates a relatively high concentration of H_2 in the product gas, without suffering from product gas dilution by N_2, despite using inexpensive air for char combustion [14]. Note that the biomass ash accumulates inside the system and, together with the circulating bed material, transfers sensible heat.

Two important criteria for measuring the effectiveness of gasification include the gas composition (in particular, the H_2 content) and the gas quality (tar content) of the product gas. Generally speaking, higher concentrations of H_2 and lower tar contents in the product gas are desirable [5]. Tar can be highly problematic for gasification commercialization because of problems associated with condensation, formation of tar aerosols and polymerization to form complex structures causing blockage of process equipment, as well as engines and turbines that burn producer gas [6, 15]. Aside from operational issues, not being able to destroy tar and

convert its chemical energy content to useful products such as H_2 and CO within the gasifier also lowers H_2 yields, thus reducing the heating value of the product gas.

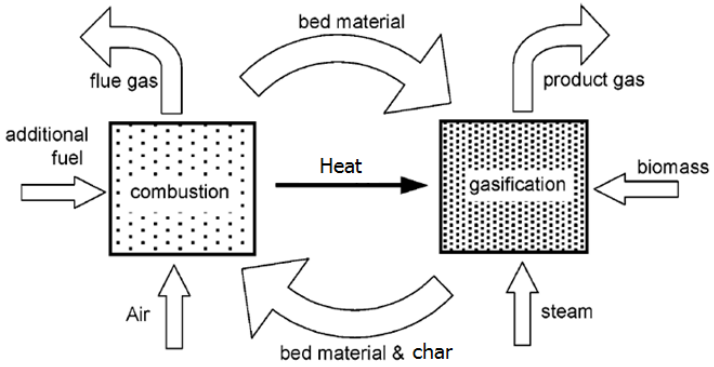

Figure 1.3. Operation of dual fluidized bed steam gasifier [14]. A circulation loop of bed material is created between a gasification zone and a combustion zone, but the gases remain separated. The circulating particles act as heat carriers from the combustion zone to the gasification zone.

There are a number of reasons why biomass gasification needs to be improved before being able to meet the demands of many commercialized process. These include low yields of produced H_2 (e.g. 40% volume, dry), high tar contents (e.g. ~10 g/Nm^3) in the product gas and high operating temperatures (>800^oC), which is costly to achieve with steam. In addition, less than 10% steam conversion during steam gasification of biomass translates to a waste of money and energy [3].

Although biomass gasification has been identified [7] as the most efficient and economical route for hydrogen production, it needs to be combined with other advanced new technologies to lead to a sustainable energy process.

1.2 Carbon capture and storage (CCS)

The term carbon capture and storage (CCS) includes a range of technologies involving capture, purification, compression, transportation and sequestration of CO_2 produced by combustion and other processes in a permanent location [16]. In 2005, the IPCC Special Report on CCS [17] recognized the large potential for developing and scaling up a wide range of emerging CO_2 capture technologies with the possibility of delivering lower energy penalties and cost [18, 19]. Three different categories of CCS exist: post-combustion, pre-combustion, and oxy-fuel combustion. In post-combustion capture, CO_2 is removed from the flue gas after combustion of a

fuel (usually fossil fuel). For example, this may be applied to fossil-fuel burning power plants. In pre-combustion cases, the fossil fuel is partially converted, for instance in a gasifier, and the carbon dioxide is removed before combustion takes place. Pre-combustion technologies are widely applied in fertilizer, chemical, gaseous fuel (H_2, CH_4), and power production, in particular in new fossil fuel burning power plants, or existing plants where re-powering is an option.

In oxy-fuel combustion, the fuel is burned in contact with oxygen, instead of air. To limit the resulting flame temperatures to levels common during conventional combustion, cooled flue gas is recirculated and injected into the combustion chamber. The flue gas consists of mainly carbon dioxide and water vapor, the latter being condensed by cooling, resulting in an almost pure carbon dioxide stream that can be transported to the sequestration site and stored. Power plant processes based on oxy-fuel combustion are sometimes referred to as "zero emission" cycles, because the CO_2 stored is not a fraction removed from the flue gas stream (as in the cases of pre- and post-combustion capture), but the flue gas stream itself. A fraction of the CO_2 generated during combustion inevitably ends up in the condensed water. To warrant the label "zero emission", the water would need to be treated or disposed of appropriately. The technique is promising, but the initial air separation step requires substantial energy.

1.2.1 Calcium looping

The objective of CO_2 capture, as the most costly stage in the CCS process, is to obtain a purified stream of CO_2 (typically >95 % by volume) suitable for storage. One promising technology for capturing CO_2 involves the use of a Calcium-based solid sorbent, typically derived from limestone, in a process known as ‘Calcium Looping’ [20]. Ca-looping offers a number of advantages relative to the well-established industrial CO_2 capture technology of ‘scrubbing’ by amine-based liquid sorbents. Potential advantages include reduced overall efficiency penalty of the process due to high-grade excess heat recovery from capturing CO_2 at high temperatures; use of widely available and environmentally-benign materials (derived from limestones/dolomites) for CO_2 capture; affinity of the materials to SO_2, providing simultaneous desulphurisation of the industrial flue gas; and potential use of waste materials (e.g. in the cement industry). Furthermore, Ca-looping has the potential for retrofitting existing power stations or other

stationary industrial sources with relatively low parasitic energy demands imposed on existing processes.

Calcined limestone (CaO) is able to absorb CO_2 by means of exothermic gas-solid carbonation and reversible release of that captured CO_2 via calcination:

Carbonation-calcination: $CaO(s) + CO_2(g) \rightleftharpoons CaCO_3(s) \qquad \Delta H^o_{rxn} = -178 \text{ kJ / mol}$ (1.1)

As illustrated in Figure 1.4, carbonation occurs when the partial pressure of CO_2 exceeds its equilibrium partial pressure at a given temperature. On the other hand, the endothermic calcination reaction, which readily goes to completion for a wide range of conditions, is favored for CO_2 partial pressures less than the equilibrium value. As a result, if a sorbent is cycled between two vessels at suitable temperatures and pressures, carbonation of sorbent can be performed in one and calcination in the other. It must be highlighted that an important aspect of this reaction is its reversibility, so that the limestone particles can, at least in principle, be used repeatedly under cyclic carbonation-calcination operation. Both the carbonator and calciner can use fluidized bed technology due to favorable gas-solid contacting, uniform bed temperature and the viability of large scale reactors [21].

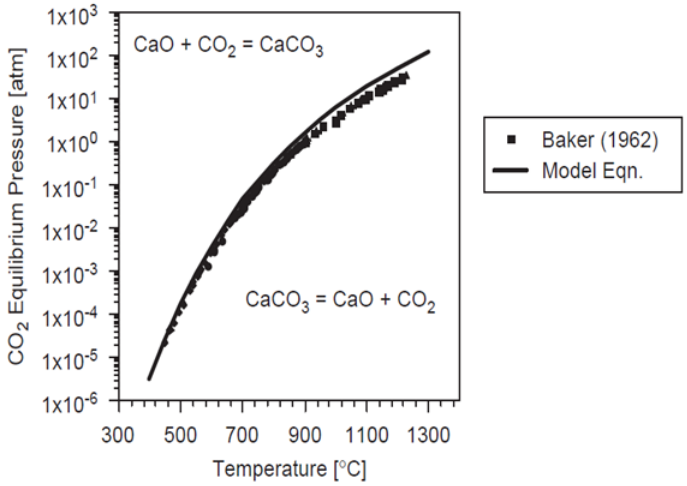

Figure 1.4. Equilibrium partial pressure of CO_2 resulting from decomposition of $CaCO_3$ for a range of temperatures from 400 to 1300°C [10]. Carbonation occurs when the partial pressures of CO_2 is greater than its equilibrium partial pressure at a given temperature. The endothermic calcination reaction, is favored when the CO_2 partial pressure is less than its equilibrium value.

Shimizu *et al.* (1999) proposed a Ca-looping process for post-combustion CO_2 capture from a stationary industrial CO_2 point source [22]. As shown in Figure 1.5, this process consists of two fluidized bed reactors connected by solids transfer lines. In one reactor (the Carbonator), a flue gas stream containing diluted CO_2 contacts a sorbent containing CaO at atmospheric pressure and temperatures 650-700^oC. The captured CO_2 in the form of solid $CaCO_3$ is transferred to another reactor (the Calciner) where $CaCO_3$ is decomposed to CaO at a higher temperature (e.g. 900-950^oC) releasing CO_2, and the regenerated sorbent (CaO) is returned to the carbonator. The heat of decomposition in the calciner is supplied by feeding fuel and pure oxygen. Thus the flue gas from the calciner contains high-purity CO_2 (>95% on a dry basis). Due to the coexistence of SO_2 in the flue gas of industrial CO_2 point sources, simultaneous sulfation of limestone occurs within the carbonator, leading to sorbent pore blockage by $CaSO_4$, which does not decompose at typical calcination temperatures. To maintain the overall reactivity of the sorbent in the system, fresh make-up limestone must be continuously introduced to the calciner, while a solid stream of spent CaO is purged from the system. To perform endothermic calcination of $CaCO_3$, the Ca-looping cycle requires that heat be supplied to the calciner. Heat is also required to raise the temperature of the regenerated sorbent from the carbonator temperature to the calciner temperature (typically by ~250^oC), as well as raising the temperature of fresh limestone from ambient to ~900°C. Because the overall process operates at relatively high temperatures (> 650 °C), much of the energy input can be recuperated from the hot gas and solid streams exiting the system by means of a steam cycle [16].

The gas stream leaving the calciner (acting as a sorbent regenerator) contains high concentrations of carbon dioxide. The purity of CO_2 in this gas depends on the method of providing the heat required by the calciner. Direct heating of the calciner by combustion of the fuel with air would reduce the CO_2 purity, because of the nitrogen in the air. This, on the other hand, would have the benefit of reducing the CO_2 partial pressure within the regenerator, allowing more moderate calcination temperatures according to the equilibrium curve of Figure 1.4. Moderate calcination temperatures limit structural decay of the sorbent particles, maintaining their reactivity for more effective carbonation. This is particularly important for achieving high CO_2 capture efficiencies over long-term cyclic operation.

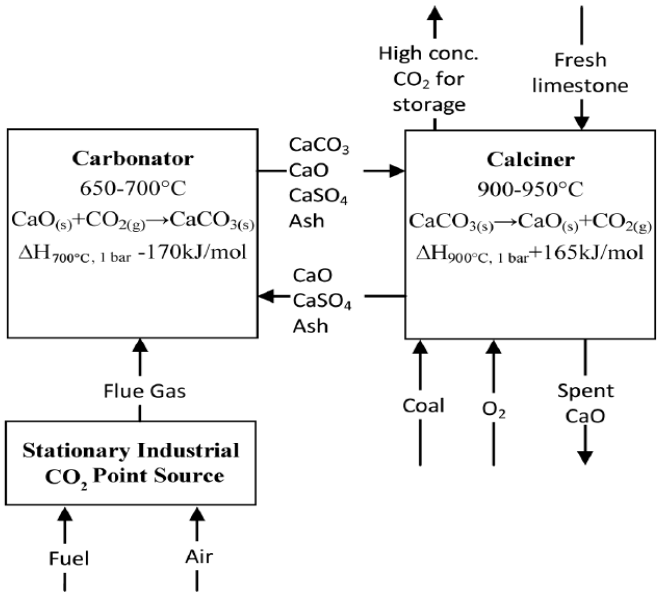

Figure 1.5. Typical scheme for Ca-looping post-combustion CO_2 capture from a stationary industrial CO_2 point source proposed by Shimizu *et al.* [22].

Certain emerging CO_2 capture processes have rapidly increased their technical readiness level (TRL) since the publication of the 2005 IPCC Special Report on CCS [17], reaching pilot scale demonstration at the MW_{th} range in industrially relevant environments. Abanades *et al.* [18] classified CO_2 capture technologies by the gas separation principle and by post-, pre-, oxy-combustion process schemes with reference to the progress of TRL from 2005 to 2015. Compared to other emerging CO_2 capture technologies based on high-temperature solids, Ca-Looping has experienced the largest progress in technology readiness level. This has been possible due to the similarity of the key reactor technology (carbonator and calciner) with existing combustion technologies based on circulating fluidized bed reactors. Nevertheless. the cost of CO_2 capture using emerging technologies is highly uncertain because of the inherent gaps of knowledge regarding the design and operational aspects of these systems when applied at large scale [23, 24].

1.3 Lime-enhanced biomass gasification

Bio-energy with carbon capture and storage (BECCS) is a future greenhouse gas mitigation technology which produces negative carbon dioxide emissions by

combining bioenergy (energy from biomass) with geologic carbon capture and storage. The main appeal of BECCS is its ability to result in negative emissions of CO_2. The capture of carbon dioxide from bioenergy sources effectively removes CO_2 from the atmosphere [25-27].

1.3.1 Overview

In addition to separating CO_2 (3-30% by volume) from an exhaust gas resulting from industrial power plants (i.e. post-combustion CO_2 capture), Ca-looping technology is also finding advanced applications in pre-combustion techniques, such as Sorption-Enhanced Water-Gas-Shift (SEWGS) and gasification of solid carbonaceous feedstocks to generate H_2-rich fuel gas. SEWGS is a concept for pre-combustion CO_2 capture which integrates the water-gas-shift reaction and CO_2 separation

Water-gas shift reaction: $CO + H_2O \rightleftharpoons CO_2 + H_2 \qquad \Delta H^o_{rxn} = -41 \text{ kJ / mol}$ (1.2)

This can be achieved by selectively removing CO_2 *in situ*, shifting the thermodynamic barrier of equilibrium reactions, such as the water-gas-shift reaction, towards more H_2 production. Furthermore, the heat generated by the exothermic carbonation reaction is utilized by the endothermic biomass gasification reactions.

The most important reason for selecting a lime-based sorbent is the high reactivity of CaO particles for selective CO_2 capture over a typical temperature range for gasification (550-750^{o}C). Moreover, the decomposition temperature of its carbonated form ($CaCO_3$) is higher than this temperature range, but not too high (<900^{o}C). As a naturally-occurring solid, another attractive characteristic of limestone is its abundance at low cost, making it a favorable candidate for *in situ* CO_2 capture. Other essential properties of a sorbent include acceptable resistance to physical and chemical deterioration (such as attrition), and maintaining reactivity over multiple capture and release cycles [10]. Sorbents other than limestone have also been tested for their ability to enhance biomass gasification. The best known is naturally occurring dolomite ($MgCO_3.CaCO_3$) with effective reactivity to both tar elimination and CO_2 capture. However, its relative friability limits its applicability in fluidized beds [5, 28].

Given the concept of the dual fluidized bed gasifier, where two reactors perform separate, but complementary, gasification and combustion processes and also reversible carbonation-calcination reactions of lime-based sorbents, one can potentially benefit from several advantages of coupling biomass gasification to high temperature CO_2 capture by limestone, including:

I. Enhanced H_2 production, e.g. from 40 to 80% vol dry (based on equilibrium modeling and literature data [29, 30]);

II. Production of a concentrated stream of CO_2 for sequestration as a byproduct;

III. Exothermic gas-solid absorption, which could partially supply the heat required by the endothermic gasification reactions;

IV. Weak catalytic activity of the Ca sorbent for tar cracking and reforming, water-gas shift and other gasification reactions [31-35].

Successful demonstration results at scales larger than 100 kW_{th} have been realized at Ca-Looping plants at La Robla power plant (Spain) [36], Darmstadt University of Technology (Germany) [37] and ITRI (Taiwan) [38]. These have been crucial in setting the basis for further demonstrations. The La Robla project in Spain provides an especially good example of Bio-Energy with Carbon Capture and Storage (BECCS) with Calcium Looping.

The Ca-looping process was originally developed on a large scale [16] for improving the heating value of product gas from gasification processes by removing CO_2 and promoting gasification. As a result of climate change, concern has switched to capture of CO_2 for storage [16]. In the 1960s-1980s, the Consolidation Coal Company developed the CO_2 Acceptor Process [39] consisting of two bubbling fluidized beds with solid particle streams linking the two; one gasifier/carbonator operated at 10 bar and 825^oC under steam, while a combustor/calciner operated at 1000^oC. More recently, the Adsorption Enhanced Reforming (AER) process has been developed by a consortium under the European Commission's 6th Framework Programme to enhance steam gasification of biomass [40]. Pilot plant investigations of the AER process have been performed at the Vienna University of Technology, using so-called "Fast Internally Circulating Fluidized Bed" (FICFB) technology [41]. This system includes a dual fluidized bed

with a gasifier/carbonator operating at 600–700^{o}C at atmospheric pressure and a combustor/calciner, which can handle 100 kWth power. AER operation can increase H_2 production from biomass – from ~40% to ~75% v/v – compared to an analogous commercial process without the CO_2 sorbent, while facilitating a lower gasification temperature and producing lower tar emissions (thought to be due to cracking catalysed by CaO). The process has been modeled [42] and has been subject to much larger trials in an 8 MWth fuel input Combined Heat and Power (CHP) unit in Guessing, Austria [43], deemed to be successful in demonstrating the feasibility of the AER process on an industrial scale. Results from the AER process should be watched keenly for application of Ca-looping techniques for CO_2 capture with storage.

Figure 1.6 shows a simple schematic of steam gasification of biomass coupled with *in situ* CO_2 capture. Replacement of inert bed material such as silica sand by limestone particles within the dual fluidized bed configuration, gives these limestone particles a dual role of heat carrier and selective sorbent and transporter of CO_2. The calcined limestone (CaO) captures CO_2 under desirable operating conditions for gasification (simultaneous biomass gasification and sorbent carbonation), produces an H_2-rich product gas through equilibrium shift and transports the captured CO_2 in the form of $CaCO_3$ to the regenerator. Within the regenerator, the calcium carbonate particles, accompanied by unreacted char, are fluidized by air. Note that this system is capable of producing a concentrated stream of CO_2 if pure oxygen or an oxygen-enriched air stream is used for the calciner/combustor. Burning char particles (and additional fuel) within the regenerator, provides the heat of sorbent calcination and thus regenerates a hot solid stream containing lime (CaO) to be circulated back to the gasifier.

A number of researchers have investigated the possibility of using the integrated reaction scheme for gasification of solid fuels, e.g., coal and biomass. Lin *et al.* (2004a) [44] developed a process named ‘HyPr- RING’, involving high-pressure steam-gasification of coal in the presence of CaO. They used a continuous pressurized reactor to gasify sub-bituminous coal in the presence of CaO at 650°C and pressures up to 60 atm (steam partial pressure 30 atm). They observed an increase in H_2 concentration with increasing pressure and reported a maximum concentration of 77 vol. % H_2 (dry basis) at 60 atm [45]. Florin and Harris [10] examined the potential of coupling steam gasification with *in situ* CO_2 capture at atmospheric pressure with low-rank fuels, including biomass. The addition of CaO was shown to significantly increase the output of H_2 during

primary pyrolysis of biomass due to the water-gas shift reaction; CaO was also observed to further increase the H_2 output by catalysing tar cracking and char decomposition, based on combined Thermogravimetric Analysis/Mass Spectrometry (TGA-MS) experiments [10].

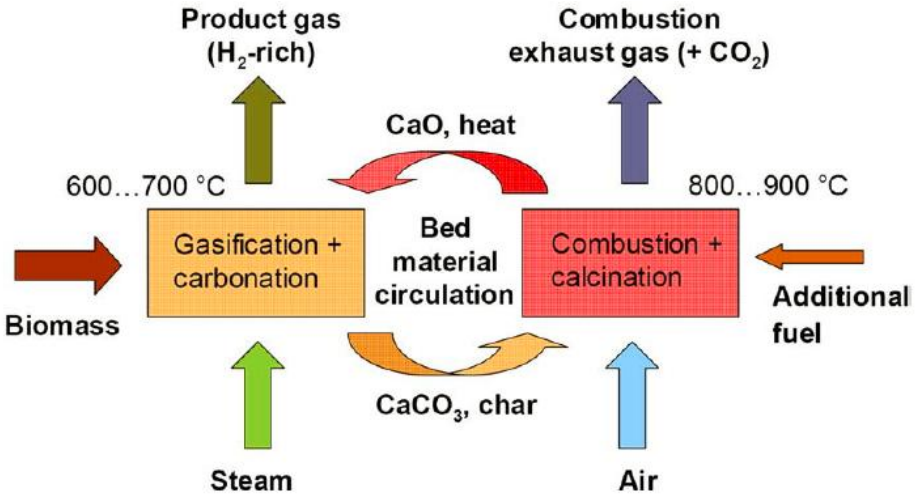

Figure 1.6. Schematic of dual vessel system for lime-enhanced biomass steam gasification [42]. The calcined limestone (CaO) captures CO_2, produces an H_2-rich product gas and transports the captured CO_2 in the form of $CaCO_3$ to the regenerator.

1.3.2 Operability limitations

Although pre-combustion calcium looping systems for CO_2 capture offer the promise of a higher energy efficiency, inherent to H_2 production and downstream conversion routes (i.e. fuel cells or advanced combined cycles fired for H_2), they are still in need of further development and experimental testing at a small scale to obtain relevant design parameters for large scale systems [18]. A number of operability limitations for limestone-enhanced biomass gasification have been identified by previous researchers [10, 28]. In particular, the effectiveness of limestone particles decays due to:

- Loss of specific area due to sintering.
- Pore blockage by $CaSO_4$, originating from the sulfur content of the biomass.
- Attrition, leading to mechanical fragmentation and entrainment from the system.

Deactivation of sorbent particles due to coke (carbon) deposition covering active CaO sites can also compete directly with the carbonation reaction and hamper effective CO_2 capture [28, 45].

Physical deterioration due to sintering is the main contributor to decreasing CO_2 carrying capacity of the sorbent over repeated cycles [46, 47]. Sintering, mainly attributed to the calcination stage, reduces available surface of the sorbent and increases pore diffusion resistance for carbonation [48]. Scanning Electron Microscope (SEM) images show that sorbent particles subjected to multiple capture and release cycles decrease in micro-porosity and increase in meso-porosity [47], reducing the surface area available for the capture of CO_2. Figure 1.7 compares the general trend for decay of sorbent chemical reactivity as a function of cycle number from different sources. Decay in sorbent reactivity is seen to be most severe during the first few cycles, then becomes slower as calcium utilization gradually converges to a residual value after a large number of cycles [46, 47].

While Figure 1.7 shows the general trend, the sintering behavior needs to be assessed on a case-by-case basis due to the wide range of impurity levels in different limestones [10]. The negative effects of sintering can be minimized by using a 'mild' calcination environment, in particular moderate calcination temperatures. It has been reported that the conversion capacity and sorbent reversibility are negatively affected by high concentrations of CO_2 in the calcination environment [48]. If an inert gas stream is applied to the calciner, the resulting decrease in the CO_2 partial pressure allows lower calcination temperatures [48]. Steam is a better candidate for sweep gas than air or N_2 due to its higher thermal conductivity, leading to faster heat transfer, and thus higher calcination rates. Another important advantage of steam is that it can be easily condensed from the exhaust gas, providing a higher-purity CO_2 product stream. Recycling a fraction of the product CO_2 stream back to the calciner to generate high CO_2 outlet concentrations (Oxy-Fuel Calcination) promotes sorbent sintering compared to oxygen or air-fired calcination. The presence of SO_2 from the sulfur content of the biofuel has severe negative effects on CO_2 conversion capacity, as sulfation competes with carbonation, leading to sorbent pore blockage by $CaSO_4$ which is impossible to decompose at typical calcination temperatures.

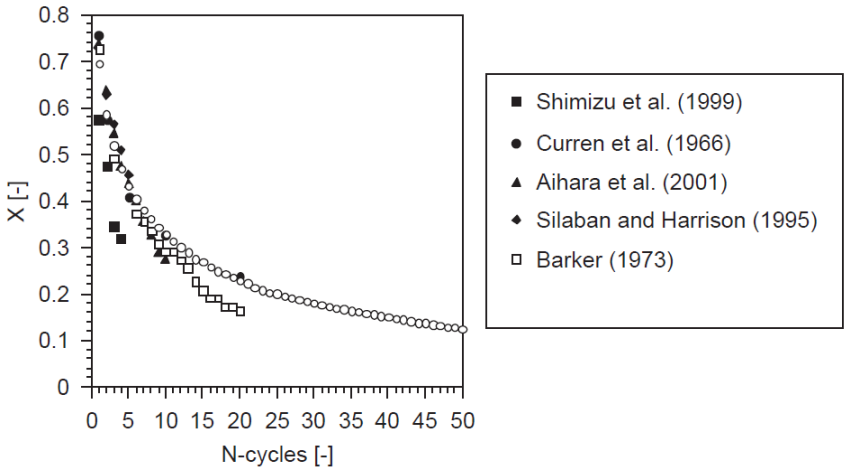

Figure 1.7. Decay in the maximum carbonation conversion as a function of number of cycles [10]. Decay in sorbent reactivity is seen to be most severe during the first few cycles, and then becomes slower as the calcium utilization gradually converges to a residual value after a large number of cycles.

The sulfur contained in solid fuel reacts in the reducing atmosphere of a gasifier to form mainly H_2S. An advantage of calcium-based sorbents in gasifiers is that the H_2S can be removed simultaneously because of the parallel reactions [49]:

Sulfidation: $CaO + H_2S \rightarrow CaS + H_2O$ (1.3)

Direct Sulfidation: $CaCO_3 + H_2S \rightarrow CaS + H_2O + CO_2$ (1.4)

The CaO-H_2S reaction was found to be fast and capable of achieving high, or even complete, conversions [50], whereas the $CaCO_3$-H_2S reaction is much slower and typically achieves much lower conversions [51]. Although particle-size-dependent, both sulfidation and direct sulfidation have usually been reported to be controlled by product layer diffusion [50, 51]. In a practical system, sulfidation will not increase the amount of sorbent required for CO_2 capture very much, given the high stoichiometric ratio of carbon to sulfur in most fuels. However, H_2S competes with CO_2 for fresh CaO, so that a higher extent of sulfidation is unhelpful in achieving good CO_2 capture [49].

For carbonation at lower temperatures (e.g. <700^{o}C), longer reaction times enhance the extent of reaction. After a fast kinetically-controlled stage (near equilibrium), with the reaction rate largely dependent on the surface area of the reacting particles, the CaO-CO_2 reaction turns into an extremely slow diffusion-controlled regime due to $CaCO_3$ product layer formation on the surface of the CaO particles [52]. The shift between these two regimes occurs quickly after the product

layer reaches a thickness of ~10 nm. Due to closure of small pores and accumulated resistance to CO_2 diffusion into the unreacted core of CaO particles, incomplete conversion of CaO to $CaCO_3$ (typically 70-80% of the stoichiometric value) takes place. The calcium utilization decreases further after each carbonation-calcination cycle. To achieve compact design of the carbonator, only the first stage of carbonation reaction (1^{st} order kinetically controlled) is of interest. There is also evidence that partial carbonation of CaO particles within the carbonator substantially improves the overall particle CO_2 carrying capacity and their longevity over long-term cyclic operation [53].

Attrition of limestone particles due to fragmentation is another serious problem. The attrition rate depends on particle properties such as size, surface area, porosity, hardness, cracks, density, shape, strength, as well as reactor characteristics, particle velocity and exposure time. Studies in a dual fluidized bed configuration have demonstrated that rapid initial limestone particle attrition (mostly during the calcination stage) is followed by a more stable period with negligible particle size change [54, 55]. To keep the system in a stable state, one needs to account for attrition. On the other hand, to maintain reactor dimensions and total solid circulation rates within a technically feasible range, the average activity of the sorbent has to be maintained at a sufficient level [56]. Providing sufficient active CaO sites for carbon dioxide capture requires addition of fresh sorbent and adjustment of sorbent circulation rates between the two fluidized beds. High circulation rates, however, are physically and thermally demanding, increasing the rate of fragmentation of the sorbent particles and thus the carryover and loss of fines from the system. High circulation rates also increase the heat requirements for calcination of more carbonated sorbent particles.

Depending on operating conditions, the coverage of active sites of CaO through coke formation (carbon deposition) can compete significantly with carbonation, thereby preventing effective CO_2 capture. Experiments with coal have shown that high concentrations of tar (> 2 g/Nm^3) are likely to occur at moderate temperatures (~650^oC) which are required for simultaneous gasification and carbonation reactions [28, 45]. On the other hand, steam and/or dry reforming of the carbon deposited on CaO have been reported to be fast enough to weaken the effect of coking [4]. Further research is required to elucidate the reaction mechanisms and extent of coke formation.

Research [28, 57] shows that the presence of limestone in biomass gasification affects the entire reaction network in a number of ways. The key parameters found to have major impacts on the outcome of the process should be selected carefully. For example, when selecting the gasifier bed temperature, while high temperature favors endothermic cracking and reforming of tar, it could prevent the exothermic carbonation reaction, to the point where CaO particles are unable to capture CO_2 [28]. Reduced CO_2 capture efficiency and low yield of H_2 production would then occur.

1.3.3 Advanced sorbents

The development of a CO_2 sorbent, which is resistant to physical deterioration and maintains high chemical reactivity through multiple CO_2 capture and release cycles, is the limiting step in the scale-up and commercial operation of coupled gasification-CO_2 capture processes [10]. Encouraged by findings that calcined dolomite ($MgCO_3$–$CaCO_3$) has superior CO_2 capture performance, compared to limestone, several investigators have attempted to improve the multi-cycle performance of CaO by incorporating CaO into an inert porous matrix, such as calcium titanate ($CaTiO_3$) [58] and alumina (Al_2O_3) [59, 60]. A novel extension of this idea is the development of a combined sorbent and catalyst, called 'core-in-shell' sorbent, which incorporated CaO, alumina as the core material and Ni-catalyst embedded in a hard alumina shell. There is merit in investigating the incorporation of foreign ions into the CaO crystal structure to enhance CO_2 capture rates during the diffusion-controlled regime. Superior multi-cycle performance using nano-sized sorbent particles suggests that there is an opportunity for process enhancement by introducing tailored Ca-based CO_2 sorbents, incorporating nanomaterials in an inert porous matrix. Another promising approach involves a precipitation technique for synthesizing $CaCO_3$ with tailored morphological properties. Strategies to counteract attrition, such as pelletisation of highly reactive materials, have succeeded in reducing, though not in eliminating, this problem.

1.4 Reactor modeling

Lime-enhanced biomass gasification in a dual fluidized bed has recently captured wide attention, with an ongoing quest to enhance the economic feasibility of the process [18]. Engineering techniques such as modeling, simulation and heat integration are invaluable tools which can be used to optimize trade-offs, taking into account the process, energy, economic and environmental constraints.

For biomass gasifiers, previous reactor models range from simple equilibrium models, useful for overall estimation of the process [61, 62], to comprehensive kinetic models, which take into account a complicated network of kinetic reactions, mass and heat balances and hydrodynamic constraints to predict species concentrations, solids hold-up and temperature profiles along the reactor [63-66]. Each type of model has its strengths and limitations. Equilibrium models possess generic applicability for simulating different gasifier configurations as they are independent of gasifier design and not limited to a specified range of operating conditions. However, experimental results show that some gasification reactions do not reach equilibrium due to kinetic, heat and mass transfer limitations. Kinetic models, on the other hand, are capable of estimating the composition of product gas with varying operating conditions, which is essential for designing, evaluating and improving gasifiers. Nevertheless, the problem with kinetic models is that many of the reactions are catalyzed by solids and the reaction kinetics are highly dependent on metallic components of biomass fuel and therefore always difficult to represent accurately.

Equilibrium models are important to predict the highest gasification or thermal efficiency that could possibly be attained for a given feedstock. Based on the second law of thermodynamics, the chemical equilibrium for a reacting system is achieved when its Gibbs free energy is minimized. Therefore, the solution of chemical equilibrium problems is to find the set of species compositions which minimize the total free energy.

There are two formulations of the equilibrium conditions, stoichiometric and non-stoichiometric, leading to two approaches to equilibrium modeling [62]. Although essentially equivalent, these two formulations differ in many ways. The widely used stoichiometric formulation requires a

clearly-defined reaction mechanism, expressed by a set of simultaneous reversible chemical reactions [62]. In stoichiometric formulations, it is possible to simplify the complex chemical reaction systems in gasification or combustion reactors into lumped mechanisms, with a small number of reactions involving a limited number of species. The quality of the solution depends on the appropriateness of the lumping mechanism. Furthermore, in biomass gasification where the chemical formula of the biomass feed is either unknown, or identified as a mixture of a large number of chemical species, it is difficult to choose a few particular compounds to represent the equilibrium constants of the reactions. In stoichiometric modeling, one assumes a composition of pyrolysis products, with a few major species as inputs for numerical solution. Although this method is simple and practical, it deviates from reality and implies that the numerical solution only commences after the pyrolysis stage [62]. In a non-stoichiometric formulation, on the other hand, no particular reaction mechanism or species is required for the numerical solution. The only input needed to specify the feedstock is the elemental composition, which can be readily obtained from the ultimate analysis. Since there is no need to reduce a complex reaction system to a simplified mechanism with a few reactions, the Gibbs free energy found by the numerical model is guaranteed to be a global minimum value. This method is particularly suitable for problems with unclear reaction mechanisms and feed streams whose precise compositions are unknown. The non-stoichiometric formulation is common and is claimed to be applicable, even for complicated reaction networks [62].

Due to its complexity, kinetic modeling of biomass gasifiers is at an early phase. Important information is missing from the circulating fluidized bed gasifier kinetic model of Corella *et al.* [63], mostly due to its proprietary nature. The kinetic model of Radmanesh *et al.* [64], applied to a single bubbling fluidized bed gasifier, contains some useful reaction kinetic information. Lü *et al.* [65] developed a kinetic model of biomass air–steam gasification in a fluidized bed reactor, assuming steady state conditions and instantaneous pyrolysis. The accuracy of this model was tested with experimental data from the literature. The two separate kinetic models developed by Kaushal *et al.* for a bubbling fluidized bed gasifier [66] and a circulating fluidized bed combustor [67] are closest to our purpose because of their similar reactor configuration to the UBC DFB gasifier. However, there is enormous diversity in reaction mechanisms and kinetic rate expressions in the literature for biomass gasification. The reaction rates may differ by 2-3 orders

of magnitudes from one reference to another, making the kinetic modeling of biomass gasification uncertain. In developing models, various assumptions are included to simplify the models for practical applications. For instance, while some assume instantaneous drying and pyrolysis, others consider these phenomena to be crucial components of the model [66, 68]. Moreover, although the gasification product gas is often assumed to be free from tar [69], some models include a sub-model for tar generation and cracking [68].

The majority of models for integrated biomass gasification and CO_2 capture are based on thermodynamic equilibrium, with a few models based on reaction kinetics. Thermodynamic equilibrium is considered the upper limit for representing fuel conversion. Equilibrium models developed in Aspen Plus have been used to identify a suitable operating window for sorbent-enhanced biomass gasification [29, 30, 56, 70]. Proell *et al.* [42] developed a process simulation model for gasification of biomass in a dual fluidized bed gasifier with and without lime-based CO_2 capture in IPSEpro equation-oriented steady state simulation software. According to this study, CO_2 capture enhances the hydrogen content in the product gas and increases the energy efficiency of the process. Ahmad *et al.* [71] simulated pressurized gasification of biomass coupled with CO_2 adsorption for hydrogen production using PETRONAS iCON. They reported that increasing pressure, temperature and steam-to-biomass ratio increase the hydrogen yield. The influences of temperature, steam/biomass ratio (S/B) and sorbent/biomass ratio on steam gasification were analyzed by Inayat *et al.* [72] based on MATLAB. The thermodynamic efficiency of the gasifier was observed to increase with increasing temperature and S/B. Furthermore, they predicted that using CaO as a sorbent in the gasifier increased the thermodynamic efficiency by 10% compared to conventional gasification.

Two comprehensive recent reviews on modeling of fluidized bed biomass gasifiers [13, 73] are helpful to identify the knowledge gaps. Based on a survey of the main reactor models for biomass gasification in fluidized beds, Gómez-Barea and Leckner [13] outlined the following main conclusions: (1) Pyrolysis or devolatilisation is a key step affecting greatly the model results. To support a reliable model, measurements of the gas composition and yield of pyrolysis in laboratory scale at high heating rates with the biomass of interest are required, if such results are not available in literature. (2) Char and tar conversion are the processes whose modeling is least satisfactory. A great research effort is still needed to improve the tar chemistry. (3) There

are still uncertainties about the models structure. There is a lack of comparison with experimental results from large-scale fluidized bed gasifiers. Basu and Kaushal [73] noted that experimental data from commercial plants, required for validation of models, are difficult to obtain due to measurement difficulties. However, such data are necessary to make models comprehensive and reliable. Owing to the lack of representative data, the prediction capability of even the most sophisticated model goes untested. They also question the applicability of models developed for coal gasification for biomass gasification unless suitable modifications are made. The major obstacle is to correctly fit the kinetic parameters based on experimental measurements, to be able to depict a wide range of operating cases.

Table 1.1 compares key properties of the model developed in this thesis with a number of kinetic models of fluidized bed biomass gasifiers reviewed in the literature [7]. As elaborated in the next section, the model developed in this thesis is a one-dimensional two-phase phase kinetic model that includes different features such as reaction kinetics, mass transfer between phases, hydrodynamic calculations and energy balances. Through developing a coupled particle and reactor model, the different phenomena biomass particles experience (e.g. drying, pyrolysis and gasification) upon entrance to a fluidized bed reactor are modeled, leading to better predictions of the overall process. The adopted two-step biomass pyrolysis kinetic mechanism allows for predicting tar generation and cracking, as well as predicting pyrolysis products yield and composition. By using ultimate analysis to define tar as a mixture of carbon, hydrogen and oxygen, uncertainties in tar measurement and analysis are addressed. Another contribution of the thesis model is the incorporation of *in situ* CO_2 capture integrated with biomass steam gasification.

Table 1.1. Summary of kinetics models of fluidized bed biomass gasifiers.

Authors	Reactor type, operation mode, biomass and gasifying agent	Model dimension, multiphase modeling approach	Fundamentals of model formulation
Fiaschi and Michelini, 2001 [69]	BFBG Dynamic Sawdust Air and oxygen	1 dimensional Two-phase (bubble and dense phases)	-Reaction kinetics (in dense phase), mass transfer between the phases, quantitative estimation of local bubble and particle properties -Freeboard area considered chemically inert -Instantaneous dying and devolatilization -Tar content assumed to be assimilated in CH_4
Hamel and Krumm, 2001 [68]	BFBG Straw Air, air-steam and oxygen-steam	Two-phase (bubble & emulsion phases)	-Reaction kinetics (including drying and devolatilization), bed and freeboard hydrodynamics -Predict amount of tar in product gas
Sadaka *et al.*, 2002 [74]	BFBG Dynamic and steady state Agricultural waste- Straw Air-steam	Two-phase (bubble & emulsion phases)	-Kinetic parameters and hydrodynamics, transport and thermodynamic properties of fluidized bed -Free energy minimization used to calculate gas mole fractions in the devolatilization stage
Petersen and Werther, 2005 [75]	CFBG Dynamic Sewage sludge Air and CO_2/N_2-mixture	1.5 dimensional (pseudo two dimensional) Core-annulus approach	-Fluid dynamics of CFBG, kinetics of pyrolysis and gasification steps -Benzene taken as model component for biomass tar
Petersen and Werther, 2005 [76]	CFBG Dynamic Sewage sludge Air	3 dimensional Core-annulus approach	-Uses continuous radial profiles of velocities and solids hold-up to describe fluid mechanics

Authors	Reactor type, operation mode, biomass and gasifying agent	Model dimension, multiphase modeling approach	Fundamentals of model formulation
Corella and Sanz, 2005 [63]	CFBG Steady state Pine wood Air	1 dimensional Core-annulus approach	-Reaction kinetics, mass and energy balances, with sub-model for tar generation-elimination and some empirical aspects
Radmanesh *et al.*, 2006 [64]	BFBG Dynamic Beech wood Air	1 dimensional Two-phase (bubble and Emulsion phases)	-Takes into account pyrolysis and various heterogeneous and homogeneous reaction kinetics, as well as hydrodynamics of bed and freeboard. -Solid phase (char) modeled by countercurrent back-mixing model. -First-order kinetic models of Boroson *et al.* and Bryden *et al.* used to represent homogenous cracking of tar and combustion of tar respectively.
Lu *et al.*, 2008 [65]	BFBG Steady state Wood	1 dimensional Two-phase (bubble and emulsion)	-Reaction kinetics, axial gas dispersion in both phases -Pyrolysis taken to be instantaneous
Kaushal *et al.*, 2008 [67]	BFBG Steady state Biomass char Steam and air	1 dimensional Bottom bed: two-phase (bubble and emulsion phases) Freeboard: core- annulus	-Plug flow in both phases with mass exchange between phases. -Sub-models for bed hydrodynamics, conversion and conservation (mass and energy)
Kaushal *et al.*, 2010 [66]	BFBG Steady state Wood Air, oxygen, steam	1 dimensional Two-phase (bubble and emulsion phases)	-Global reaction kinetics, mass & energy balances, hydrodynamics, material properties and sub-model for tar generation and cracking

Authors	Reactor type, operation mode, biomass and gasifying agent	Model dimension, multiphase modeling approach	Fundamentals of model formulation
Gordillo and Belghit, 2011 [77]	BFBG Dynamic and steady state Biomass char Steam	1 dimensional Two-phase (bubble and emulsion phases)	-Reaction kinetics, mass and energy balances -Mass and heat transfer occur only between bubbles and emulsion and between emulsion and solid particles
Linbo *et al.*, 2016 [78]	DFBG Steady-state Wood pellets Steam	1 dimensional Bottom bed: two-phase (bubble: PFRs in series and emulsion: CSTRs in series) Freeboard: CSTRs in series	-Hydrodynamic and kinetic parameters -Heat and mass transfer between phases -Instantaneous biomass pyrolysis with product distribution from empirical correlation -Phenol used as tar model compound
Model developed in this thesis	DFBG Steady-state Pine sawdust Steam	1 dimensional Bottom bed: two-phase (bubble and emulsion phases) Freeboard: plug flow Riser: two-phase (core-annulus)	-Reaction kinetics, mass transfer between phases, hydrodynamic calculations, global energy balances -Particle reaction model: Progressive Conversion Model with two-step biomass pyrolysis kinetic mechanism -Coupled single particle to reactor model constrained with CHO elemental balances -Kinetic models for predicting tar generation and cracking -*In situ* CO_2 capture with CaO

1.5 Thesis scope and objectives

The overall objective of this research study is to develop a comprehensive reactor model for prediction of the performance of steam gasification of biomass, with and without lime-based CO_2 capture. The predictions should be compared with experimental results from reactors, including the UBC pilot scale DFB reactor. See Appendix A for a schematic and brief description of that facility.

Based on a stepwise approach, Table 1.2 summarizes the steps taken within the scope of this thesis to accomplish the task of modeling Ca-looping in a dual fluidized bed gasifier. The predictions of the models developed in each step are compared with literature experimental data in the process of developing a comprehensive reactor model. The objectives of different parts of this thesis are as follows:

As the first step, reaction kinetic data and mechanisms for biomass drying, pyrolysis, gasification, and combustion as well as sorbent carbonation-calcination in a cyclic operation are acquired from the literature. Fuel-related and process-related operating parameters are obtained from references that are selected for the verification of model predictions.

Chapter 2 develops a single-particle model to study biomass drying, pyrolysis and gasification phenomena. A Progressive Conversion Model is used to describe the drying and pyrolysis of a single non-shrinking biomass particle, taking into account the transport phenomena in a porous medium and change in particle thermo-physical properties during release of volatiles from particles and heat-up to the reactor temperature. To predict biomass pyrolysis products yield and composition, a two-step biomass pyrolysis kinetic mechanism is adopted, with primary pyrolysis simulated by two different reaction kinetic schemes: (a) Three parallel first-order reactions producing primary pyrolysis products (non-condensable gas, tar/bio-oil and char), and (b) A detailed solid state kinetics mechanism based on multiple reactions of lignin, cellulose, and hemicellulose of two important biomass species (poplar and lodgepole pine). Secondary pyrolysis is modeled by two parallel reactions describing homogeneous thermal cracking of tar to non-condensable gas and char. Furthermore, for char gasification, a Shrinking Particle Model with constant density and decreasing diameter is adopted.

In **Chapter 3**, the comprehensive single particle model of biomass drying and pyrolysis from the previous chapter is coupled with an ideal reactor model for a bubbling fluidized bed, with nitrogen as the fluidizing agent. The resulting predictive model provides a useful tool to relate biomass pyrolysis products yield and composition to process operating parameters (e.g. biomass ultimate analysis, reactor temperature, gas residence time, mean solids residence time, biomass particle size and moisture content). In addition to the yields of pyrolysis products that are often modeled as lumped species, the model attempts to address an existing gap of knowledge in predicting the composition of major compounds in pyrolysis gas, based on a few simplifying assumptions and CHO elemental balances. The predictions are compared with available experimental data of a bench-scale bubbling fluidized bed reactor from the literature.

Chapter 4 extends the coupled particle and reactor model of biomass drying and pyrolysis in a BFB reactor to develop a kinetic model for steam gasification of biomass in a BFB gasifier. This is achieved by including heterogeneous and homogeneous gasification reactions on the particle and reactor level. The accuracy of the gasifier model is tested by comparing predictions with independent experimental data of a pilot-scale bubbling fluidized bed gasifier from the literature.

In **Chapter 5**, the kinetic gasifier model from the previous chapter evolves into a comprehensive version of two-phase kinetic model of a bubbling fluidized bed gasifier. By incorporating reaction kinetics and reactor hydrodynamics, the two kinetic models of biomass steam gasification in the BFB and char (and natural gas) combustion with air in the CFB riser of the UBC DFB reactor are developed and integrated by performing mass and energy balances over both reactors. These models are capable of predicting species concentrations, solids hold-up, temperature, pressure and superficial gas velocity profiles along each reactor, as well as key operating parameters such as solids circulation rate and natural gas flow rate required for stable operation of the process. Experimental data from the UBC dual fluidized bed gasifier runs is required to test the accuracy of the model.

A model is developed in **Chapter 6** to capture the essence of integrated biomass gasification with cyclic CO_2 capture in a dual fluidized bed reactor, with limestone particles constituting all or a fraction of the bed material. Conversion of solid biomass particles to the dominant gaseous products (H_2, CO, CH_4 and CO_2) is modeled in this chapter only by a simple stoichiometric

equilibrium model. By adopting an empirical kinetic model for the carbonation rate of limestone particles from the literature, the effect of sorbent loss of reactivity due to sintering during cyclic operation is also taken into account.

Chapter 7 modifies the two-phase kinetic model of UBC DFB gasifier developed in Chapter 5 to also account for the effects of lime-based CO_2 capture under cyclic operation.

In **Chapter 8**, overall conclusions are summarized, and recommendations for future research are elaborated.

Table 1.2. Research scope of this thesis

Acquiring accurate reaction kinetics data and mechanism for: • biomass drying, pyrolysis, gasification, combustion, • sorbent carbonation, calcination, • catalytic effects of ash and sorbent, etc.	Developing single particle model that takes into account reaction kinetics, transport phenomena in porous medium, change in particle physical and thermo-physical properties (e.g. porosity, heat capacity, conductivity, permeability, density, size, shape, etc.) during biomass drying, pyrolysis and gasification	Coupling single particle model of biomass drying and pyrolysis with a hydrodynamic reactor model of BFB reactor with N_2 as the fluidizing gas to predict product yields and compositions constrained by CHO elemental balances (steady-state conditions)	Kinetic modeling of biomass drying, pyrolysis and gasification in a BFB with steam as the fluidizing gas to predict product yields and composition from steam gasification of biomass (steady-state conditions)	One -dimensional two-phase kinetic modeling of DFB gasifier with biomass drying, pyrolysis and gasification in a BFB and char (fuel) combustion in a CFB (steady-state conditions)	Equilibrium and kinetic modeling of DFB gasifier coupled with Ca-looping to increase the H_2 content of product gas and capture CO_2 (steady-state conditions)
Obtaining detailed information about process operating parameters: • **Fuel-related:** Molecular composition (cellulose, hemicellulose and lignin content), ultimate and proximate analysis, other physical qualities such as size, shape and density of the fuel particles • **Process-related:** Design and operation of the gasifier itself.					
	Chapter 2	**Chapter 3**	**Chapter 4**	**Chapter 5**	**Chapters 6 & 7**

Chapter 2: Single Particle Model of Biomass Pyrolysis and Gasification

Upon entering a fluidized bed gasifier, biomass particles are exposed to very high heating rates causing a rapid increase in the particle temperature, evaporation of moisture and devolatilization into volatile matter that constitutes more than 80% of the original dry particle mass. The rest remains in the form of solid char which is subsequently mostly consumed in heterogeneous gasification reactions in the presence of an oxidizing agent such as air or steam. Due to the difference in time scales, it is computationally expensive to develop a combined pyrolysis and gasification single particle model. As a compromise between the complexity and applicability of models, we assume pyrolysis and gasification to be consecutive processes. This is a fair assumption because during biomass drying and pyrolysis, the gasifying agent may not reach the particle surface due to much higher evaporation and devolatilization fluxes compared to gas diffusion fluxes, whereas during gasification, the gasifying agent from the bulk gas stream is transported to the char surface, where it reacts heterogeneously. Without any ash layer formation, the char particle shrinks during gasification, finally disappearing. As schematically illustrated in Figure 2.1, a Progressive Conversion Model (PCM) is used to describe the drying and pyrolysis of a single non-shrinking biomass particle which takes into account the transport phenomena in a porous medium and change in particle thermo-physical properties during particle heat-up to the reactor temperature. Furthermore, for char gasification, a Shrinking Particle Model with constant density and decreasing diameter with isothermal conditions within the char particle is assumed. The Shrinking Particle Model combines the kinetic and external mass transfer resistances to predict the effect of particle size on char gasification. Although for low bulk temperatures (up to ~1000 K), reaction kinetics control char gasification, at higher bulk temperatures gas diffusion (mass transfer) resistances cannot be neglected [66]. For a critical review of the literature on kinetic modeling of biomass pyrolysis and gasification in a BFB reactor, see the introductory section of Chapter 3.

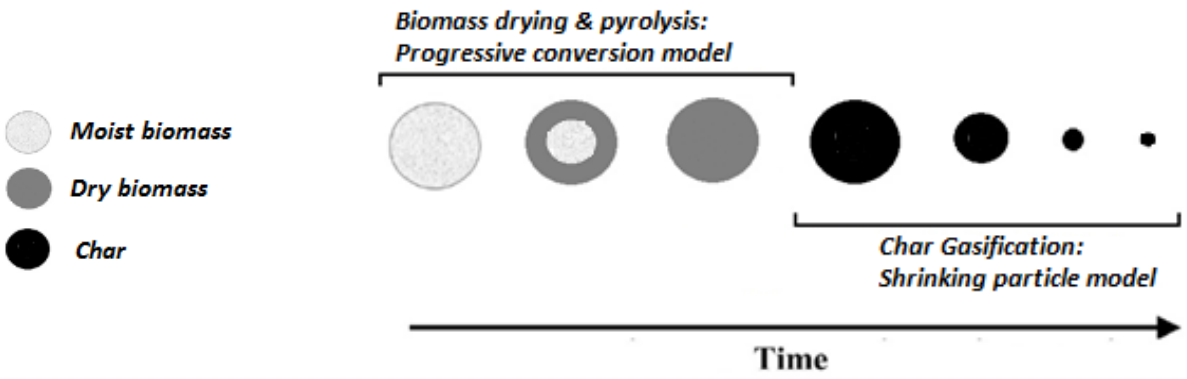

Figure 2.1. Particle reaction model schematic. Biomass drying and pyrolysis: Progressive Conversion Model with constant particle size. Char gasification: Shrinking Particle Model with constant density.

2.1 Biomass drying and pyrolysis model

During drying and pyrolysis, biomass particles act as porous media, allowing outflow of water vapor and volatiles into the reactor environment. To study transport phenomena with reaction kinetics inside a biomass particle, a single particle model is developed for drying and pyrolysis in which temperature and concentration gradients inside the particle of changing thermo-physical properties are modeled based on conservation of mass, energy and momentum. For small enough particles (<1 mm in diameter), the effect of particle volume shrinkage during thermo-degradation is negligible [79] and the pyrolysis of single unchanging-size biomass particles is described by the Progressive Conversion Model [80], in which a constant biomass particle size is assumed, while its density decreases due to increasing porosity during the course of the reaction. Based on the following simplifying assumptions, a detailed particle model for biomass drying and pyrolysis is developed:

1. Local thermal equilibrium between gas and solid phases inside biomass particles.
2. Ideal gas law for all volatiles (gas and bio-oil) released from biomass pyrolysis.
3. Un-changing particle size and shape during the drying and pyrolysis process, i.e. shrinkage, cracking and fragmentation are neglected.
4. First-order chemical reactions with constant heats of reaction are assumed for drying and pyrolysis.

If m_{B0} denotes the initial mass of a dry biomass particle and m_{Cf} is the mass of final char in the completely-converted particle, the dry-ash-free biomass conversion is defined as:

$$X_B = \left(m_{\mathrm{B}0} - \left(m_{\mathrm{B}} + m_C\right)\right) \Big/ \left(m_{\mathrm{B}0} - m_{Cf}\right) \tag{2.1}$$

where m_B and m_C are the instantaneous masses of biomass and char in the solid particle, respectively. The dry-ash-free biomass conversion can also be written in terms of mass densities of biomass and char at constant particle volume as:

$$X_B = \left(\rho_{\mathrm{B}0} - \left(\rho_{\mathrm{B}} + \rho_C\right)\right) \Big/ \left(\rho_{\mathrm{B}0} - \rho_{Cf}\right) \tag{2.2}$$

Figure 2.2 illustrates the generic two-step biomass pyrolysis reaction mechanism originally proposed by Shafizadeh *et al.* [81] where dry biomass is converted through three competitive paths to non-condensable gas, tar and char during primary pyrolysis. This is followed by secondary pyrolysis at higher temperatures in which thermal cracking of tar generates more gas and char. Parallel to biomass pyrolysis, the evaporation of biomass particle moisture content to water vapor is expressed as an independent chemical reaction [82]. The selected kinetic parameters for primary pyrolysis are adopted from Di Blasi *et al.* [83] who examined the kinetics of primary degradation of thin layers of beech wood powder (150 μm) in a tube furnace in the 300–435^{o}C temperature range with high heating rates (1000 K/min) under kinetically-controlled and isothermal conditions. The kinetic parameters of Di Blasi *et al.* [83] for primary pyrolysis are adopted because this model reproduces correctly the experimental trends. On the contrary, other kinetic parameters are inaccurate because of the use of large particles which clearly give rise to heat and mass transfer limitations, very narrow temperature range, secondary reaction activity, and the absence of temperature measurement/control [83]. The kinetic parameters for thermal cracking of tar to non-condensable gas are adapted from Liden *et al.* [84] who correlated experimental data from a flash pyrolysis pilot plant which used whole tree poplar wood and clean aspen-poplar wood in a fluidized bed reactor in the temperature range 500–650^{o}C, also extendable with caution to 400–700^{o}C. For first-order reactions, all reaction rate constants are expressed in Arrhenius form:

$$k_j = k_{0j} \exp\left(-E_j / R.T\right) \tag{2.3}$$

where the kinetic parameters and heats of reaction are summarized in Table 2.1. Note that although heats of reaction are commonly assumed to be constant in the literature, it is also possible to more accurately formulate them as functions of temperature [88].

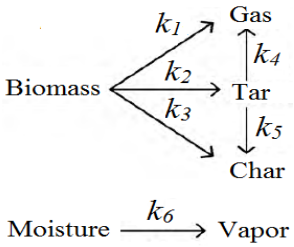

Figure 2.2. Kinetic mechanism of biomass pyrolysis and drying [81, 82].

Table 2.1. Kinetic parameters for biomass drying and pyrolysis.

Rxn.(j)	*k_{0j} (1/s)*	*E_j (kJ/mole)*	*$\Delta H_{rxn,j}$ (kJ/kg)*	*Ref.*
1	*4.38×10^9*	*152.7*	*64*	*[83,85]*
2	*1.08×10^{10}*	*148*	*64*	*[83,85]*
3	*3.27×10^6*	*111.7*	*64*	*[83,85]*
4	*4.28×10^6*	*107.5*	*-42*	*[84,82]*
5	*1×10^5*	*108*	*-42*	*[86,82]*
6	*5.13×10^{10}*	*88*	*2440*	*[87]*

In the particle model, a total of seven species are included where, for simplicity, the densities of the solid phase species, i.e. biomass (B), char (C) and moisture (M), are defined per total particle volume, while the densities of the gas phase species i.e. gas (G), tar (T), water vapor (V) and inert gas (N_2) are defined per pore volume inside the particle. For the solid phase, conservation of mass with constant particle volume gives:

$$\left(\partial \rho_B / \partial t\right) = -\left(k_1 + k_2 + k_3\right).\rho_B \tag{2.4}$$

$$\left(\partial \rho_C / \partial t\right) = k_3.\rho_B + k_5.\left(\varepsilon_P.\rho_T\right) \tag{2.5}$$

$$\left(\partial \rho_M / \partial t\right) = -k_6.\rho_M \tag{2.6}$$

The second term on the right hand side of equation (2.5) is for secondary char generation through repolymerization of tar within the pores of the particle. The particle porosity, ε_P, can be approximated as a linear function of biomass conversion:

$$\varepsilon_P = \varepsilon_{B0}.\left(1 - X_B\right) + \varepsilon_{Cf}.X_B \tag{2.7}$$

where ε_{B0} and ε_{Cf} are the porosities of virgin biomass and final char, respectively.

As the two-step pyrolysis kinetic model is reported to have limitations with regards to decomposition kinetics of different types of biomass with varying properties [89], we also apply a correlation from Mochulski [90] who developed a solid state kinetics model for multiple reactions of biomass pyrolysis based on comprehensive experimental TGA analysis of two specific types of woody biomass (poplar and lodgepole pine) as a function of their lignin, cellulose, and hemicellulose contents:

$$\begin{aligned}\left(\partial X_B/\partial t\right) &= \left[2.74\times10^{12}\,exp\left(-172310/\left(R.T_P\right)\right)\times\frac{3}{2}\left(1-X_B\right)^{2/3}\left(1-\left(1-X_B\right)^{1/3}\right)^{-1}\times 0.06\right] \\ &+\left[1.77\times10^{8}\,exp\left(-113500/\left(R.T_P\right)\right)\times\left(1-X_B\right)\times\left(-0.12\times cellulose+0.72\times hemicellulose+0.67\times lignin\right)\right] \\ &+\left[4.06\times10^{8}\,exp\left(-135000/\left(R.T_P\right)\right)\times 2\left(1-X_B\right)^{1/2}\times\left(1.05\times cellulose+0.62\times lignin\right)\right]\end{aligned} \tag{2.8}$$

where from differentiation of both sides of equation (2.2) with respect to time:

$$\left(\partial X_B/\partial t\right) = -\left(\left(\partial\rho_B/\partial t\right)+\left(\partial\rho_C/\partial t\right)\right)/\left(\rho_{B0}-\rho_{Cf}\right) \tag{2.9}$$

Note that this kinetic model gives the global rate of biomass conversion (i.e. primary pyrolysis) without providing information about the distribution of pyrolysis products. Therefore, two additional adjustable parameters are required to fully predict the pyrolysis products distribution:

$$Biomass \rightarrow Y_C Char + Y_{T,\max} Tar + Y_G Gas \tag{2.10}$$

As a first approximation, we use the fixed-carbon fraction (*FC*) obtained from proximate analysis to estimate the yield of char generation as:

$$\left(\partial\rho_C/\partial t\right) = -FC.\left(\partial\rho_B/\partial t\right) \tag{2.11}$$

where *FC*=10 wt% according to Wagenaar *et al.* [91] who pyrolysed pine in a rotating cone reactor. Upon combination of equations (2.9) and (2.11), the overall rate of biomass consumption is obtained as:

$$\left(\partial\rho_B/\partial t\right) = -\left(\partial X_B/\partial t\right).\left(\rho_{B0} - \rho_{Cf}\right)\Big/\left(1-FC\right) \tag{2.12}$$

As the second adjustable parameter, ultimate tar yield is set as $Y_{T,max}$=0.703 from Liden *et al.* [84] from which the kinetic parameters for thermal cracking of tar to non-condensable gas are adopted.

Assuming a one-dimensional and time-dependent domain and accounting for convective and diffusive transport phenomena of gas phase species inside the pores of the particle, we formulate the gas phase continuity equations as a function of radial coordinate (r) and time (t):

$$\partial\left(\varepsilon_P.\rho_i\right)/\partial t + \left(1/r^n\right).\partial\left(r^n\varepsilon_P.\rho_i.u\right)/\partial r = \left(1/r^n\right).\partial\left(r^n\varepsilon_P.D_{eff,i}.\left(\partial\rho_i/\partial r\right)\right)/\partial r + \begin{cases} i=G:\left(\partial\rho_G/\partial t\right)_{primary} + k_4.\left(\varepsilon_P.\rho_T\right) \\ i=T:\left(\partial\rho_T/\partial t\right)_{primary} - \left(k_4+k_5\right).\left(\varepsilon_P.\rho_T\right) \\ i=V: k_6.\rho_M \\ i=N_2: 0 \end{cases} \tag{2.13}$$

where *n* is 0 for a flat plate or a slab-shaped particle, 1 for a cylindrical particle, and 2 for a spherical particle. The rates of tar and gas generation from primary pyrolysis are calculated for the two kinetic schemes as:

$$\left(\partial\rho_G/\partial t\right)_{primary} = \begin{cases} k_1.\rho_B & \textit{Two - step kinetic model} \\ -\left(1-Y_C-Y_{T,\max}\right).\left(\partial\rho_B/\partial t\right) & \textit{Solid - state kinetic model} \end{cases} \tag{2.14}$$

$$\left(\partial\rho_T/\partial t\right)_{primary} = \begin{cases} k_2.\rho_B & \textit{Two - step kinetic model} \\ -Y_{T,\max}.\left(\partial\rho_B/\partial t\right) & \textit{Solid - state kinetic model} \end{cases} \tag{2.15}$$

Given the overall gas phase density,

$$\rho_g = \sum_{i=G,T,V,N_2} \rho_i \tag{2.16}$$

the overall continuity equation for the gas phase inside the particle is obtained as:

$$\partial\left(\varepsilon_P.\rho_g\right)/\partial t+\left(1/r^n\right).\partial\left(r^n\varepsilon_P.\rho_g.u\right)/\partial r=\begin{cases}\left(k_1+k_2\right)\rho_B-k_5.\left(\varepsilon_P.\rho_T\right)+k_6.\rho_M & \textit{Two-step kinetic model}\\ -\left(1-Y_C\right).\left(\partial\rho_B/\partial t\right)-k_5.\left(\varepsilon_P.\rho_T\right)+k_6.\rho_M & \textit{Solid-state kinetic model}\end{cases} \tag{2.17}$$

In equation (2.13), $D_{eff,i}$, the effective diffusion coefficient of gaseous species i is obtained from D_i the molecular diffusivity of ith species (neglecting the contribution of Knudsen diffusion):

$$D_{eff,i}=\left(\varepsilon_P.D_i\right)/\tau \tag{2.18}$$

where τ is the tortuosity[1] and ε_P is the porosity of the particle. In equation (2.17), u is the one-dimensional gas phase velocity calculated from Darcy's law inside a porous medium as:

$$u=-\left(\beta_{g,P}/\mu_g\right).\left(\partial P/\partial r\right) \tag{2.19}$$

where the dynamic viscosity of the gas phase is calculated as:

$$\mu_g=\sum_{i=G,T,V,N_2}\left(\rho_i.\mu_i\right)/\rho_g \tag{2.20}$$

and the permeability of the gas phase is approximated by a linear function of conversion:

$$\beta_{g,P}=\beta_{g,B0}.\left(1-X_B\right)+\beta_{g,Cf}.X_B \tag{2.21}$$

Large variations in permeability of solid biomass and char along and across the grain direction have been reported [93, 94]. In order to account for particle anisotropy, these physical properties are averaged across and along the grain direction [80, 95] as:

$$\beta_{g,B0}=\left(\beta_{g,B0,along}+\beta_{g,B0,across}\right)/2 \tag{2.22}$$

$$\beta_{Cf}=\left(\beta_{g,Cf,along}+\beta_{g,Cf,across}\right)/2 \tag{2.23}$$

[1] As reported in the literature, the tortuosity for biomass particles usually lies between 1.5 and 5 [92]. For modeling purposes of this thesis, the value of 1 is used for simplification.

Note that while ideal gas behaviour can be assumed for the pyrolysis gas, it may not be a suitable assumption for tar (bio-oil) consisting of high-molecular-weight condensable hydrocarbons. Nevertheless, in the absence of a better model, the ideal gas law is commonly used in the literature. Assuming the gas and solid phases are at local thermal equilibrium, the local instantaneous pressure is:

$$P=\left(\rho_g.R.T_P\right)\Big/MW_g \tag{2.24}$$

where the average molecular weight of the gas phase is calculated as:

$$MW_g=\left(\sum_{i=G,T,V,N_2}\left(\rho_i\Big/\left(\rho_g.MW_i\right)\right)\right)^{-1} \tag{2.25}$$

The particle temperature T_P is obtained as a function of time and radial coordinate from an energy balance on a single particle. For porous biomass particles, the energy balance is obtained by combining the gas and solid phases in a single conservation equation [80], expressed in terms of species specific heat capacities (C_p) and densities:

$$\begin{aligned}&\left(\rho_B C_{p,B0}+\rho_C C_{p,Cf}+\rho_M C_{p,M}+\varepsilon_P.\rho_g C_{p,g}\right).\left(\partial T_P/\partial t\right)+\left(\frac{1}{r^n}\right).\partial\left(r^n\varepsilon_P.\rho_g C_{p,g}.T_P.u\right)\Big/\partial r=\left(\frac{1}{r^n}\right).\partial\left(r^n k_{eff}.\left(\partial T_P/\partial t\right)\right)\Big/\partial r\\&-\left\{\left(k_1.\Delta H_{rxn,1}+k_2.\Delta H_{rxn,2}+k_3.\Delta H_{rxn,3}\right).\rho_B+\left(k_4.\Delta H_{rxn,4}+k_5.\Delta H_{rxn,5}\right).\left(\varepsilon_P\rho_T\right)+\left(k_6.\Delta H_{rxn,6}\right).\rho_M\right\}\end{aligned} \tag{2.26}$$

where the heat capacity of the gas mixture is:

$$C_{p,g}=\sum_{i=G,T,V,N_2}\left(\rho_i.C_{p,\mathrm{i}}\right)\Big/\rho_g \tag{2.27}$$

Heat transfer inside the porous structure of biomass particle takes place through complex interaction between the transfer mechanisms: conduction, convection, and radiation [94]. The effective thermal conductivity due to the contribution of both molecular conductivity and radiative thermal conductivity, accounting for radiation in the pore system [80, 93, 94] is:

$$k_{eff} = k_{cond} + k_{rad} \tag{2.28}$$

where k_{rad} can be expressed as a function of third power of particle temperature [94]:

$$k_{rad} = 4.\omega_P.\varepsilon_P.\sigma.T_P^{\,3}.d_{pore}\big/\left(1-\varepsilon_P\right) \tag{2.29}$$

Here $\sigma = 5.67\times10^{-8}\ W/\left(m^2.K^4\right)$ is the Stefan-Boltzmann constant. k_{cond} is dependent on the thermal conductivities of the solid and gas phases [80, 93, 94]:

$$k_{cond} = k_P + \varepsilon_P.k_g \tag{2.30}$$

with the solid phase thermal conductivity [80, 93, 94]:

$$k_P = k_{B0}.\left(1-X_B\right) + k_{Cf}.X_B \tag{2.31}$$

The pore diameter and particle surface emissivity are estimated as:

$$d_{pore} = d_{pore,B0}.\left(1-X_B\right) + d_{pore,Cf}.X_B \tag{2.32}$$

$$\omega_P = \omega_{B0}.\left(1-X_B\right) + \omega_{Cf}.X_B \tag{2.33}$$

The thermal conductivity of wood varies with the direction with respect to the grain, as well as with temperature, density, and moisture content. As with the permeability, the thermal conductivities of biomass and char are averaged across and along the grain direction [95]:

$$k_{B0} = \left(k_{B0,along} + k_{B0,across}\right)\big/2 \tag{2.34}$$

$$k_{Cf} = \left(k_{Cf,along} + k_{Cf,across}\right)\big/2 \tag{2.35}$$

After specifying initial and boundary conditions, the coupled partial differential equations describing mass, energy and momentum balances are solved for lumped species densities inside

the particle, as well as particle temperature, gas phase pressure and velocity as functions of one-dimensional radial coordinate (r) and time (t). At time zero:

$$\rho_B(t=0,r)=\rho_{B0}\ ;\ \ \rho_M(t=0,r)=\rho_{M0}\ ;\ \ \rho_C(t=0,r)=0 \tag{2.36}$$

$$\rho_G(t=0,r)=\rho_T(t=0,r)=\rho_V(t=0,r)=0\,;\,\rho_{N_2}(t=0,r)=P(t=0,r).MW_{N_2}/R.T_P(t=0,r) \tag{2.37}$$

$$T_P(t=0,r)=25^oC\ ;\ \ P(t=0,r)=1\,atm\,;\qquad u(t=0,r)=0 \tag{2.38}$$

When a biomass particle is decomposing, the boundary conditions are given in terms of pressure, heat and mass fluxes at the centre and surface of the particle. From symmetry at the particle centre:

$$\left(\partial\rho_i/\partial r\right)\Big|_{t,r=0}=0 \qquad\qquad (i=G,T,V,N_2) \tag{2.39}$$

$$\left(\partial T_P/\partial r\right)\Big|_{t,r=0}=0 \tag{2.40}$$

$$\left(\partial P/\partial r\right)\Big|_{t,r=0}=0 \tag{2.41}$$

Given reactor conditions at the particle surface:

$$-D_{eff,i}.\left(\partial\rho_i/\partial r\right)\Big|_{t,r=R_P}=h_{mass,i}.\left(\rho_i(t,r=R_P)-\rho_{i,bulk}\right) \qquad (i=G,T,V,N_2) \tag{2.42}$$

$$-k_{eff}.\left(\partial T_P/\partial r\right)\Big|_{t,r=R_P}=h_{conv}.\left(T_P(t,r=R_P)-T_{bulk}\right)+\omega_P.\sigma.\left(T_P{}^4(t,r=R_P)-T_{wall}^4\right)+q_{flux} \tag{2.43}$$

$$P(t,r=R_P)=1\,atm \tag{2.44}$$

where $h_{mass,i}$ and $\rho_{i,bulk}$ are the mass transfer coefficient and bulk density of i^{th} species inside the reactor, h_{conv} is the convective heat transfer coefficient, T_{bulk} the bulk gas temperature inside the reactor, T_{wall} reactor wall temperature and q_{flux} is the heat flux from a heat source, such as a furnace or arc lamp (not considered in our case). As a first approximation, the bulk densities of gas phase species (except for the fluidizing medium N_2) are assumed to be negligible compared

to species densities at the surface of the particles i.e. $\rho_{i,bulk} \ll \rho_i\left(t, r = R_P\right)$ and the reactor wall temperature is approximated to be the same as the bulk gas temperature i.e. $T_{wall} \cong T_{bulk}$. The convective heat transfer coefficient between the bulk gaseous phase and the biomass particle in the dense bed is calculated using correlations for forced convection around submerged objects [96]. Agarwal *et al.* [97] provided an equation to calculate the convection coefficient in the dense bed for devolatilization of spherical coal particles (diameter d_p) in fluidized beds:

$$Nu = h_{\text{conv}}.d_p/k_g = \begin{cases} 0.03.Re_p^{1.3} & Re_p < 100 \\ 2 + 0.6.Pr^{1/3}.Re_p^{1/2} & Re_p > 100 \end{cases} \tag{2.45}$$

where the Reynolds and Prandtl numbers are based on bulk gas physical properties:

$$Re_p = \rho_{bulk}.U_{bulk}.d_p/\mu_{bulk} \tag{2.46}$$

$$Pr = \mu_{bulk}.C_{Pbulk}/k_{bulk} \tag{2.47}$$

Through analogies, mass transfer coefficients for each species can be approximated from the Sherwood number and Frössling equation [98]:

$$Sh = h_{mass,i}.d_p/D_{eff,i} = 2 + 0.6.Sc^{1/3}.Re_p^{1/2} \tag{2.48}$$

where the Schmidt number is:

$$Sc = \mu_{bulk}/\left(\rho_{bulk}.D_{eff,i}\right) \tag{2.49}$$

The thermo-physical and transport properties of the biomass, final char and gas phase species are summarized in Table 2.2. For a given set of process conditions, the final char density is calculated iteratively from the particle model. Koch [99] and Grønli *et al.* [94] correlated the specific heat of pine and spruce as linear functions of temperature. Consistent with [94], we use the data from [100] to correlate the heat capacity of the solid and gas species and dynamic viscosity of the gas phase species as functions of temperature. Constant molecular weight, thermal conductivity and molecular diffusivity of the gas phase are assumed, with values given

in Table 2.2. More accurate estimation of thermo-physical properties is possible after determining the compositions of tar and gas from elemental balances.

Table 2.2. Thermo-physical and transport properties of gas and solid species.

Property	*Ref.*	*Property*	*Ref.*
$C_{p,Pine}\left[J/kg.K\right] = -91.2 + 4.4 \times T_P\left[K\right]$	*[94]*	$MW_G = 38\ g/mol$	*[94]*
$C_{p,Spruce}\left[J/kg.K\right] = 1500 + T_P$		$MW_T = 110\ g/mol$	
$C_{p,Cf}\left[J/kg.K\right] = 420 + 2.09 \times T_P - 6.85 \times 10^{-4} \times T_P^{\ 2}$		$\mu_G\left[kg/m.s\right] = 7.85 \times 10^{-6} + 3.18 \times 10^{-8} \times T_P$	*[94]*
$C_{p,G}\left[J/kg.K\right] = 770 + 0.629 \times T_P - 1.91 \times 10^{-4} \times T_P^{\ 2}$		$\mu_T\left[kg/m.s\right] = -3.73 \times 10^{-7} + 2.62 \times 10^{-8} \times T_P$	
$C_{p,T}\left[J/kg.K\right] = -100 + 4.4 \times T_P - 1.57 \times 10^{-3} \times T_P^{\ 2}$		$\mu_V\left[kg/m.s\right] = -1.47 \times 10^{-6} + 3.78 \times 10^{-8} \times T_P$	
$C_{p,V}\left[J/kg.K\right] = 1670 + 0.64 \times T_P$		$\mu_{air}\left[kg/m.s\right] = 9.12 \times 10^{-6} + 3.27 \times 10^{-8} \times T_P$	
$C_{p,air}\left[J/kg.K\right] = 950 + 0.188 \times T_P$		$\beta_{g,B0,along} = 10^{-11}\ m^2$	*[95]*
$d_{pore,B0} = 5 \times 10^{-5}\ m$	*[94]*	$\beta_{g,B0,across} = 10^{-14}\ m^2$	
$d_{pore,Cf} = 10^{-4}\ m$		$\beta_{g,Cf,along} = 5 \times 10^{-11}\ m^2$	
$D_g = 10^{-6}\ m^2/s$	*[82]*	$\beta_{g,Cf,across} = 5 \times 10^{-12}\ m^2$	
$k_{B0,along} = 0.255\ W/m.K$	*[95]*	$\varepsilon_{B0} = 0.4$	*[80]*
$k_{B0,across} = 0.1046\ W/m.K$		$\varepsilon_{Cf} = 0.91$	
$k_{Cf,along} = 0.105\ W/m.K$		$\rho_{B0} = 570\ kg/m^3$	
$k_{Cf,across} = 0.071\ W/m.K$		$\omega_{B0} = 0.6$	*[80]*
$k_g = 2.577 \times 10^{-2}\ W/m.K$		$\omega_{Cf} = 1$	

The continuity equations are solved using the MATLAB PDE solver (PDEPE) which solves initial-boundary value problems of parabolic and elliptic type with one space and one time variable. Based on a specified grid size, the solver converts the PDEs to ODEs and, for a given time step, the ODEs are integrated with respect to time by the MATLAB differential-algebraic equation solver. Details of converting the differential equations into the acceptable format of MATLAB PDE solver are provided in Appendix B.

2.2 Char gasification model

The char gasification process involves transportation of gasifying agent(s) from the main body of gas to the char surface and heterogeneous gasification reactions at the char surface. Note that the ash layer peels off (if it exists) and does not contribute any resistance. With the neglect of catalytic effects of metal components (e.g. Ca, Na and K) present in ash, the kinetic rate expressions for heterogeneous gasification reactions are listed in Table 2.3. The initial char

particle size (R_{C0}) is the same as the biomass particle size, and its unchanging density (ρ_{Cf}) is calculated from the above biomass pyrolysis model. For shrinking spherical particles, the instantaneous char particle radius (R_C) is estimated from:

$$R_C = R_{C0}\left(1 - X_C\right)^{1/3} \tag{2.50}$$

where the char gasification conversion (X_C) is calculated from numerical integration of heterogeneous gasification kinetics rates with respect to time:

$$dX_C/dt = \left(r_{C1}\right)\Big|_{P_{CO_2}=P_{CO_2,surf}} + \left(r_{C2}\right)\Big|_{P_{H_2O}=P_{H_2O,surf}} + \left(r_{C3}\right)\Big|_{P_{H_2}=P_{H_2,surf}} \tag{2.51}$$

The partial pressures of gasifying agents at the char surface are obtained from the steady-state assumption:

$$\left(m_{C0}/MW_C\right).\left(r_{C1}\right)\Big|_{P_{CO_2}=P_{CO_2,surf}} = 4\pi R_C^2.h_{mass,CO_2}.\left(P_{CO2,bulk} - P_{CO2,surf}\right)\Big/\left(R.T_m\right) \tag{2.52}$$

$$\left(m_{C0}/MW_C\right).\left(r_{C2}\right)\Big|_{P_{H_2O}=P_{H_2O,surf}} = 4\pi R_C^2.h_{mass,H_2O}.\left(P_{H_2O,bulk} - P_{H_2O,surf}\right)\Big/\left(R.T_m\right) \tag{2.53}$$

$$\left(m_{C0}/MW_C\right).\left(r_{C3}\right)\Big|_{P_{H_2}=P_{H_2,surf}} = 4\pi R_C^2.\left(h_{mass,H_2}/2\right).\left(P_{H_2,bulk} - P_{H_2,surf}\right)\Big/\left(R.T_m\right) \tag{2.54}$$

where m_{C0} is the initial mass of char particle, $h_{mass,i}$ is the mass transfer coefficient on the basis of instantaneous diameter of char particle and T_m is the average gas film temperature.

Table 2.3. Major heterogeneous gasification reactions

Gasification reactions		*Reaction kinetics rate expression*	*Ref.*
Boudouard	$C(s)+CO_2 \rightarrow 2CO$ $\Delta H^o_{rxn} = +172\,{}^{kJ}\!/_{mole}$	$r_{C1}\left(s^{-1}\right) = 3.9\times10^4 \exp\left(-215000/R.T\right)\times P_{CO_2}^{0.38}\left[Pa\right]$	*[101]*
Water-Gas	$C(s)+H_2O \rightarrow CO+H_2$ $\Delta H^o_{rxn} = +131\,{}^{kJ}\!/_{mole}$	$r_{C2}\left(s^{-1}\right) = 3.7\times10^5 \exp\left(-237000/R.T\right)\times P_{H_2O}^{0.57}\left[Pa\right]$	*[102]*
Methanation	$C(s)+2H_2 \rightarrow CH_4$ $\Delta H^o_{rxn} = -75\,{}^{kJ}\!/_{mole}$	$r_{C3}\left(s^{-1}\right) = 4.3\times10^{-5} \exp\left(-94800/R.T\right)\times P_{H_2}^{0.93}\left[Pa\right]$	*[103]*

2.3 Predictions of single particle model

For the single particle model, drying and pyrolysis of spherical biomass particles of two different sizes are studied at two different reactor temperatures in an atmospheric bubbling fluidized bed of silica sand with nitrogen as the fluidizing gas[1]. For spherical biomass particles of 5 mm and 500 µm diameters and a reactor temperature of 600^{o}C at atmospheric pressure, the predicted changes in particle conversion and temperature upon entering the reactor are illustrated in Figures 2.3 and 2.4 as functions of time and radial position inside a biomass particle. Note that the first maximum in the curves is due to initial drying of wet biomass particle that precedes biomass pyrolysis, leading to second maxima in Figures 2.3 and 2.4. As seen, the predicted effect of particle diameter on the biomass pyrolysis rate is significant. The time required for complete conversion (drying and pyrolysis) and heat-up to reactor temperature of a single particle is predicted to be approximately one minute for a 5 mm diameter particle and less than 5 s for a biomass particle of 500 µm diameter.

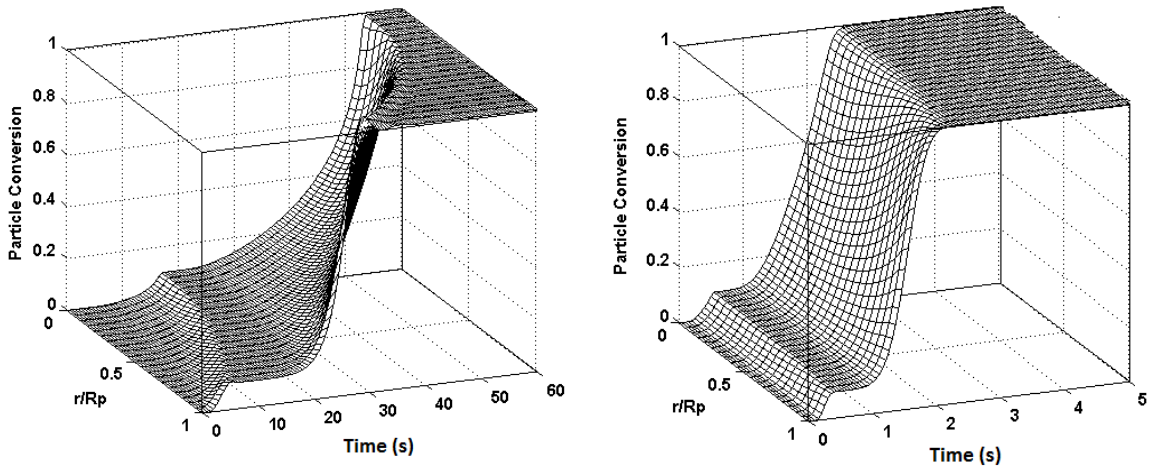

(a) **(b)**

Figure 2.3. Single biomass particle conversion as a function of time and radial position inside particle: (a) d_p=5 mm, (b) d_p=500 µm, reactor temperature=600^{o}C, reactor pressure=1 atm, biomass moisture content= 9 wt%.

[1] See Chapter 3, for a coupled particle and reactor model of biomass drying and pyrolysis in a BFB.

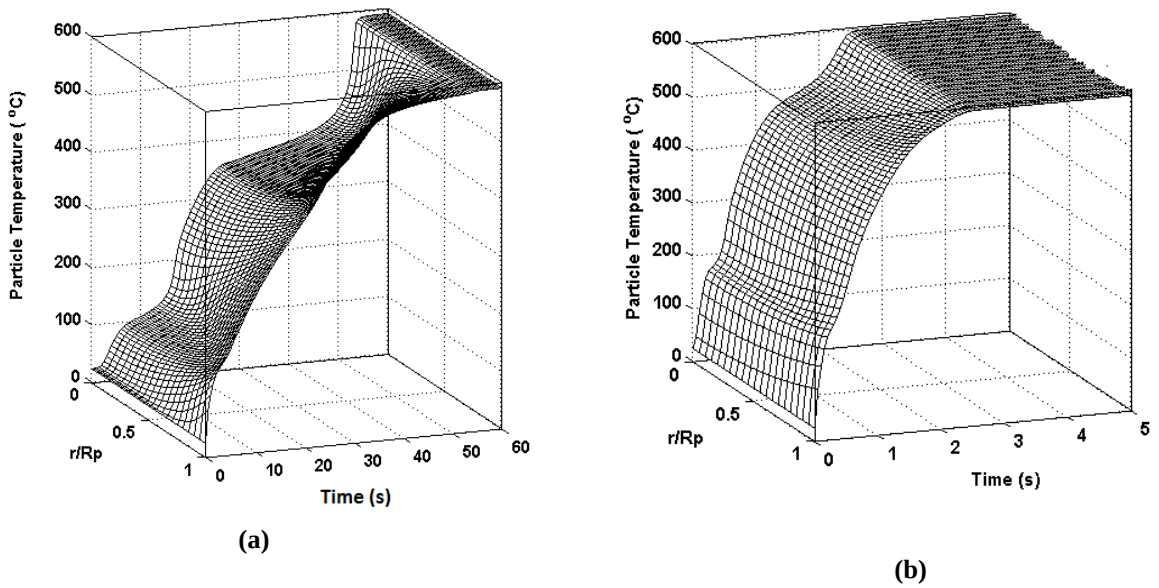

Figure 2.4. Single biomass particle temperature as a function of time and radial position inside particle: (a) d_p=5 mm, (b) d_p=500 µm, reactor temperature=600°C, reactor pressure=1 atm, biomass moisture content= 9 wt%.

Figures 2.5 and 2.6 plot the total particle bulk density (sum of un-reacted biomass, bound moisture and char) and gas-phase density (sum of tar, pyrolysis gas and water vapor) as functions of time and radial position inside the biomass particle, respectively. While the first peak of gas-phase concentration inside the particle is due to accumulation of water vapor from drying, the second peak originates from the accumulation of volatiles generated by biomass pyrolysis. Because of the faster kinetics of drying compared to pyrolysis, the first peak happens within a smaller time scale. Due to evolution of water vapor and volatiles, a negative pressure gradient forms inside the biomass particle, but it disappears with time due to the release of volatiles at the particle surface. Comparing Figures 2.6(a) and (b), the second peak of gas-phase density is considerably greater for the larger particle, demonstrating greater accumulation of pyrolysis products inside the larger particle due to internal mass transfer resistances.

In Figure 2.7, the predicted drying and pyrolysis product yields are compared for the particle diameters of 5 mm and 500 µm, and two reactor temperatures of 600°C and 700°C. As expected, smaller particles and higher reactor temperatures lead to much faster conversion of biomass particles. General agreement of the model predictions is observed with the model of Sharma *et al.* [80], who compared their biomass pyrolsysis particle model predictions with experimental

data of Park *et al.* [85]. Furthermore, the predictions of this model are in satisfactory agreement with the biomass particle pyrolysis model of Haseli *et al.* [88] which was shown to be in good agreement with modeling and experimental data of Wurzenberger *et al.* [104]. Note that no data were found in the literature giving yields of gas-phase products as a function of reaction time.

The effects of particle diameter and reactor temperature on tar, non-condensable gas and char yields are more obvious in Figure 2.8. Due to more secondary tar cracking inside the porous structure of the larger biomass particle, lower tar yield and higher char yield are produced for larger particles. Furthermore, at the lower reactor temperature, lower secondary tar cracking rates leads to increased char contents.

Figure 2.9 illustrates the mass fraction of single char particles (per initial biomass particle mass) for particle diameters of 500 μm and 5 mm as a function of reaction time under atmospheric pure steam and gasification temperatures of 700^{o}C and 750^{o}C. First of all, the mass fraction of unconverted char initially generated from pyrolysis is higher for the larger particle size, and slightly decreases with increasing reactor temperature. Secondly, the time required for complete conversion (gasification) of a single char particle is virtually independent of its initial size, but decreases noticeably with increasing gasification temperature. This implies that char gasification is a kinetically-controlled process for the investigated operating conditions.

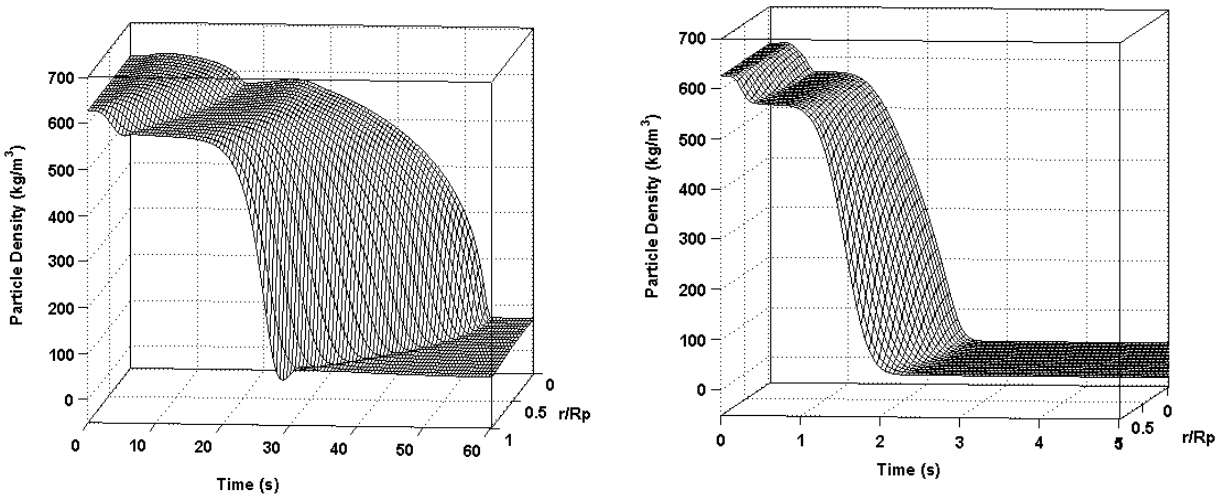

Figure 2.5. Biomass particle density as a function of time and radial position inside particle : (a) d_p=5 mm, (b) d_p=500 µm, reactor temperature=600^{o}C, reactor pressure=1 atm, biomass moisture content= 9 wt%.

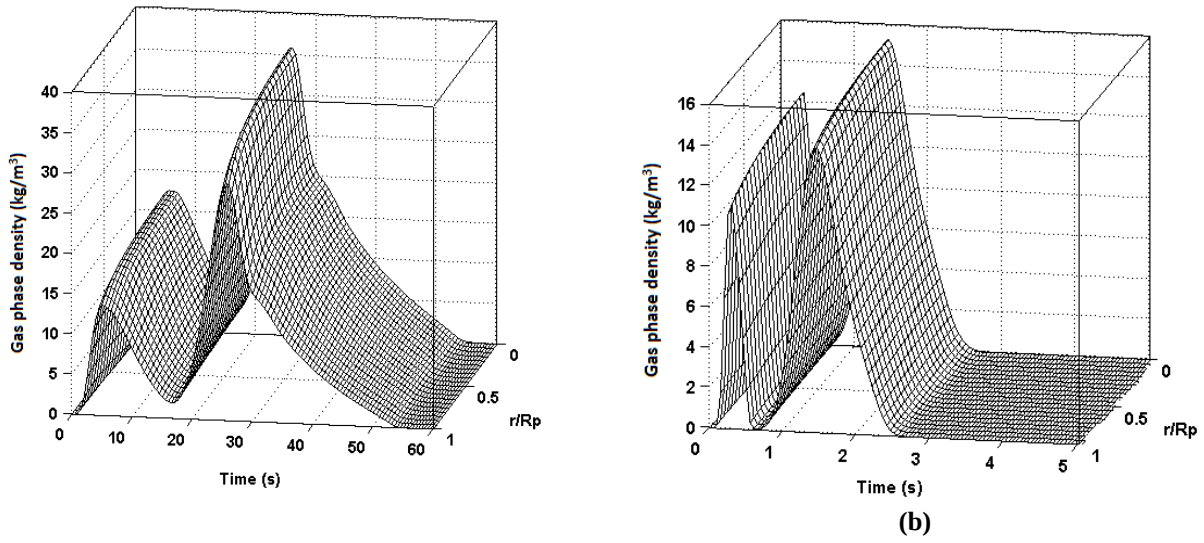

Figure 2.6. Gas-phase density as a function of time and radial position inside particle : (a) d_p=5 mm, (b) d_p=500 µm, reactor temperature=600^{o}C, reactor pressure=1 atm, biomass moisture content= 9 wt%.

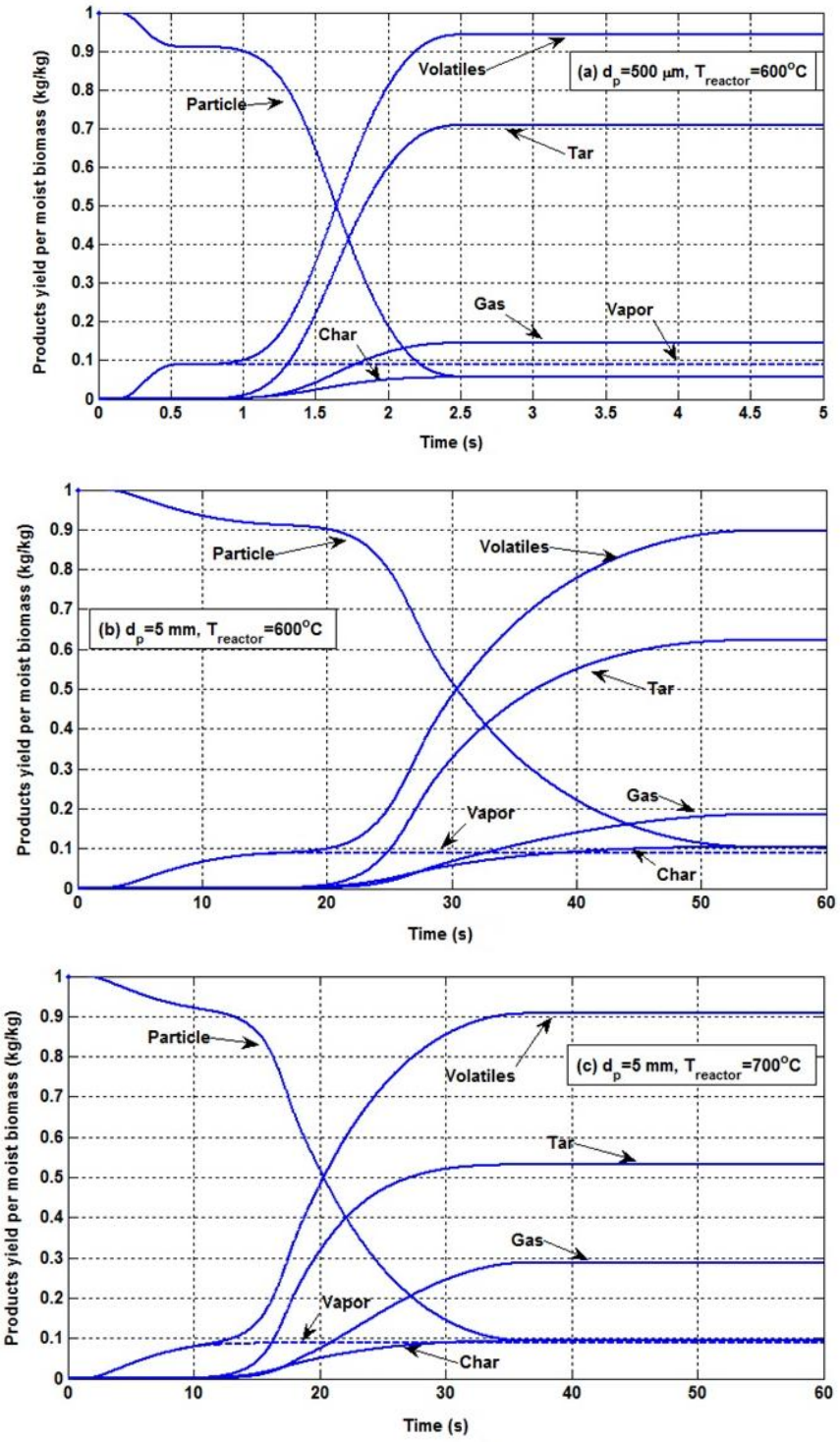

Figure 2.7. Instantaneous drying and pyrolysis product yields for an individual particle : (a) d_p = 500 µm, Reactor temperature = 600°C, (b) d_p = 5 mm, Reactor temperature = 600°C, (c) d_p = 5 mm, reactor temperature = 700°C, reactor pressure = 1 atm, biomass moisture content = 9 wt%.

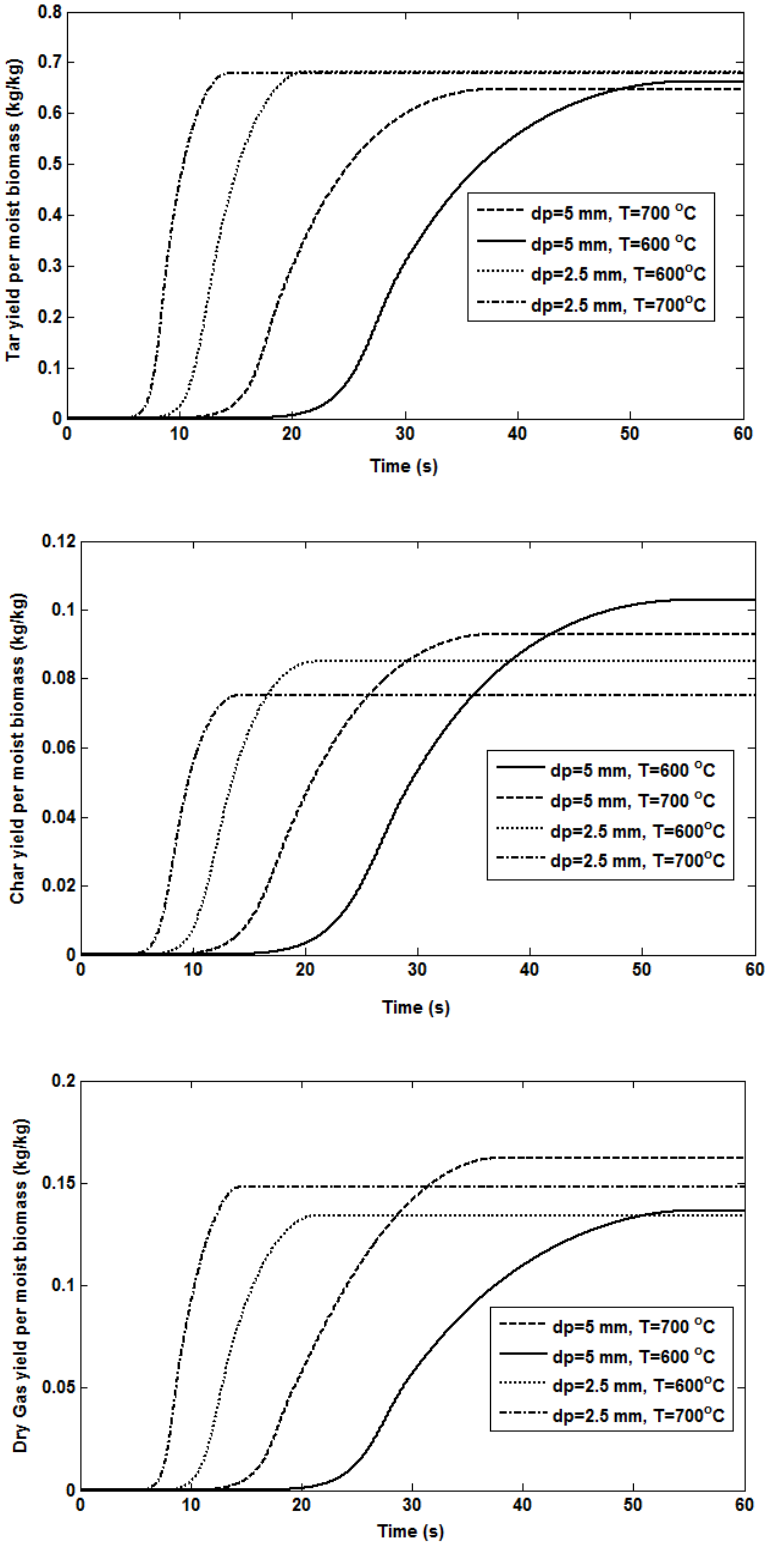

Figure 2.8. Pyrolysis product yield distribution as a function of time for two different biomass particle diameters and reactor temperatures.

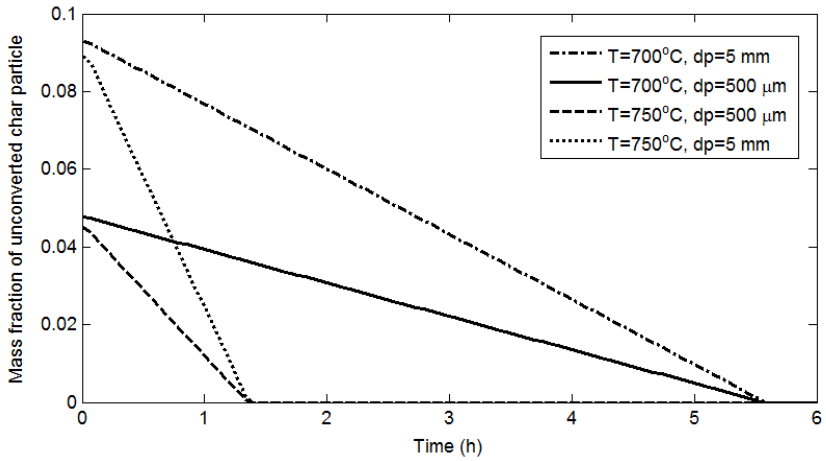

Figure 2.9. Unconverted char mass fraction (per initial biomass particle mass) as a function of time under pure steam gasification for two different char particle diameters and reactor temperatures.

2.4 Summary

The time required for complete drying, pyrolysis and heat-up of a biomass particle to reactor temperature is predicted to decrease strongly with increasing reactor temperature and/or decreasing biomass particle size. Due to evolution and accumulation of water vapor and volatiles, a negative pressure gradient forms inside the porous structure of biomass particle disappearing over time with the release of volatiles at the particle surface. For larger particles, greater accumulation of pyrolysis products is observed, related to increased internal mass transfer resistances. The time required for complete gasification of a single char particle is virtually independent of its initial size, but decreases noticeably with increasing gasification temperature. Although the external mass transfer resistances are negligible for char gasification under the range of operating conditions investigated, they can become important at higher temperatures. Whereas biomass drying and pyrolysis are completed within seconds, the time required for complete gasification of char particles is of the order of hours.

Chapter 3: Kinetic Modeling of Biomass Pyrolysis in a Bubbling Fluidized Bed Reactor

Enhancing the feasibility of biomass pyrolysis and gasification in fluidized bed reactors is of both scientific and industrial significance. The sensitivity of pyrolysis gas and tar compositions to key process parameters such as biomass properties, reactor temperature, gas residence time, solids mean residence time inside the reactor, as well as biomass particle size and moisture content have mostly been overlooked in the literature. For instance, many researchers have assumed instantaneous pyrolysis of biomass particles when modelling biomass gasifiers [13, 65, 69, 74, 105, 106]. This assumption limits the numerical solution to post- pyrolysis stage, possibly leading to under-prediction of methane in the syngas [107].

For almost all engineering applications, researchers resort to fixed values or temperature-dependent experimental correlations for the composition of the pyrolysis gas [108-112]. In those gasification and pyrolysis kinetic models, Arrhenius-type correlations have been adopted to capture the temperature dependency of pyrolysis reactions [66, 113]. The effect of other process parameters is often not taken into account. Note that biomass particle size, for instance, can change the pyrolysis product distributions (yield and composition) due to the change in the heating rate of biomass particles inside the reactor. For almost all the gasification and pyrolysis models developed in the literature, the values adopted for pyrolysis gas and tar compositions do not satisfy elemental balances and, in the few cases where they do (e.g. [113]), information on bio-oil composition as a model input parameter is missing. Moreover, only a subset of tar compounds (e.g. acetic acid (CH_3COOH), acetone (CH_3COCH_3), ethanol (CH_3CH_2OH), phenol (C_6H_5OH), naphthalene ($C_{10}H_8$), etc. [107, 113-115]) is considered that cannot fully represent the myriad of low- and high-molecular-weight organic compounds detected in the tar (bio-oil) generated from biomass pyrolysis.

In this modeling study, a more fundamental modeling approach is taken to improve on the previous research, address some gaps in knowledge and shed light on areas of research that deserve further scrutiny. By coupling the single particle model of biomass drying and pyrolysis with an ideal reactor model of a bubbling fluidized bed and constraining the coupled single particle and reactor model with CHO elemental balances, biomass drying and pyrolysis products

yields, as well as the composition of principal components in the pyrolysis gas, are predicted as functions of the most important operating parameters, in particular temperature and particle size. To address the uncertainties in tar measurement and analysis, we treat tar containing a mixture of carbon, hydrogen and oxygen. In addition to kinetic parameters and fuel-related and process-related parameters, the only other model input parameters are tar and char elemental compositions which are straightforward to obtain experimentally from ultimate and proximate analyses. Our objective is to build a detailed kinetic model of drying and pyrolysis of biomass particles in a bubbling fluidized bed (BFB) reactor with nitrogen as the fluidizing gas.

Another advantage of developing an independent kinetic model of biomass drying and pyrolysis is that it can be tested against experimental data to provide the basis for developing a seamless kinetic model of a BFB gasifier by incorporating homogeneous and heterogeneous biomass gasification reactions both for single particles and on a reactor level. Taking into account the drying and pyrolysis steps contributes to kinetic models that are capable of more realistically evaluating the overall performance of biomass gasifiers.

3.1 Model development

3.1.1 Simplifying assumptions

Based on the following simplifying assumptions, a detailed particle model for drying and pyrolysis of biomass particles is developed and coupled to an idealized model of a BFB reactor:

1. The reactor operates under steady-state operating conditions.
2. The freeboard region of the BFB is ignored.
3. Solids entrainment is ignored.
4. No sorbent particles are added.
5. Uniform temperature and atmospheric pressure throughout the bed.
6. Perfect mixing of solids for the BFB reactor.

7. Plug flow of gases inside the reactor.

8. Sand particles are inert and do not catalyze reactions.

9. Ash plays a negligible role in catalyzing reactions.

10. Ideal gas law for all volatiles released from biomass pyrolysis.

3.1.2 Coupled reactor and particle model

In the present work, the gas and particle flows are treated separately. While perfect mixing provides a reasonable representation of solid mixing inside a bubbling fluidized bed reactor, the gas flow is closer to plug flow. Let us define the conversion of a single biomass particle of unchanging size as:

$$X_P = \left(\left(m_{\mathrm{B}0} + m_{M0}\right) - \left(m_{\mathrm{B}} + m_M + m_C\right)\right) \Big/ \left(m_{\mathrm{B}0} + m_{M0} - m_{Cf}\right) \tag{3.1}$$

where m_{B0} and m_{M0} denote the initial biomass and moisture contents of un-reacted particles, m_B , m_M and m_C are the instantaneous masses of biomass, moisture and char in the solid particle, and m_{Cf} is mass of final char in the completely-converted particle. During drying and pyrolysis of a biomass particle (radius R_P), some water vapor, gas and tar accumulate within the pores of the particle, whereas the rest flows to the reactor environment at the particle surface. From conservation of mass over a single particle at any time:

[Initial particle mass] = [Instantaneous particle mass] +

[Cumulative mass of gas phase released from the surface of the particle from time 0 to "t"]. (3.2)

In mathematical terms:

$$m_{\mathrm{B}0} + m_{M0} = \int_0^{R_p} \rho_P .4\pi r^2 dr + \int_0^t \left(\left(\partial m_T / \partial t\right)\Big|_{r=R_p} + \left(\partial m_G / \partial t\right)\Big|_{r=R_p} + \left(\partial m_V / \partial t\right)\Big|_{r=R_p} \right).dt \tag{3.3}$$

where the instantaneous particle bulk density ρ_P is calculated from:

$$\rho_P = \rho_B + \rho_M + \rho_C + \varepsilon_P.\left(\rho_T + \rho_G + \rho_V\right) \tag{3.4}$$

The second term on the right side of equation (3.3) is obtained from boundary conditions of PDEs describing gas phase species mass balances in the single particle model as:

$$\left(\partial m_T/\partial t\right)\Big|_{r=R_P} = \left(4\pi R_P^2\right).\left(\varepsilon_P.\rho_T.u\right)\Big|_{r=R_P} \tag{3.5}$$

$$\left(\partial m_G/\partial t\right)\Big|_{r=R_P} = \left(4\pi R_P^2\right).\left(\varepsilon_P.\rho_G.u\right)\Big|_{r=R_P} \tag{3.6}$$

$$\left(\partial m_V/\partial t\right)\Big|_{r=R_P} = \left(4\pi R_P^2\right).\left(\varepsilon_P.\rho_V.u\right)\Big|_{r=R_P} \tag{3.7}$$

Each solid particle behaves as a tiny batch reactor inside the fluidized bed reactor. The conversion of reactants (dry biomass and moisture) in a solid particle depends on the duration of its stay in the reactor. However, the length of stay is not the same for all particles, and the average particle conversion of solid particles leaving the reactor is calculated in a manner similar to a macrofluid (non-coalescing droplets of very viscous liquids) [116] as:

$$\bar{X}_P = \int_0^\infty \left(X_P\right)_{\substack{individual \\ particle}} .E\left(t\right) dt \tag{3.8}$$

where we utilize the residence time distribution function, *E(t)*, for perfectly-mixed solids:

$$E\left(t\right) = \frac{1}{\tau_s}.\exp\left(-t/\tau_s\right) \tag{3.9}$$

Given the reactor solids residence time distribution (RTD) function, the change in the average mass of biomass particles inside the reactor is equal to the cumulative mass of gas released from the surface of the same particles into the reactor environment. Integrating both sides of equation (3.3) for reactor particles with RTD function, *E(t)* gives:

$$\left(m_{B0} + m_{M0}\right) - \int_0^\infty \left(\int_0^{R_P} \rho_P.4\pi r^2 dr\right).E\left(t\right) dt = \int_0^\infty \left(\int_0^t \left(\left(\partial m_T/\partial t\right)\Big|_{r=R_P} + \left(\partial m_G/\partial t\right)\Big|_{r=R_P} + \left(\partial m_V/\partial t\right)\Big|_{r=R_P}\right).dt\right).E\left(t\right) dt \tag{3.10}$$

The average biomass particle density $\bar{\rho}_p$ as well as the biomass drying and pyrolysis product yields of different species leaving the reactor are obtained as:

$$\bar{\rho}_P = \int_0^{\infty}\left(\int_0^{R_p}\left(\rho_B+\rho_M+\rho_C\right).4\pi r^2 dr\right).E(t)\,dt \Big/ \left(\tfrac{4}{3}\pi R_P^3\right) \tag{3.11}$$

$$\bar{Y}_i = \int_0^{\infty}\left(\int_0^{R_p}\rho_i.4\pi r^2 dr\right).E(t).dt \Big/ \left(m_{\mathrm{B}0}+m_{M0}\right) \qquad (i=B,C,M) \tag{3.12}$$

$$\bar{Y}_i = \int_0^{\infty}\left(\int_0^{R_p}\left(\varepsilon_P.\rho_i\right).4\pi r^2 dr + \int_0^{t}\left(\frac{\partial m_i}{\partial t}\right)\Big|_{r=R_p}.dt\right).E(t).dt \Big/ \left(m_{\mathrm{B}0}+m_{M0}\right) \qquad (i=T,G,V) \tag{3.13}$$

The mean solids residence time inside the BFB is obtained from the mass hold-up of biomass particles inside the BFB divided by the mass flow rate of particles leaving the reactor:

$$\tau_s = M_P/\dot{m}_{\mathrm{P},out} \tag{3.14}$$

where $\dot{m}_{\mathrm{P},out}$ is the mass flow rate of biomass particles leaving the reactor.

For given sand inventory M_{sand}, average voidage $\bar{\varepsilon}$, cross-sectional area A and height L_{bed} of the dense bubbling bed, the total solids volume hold-up is:

$$\left(1-\bar{\varepsilon}\right).A.L_{bed} = \left(M_P/\bar{\rho}_P\right)+\left(M_{sand}/\rho_{sand}\right) \tag{3.15}$$

The average bubbling bed voidage and height are obtained iteratively:

$$\bar{\varepsilon} = \left(\int_0^{L_{bed}}\varepsilon.dz\right)\Big/ L_{bed} \tag{3.16}$$

where the bed voidage (ε) and bubble size (d_b) at height z in the bed are estimated from two-phase correlations [117, 118]:

$$\varepsilon = 1-\left(1-\varepsilon_{mf}\right)\Big/\left(1+\left(U-U_{mf}\right)\Big/\left(0.711\sqrt{g.d_b}\right)\right) \tag{3.17}$$

$$d_b = 0.54 g^{-0.2} \left(U - U_{mf}\right)^{0.4} \left(z + 4\sqrt{A/N_{or}}\right)^{0.8} \tag{3.18}$$

As shown in the schematic diagram of the dense bubbling fluidized bed, Figure 3.1, we assume a uniform distribution of drying and pyrolysis products throughout the entire dense bed, while homogeneous tar cracking also occurs along the reactor. For one-dimensional plug flow of gas phase, the mass balances at height z in the bed with cell size (Δz) are:

$$\dot{m}_T(z) - \dot{m}_T(z+\Delta z) + \bar{Y}_T.\left(\dot{m}_{\mathrm{B},in} + \dot{m}_{\mathrm{M},in}\right).\left(\Delta z / L_{bed}\right) - k_4.\left(\dot{m}_T(z).\Delta\tau_g\right) = 0 \tag{3.19}$$

$$\dot{m}_G(z) - \dot{m}_G(z+\Delta z) + \bar{Y}_G.\left(\dot{m}_{\mathrm{B},in} + \dot{m}_{\mathrm{M},in}\right).\left(\Delta z / L_{bed}\right) + k_4.\left(\dot{m}_T(z).\Delta\tau_g\right) = 0 \tag{3.20}$$

$$\dot{m}_V(z) - \dot{m}_V(z+\Delta z) + \bar{Y}_V.\left(\dot{m}_{\mathrm{B,in}} + \dot{m}_{\mathrm{M,in}}\right).\left(\Delta z / L_{bed}\right) = 0 \tag{3.21}$$

As discussed above, $\bar{Y}_T$, $\bar{Y}_G$ and $\bar{Y}_V$ denote the average yields of tar, non-condensable gas, and water vapor released from the surface of biomass particles into the reactor and, as denoted in Figure 3.1, $\bar{Y}_B$, $\bar{Y}_C$ and $\bar{Y}_M$ are the average yields of unreacted biomass, char and moisture content of solid particles exiting the reactor, respectively. The gas residence time in each cell is calculated as the volume of the gas phase divided by its volumetric flow rate:

$$\Delta\tau_g = \left(\varepsilon.A.\Delta z\right) / \left(Q_T + Q_G + Q_V + Q_{N_2}\right) = \left(\varepsilon.A.\Delta z\right) / \left(U.A\right) \tag{3.22}$$

where $Q_{i=G,T,V,N_2}$ are the total volumetric flow rates of gas phase species.

The superficial gas velocity (*U*) inside the fluidized bed is related to the uniform operating conditions (i.e. *T* & *P*) of the reactor by the ideal gas law as:

$$U = \left(R.T\right) / \left(P.A\right).\left(\left(\dot{m}_{N_2} / MW_{N_2}\right) + \left(\dot{m}_T(z) / MW_T\right) + \left(\dot{m}_G(z) / MW_G\right) + \left(\dot{m}_V(z) / MW_{H_2O}\right)\right) \tag{3.23}$$

Substituting for the differential gas residence time from equation (3.22), dividing both sides of equations (3.19) to (3.21) by Δz, and letting $\Delta z \rightarrow 0$:

$$d\dot{m}_T / dz = \bar{Y}_T.\left(\dot{m}_{\mathrm{B},in} + \dot{m}_{\mathrm{M},in}\right) / L_{bed} - k_4.\left(\dot{m}_T.\varepsilon / U\right) \qquad B.C.: \dot{m}_T(z=0) = 0 \tag{3.24}$$

$$d\dot{m}_G/dz = \bar{Y}_G.\left(\dot{m}_{\mathrm{B},in} + \dot{m}_{\mathrm{M},in}\right)/L_{bed} + k_4.\left(\dot{m}_T.\varepsilon/U\right) \qquad B.C.: \dot{m}_G\left(z=0\right)=0 \tag{3.25}$$

$$d\dot{m}_V/dz = \bar{Y}_V.\left(\dot{m}_{\mathrm{B,in}} + \dot{m}_{\mathrm{M,in}}\right)/L_{bed} \qquad B.C.: \dot{m}_V\left(z=0\right)=0 \tag{3.26}$$

With the aid of MATLAB ODE solver (ODE45), the above ODEs are solved numerically to give the axial profiles of vapor, tar and gas mass flow rates along the reactor, as well as the axial profile of superficial gas velocity.

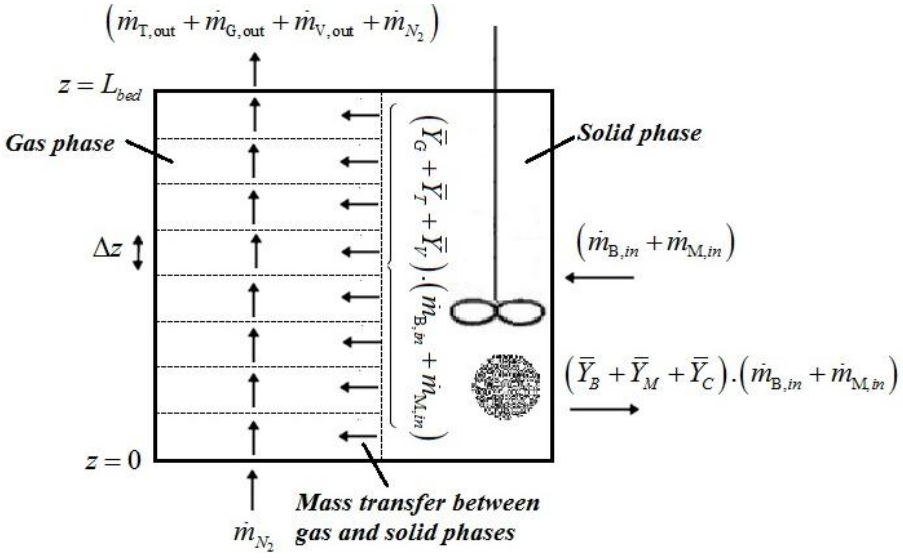

Figure 3.1. Schematic diagram of a bubbling fluidized bed reactor, assuming uniform distribution of drying and pyrolysis products throughout the entire dense bed height with perfectly-mixed solids and plug flow of gases.

3.1.3 Elemental balance on coupled particle and reactor model

In this study, an attempt is made to estimate major compounds composition in pyrolysis gas. Assuming that each lumped species is a homogeneous mixture of carbon, hydrogen and oxygen, the coupled particle and reactor model is constrained with CHO elemental balances. An average overall mass balance on biomass particles inside the BFB gives:

$$1 = \bar{Y}_B + \bar{Y}_C + \bar{Y}_M + \bar{Y}_V + \bar{Y}_T + \bar{Y}_G \tag{3.27}$$

For given steady-state operating conditions of the reactor, average elemental compositions are assigned to each lumped species and the particle mass balance is broken down into three elemental balances:

$$\left(m_{\mathrm{B}0}/\left(m_{\mathrm{B}0}+m_{M0}\right)\right).w_{\mathrm{j,B}}+\left(m_{M0}/\left(m_{\mathrm{B}0}+m_{M0}\right)\right).w_{\mathrm{j,H_2O}}=\bar{Y}_B.w_{\mathrm{j,B}}+\bar{Y}_{\mathrm{C}}.w_{\mathrm{j,C}}+\left(\bar{Y}_M+\bar{Y}_V\right)w_{\mathrm{j,H_2O}}+\bar{Y}_T.w_{\mathrm{j,T}}+\bar{Y}_G.w_{\mathrm{j,G}}$$
$$\left(j=C,\ H,\ O\right) \tag{3.28}$$

where the elemental composition of dry-ash-free biomass ($w_{\mathrm{j,B}}$) is obtained from its ultimate analysis. For moisture/water vapor:

$$w_{\mathrm{C,H_2O}}=0,\quad w_{\mathrm{H,H_2O}}=2/18,\quad w_{\mathrm{O,H_2O}}=16/18 \tag{3.29}$$

The elemental composition of char ($w_{\mathrm{j,C}}$) is approximated from an empirical formula ($CH_{0.2526}O_{0.0236}$) from the literature [119].

Solving equation (3.28) for average elemental composition of tar released from the surface of the average particle ($w_{\mathrm{j,T}}$) gives:

$$w_{\mathrm{j,T}}=\left(\left(m_{\mathrm{B}0}/\left(m_{\mathrm{B}0}+m_{M0}\right)-\bar{Y}_B\right).w_{\mathrm{j,B}}+\left(m_{M0}/\left(m_{\mathrm{B}0}+m_{M0}\right)-\bar{Y}_M-\bar{Y}_V\right).w_{\mathrm{j,H_2O}}-\bar{Y}_{\mathrm{C}}.w_{\mathrm{j,C}}-\bar{Y}_G.w_{\mathrm{j,G}}\right)\Big/\bar{Y}_T$$
$$\left(j=C,\ H,\ O\right) \tag{3.30}$$

Note that the kinetic constants for tar (bio-oil) yields reported by Di Blasi *et al.* [83] include both organic compounds and pyrolytic water produced from dehydration of the chemical structure of dry biomass. Although the tar derived from the pyrolysis of biomass is a complex mixture of low- and high-molecular-weight oxygenated compounds, such as carboxylic acids, aldehydes, ketones, alcohols and phenols [120], its dry-basis elemental composition is a very weak function of temperature [112]. As a model input parameter, we adopt the following empirical mass ratios for the organic constituents of tar [112]:

$$w_{\mathrm{C,T,organic}}=1.14.w_{\mathrm{C,B}};\quad w_{\mathrm{H,T,organic}}=1.13.w_{\mathrm{H,B}};\quad w_{\mathrm{O,T,organic}}=1-w_{\mathrm{C,T,organic}}-w_{\mathrm{H,T,organic}} \tag{3.31}$$

If $\bar{Y}_{H_2O,pyr}$ denotes the average pyrolytic water yield released from the surface of the particles inside the reactor, the overall tar (bio-oil) composition is related to its organic part elemental composition as:

$$w_{\mathrm{j,T}} = \left(\left(\bar{Y}_T - \bar{Y}_{H_2O,pyr} \right).w_{\mathrm{j,T,organic}} + \bar{Y}_{H_2O,pyr}.w_{\mathrm{j,H_2O}} \right) \Big/ \bar{Y}_T \qquad (j = C,\ H,\ O) \tag{3.32}$$

Solving for the pyrolytic water yield divided by the tar yield, we obtain the following relationships for the elemental compositions of tar/bio-oil:

$$\frac{\bar{Y}_{H_2O,pyr}}{\bar{Y}_T} = \frac{w_{\mathrm{C,T}} - w_{C,\mathrm{T,organic}}}{w_{\mathrm{C,H_2O}} - w_{\mathrm{C,T,organic}}} = \frac{w_{\mathrm{H,T}} - w_{\mathrm{H,T,organic}}}{w_{\mathrm{H,H_2O}} - w_{\mathrm{H,T,organic}}} = \frac{w_{\mathrm{O,T}} - w_{\mathrm{O,T,organic}}}{w_{\mathrm{O,H_2O}} - w_{\mathrm{O,T,organic}}} \tag{3.33}$$

The average elemental composition of non-condensable gas released from the surface of an average particle ($w_{\mathrm{j,G}}$) can be restricted by placing additional constraints on its composition. It is customary to assume that non-condensable pyrolysis gas is composed of four major compounds: H_2, CO, CO_2 and CH_4, with other light hydrocarbons (e.g. C_2-C_3) lumped into methane. The average gas elemental composition is then related to its composition:

$$w_{\mathrm{C,G}} = (12/28).w_{CO,\mathrm{G}} + (12/44).w_{CO_2,\mathrm{G}} + (12/16).w_{CH_4,\mathrm{G}} \tag{3.34}$$

$$w_{\mathrm{H,G}} = (4/16).w_{CH_4,\mathrm{G}} + w_{H_2,\mathrm{G}} \tag{3.35}$$

$$w_{\mathrm{O,G}} = (16/28).w_{CO,\mathrm{G}} + (32/44).w_{CO_2,\mathrm{G}} \tag{3.36}$$

Experimental evidence [82, 112] shows that the hydrogen content of the non-condensable gas is almost negligible. Hence, we set:

$$w_{H_2,\mathrm{G}} \cong 0 \tag{3.37}$$

Given that each compound composition in pyrolysis gas must also fall between zero and unity, the following constraints are obtained:

$$\begin{bmatrix} 0 < w_{\mathrm{H,G}} < 0.25 \\ 0.2727 + 1.9091.w_{\mathrm{H,G}} < w_{\mathrm{C,G}} < 0.4286 + 1.9091.w_{\mathrm{H,G}} \\ 0.5714 - 2.2857.w_{\mathrm{H,G}} < w_{\mathrm{O,G}} < 0.7273 - 2.2857.w_{\mathrm{H,G}} \end{bmatrix} \tag{3.38}$$

Simultaneous solution of equations (3.30) and (3.32) subject to the above constraints gives a range of acceptable results for tar and gas compositions, as well as pyrolytic water yield released from the surface of the average particle at different reactor temperatures.

On the other hand, according to the widely adopted reaction stoichiometry of Boroson *et al.* [121] for thermal cracking of tar (bio-oil) in the temperature range 500-800^{o}C:

$$Tar \rightarrow \gamma_{CO}\,\mathrm{CO} + \gamma_{CO_2}\,\mathrm{CO_2} + \gamma_{H_2} H_2 + \gamma_{CH_4} CH_4 + \gamma_{Tar_{inert}} Tar_{inert} \tag{3.39}$$

where the mass-based stoichiometric coefficients (γ_i) are:

$$\gamma_{CO} = 0.5633,\ \gamma_{CO_2} = 0.1109,\ \gamma_{H_2} = 0.0173,\ \gamma_{CH_4} = 0.0884,\ \gamma_{Tar_{inert}} = 0.22 \tag{3.40}$$

As the amount of tar (bio-oil) cracked is known from reaction kinetics, the yield of inert tar is assigned a zero value, and the associated yield is loaded on the remaining gases [113]. Therefore, the compositions of the pyrolysis gas generated from tar thermal cracking are estimated:

$$w_{CO,\mathrm{G}_2} = \gamma_{CO} \Big/ \left(\gamma_{CO} + \gamma_{CO_2} + \gamma_{H_2} + \gamma_{CH_4}\right) = 0.7222 \tag{3.41}$$

$$w_{CO_2,\mathrm{G}_2} = \gamma_{CO_2} \Big/ \left(\gamma_{CO} + \gamma_{CO_2} + \gamma_{H_2} + \gamma_{CH_4}\right) = 0.1422 \tag{3.42}$$

$$w_{H_2,\mathrm{G}_2} = \gamma_{H_2} \Big/ \left(\gamma_{CO} + \gamma_{CO_2} + \gamma_{H_2} + \gamma_{CH_4}\right) = 0.0222 \tag{3.43}$$

$$w_{CH_4,\mathrm{G}_2} = \gamma_{CH_4} \Big/ \left(\gamma_{CO} + \gamma_{CO_2} + \gamma_{H_2} + \gamma_{CH_4}\right) = 0.1133 \tag{3.44}$$

As illustrated in Figure 3.1, the tar (bio-oil) yield released from the surface of the average particle into the reactor is thermally cracked along the reactor. Therefore, the decrease in tar

(bio-oil) yield due to homogeneous tar cracking must be equal to the increase in pyrolysis gas yield as:

$$\bar{Y}_T.\left(\dot{m}_{\mathrm{B},in}+\dot{m}_{\mathrm{M},in}\right)-\dot{m}_{T,out}=\dot{m}_{\mathrm{G},out}-\bar{Y}_G.\left(\dot{m}_{\mathrm{B},in}+\dot{m}_{\mathrm{M},in}\right) \tag{3.45}$$

where $\dot{m}_{T,out}$ and $\dot{m}_{\mathrm{G},out}$ are the mass flow rates of tar (bio-oil) and dry-nitrogen-free pyrolysis gas leaving the reactor. Breaking down this equation into CHO elemental balances, we obtain:

$$\bar{Y}_T.\left(\dot{m}_{\mathrm{B},in}+\dot{m}_{\mathrm{M},in}\right).w_{\mathrm{j,T}}-\dot{m}_{\mathrm{T},out}.w_{\mathrm{j,T,out}}=\dot{m}_{\mathrm{G},out}.w_{\mathrm{j,G,out}}-\bar{Y}_G.\left(\dot{m}_{\mathrm{B},in}+\dot{m}_{\mathrm{M},in}\right).w_{\mathrm{j,G}}=\left(\dot{m}_{\mathrm{G},out}-\bar{Y}_G.\left(\dot{m}_{\mathrm{B},in}+\dot{m}_{\mathrm{M},in}\right)\right).w_{\mathrm{j,G_2}}$$
$$\left(j=C,\ H,\ O\right) \tag{3.46}$$

Given the average elemental composition of tar and gas released from the surface of the average particle ($w_{\mathrm{j,T}}$) and compounds composition in secondary pyrolysis gas ($w_{\mathrm{j,G_2}}$), the composition of the pyrolysis gas leaving the reactor is estimated as:

$$w_{\mathrm{j,G,out}}=\frac{\bar{Y}_G.\left(\dot{m}_{\mathrm{B},in}+\dot{m}_{\mathrm{M},in}\right).w_{\mathrm{j,G}}+\left(\dot{m}_{\mathrm{G},out}-\bar{Y}_G.\left(\dot{m}_{\mathrm{B},in}+\dot{m}_{\mathrm{M},in}\right)\right).w_{\mathrm{j,G_2}}}{\dot{m}_{\mathrm{G},out}} \qquad \left(j=C,\ H,\ O\right) \tag{3.47}$$

Solving for compounds composition:

$$\begin{bmatrix} w_{CO,\mathrm{G,out}} \\ w_{CO_2,\mathrm{G,out}} \\ w_{CH_4,\mathrm{G,out}} \end{bmatrix}=\begin{bmatrix} 12/28 & 12/44 & 12/16 \\ 0 & 0 & 4/16 \\ 16/28 & 32/44 & 0 \end{bmatrix}^{-1}.\begin{bmatrix} w_{\mathrm{C,G,out}} \\ w_{\mathrm{H,G,out}}-w_{\mathrm{H_2,G,out}} \\ w_{\mathrm{O,G,out}} \end{bmatrix} \tag{3.48}$$

The MATLAB code for solving the equations describing coupled particle and reactor model of biomass drying and pyrolysis is provided in Appendix C.

3.1.4 Particle size distribution

Note that the biomass particles fed to fluidized beds reactor normally have a wide particle size distribution. Let $W(R_{\mathrm{P}})$ be the mass fraction of biomass particles with radius R_P and average

conversion $\bar{X}_P(R_P)$ inside a CSTR. From the perfect mixing assumption of solid particles, the mean solids residence time is the same for particles of different sizes. Thus:

$$\bar{X}_P(R_P) = \int_0^{\infty} (X_P)_{\substack{individual \\ particle}} . \frac{1}{\tau_s} . \exp\left(-t/\tau_s\right) dt \tag{3.49}$$

The overall average particle conversion for a feed stream with particle sizes ranging from radius $R_{P,min}$ to $R_{P,max}$ is calculated [116] as:

$$\bar{\bar{X}}_P = \sum_{R_P=R_{P,min}}^{R_{P,max}} W(R_P).\bar{X}_P(R_P) \tag{3.50}$$

Similarly, the average pyrolysis products yield for a biomass feed of known particle size distribution can be estimated as:

$$\bar{\bar{Y}}_i = \sum_{R_P=R_{P,min}}^{R_{P,max}} W(R_P).\bar{Y}_i(R_P) \qquad (i=B,C,M,G,T,V) \tag{3.51}$$

Note that, in general, the properties of individual biomass particles change due to shrinkage, cracking and fragmentation, especially for larger particles [79, 80]. Furthermore, fluidization of biomass particles with relatively fine silica sand particles inside the BFB leads to severe attrition and change in biomass particle size distribution. Therefore, a population balance model that relates the feed particle size distribution to the steady-state particle size distribution of biomass particles inside the BFB is recommended.

3.2 Predictions of coupled particle and reactor model

Westerhof [122] studied the effect of temperature on fast pyrolysis of pine in a continuous bench-scale bubbling fluidized bed with silica sand as the fluidization medium and nitrogen as the fluidizing gas. The properties of pine and experimental operating conditions are summarized in Tables 3.1 and 3.2, respectively.

Table 3.1. Properties of pine [122].

Bio-chemical composition (wt%, dry)	*Cellulose*	*35*
	Hemicellulose	*29*
	Lignin	*28*
Ultimate analysis (wt%, dry-ash-free)	*C*	*46.58*
	H	*6.34*
	O	*46.98*
	N	*0.04*
	S	*0.06*
Alkali metals (mg/kg, dry)	*K*	*34*
	Ca	*134*
	Mg	*768*
	Total ash	*2600*
Biomass moisture (wt%)		*9-10*
Biomass bulk density (kg/m^3)		*570*

Table 3.2. Operating conditions of biomass drying and pyrolysis in a BFB reactor [122].

Biomass feed rate (as received)	*1 kg/h*
Initial sand bed inventory	*2.1 kg*
Average sand particle diameter	*250 µm*
Sand particle density	*2600 kg/m^3*
Bed height	*0.25 m*
Column diameter	*0.1 m*
Superficial gas velocity (U)	*0.14 m/s*
U/U_{mf}	*3.5*
Gas/vapor residence time of the bed	*0.8 s*
Gas/vapor residence time of cyclones	*0.45-0.55 s*
Biomass particles mean residence time	*20-25 min*
Freeboard temperature	*330-580^{o}C*
Gas temperature in freeboard outlet/cyclones	*400-540^{o}C*

Figure 3.2 illustrates the yields of tar (bio-oil), dry nitrogen-free pyrolysis gas and remaining solid particles (referred to as char) generated from biomass pyrolysis in the BFB reactor as a function of reactor temperature. The dashed and solid curves are for the two-step and solid-state kinetic mechanism (see Chapter 2), respectively. It is seen that increasing the pyrolysis temperature leads to an increase in the predicted pyrolysis gas and decreased char yields. The yield of tar (bio-oil) is predicted to go through a maximum with increasing reactor temperature due to the primary generation of bio-oil at lower temperatures and its subsequent thermal cracking at higher temperatures inside the reactor. As seen in Figure 3.2, the pyrolysis products yield predicted by the two-step kinetic model (dashed curves) are in better agreement with the experimental data than those from the solid-state kinetic mechanism (solid curves). In the latter case, the char yields are under-predicted (at the expense of over-prediction of tar) at temperatures below 400^{o}C where primary pyrolysis is dominant.

The limitations in the predictions of the solid-state kinetic mechanism may be associated with the two adjustable parameters adopted to develop a complete model, in view of the lack of experimental analyses of pyrolysis products distribution. Discrepancies between the model

predictions and experimental data could also originate from the adopted pyrolysis kinetic parameters and/or reaction mechanisms to secondary tar cracking reactions that are likely to occur in cyclones and other downstream equipment. For the adopted empirical formulas of char ($CH_{0.25}O_{0.024}$) and organic tar ($CH_{1.62}O_{0.56}$) as model input parameters, the predicted composition in dry and nitrogen-free pyrolysis gas, as well as pyrolytic water yield (per mass of dry biomass), are shown at different reactor temperatures in Figures 3.3 (a), (b), (c) and (d), with dashed and solid curves for the two-step and solid-state kinetic mechanisms, respectively, and the experimental data points are from reference [122]. At temperatures above 400^{o}C, the concentrations of major compounds in the pyrolysis gas are estimated with reasonable accuracy from the elemental balances, and secondary pyrolysis reaction stoichiometry. However, at temperatures below 400^{o}C, where the CHO elemental balances are weakly constrained by secondary pyrolysis reaction, large variations in the carbon/oxygen content of pyrolysis gas make it difficult to predict the CO/CO_2 ratio accurately, without introduction of an additional experimental correlation e.g. [109, 112]. This limitation may arise from the limited temperature range (500–650^{o}C) suggested for the kinetic parameters for thermal cracking of tar [84]. Nevertheless, according to experimental data [82, 109, 111], CO_2 is the major component of primary pyrolysis gas at temperatures below 400^{o}C. Due to the unreliable kinetics at lower temperatures, the pyrolytic water yields predicted by both kinetic models are unreliable at temperatures below 400^{o}C.

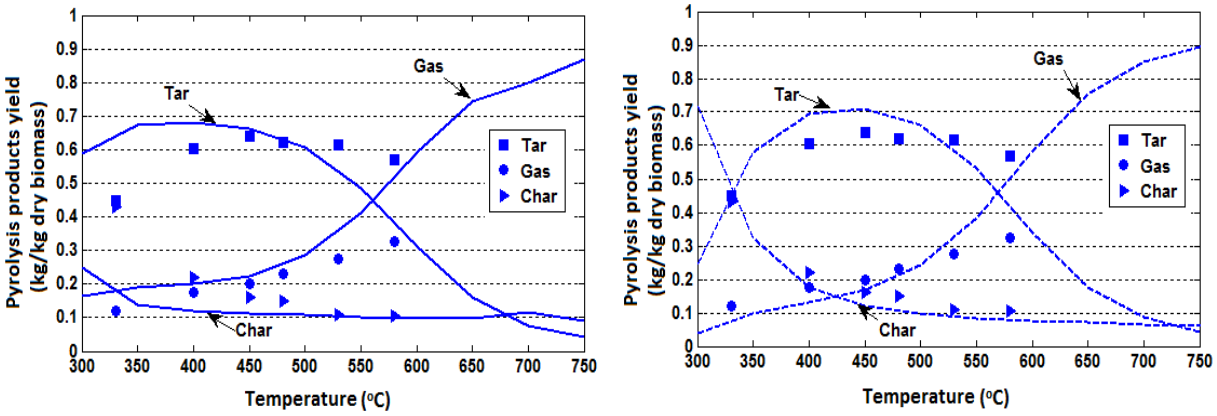

Figure 3.2. Pyrolysis product yields at reactor exit as a function of reactor temperature : Dashed and solid curves are for the two-step kinetic model and solid-state kinetic mechanism, respectively. Experimental data points are from Westerhof [122].

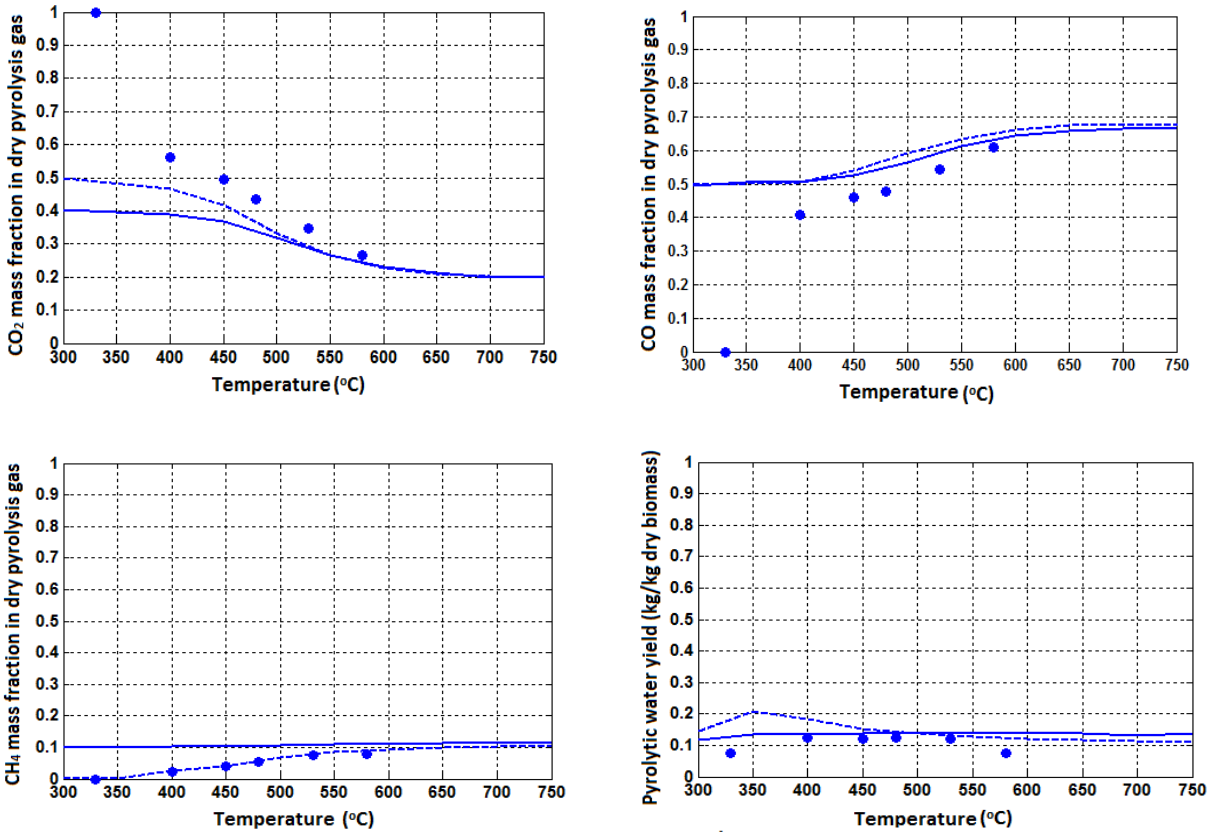

Figure 3.3. Major compounds composition in dry and nitrogen-free pyrolysis gas and pyrolytic water yield as functions of reactor temperature for empirical dry tar ($CH_{1.62}O_{0.56}$) and char ($CH_{0.25}O_{0.024}$) formulae. Dashed and solid curves are for the two-step kinetic model and solid-state kinetic mechanism, respectively. Experimental data points are from Westerhof [122].

3.3 Summary

By coupling the single particle model of biomass drying and pyrolysis with an ideal reactor model of a bubbling fluidized bed and constraining the coupled single particle and reactor model with CHO elemental balances, biomass drying and pyrolysis products yields, as well as the composition of principal components in the pyrolysis gas, are predicted as functions of the most important operating parameters. To address the uncertainties in tar measurement and analysis, we treat tar as simply a mixture of carbon, hydrogen and oxygen. In addition to kinetic parameters and fuel-related and process-related parameters, the only other model input parameters are tar and char elemental compositions which are straightforward to obtain experimentally from ultimate and proximate analyses. Taking into account the drying and pyrolysis steps contributes

to kinetic models that are capable of more realistically evaluating the overall performance of biomass gasifiers.

The coupled particle and reactor model predictions, based on two different biomass pyrolysis kinetic schemes (a two-step kinetic model and a solid-state kinetic mechanism for multiple reactions), are shown to be consistent with available experimental data. The model gives reasonable predictions of the composition of pyrolysis gas at temperatures above 400^{o}C. However, at temperatures below 400^{o}C, large variations in the carbon/oxygen content of pyrolysis gas make it difficult to predict the CO/CO_2 ratio accurately. This limitation may also arise from the limited temperature range suggested for the tar thermal cracking kinetic parameters. With increasing reactor temperature, CO and CH_4 mass fractions in dry-nitrogen-free non-condensable gas increase while the CO_2 mass fraction decreases. Limitations of the current model in predicting pyrolysis products distribution can be largely attributed to inaccurate or incomplete pyrolysis kinetics mechanisms proposed for different types of biomass with varying properties. For our modeling purpose, the two-step kinetic mechanism has proved to be useful for operational and design considerations. However, more experimental work is needed to provide reliable kinetic data and mechanisms.

Chapter 4: Kinetic Modeling of Biomass Steam Gasification in a Bubbling Fluidized Bed Reactor

In this chapter, we develop a kinetic model for steam gasification of biomass in a BFB gasifier on the basis of extending our coupled particle and reactor model that has been previously developed for biomass drying and pyrolysis in a BFB reactor.

To develop a sufficiently complex model, the following simplifying assumptions are adopted:

1. The reactor operates under steady-state conditions.
2. Solids entrainment is ignored.
3. Uniform temperature and total pressure are assumed throughout the dense bed.
4. The solids in the BFB reactor are perfectly mixed, and there is an even distribution of drying and pyrolysis products throughout the dense bed height.
5. Gases and volatiles are in plug flow inside the reactor.
6. The freeboard region of the BFB is modeled as a plug flow reactor.
7. Pyrolysis involves a two-step process with primary and secondary pyrolysis described by three parallel heterogeneous reactions and a homogeneous tar cracking reaction, respectively.
8. First-order chemical reactions with constant heats of reaction are assumed for pyrolysis.
9. The bed material (sand particles) are inert and do not catalyze reactions.
10. The ash plays a negligible role in catalyzing reactions.
11. Chemical reaction is the rate-controlling mechanism for char gasification inside the bubbling fluidized bed.

12. The ideal gas law applies for all volatiles (gas and bio-oil) released from biomass pyrolysis.

13. For elemental balances, each species, including unreacted biomass, char, non-condensable gas and tar, is treated as a homogeneous mixture of carbon, hydrogen and oxygen. Other elements, including nitrogen and sulfur, are neglected.

4.1 Reaction kinetics

As discussed in Chapter 2, section 2.1, the drying and pyrolysis of a single non-shrinking biomass particle is modelled by a generic two-step kinetic mechanism proposed by Shafizadeh *et al.* [81], with three parallel first-order reactions producing primary pyrolysis products (non-condensable gas, tar and char), and two parallel reactions for homogeneous thermal cracking of tar to non-condensable gas and char, as illustrated in Figure 4.1. Parallel to biomass pyrolysis, the evaporation of biomass particle moisture content to water vapor is expressed as an independent chemical reaction, also shown in Figure 4.1. The selected kinetic parameters for primary pyrolysis are adopted from Chan *et al.* [82] who verified their pyrolysis model predictions with experimental results for lodgepole pine wood devolatilzation. Furthermore, the reaction kinetics equation of Boroson *et al.* [121] is used to model thermal cracking of tar (bio-oil) to non-condensable gas in the temperature range of 500–800^{o}C, with the following stoichiometry:

$$Tar \rightarrow \gamma_{CO}\,\mathrm{CO} + \gamma_{CO_2}\,\mathrm{CO_2} + \gamma_{H_2} H_2 + \gamma_{CH_4} CH_4 + \gamma_{Tar_{inert}} Tar_{inert} \tag{4.1}$$

and the mass-based stoichiometric coefficients (γ_i):

$$\gamma_{CO} = 0.5633,\ \gamma_{CO_2} = 0.1109,\ \gamma_{H_2} = 0.0173,\ \gamma_{CH_4} = 0.0884,\ \gamma_{Tar_{inert}} = 0.22 \tag{4.2}$$

The above stoichiometry suggests that only 78% of the primary tar is cracked, with the rest remaining unchanged. However, studies show that operating parameters, such as fluidizing agent, temperature, residence time and ash, affect tar cracking [66, 123]. To account for these effects, the yield of inert tar is assigned a zero value ($\gamma_{Tar_{inert}} = 0$) and the remaining yield is loaded on the non-condensable gas species:

$$w_{CO,\text{tar cracking}} = \gamma_{CO} \Big/ \left(\gamma_{CO} + \gamma_{CO_2} + \gamma_{H_2} + \gamma_{CH_4} \right) = 0.7222 \tag{4.3}$$

$$w_{CO_2,\text{tar cracking}} = \gamma_{CO_2} \Big/ \left(\gamma_{CO} + \gamma_{CO_2} + \gamma_{H_2} + \gamma_{CH_4} \right) = 0.1422 \tag{4.4}$$

$$w_{CH_4,\text{tar cracking}} = \gamma_{CH_4} \Big/ \left(\gamma_{CO} + \gamma_{CO_2} + \gamma_{H_2} + \gamma_{CH_4} \right) = 0.1133 \tag{4.5}$$

$$w_{H_2,\text{tar cracking}} = \gamma_{H_2} \Big/ \left(\gamma_{CO} + \gamma_{CO_2} + \gamma_{H_2} + \gamma_{CH_4} \right) = 0.0222 \tag{4.6}$$

All reaction rate constants are expressed in first-order and Arrhenius form as:

$$k_j = k_{0j} \exp\left(-E_j / R.T \right) \tag{4.7}$$

The kinetic parameters and heats of reaction are summarized in Table 4.1. In addition, the kinetic rate expressions of five major gasification reactions included in the current model are listed in Table 4.2. The kinetics of methanation is much slower than that of the other two heterogeneous reactions. Methanation is important only if the partial pressure of H_2 is high. Note that the catalytic effects of metal components present in the biomass ash, such as Ca, Na and K, are not taken into account, despite reports that they can have significant impact on the reaction network of biomass gasification for biomass species having high ash content [124].

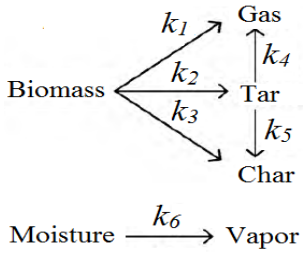

Figure 4.1. Kinetic mechanism adopted for biomass pyrolysis and evaporation of moisture [81, 82].

Table 4.1. Kinetic parameters for biomass drying and pyrolysis. For mechanism, see Figure 4.1.

Rxn.(j)	*k_{0j} (1/s)*	*E_j (kJ/mol)*	*$\Delta H_{rxn,j}$ (kJ/kg)*	*Ref.*
1	*1.30×10^8*	*140*	*64*	*[82]*
2	*2.00×10^8*	*133*	*64*	*[82]*
3	*1.08×10^7*	*121*	*64*	*[82]*
4	*1×10^5*	*93.3*	*-42*	*[121]*
5	*1×10^5*	*108*	*-42*	*[86]*
6	*5.13×10^{10}*	*88*	*2440*	*[87]*

Table 4.2. Major gasification reactions.

Gasification reaction		*Reaction kinetic rate expression*	*Ref.*
**Boudouard*	$C(s)+CO_2 \rightarrow 2CO$ $\Delta H^o_{rxn} = +172\,{}^{kJ}/_{mol}$	$r_{C1}\left(s^{-1}\right) = 3.9\times10^4 \exp\left(-215000/R.T\right)\times P_{CO_2}^{0.38}$	*[101]*
**Water-Gas*	$C(s)+H_2O \rightarrow CO+H_2$ $\Delta H^o_{rxn} = +131\,{}^{kJ}/_{mol}$	$r_{C2}\left(s^{-1}\right) = 3.7\times10^5 \exp\left(-237000/R.T\right)\times P_{H_2O}^{0.57}$	*[102]*
**Methanation*	$C(s)+2H_2 \rightarrow CH_4$ $\Delta H^o_{rxn} = -75\,{}^{kJ}/_{mol}$	$r_{C3}\left(s^{-1}\right) = 4.3\times10^{-5} \exp\left(-94800/R.T\right)\times P_{H_2}^{0.93}$	*[103]*
Steam-Methane Reforming (SMR)	$CH_4+H_2O \leftrightarrow CO+3H_2$ $\Delta H^o_{rxn} = +206\,{}^{kJ}/_{mol}$	$r_{SMR}\left(mol.m^{-3}.s^{-1}\right) = 3\times10^5 \exp\left(\frac{-125000}{R.T}\right).C_{CH_4}.C_{H_2O}$	*[125]*
Water-Gas Shift (WGS)	$CO+H_2O \leftrightarrow CO_2+H_2$ $\Delta H^o_{rxn} = -41\,{}^{kJ}/_{mol}$	$K_{WGS} = 0.0265\exp\left(\frac{3968}{T}\right)$ $r_{WGS}\left(mol.m^{-3}.s^{-1}\right) = 2.78\exp\left(\frac{-1510}{T}\right).\left(C_{CO}.C_{H_2O} - \frac{C_{CO_2}.C_{H_2}}{K_{WGS}}\right)$	*[126, 127]*

*First order reactions with respect to solid Carbon. R=8.314 $J.mol^{-1}.K^{-1}$, T $[K]$, P_i $[Pa]$ and C_i $[mol.m^{-3}]$.

4.2 BFB gasifier kinetic model

In the reactor model, the gas and particle flows are treated separately. While perfect mixing provides a reasonable representation of solid mixing inside a bubbling fluidized bed reactor, the gas flow is closer to plug flow as shown schematically in Figure 4.2.

As discussed in the previous chapter, treating a biomass particle as an aggregate that behaves like a batch reactor inside the fluidized bed reactor, the average particle conversion of solid particles leaving the reactor is calculated in a manner similar to a macrofluid (non-coalescing droplets of very viscous liquids) as

$$\bar{X}_P = \int_0^{\infty} \left(X_P\right)_{\substack{individual\\particle}} .\frac{1}{\tau_s}.\exp\left(\frac{-t}{\tau_s}\right) dt \tag{4.8}$$

where the mean solids residence time is defined as the fraction of solids hold-up inside the bubbling bed divided by mass flow rate of solid particles leaving the dense bed:

$$\tau_s \equiv \frac{M_P}{\dot{m}_{P,out}} \tag{4.9}$$

For gasifiers that operate at high temperatures, the unreacted biomass content of solid particles leaving the reactor is negligible especially for smaller particles. If M_{Char} is the char hold-up (kg) in the dense bed and $\dot{m}_{Char,out}$ is the mass flow rate of char (kg/s) leaving the dense bed, the mean solids residence time can be approximated by:

$$\tau_s = \frac{M_{Char}}{\dot{m}_{Char,out}} \tag{4.10}$$

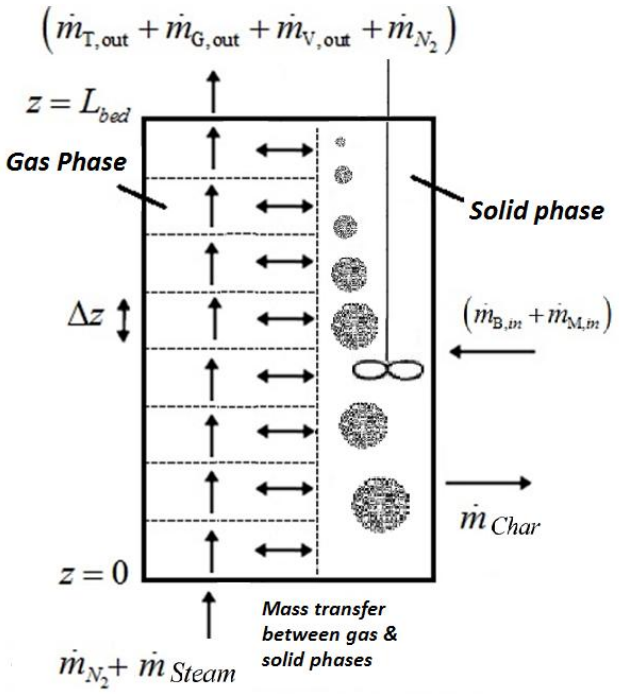

Figure 4.2. Reactor model schematic. CSTR for solids and PFR for gas.

Assuming that tar, char and non-condensable gas produced from pyrolysis of biomass particles are homogeneous mixtures of carbon, hydrogen and oxygen, the product gas composition is approximated from CHO elemental balances on the average particle going through drying and pyrolysis inside the reactor. In this kinetic scheme, tar (bio-oil) includes both organic compounds and water produced during pyrolysis of dry biomass.

Summarizing from the previous chapter:

Given the ultimate analysis of tar as model input parameter [112]:

$$w_{\mathrm{C,T,organic}} = 1.14.w_{\mathrm{C,B}};\ w_{\mathrm{H,T,organic}} = 1.13.w_{\mathrm{H,B}};\quad w_{\mathrm{O,T,organic}} = 1 - w_{\mathrm{C,T,organic}} - w_{\mathrm{H,T,organic}} \tag{4.11}$$

and approximating char as pure carbon:

$$w_{\mathrm{C},C} = 1;\quad w_{H,C} = 0;\qquad w_{O,C} = 0 \tag{4.12}$$

Overall mass balance on the average biomass particle that goes through drying and pyrolysis:

$$1 = \bar{Y}_B + \bar{Y}_M + \bar{Y}_V + \bar{Y}_{C,pyro} + \bar{Y}_{T,pyro} + \bar{Y}_{G,pyro} \tag{4.13}$$

Breaking down to CHO elemental balances:

$$\begin{aligned} &\left(m_{\mathrm{B}0}/\left(m_{\mathrm{B}0} + m_{M0}\right)\right).w_{\mathrm{j,B}} + \left(m_{M0}/\left(m_{\mathrm{B}0} + m_{M0}\right)\right).w_{\mathrm{j,H_2O}} = \\ &\bar{Y}_B.w_{\mathrm{j,B}} + \bar{Y}_{\mathrm{C},pyro}.w_{\mathrm{j,C}} + \left(\bar{Y}_M + \bar{Y}_V\right)w_{\mathrm{j,H_2O}} + \bar{Y}_{T,pyro}.w_{\mathrm{j,T}} + \bar{Y}_{G,pyro}.w_{\mathrm{j,G}} \qquad \left(j = C,\ H,\ O\right) \end{aligned} \tag{4.14}$$

Solving for average elemental composition of tar released from the surface of the average particle:

$$w_{\mathrm{j,T}} = \left(\left(m_{\mathrm{B}0}/\left(m_{\mathrm{B}0} + m_{M0}\right) - \bar{Y}_B\right).w_{\mathrm{j,B}} + \left(m_{M0}/\left(m_{\mathrm{B}0} + m_{M0}\right) - \bar{Y}_M - \bar{Y}_V\right).w_{\mathrm{j,H_2O}} - \bar{Y}_{\mathrm{C},pyro}.w_{\mathrm{j,C}} - \bar{Y}_{G,pyro}.w_{\mathrm{j,G}}\right)\Big/\bar{Y}_{T,pyro}$$
$$\left(j = C,\ H,\ O\right) \tag{4.15}$$

Accounting for pyrolytic water content ($\bar{Y}_{H_2O,pyr}$) of tar (bio-oil):

$$w_{\mathrm{j,T}} = \left(\left(\bar{Y}_{T,pyro} - \bar{Y}_{H_2O,pyr}\right).w_{\mathrm{j,T,organic}} + \bar{Y}_{H_2O,pyr}.w_{\mathrm{j,H_2}O}\right)\Big/\bar{Y}_{T,pyro} \qquad \left(j = C,\ H,\ O\right) \tag{4.16}$$

Assuming non-condensable pyrolysis gas is composed of four major compounds: H_2, CO, CO_2 and CH_4, with other light hydrocarbons (e.g. C_2-C_3) lumped into methane, the average dry gas elemental composition from biomass pyrolysis is:

$$w_{\mathrm{C,G}} = (12/28).w_{CO,pyro} + (12/44).w_{CO_2,pyro} + (12/16).w_{CH_4,pyro} \tag{4.17}$$

$$w_{\mathrm{H,G}} = (4/16).w_{CH_4,pyro} + w_{H_2,pyro} \tag{4.18}$$

$$w_{\mathrm{O,G}} = (16/28).w_{CO,pyro} + (32/44).w_{CO_2,pyro} \tag{4.19}$$

Assuming plug flow of gas phase and uniform distribution of drying and pyrolysis products throughout the entire dense bed height, L_{bed}, with uniform temperature, the one-dimensional tar (bio-oil) mass balance at height z of the bed with cell height (Δz) is written:

$$\dot{m}_T(z) - \dot{m}_T(z+\Delta z) + \bar{Y}_{T,pyro}.(\dot{m}_{\mathrm{B},in} + \dot{m}_{\mathrm{M},in}).(\Delta z/L_{bed}) - k_4.(1-\gamma_{Tar_{inert}}).(\dot{m}_T(z).\Delta\tau_g) = 0 \tag{4.20}$$

The incremental gas residence time for a bed of cross-sectional area A is calculated from local bed voidage (ε) and superficial gas phase velocity (U):

$$\Delta\tau_g = \frac{\varepsilon.A.\Delta z}{U.A} \tag{4.21}$$

where the local bed voidage (ε) is obtained from Clift and Grace [117]:

$$\varepsilon = 1-(1-\varepsilon_{mf})\Big/\left(1+(U-U_{mf})\Big/(0.711\sqrt{g.d_b})\right) \tag{4.22}$$

and bubble size (d_b) is estimated from the Darton correlation as a function of height z [118]:

$$d_b = 0.54g^{-0.2}(U-U_{mf})^{0.4}\left(z+4\sqrt{A/N_{or}}\right)^{0.8} \tag{4.23}$$

Substituting $\Delta\tau_g$ into the tar mass balance and letting $\Delta z \to 0$ leads to:

$$\frac{d\dot{m}_T}{dz} = \bar{Y}_{T,pyro}.(\dot{m}_{\mathrm{B},in} + \dot{m}_{\mathrm{M},in})\Big/L_{bed} - k_4.(1-\gamma_{Tar_{inert}}).(\dot{m}_T(z).\varepsilon/U)$$

$$B.C.: \dot{m}_T(z=0) = 0 \tag{4.24}$$

Similarly, one-dimensional differential equations are written for non-condensable gas:

$$\frac{d\dot{m}_G}{dz} = \bar{Y}_{G,pyro}.\left(\dot{m}_{\mathrm{B},in} + \dot{m}_{\mathrm{M},in}\right)/L_{bed} + k_4.\left(1-\gamma_{Tar_{inert}}\right).\left(\dot{m}_T\left(z\right).\varepsilon/U\right) + \frac{d\dot{m}_{G,gasification}}{dz}$$

$$B.C.: \dot{m}_G\left(z=0\right) = 0 \tag{4.25}$$

The third term on the right side of equation (4.25) is the net rate of generation/consumption of gaseous species due to homogeneous and heterogeneous gasification reactions:

$$\frac{d\dot{m}_{G,gasification}}{dz} = \frac{d\dot{m}_{CO,gasification}}{dz} + \frac{d\dot{m}_{CO_2,gasification}}{dz} + \frac{d\dot{m}_{CH_4,gasification}}{dz} + \frac{d\dot{m}_{H_2,gasification}}{dz} \tag{4.26}$$

where, according to major gasification reactions listed in Table 4.2:

$$\frac{d\dot{m}_{CO,gasification}}{dz} = \left(\varepsilon.\left(r_{SMR} - r_{WGS}\right) + \left(1-\varepsilon\right).\frac{\left(M_{Char}/MW_{Char}\right)}{\left(A.L_{bed}.\left(1-\varepsilon\right)\right)}.\left(2.r_{C1} + r_{C2}\right)\right).A.MW_{CO} \tag{4.27}$$

$$\frac{d\dot{m}_{CO_2,gasification}}{dz} = \left(\varepsilon.\left(r_{WGS}\right) + \left(1-\varepsilon\right).\frac{\left(M_{Char}/MW_{Char}\right)}{\left(A.L_{bed}.\left(1-\varepsilon\right)\right)}.\left(-r_{C1}\right)\right).A.MW_{CO_2} \tag{4.28}$$

$$\frac{d\dot{m}_{CH_4,gasification}}{dz} = \left(\varepsilon.\left(-r_{SMR}\right) + \left(1-\varepsilon\right).\frac{\left(M_{Char}/MW_{Char}\right)}{\left(A.L_{bed}.\left(1-\varepsilon\right)\right)}.\left(r_{C3}\right)\right).A.MW_{CH_4} \tag{4.29}$$

$$\frac{d\dot{m}_{H_2,gasification}}{dz} = \left(\varepsilon.\left(3.r_{SMR} + r_{WGS}\right) + \left(1-\varepsilon\right).\frac{\left(M_{Char}/MW_{Char}\right)}{\left(A.L_{bed}.\left(1-\varepsilon\right)\right)}.\left(r_{C2} - 2.r_{C3}\right)\right).A.MW_{H_2} \tag{4.30}$$

Given $w_{i,pyro}$ and $w_{i,\text{tar cracking}}$ from elemental balances on the average biomass particle during pyrolysis and the adopted thermal tar cracking kinetic model, respectively, the mass balances for the individual gas species (i=*CO, CO₂, CH₄, H₂*) are:

$$\frac{d\dot{m}_i}{dz} = \bar{Y}_{G,pyro}.\left(\dot{m}_{\mathrm{B},in} + \dot{m}_{\mathrm{M},in}\right)/L_{bed}.w_{i,pyro} + k_4.\left(1-\gamma_{Tar_{inert}}\right).\left(\dot{m}_T\left(z\right).\varepsilon/U\right).w_{i,\text{tar cracking}} + \frac{d\dot{m}_{i,gasification}}{dz}$$

$$B.C.: \dot{m}_i\left(z=0\right) = 0 \tag{4.31}$$

The differential equation for water vapor/steam mass balance is:

$$Water: \frac{d\dot{m}_{H_2O}}{dz} = \bar{Y}_V.\left(\dot{m}_{\mathrm{B,in}} + \dot{m}_{\mathrm{M,in}}\right)\Big/ L_{bed} + \frac{d\dot{m}_{H_2O,gasification}}{dz} \qquad B.C.: \dot{m}_{H_2O}\left(z=0\right) = \dot{m}_{Steam,in} \tag{4.32}$$

where the rate of water consumption due to gasification is estimated as:

$$\frac{d\dot{m}_{H_2O,gasification}}{dz} = \left(\varepsilon.\left(-r_{SMR} - r_{WGS}\right) + \left(1-\varepsilon\right).\frac{\left(M_{Char}/MW_{Char}\right)}{\left(A.L_{bed}.\left(1-\varepsilon\right)\right)}.\left(-r_{C2}\right) \right).A.MW_{H_2O} \tag{4.33}$$

Given an initial guess for the char hold-up of the dense bubbling bed, the above coupled ODEs are solved numerically to give the axial profiles of steam, tar and non-condensable gas species mass flow rates along the reactor using the MATLAB ODE solver (ODE45).

The char hold-up of the dense bubbling bed with a given mean solids residence time τ_s is updated by performing a char balance over the bed at steady-state, with no char in the feed:

$$\dot{m}_{Char,out} = \dot{m}_{Char,gen} - \dot{m}_{Char,cons} \tag{4.34}$$

where:

$$\dot{m}_{Char,out} = M_{char}/\tau_s \tag{4.35}$$

$$\dot{m}_{Char,gen} = \bar{Y}_{\mathrm{C},pyro}.\left(\dot{m}_{\mathrm{B},in} + \dot{m}_{\mathrm{M},in}\right) \tag{4.36}$$

Fluidized bed particles are often small enough that internal resistances to transfer are small. External transfer resistances are also likely to be smaller than those related to chemical reaction. Furthermore, the char particles are subject to severe fragmentation inside the bed. As discussed in Chapter 2 (Fig. 2.9), it is reasonable to neglect the internal and external mass transfer resistances and assume that heterogeneous reactions are the rate-controlling mechanism for char gasification. The rate of char consumption due to heterogeneous gasification reactions is approximated (see Table 4.2) as:

$$\dot{m}_{Char,cons} = \int_0^{L_{bed}} \left(d\dot{m}_{Char,gasification} / dz \right).dz = \int_0^{L_{bed}} \left(r_{C1}(z) + r_{C2}(z) + r_{C3}(z) \right).\left(M_{char} / L_{bed} \right).dz \tag{4.37}$$

Substituting the above values in the char balance equation:

$$M_{char} = \overline{Y}_{C,pyro}.\left(\dot{m}_{B,in} + \dot{m}_{M,in} \right) \Big/ \left(1/\tau_s + \int_0^{L_{bed}} \left(r_{C1}(z) + r_{C2}(z) + r_{C3}(z) \right).dz \Big/ L_{bed} \right) \tag{4.38}$$

where the local partial pressures and concentrations of reacting species, as well as superficial gas velocity at height z in the bed with uniform operating temperature (T) and pressure (P), are estimated from gaseous species mass flow rates and the ideal gas law:

$$y_i(z) = \left(\dot{m}_i(z) / MW_i \right) \Big/ \sum_i \left(\dot{m}_i(z) / MW_i \right) \qquad \left(i = CO, CO_2, CH_4, H_2, H_2O, N_2, \text{Tar} \right) \tag{4.39}$$

$$P_i(z) = y_i(z).P \tag{4.40}$$

$$C_i(z) = P_i(z) / (R.T) \tag{4.41}$$

$$U(z) = \left(\frac{R.T}{P.A} \right).\sum_i \left(\dot{m}_i(z) / MW_i \right) \tag{4.42}$$

Given the total bed inventory (W_{bed}) or the dense bed height (L_0) at minimum fluidization ($\varepsilon=\varepsilon_{mf}$), the height of the expanded dense bubbling bed (L_{bed}) must also be obtained iteratively:

$$W_{bed} = \rho_{sand}.A.L_{bed}.\left(1 - \overline{\varepsilon} \right) = \rho_{sand}.A.L_0.\left(1 - \varepsilon_{mf} \right) \tag{4.43}$$

where the average bed voidage is calculated as:

$$\overline{\varepsilon} = \left(\int_0^{L_{bed}} \varepsilon.dz \right) \Big/ L_{bed} \tag{4.44}$$

Note that the assumptions of uniform total pressure, temperature and solids hold-up are reasonable approximations due to effective radial dispersion in the dense section of a bubbling fluidized bed reactor. The axial variations of temperature and pressure are taken into account by

coupling ODE's describing energy and pressure balances along the bed. Neglecting the entrainment of char and sand particles, the freeboard region is modeled as an ideal plug flow reactor ($\varepsilon_{fb}=1$) in which only homogeneous tar cracking and gasification reactions (SMR & WGS) take place. The boundary conditions for the ODE's describing the freeboard region are from the values obtained at the top of the dense bubbling bed.

4.3 Verification of BFB gasifier kinetic model

The predictions of the BFB gasifier model are compared with experimental results of Herguido *et al.* [128] who studied the steam gasification of different types of biomass species in a BFB gasifier of 0.15 m internal diameter in the temperature range 650–780^{o}C and steam-to-biomass ratios of 0.4–3. The properties of pine (sawdust and wood chips), as well as the experimental operating conditions used in their study, are summarized in Tables 4.3 and 4.4, respectively. In their experimental runs, the biomass flow rate was varied to provide the desired steam-to-biomass ratios at a constant steam volumetric flow rate.

Table 4.3. Properties of biomass species [128].

Type of pine	*Sawdust*	*Wood chips*
Particle size	*500 µm*	*2×5×10 mm*
Proximate analysis (wt% basis)		
Moisture	*8.5*	*11.1*
Ash	*1.2*	*2.1*
Volatiles	*77.4*	*74.4*
Fixed carbon	*12.9*	*12.4*
Ultimate analysis (wt%,)		
C	*42.5*	*41.8*
H	*6.3*	*5.3*
O	*51*	*52.7*
N	*0.2*	*0.2*
Low heating value (MJ/kg dry-ash-free biomass)	*18.8*	*18.5*

Table 4.4. BFB gasifier operating conditions [128].

Bed diameter	*0.15 m*
Freeboard diameter	*0.15 m*
Total column height	*1.2 m*
Bed height (L_0) at $U_0=U_{mf}$	*0.32 m*
Number of holes in distributor plate	*220*
Fluidizing gas mixture	*90% H_2O /10% N_2*
Reactor temperature range	*650 – 780^{o}C*
Total reactor pressure	*1.1 atm*
Superficial gas velocity at inlet (U_0) at reactor temperature	*0.25 m/s*
Biomass flow rate	*3.94 – 3.46 kg/h*
Steam/biomass ratio	*0.4 – 3*
Silica sand bed inventory	*8 kg*
Average sand particle diameter	*200-300 µm*
Sand particle density	*2600 kg/m^3*

The curves of Figures 4.3 (a) and (b) illustrate the model predictions for yields of tar, dry nitrogen-free product gas and char generated from steam gasification of pine sawdust in the BFB reactor as a function of steam-to-biomass and reactor temperature, respectively. As observed, the yields of gas are predicted to increase with increasing S/B ratio and reactor temperature, whereas tar and char yields decrease. Comparing model predictions with the experimental data, the char and tar yields are reasonably predicted, whereas the product gas yield is always over-predicted. This discrepancy may be attributed to the temperature drop in the freeboard and downstream equipment such as a cyclone, exit gas line and heat exchanger that are externally heated and insulated. Our model predictions do not account for the temperature drop in the freeboard given the difficulty of estimating the contribution of the different heating elements in the absence of overall heat balances in the original paper [128].

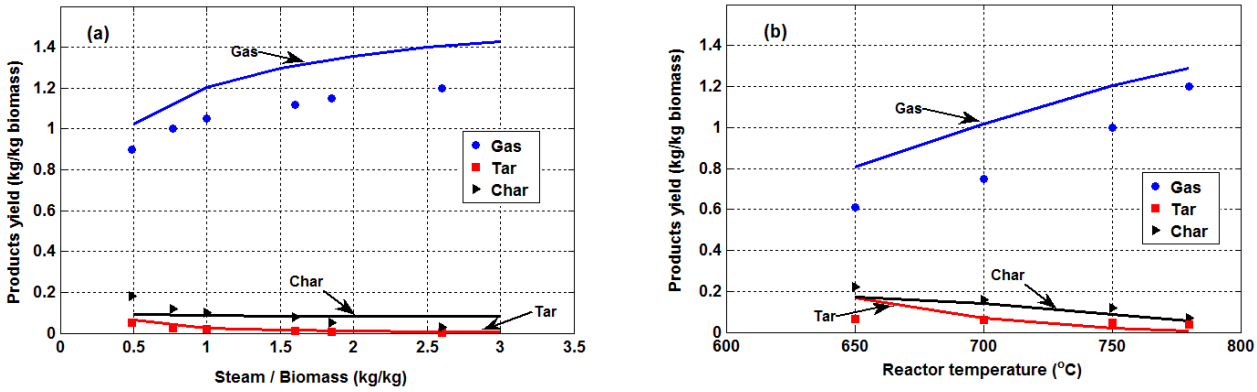

Figure 4.3. Predicted yield distribution of products from steam gasification of pine sawdust (line) compared with experimental data (points) from Herguido *et al.* [128]:(a) Effect of S/B ratio at reactor temperature 750°C, (b) Effect of reactor temperature at S/B ratio of 0.86.

Figure 4.4 illustrates the effect of S/B ratio on dry and N_2-free product gas composition for steam gasification of pine sawdust at a reactor temperature of 750°C. As expected, the H_2 mole fraction in the product gas increases with increasing S/B because of the water-gas, steam methane reforming and water-gas shift reactions. The CO_2 mole fraction also increases with increasing S/B, probably due to the water gas shift reaction that is dominant at high temperatures. Upon increasing the S/B ratio, the mole fractions of CO and CH_4 decrease due to enhanced WGS and SMR reactions.

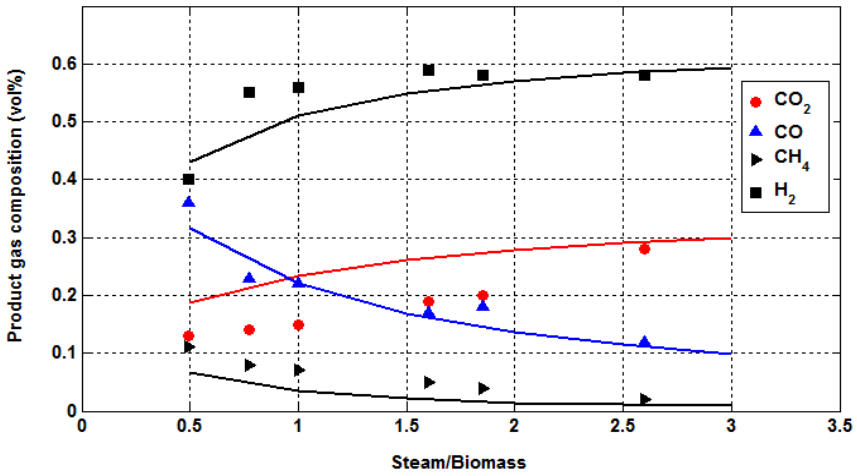

Figure 4.4. Effect of steam-to-biomass ratio on dry and N_2-free product gas composition for steam gasification of pine sawdust at a reactor temperature of 750°C. Experimental data points are from Herguido *et al.* [128]. Lines are the predictions from the model developed in this thesis.

The model predictions for product gas composition are shown in Figure 4.5 as a function of reactor temperature, together with experimental data points for steam gasification of pine [128]. At higher temperatures, H_2 and CO production is promoted by endothermic Boudouard, water-gas and steam methane reforming reactions. Furthermore, elevating the temperature reverses the exothermic WGS reaction towards CO production and CO_2 consumption. Note that the CO_2 mole fraction reported for sawdust pine in reference [128] increases slightly with increasing temperature, a trend which is inconsistent with other models and with experimental data from the literature [107, 129]. This discrepancy most probably comes from a biomass pyrolysis kinetic model from which the prediction of CO/CO_2 ratio is difficult without introduction of an additional experimental correlation (see Chapter 3). This may also arise from the limitation of the two-step pyrolysis kinetic mechanism, as well as the oversimplified kinetic mechanism adopted for tar cracking and reforming.

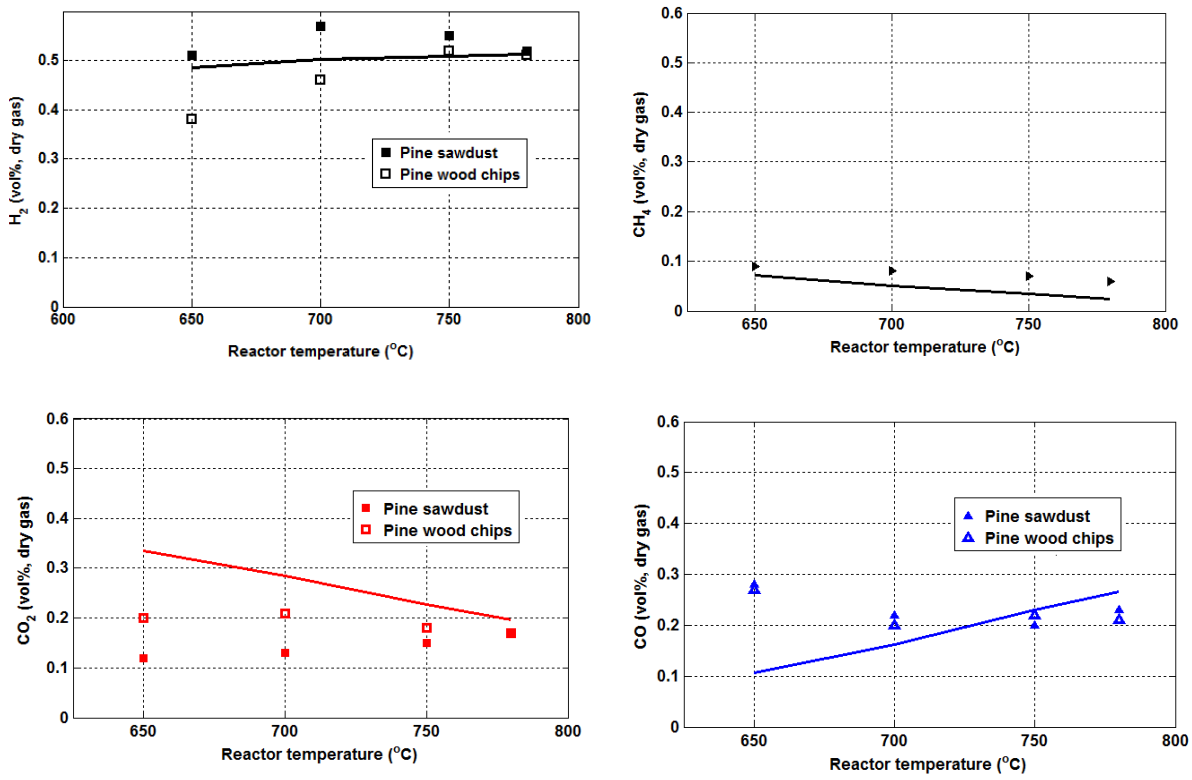

Figure 4.5. Effect of reactor temperature on dry N_2-free product gas composition for steam gasification of pine at S/B ratio of 0.86. Experimental data points are from Herguido *et al.* [128]. Lines are the predictions from the model developed in this thesis.

As shown in Chapter 3 (Figure 3.3), the methane content of biomass pyrolysis gas is in good agreement with the experimental data. However, for biomass steam gasification, SMR consumes most of the methane generated from biomass pyrolysis. leading to under-prediction of methane in the syngas generated from a biomass gasifier. In reality, steam conversion is less than predicted, suggesting that the steam is not completely available for gasification reactions.

The product gas composition from steam gasification of pine wood chips in Figure 4.5 shows better agreement with the model predictions. Although the particle size does not affect char gasification, it has an impact on the pyrolysis product distribution. Other physical properties, such as biomass shape and porosity, could also contribute to differences in results for sawdust and wood chips.

4.4 Summary

Steam gasification of biomass is modeled in a BFB gasifier by including heterogeneous and homogeneous gasification reactions in the coupled particle and reactor model of biomass drying and pyrolysis. The effects of steam-to-biomass ratio and reactor temperature on the distribution of products generated from steam gasification of pine sawdust and pine chips are predicted and compared with experimental data from the literature. The H_2 mole fraction in the product gas increases with increasing steam-to-biomass ratio because of the water-gas, steam methane reforming and water-gas shift (WGS) reactions. Raising the reactor temperature reverses the exothermic WGS reaction towards more CO production and less CO_2. The product gas composition from steam gasification of pine shows good agreement with the model predictions.

Chapter 5: Kinetic Modeling of Biomass Steam Gasification in a Dual Fluidized Bed Reactor

The purpose of this chapter is to develop an integrated steady-state kinetic model for predicting the performance of the dual fluidized bed gasifier at UBC. As shown schematically in Figure 5.1, this reactor consists of two interconnected fluidized beds, referred to as the gasifier and riser/combustor. Superheated steam fluidizes the gasifier in the bubbling flow regime to produce syngas by partial oxidation of solid biomass that is fed to the gasifier. Unreacted char (a by-product of biomass gasification), together with bed material, i.e. inert silica sand (SiO_2), are circulated from the bottom of the gasifier to the bottom of the combustor, which operates at a higher temperature. The combustor is fluidized with air at a high superficial gas velocity in the fast fluidization flow regime as in a circulating fluidized bed riser. The heat requirements of the highly endothermic biomass gasification reactions are provided by the cyclic circulation of hot bed material (mostly sand) from the top of the combustor through a cyclone to the gasifier. The combustion of unreacted char is not sufficient to maintain the combustor temperature at the desired level due to the large heat losses experienced by a pilot scale unit. Therefore, additional fuel (here natural gas) is burnt with air in an air pre-heater/natural gas burner prior to the combustor[1].

In this chapter, by incorporating reaction kinetics and reactor hydrodynamics, two separate kinetic models, one for biomass steam gasification in the bubbling fluidized bed (BFB) gasifier and the other for char (and natural gas) combustion with air in the circulating fluidized bed (CFB) riser of the DFB gasifier are developed and implemented by performing mass and energy balances over the two reactors. These models are capable of predicting species concentrations, solids hold-up, temperature, pressure and superficial gas velocity profiles along each reactor, as well as key operating parameters such as solids circulation rate and natural gas flow rate required for stable operation of the process. The dual fluidized bed gasifier model predictions will ultimately be compared with experimental measurements from the UBC dual fluidized bed unit that are currently proceeding, with a paper currently under preparation [130].

[1] In commercial operations, instead of methane, a fraction of product syngas can be burnt to provide heat.

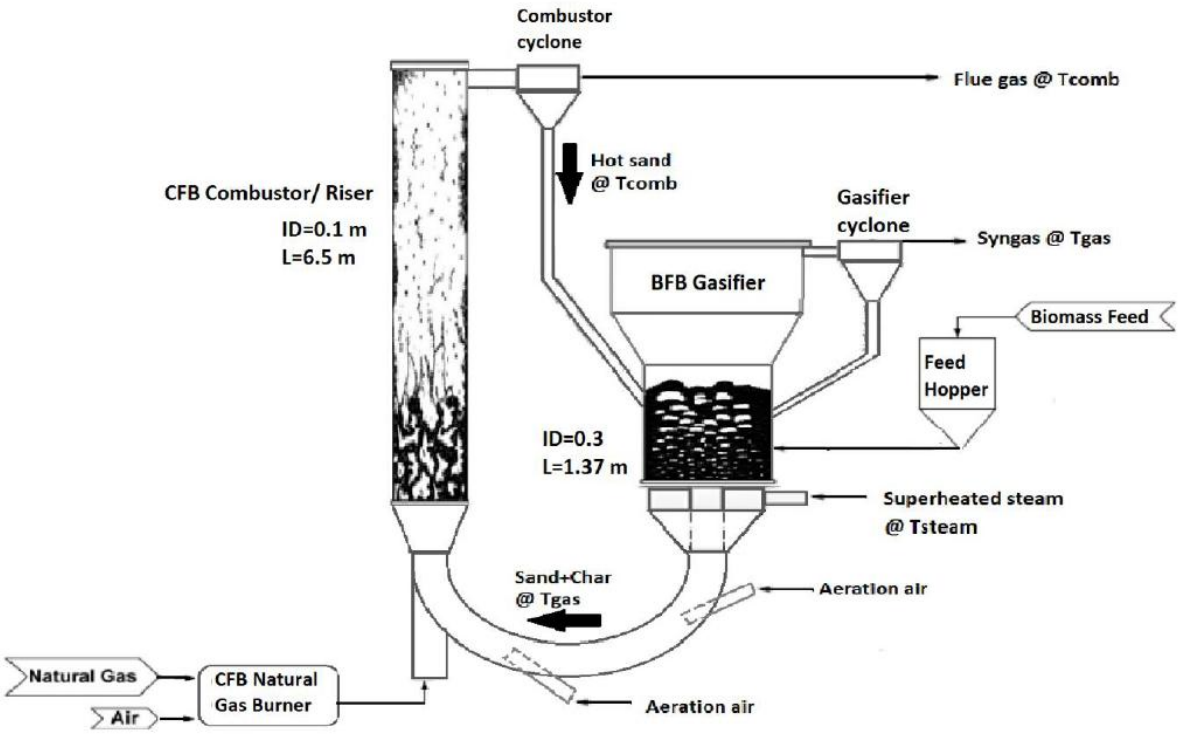

Figure 5.1. Schematic of Dual Fluidized Bed experimental gasification system at UBC.

5.1 Reaction kinetics

The kinetic parameters and heats of reaction for biomass drying and pyrolysis, modeled by a generic two-step kinetic mechanism, are summarized in Table 4.1. The kinetic rate expressions of major gasification and combustion reactions included in the model are listed in Table 5.1. Note that the catalytic effects of metal components present in the biomass ash, such as Ca, Na and K, are not directly taken into account.

Table 5.1. Major gasification and combustion reactions

Reaction		*Kinetics rate expression*	*Ref.*
**Boudouard*	$C(s)+CO_2 \rightarrow 2CO$ $\Delta H^o_{rxn} = +172\,{}^{kJ}\!/_{mole}$	$r_{C1}\left(s^{-1}\right) = 3.9\times10^{4}\exp\left(-215000/R.T\right)\times P_{CO_2}^{0.38}$	*[101]*
**Water-Gas*	$C(s)+H_2O \rightarrow CO+H_2$ $\Delta H^o_{rxn} = +131\,{}^{kJ}\!/_{mole}$	$r_{C2}\left(s^{-1}\right) = 3.7\times10^{5}\exp\left(-237000/R.T\right)\times P_{H_2O}^{0.57}$	*[102]*
**Methanation*	$C(s)+2H_2 \rightarrow CH_4$ $\Delta H^o_{rxn} = -75\,{}^{kJ}\!/_{mole}$	$r_{C3}\left(s^{-1}\right) = 4.3\times10^{-5}\exp\left(-94800/R.T\right)\times P_{H_2}^{0.93}$	*[103]*
Steam-Methane Reforming	$CH_4+H_2O \leftrightarrow CO+3H_2$ $\Delta H^o_{rxn} = +206\,{}^{kJ}\!/_{mole}$	$r_{SMR}\left(mol.m^{-3}.s^{-1}\right) = 3\times10^{5}\exp\left(\frac{-125000}{R.T}\right)\times C_{CH_4}.C_{H_2O}$	*[125]*
Water-Gas Shift (WGS)	$CO+H_2O \leftrightarrow CO_2+H_2$ $\Delta H^o_{rxn} = -41\,{}^{kJ}\!/_{mole}$	$K_{WGS} = 0.0265\exp\left(\frac{3968}{T}\right)$ $r_{WGS}\left(mol.m^{-3}.s^{-1}\right) = 2.78\exp\left(\frac{-1510}{T}\right)\times\left(C_{CO}.C_{H_2O} - \frac{C_{CO_2}.C_{H_2}}{K_{WGS}}\right)$	*[126]*, *[127]*
**Carbon oxidation*	$\frac{2(\eta+1)}{(\eta+2)}C(s)+O_2 \rightarrow \frac{2\eta}{(\eta+2)}CO+\frac{2}{(\eta+2)}CO_2$	$\eta = 3\times10^{8}\exp\left(\frac{-30178}{T}\right)$ $r_{C,ox}\left(s^{-1}\right) = 1.52\times10^{11}\exp\left(\frac{-13078}{T}\right)\times P_{O_2}\times\left(1-X_C\right)^{1.2}$	*[131]*, *[132]*
Hydrogen oxidation	$H_2+{}^{1}\!/_{2}O_2 \rightarrow H_2O$ $\Delta H^o_{rxn} = -241.83\,{}^{kJ}\!/_{mole}$	$r_{H_2,ox}\left(mol.m^{-3}.s^{-1}\right) = 51.8T^{3/2}\exp\left(\frac{-3420}{T}\right)\times C_{H_2}^{1.5}.C_{O_2}$	*[133]*
Carbon monoxide oxidation	$CO+{}^{1}\!/_{2}O_2 \rightarrow CO_2$ $\Delta H^o_{rxn} = -283\,{}^{kJ}\!/_{mole}$	$r_{CO,ox}\left(mol.m^{-3}.s^{-1}\right) = 1.3\times10^{8}\exp\left(\frac{-125400}{R.T}\right)\times C_{CO}.C_{O_2}^{0.5}.C_{H_2O}^{0.5}$	*[134]*
Methane oxidation	$CH_4+{}^{3}\!/_{2}O_2 \rightarrow CO+2H_2O$ $\Delta H^o_{rxn} = -802.28\,{}^{kJ}\!/_{mole}$	$r_{CH_4,ox}\left(mol.m^{-3}.s^{-1}\right) = 4.68\times10^{18}T^{0.5}\exp\left(\frac{-167000}{R.T}\right)C_{CH_4}^{0.7}.C_{O_2}^{0.8}$	*[135]*

*First order reactions with respect to solid Carbon. R=8.314 J.mol^{-1}.K^{-1}, T [K], P_i [Pa] and C_i [mol.m^{-3}].

5.2 BFB gasifier two-phase kinetic model

In our steady-state gas-solid bubbling fluidized bed reactor model, while perfect mixing is assumed for solid particles, the gas phase is modeled by a generalized version of the one dimensional two-phase model [136, 137]. As discussed in the previous chapter, if biomass particles are treated as aggregates that behave like batch reactors inside the fluidized bed reactor, the average particle conversion of solid particles leaving the reactor is calculated in a manner similar to a macrofluid (non-coalescing droplets of very viscous liquids) as

$$\bar{X}_P = \int_0^{\infty} \left(X_P\right)_{\substack{individual \\ particle}} . \frac{1}{\tau_s} . \exp\left(-t/\tau_s\right) dt \tag{5.1}$$

where the mean solids residence time is defined as the solids hold-up inside the bubbling bed divided by mass flow rate of solid particles leaving the dense bed. In a dual fluidized bed reactor configuration, the transportation of particles out of the BFB takes place by circulation of solids to the combustor reactor. Hence, the mean solids residence time inside the BFB is calculated from experimental measurement of the sand inventory of dense bubbling bed (M_{sand}) and the sand circulation mass flow rate ($\dot{m}_{sand}$):

$$\tau_s = \frac{M_{sand}}{\dot{m}_{sand}} = \frac{M_P}{\dot{m}_{P,out}} \tag{5.2}$$

For gasifiers that operate at high temperatures, the unreacted biomass content of solid particles leaving the reactor is negligible, especially for smaller particles. If M_{Char} is the char hold-up (kg) in the dense bubbling bed and $\dot{m}_{Char,out}$ is the mass flow rate of char (kg/s) leaving the BFB, the mean solids residence time can be approximated by:

$$\tau_s = \frac{M_{Char}}{\dot{m}_{Char,out}} \tag{5.3}$$

From Chapter 3, the biomass drying and pyrolysis products distribution are obtained. As shown schematically in Figure 5.2, the water vapour, gas and tar generated from the drying, pyrolysis

and gasification of biomass/char particles in the solid phase are assumed to be transferred uniformly to the high-density (emulsion) phase along the reactor height. Furthermore, there is a net flow of excess gas from the emulsion phase to the low density (bubble) phase that is almost free of solids. The mixture of fluidizing agent (i.e. N_2 and steam) and gaseous products released from gas-solid reactions are modeled to be in plug flow in both the bubble and emulsion phases.

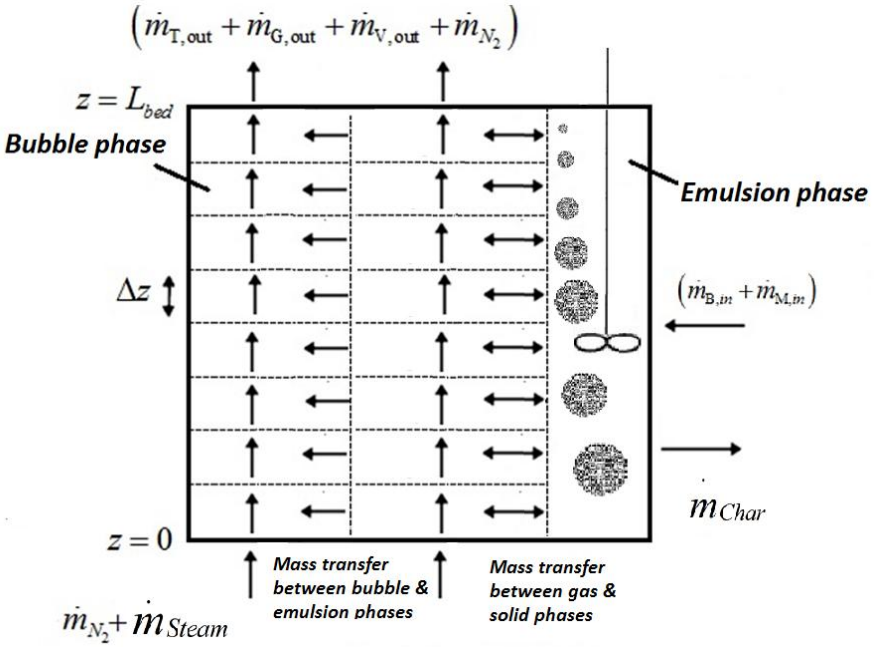

Figure 5.2. Schematic of two-phase biomass steam gasifier model for the BFB.

Due to the very good heat transfer of bubbling fluidized beds and as a first approximation, uniform temperature is assumed throughout the dense section of the BFB. In the absence of differential equations for energy balances and neglecting dispersion (second-order) terms, a system of differential equations for the gas mole balances in the low and high density phases, as well as differential equation for the reactor pressure balance along the dense bed height are solved together.

If we use the general descriptor “low-density” (L) phase for the dilute phase and “high-density” (H) phase for the dense phase, the L-phase represents the bubble phase, whereas the H-phase represents the emulsion phase.

Low-density phase:

$$-\frac{1}{A}.\frac{d}{dz}\left(\nu_L.C_{iL}\right)+\psi_L.a_{I_{L\to H}}.k_{c_{i,L\to H}}.\left(C_{iH}-C_{iL}\right)-\psi_L.\nu'''_{Bulk_{L\to H}}.C_{iL}+\psi_H.\nu'''_{Bulk_{H\to L}}.C_{iH}+\psi_L.Rate_{iL}=0 \quad (5.4)$$

High-density phase:

$$-\frac{1}{A}.\frac{d}{dz}\left(\nu_H.C_{iH}\right)+\psi_H.a_{I_{H\to L}}.k_{c_{i,H\to L}}.\left(C_{iL}-C_{iH}\right)-\psi_H.\nu'''_{Bulk_{H\to L}}.C_{iH}+\psi_L.\nu'''_{Bulk_{L\to H}}.C_{iL}+\psi_H.Rate_{iH}=0 \quad (5.5)$$

Pressure balance:

$$-\frac{dP}{dz}=\left(1-\varepsilon\right).\rho_s.g \quad (5.6)$$

where A is the bed cross-sectional area, ε the cross-sectional bed voidage and ν_φ is the volumetric flow rate of phase φ:

$$\nu_\varphi=\psi_\varphi.\varepsilon_\varphi.U_{gas_\varphi}.A \quad (5.7)$$

For phase φ: $C_{i\varphi}$ is the concentration of species i, ψ_φ the volume fraction, ε_φ is the void fraction, and U_{gas_φ} the convective gas velocity.

The variation in volumetric flow rate of each phase along the reactor is calculated by assuming that the ideal gas law applies:

$$\nu_\varphi=\frac{R.T}{P}.\sum_{i=1}^{N_C}F_{i\varphi} \quad (5.8)$$

with the molar flow rate of each species in phase φ:

$$F_{i\varphi}=\nu_\varphi.C_{i\varphi} \quad (5.9)$$

The bed superficial gas velocity at every height of the bed is:

$$U = \left(\nu_L + \nu_H\right)/A \tag{5.10}$$

The bed volume fractions add up to unity:

$$\psi_L + \psi_H = 1 \tag{5.11}$$

and for the cross-sectional area of the bed that is occupied by bubble phase:

$$\psi_L = \left(\varepsilon - \varepsilon_{mf}\right)/\left(\varepsilon_{L0} - \varepsilon_{mf}\right) \tag{5.12}$$

For solid-free bubbles $\varepsilon_L = \varepsilon_{L0} = 1$. The voidage at minimum fluidization (ε_{mf}) is obtained from experimental measurements. The overall bed voidage (ε) is estimated from Clift and Grace [117]:

$$\varepsilon = 1 - \left(\frac{1 - \varepsilon_{mf}}{1 + \left(U - U_{mf}\right)/\left(0.711\sqrt{g.d_b}\right)} \right) \tag{5.13}$$

The bubble diameter at every level of the bed is estimated from an equation of Darton *et al.* [118]:

$$d_b = 0.56 g^{-0.2} \left(U - U_{mf}\right)^{0.4} \left(z + 4\sqrt{\frac{A}{N_{or}}} \right) \tag{5.14}$$

where N_{or} is the number of holes in the orifice plate.

In the gas mole balances, the equi-molar interphase mass transfer terms due to concentration gradient are the same for both phases:

$$\psi_H . a_{I_{H\to L}} . k_{c_{i,H\to L}} . \left(C_{iL} - C_{iH}\right) = -\psi_L . a_{I_{L\to H}} . k_{c_{i,L\to H}} . \left(C_{iH} - C_{iL}\right) \tag{5.15}$$

with the inter-phase volumetric mass transfer coefficient (1/s) calculated from the correlation of Sit and Grace [138]:

$$a_{I_{L\to H}}.k_{c_{i,L\to H}} = \left(\frac{6}{d_b}\right)\left(\frac{U_{mf}}{3} + 2.\sqrt{\frac{D_i\varepsilon_{mf}U_b}{\pi d_b}}\right) \tag{5.16}$$

The minimum fluidization velocity and bubble rise velocity are calculated from Grace [139] and Davidson and Harrison [140], respectively:

$$Re_{mf} = \frac{\rho_g.U_{mf}.d_p}{\mu} = \sqrt{27.2^2 + 0.0408.Ar} - 27.2 \tag{5.17}$$

where:

$$Ar = \frac{\rho_g.\left(\rho_s - \rho_g\right).g.d_p^3}{\mu^2} \tag{5.18}$$

$$U_b = \left(U - U_{mf}\right).\left(1 + \frac{0.711}{U}\sqrt{g.d_b}\right) \tag{5.19}$$

The diffusion coefficient of each species is calculated from the method of Wilke [141]:

$$D_i = \left(1 - y_i\right) \Bigg/ \sum_{\substack{j=1 \\ j\neq i}}^{N_C}\left(\frac{y_i}{D_{ij}}\right) \tag{5.20}$$

where y_i is the overall mole fraction of component *i*, and D_{ij} is the binary diffusion coefficient between species i and j, calculated from Chapman–Enskog theory [142]:

$$D_{ij} = \frac{1.858\times10^{-3}T^{3/2}\left(\left(MW_i + MW_j\right)/\left(MW_i.MW_j\right)\right)^{1/2}}{P.\sigma_{ij}^2.\Omega} \tag{5.21}$$

Here D_{ij} is in cm^2/s, T is in degrees Kelvin, P the pressure in atmospheres, σ_{ij} is the average collision diameter and Ω is a temperature-dependent collision integral. For tabulated values, see [143].

In equations (5.4) and (5.5), the convective flow leaving the H-phase is given by:

$$\psi_H . \nu'''_{Bulk_{H\to L}} . C_{iH} \tag{5.22}$$

and that leaving the L-phase is:

$$\psi_L . \nu'''_{Bulk_{L\to H}} . C_{iL} \tag{5.23}$$

According to the Mahecha-Botero [137] algorithm of calculation, to maintain fluidizing conditions at any integration point:

a) If $\nu_H < m.U_{mf}.A$: Gas flows to the H-phase to avoid de-fluidization.

$$\nu'''_{Bulk_{H\to L}} = 0 \quad \& \quad \nu'''_{Bulk_{L\to H}} = \left(m.U_{mf}.A - \nu_H\right) \Big/ \left(\psi_H . A.\Delta z\right) \tag{5.24}$$

b) If $\nu_H = m.U_{mf}.A$: There is no cross-flow.

$$\nu'''_{Bulk_{H\to L}} = 0 \quad \& \quad \nu'''_{Bulk_{L\to H}} = 0 \tag{5.25}$$

c) If $\nu_H > m.U_{mf}.A$: Excess gas in the H-phase transfers to the L-phase.

$$\nu'''_{Bulk_{H\to L}} = \left(\nu_H - m.U_{mf}.A\right) \Big/ \left(\psi_H . A.\Delta z\right) \quad \& \quad \nu'''_{Bulk_{L\to H}} = 0 \tag{5.26}$$

Here m can be taken as 1.0 corresponding to the standard two-phase theory. Case c is often encountered for biomass gasification leading to the release of a significant amount of excess gas flow in the H-phase. Most of this excess gas then migrates to the L-phase to augment bubbles.

In the gas mole balances, $Rate_{i,\varphi}\left(mol.m_{\varphi}^{-3}.s^{-1}\right)$ represents the net reaction rate of production of species i in phase φ. To account for heterogeneous reactions, we need to know the distribution of solids between the two phases. From a solids material balance:

$$\left(1-\varepsilon\right) = \left(1-\varepsilon_H\right).\psi_H + \left(1-\varepsilon_L\right).\psi_L \tag{5.27}$$

and the mass fraction of solids going to phase φ is:

$$\left(\frac{1-\varepsilon_{\varphi}}{1-\varepsilon}\right).\psi_{\varphi} \tag{5.28}$$

Given the perfect mixing assumption for the BFB, we assume that the ratio of char hold-up (m_{Char}) in adjacent cells of the fluidized bed is the same as the ratio of total solids hold-up of those cells. With Δz being the equal cell height, we have:

$$\frac{m_{char}(z+\Delta z)}{m_{char}(z)} = \frac{\left(1-\varepsilon(z+\Delta z)\right).A.\Delta z}{\left(1-\varepsilon(z)\right).A.\Delta z} \tag{5.29}$$

If M_{Char} is the total char bed inventory and L_{bed} the expanded dense bed height, the local char hold-up in every cell can be calculated as:

$$\frac{m_{char}(z)}{M_{char}} = \frac{\left(1-\varepsilon(z)\right).A.\Delta z}{\left(1-\varepsilon_{ave}\right)A.L_{bed}} \tag{5.30}$$

where ε_{ave} is the average bed voidage:

$$\varepsilon_{ave} = \left(\int_{0}^{L_{bed}} \varepsilon.dz\right) \Big/ L_{bed} \tag{5.31}$$

Therefore, the local char hold-up in phase φ is:

$$m_{char}(z).\left(\frac{1-\varepsilon_{\varphi}}{1-\varepsilon}\right).\psi_{\varphi} = \left(\frac{M_{char}}{L_{bed}}\right).\left(\frac{1-\varepsilon_{\varphi}}{1-\varepsilon_{ave}}\right).\psi_{\varphi}.\Delta z \tag{5.32}$$

Assuming the abovementioned distribution of char particles between the cells and phases of the BFB also applies to biomass particles that go through drying and pyrolysis, the net reaction rates for different gaseous species are formulated as follows:

$$Rate_{Tar,\varphi} = \overbrace{\left(\frac{1-\varepsilon_{\varphi}}{1-\varepsilon_{ave}}\right)\frac{\bar{Y}_{T,pyro}.\left(\dot{m}_{B,in}+\dot{m}_{M,in}\right)/MW_{Tar}}{A.L_{bed}}}^{Biomass\ pyrolysis} - \overbrace{\varepsilon_{\varphi}.\left(k_4.\left(1-\gamma_{Tar_{inert}}\right).C_{Tar,\varphi}\right)}^{Tar\ cracking} \tag{5.33}$$

$$Rate_{H_2O,\varphi} = \overbrace{\left(\frac{1-\varepsilon_\varphi}{1-\varepsilon_{ave}}\right)\frac{\bar{Y}_V.\left(\dot{m}_{\mathrm{B},in}+\dot{m}_{\mathrm{M},in}\right)/MW_{H_2O}}{A.L_{bed}}}^{Drying} + \overbrace{\varepsilon_\varphi.\left(-r_{SMR}-r_{WGS}\right)}^{Homogeneous\ gasification} + \overbrace{\left(\frac{1-\varepsilon_\varphi}{1-\varepsilon_{ave}}\right)\left(\frac{M_{Char}/MW_{Char}}{A.L_{bed}}\right).\left(-r_{C2}\right)}^{Heterogeneous\ gasification} \quad (5.34)$$

For non-condensable gas species (i.e. i=H_2, CO, CO_2 and CH_4):

$$Rate_{\mathrm{i},\varphi} = \overbrace{\left(\frac{1-\varepsilon_\varphi}{1-\varepsilon_{ave}}\right).\frac{\bar{Y}_{\mathrm{G},pyro}.\left(\dot{m}_{\mathrm{B},in}+\dot{m}_{\mathrm{M},in}\right).\left(w_{i,pyro}/MW_i\right)}{A.L_{bed}}}^{Biomass\ pyrolysis} + \overbrace{\varepsilon_\varphi.\left(k_4.\left(1-\gamma_{Tar_{inert}}\right).C_{Tar,\varphi}\right).MW_{Tar}.\left(w_{i,\mathrm{tar\ cracking}}/MW_i\right)}^{Tar\ cracking} + \overbrace{Rate_{\mathrm{i},\varphi,gasification}}^{Gasification} \quad (5.35)$$

with the gasification terms:

$$Rate_{\mathrm{CO},\varphi,gasification} = \varepsilon_\varphi.\left(r_{SMR}-r_{WGS}\right)+\left(\frac{1-\varepsilon_\varphi}{1-\varepsilon_{ave}}\right).\left(\frac{M_{Char}/MW_{Char}}{A.L_{bed}}\right).\left(2.r_{C1}+r_{C2}\right) \quad (5.36)$$

$$Rate_{\mathrm{CO_2},\varphi,gasification} = \varepsilon_\varphi.\left(r_{WGS}\right)+\left(\frac{1-\varepsilon_\varphi}{1-\varepsilon_{ave}}\right)\left(\frac{M_{Char}/MW_{Char}}{A.L_{bed}}\right).\left(-r_{C1}\right) \quad (5.37)$$

$$Rate_{\mathrm{CH_4},\varphi,gasification} = \varepsilon_\varphi.\left(-r_{SMR}\right)+\left(\frac{1-\varepsilon_\varphi}{1-\varepsilon_{ave}}\right)\left(\frac{M_{Char}/MW_{Char}}{A.L_{bed}}\right).\left(r_{C3}\right) \quad (5.38)$$

$$Rate_{H_2,\varphi,gasification} = \varepsilon_\varphi.\left(3.r_{SMR}+r_{WGS}\right)+\left(\frac{1-\varepsilon_\varphi}{1-\varepsilon_{ave}}\right)\left(\frac{M_{Char}/MW_{Char}}{A.L_{bed}}\right).\left(r_{C2}-2.r_{C3}\right) \quad (5.39)$$

For solids-free bubbles, heterogeneous reactions of biomass pyrolysis and char gasification only take place in the emulsion phase.

Given an initial guess for the char hold-up of the dense bubbling bed and using the MATLAB ODE solver (ODE45), we solve the above coupled ODEs numerically to give the axial concentration profiles of steam, tar and non-condensable gas species, as well as the reactor pressure.

Performing a char balance over the dense bubbling bed at steady-state:

$$\dot{m}_{Char,out} = \dot{m}_{Char,gen} - \dot{m}_{Char,cons} \tag{5.40}$$

where:

$$\dot{m}_{Char,out} = M_{char} / \tau_s \tag{5.41}$$

$$\dot{m}_{Char,gen} = \bar{Y}_{C,pyro} . \left(\dot{m}_{B,in} + \dot{m}_{M,in} \right) \tag{5.42}$$

Given the axial partial pressures of gasifying agents in the emulsion phase of dense bed, the rate of char consumption due to heterogeneous gasification reactions is:

$$\dot{m}_{Char,cons} = \int_0^{L_{bed}} \left(d\dot{m}_{Char,gas} / dz \right) . dz = \int_0^{L_{bed}} \left(r_{C1,H}(z) + r_{C2,H}(z) + r_{C3,H}(z) \right) . \left(M_{char} / L_{bed} \right) . dz \tag{5.43}$$

Substituting the above values in the char balance equation for a given mean solids residence time, the char hold-up of the bed is updated:

$$M_{char} = \bar{Y}_C . \left(\dot{m}_{B,in} + \dot{m}_{M,in} \right) \Big/ \left(1/\tau_s + \int_0^{L_{bed}} \left(r_{C1,H}(z) + r_{C2,H}(z) + r_{C3,H}(z) \right) . dz \Big/ L_{bed} \right) \tag{5.44}$$

Note that to reduce solids entrainment from the dense bubbling bed, the reactor diameter is expanded in the upper section. For the current model, the entrainment of char and sand particles are neglected, and the freeboard region is modeled as a plug flow reactor in which only homogeneous reactions (i.e. tar cracking, SMR & WGS) take place. Six ODE's for the mole balances of gaseous species, together with one ODE for temperature variation along the freeboard, are solved simultaneously:

$$Freeboard: \begin{cases} U \dfrac{dC_{i,fb}}{dz} - Rate_{i,fb} = 0 \\ -C_{Pg} \rho_g U \dfrac{dT}{dz} - \sum_{k=1}^{Nr} \left(\Delta H_{rxn,k} . Rate_{rxn,k} \right) - h_{overall} . A_s \left(T - T_\infty \right) = 0 \end{cases} \tag{5.45}$$

where C_{Pg} is the specific heat capacity of the gas mixture, $\Delta H_{rxn,k}$ heat of reaction k, $Rate_{rxn,k}$ rate of reaction k, $h_{overall}$ overall heat-transfer coefficient, A_S external heat-transfer surface area per unit reactor volume, and T_∞ ambient temperature.

The overall heat transfer coefficient for the freeboard section is estimated from the sum of three thermal resistances on a cylindrical reactor vessel with inside and outside diameters ID and OD:

$$\frac{1}{h_{overall}} = \left(\frac{OD}{ID}\right)\frac{1}{h_{\text{int}}} + \frac{OD}{2.k_{wall}}.Ln\left(\frac{OD}{ID}\right) + \frac{1}{h_{air}} \tag{5.46}$$

where k_{wall} is the reactor wall thermal conductivity, h_{int} is the internal heat-transfer coefficient (neglecting radiation effects) calculated from the Sieder–Tate equation [144]:

$$Nu = \frac{h_{\text{int}}.ID}{k_g} = 0.023\,\text{Re}^{0.8}\,\text{Pr}^{0.33}\left(\mu/\mu_w\right)^{0.14} \tag{5.47}$$

$$\text{Re} = \frac{\rho.U.ID}{\mu}\ \&\ \text{Pr} = \frac{\mu.C_{Pg}}{k_g} \tag{5.48}$$

h_{air} is obtained from simplified equations for free convection from the surface of a vertical cylinder to air at atmospheric pressure [145]:

$$h_{air} = \begin{cases} 1.42\left(\dfrac{T_{surf} - T_\infty}{L_{bed}}\right)^{1/4} & 10^4 < Gr_f.\text{Pr}_f < 10^9 : Laminar \\ 1.31\left(T_{surf} - T_\infty\right)^{1/3} & Gr_f.\text{Pr}_f > 10^9 : Turbulent \end{cases} \tag{5.49}$$

where T_{surf} is the reactor outside wall surface temperature obtained from:

$$T_{surf} = T_\infty + \left(h_{overall}/h_{air}\right).\left(T_{bulk} - T_\infty\right) \tag{5.50}$$

and the reactor inside wall temperature is:

$$T_{wall} = T_{bulk} - \left(\frac{h_{overall}}{h_{\text{int}}}\right).\left(\frac{OD}{ID}\right).\left(T_{bulk} - T_{\infty}\right) \tag{5.51}$$

To calculate $Gr_f.Pr_f$, ambient air physical properties are used at film temperature $T_f = (T_{surf}+T_{\infty})/2$:

$$Gr_f.\mathrm{Pr}_f = \left(L_{bed}^3.\rho_{air}^2.g.C_{p,air}.\left(T_{surf} - T_{\infty}\right)/T_f\right)/\left(\mu_{air}.k_{air}\right) \tag{5.52}$$

The contribution of radiation to heat losses has not been included in our model. It is clear that including radiation would increase the temperature drop in the freeboard, affecting the product gas composition to a small extent.

For a given pressure drop across the bubbling fluidized bed, the expanded bed height (L_{bed}) is obtained, iteratively:

$$L_{bed} = \frac{-\left(P\left(z = L_{bed}\right) - P\left(z = 0\right)\right)}{\rho_{sand}.\left(1 - \varepsilon_{ave}\right).\mathrm{g}} \tag{5.53}$$

Neglecting the char weight contribution, the total bed inventory (W_{bed}) is:

$$W_{bed} = \rho_{sand}.A.L_{bed}.\left(1 - \varepsilon_{ave}\right) \tag{5.54}$$

Appendix D provides the algorithm used to simulate the BFB gasifier.

5.3 CFB combustor two-phase kinetic model

Depending on the magnitudes of superficial gas velocity (U) and solid circulation flux (G_s), the gas-solid upward transport operation of the riser falls in any of the following flow regimes [146]:

I. Homogeneous dilute flow (dilute pneumatic transport) without appreciable lateral and axial gradients of voidage. In this case, all solids move co-currently upward with the gas.

II. Core-annular dilute phase flow where there are appreciable lateral, but small axial gradients of voidage. This regime is characterized by dilute upward flow of solids in the core and descending streams of solid particle at the wall (annulus).

III. Fast fluidization or turbulent flow where both lateral and axial gradients are significant. In this case, the solids cannot be individually suspended in the riser. Consequently, a relatively dense bed forms at the bottom of the bed.

Figure 5.3 [146] shows a flow regime map where gas velocity is plotted against the solids flux divided by particle density. By increasing G_S at a given superficial gas velocity, the arrow heads show a transition from pneumatic transport (I) to core-annulus (II) and eventually to the fast fluidization flow regime (III).

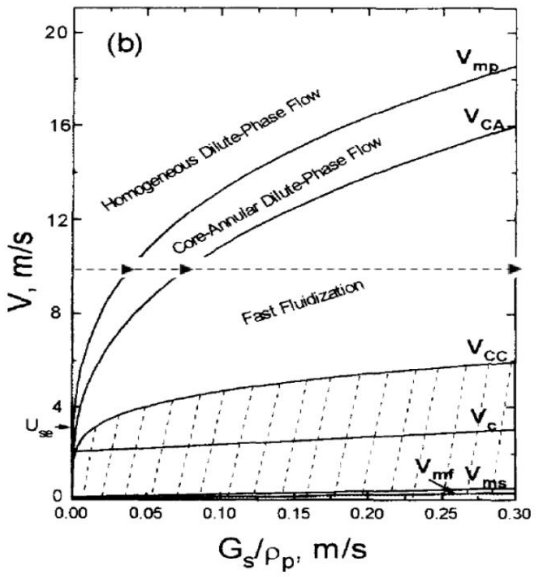

Figure 5.3. Practical flow regime maps for gas-solids upward transport in the presence of restrictions for group B sand particles, d_p=200µm, ρ_p = 2600 kg/m^3, D_{riser} = 0.15 m [146].

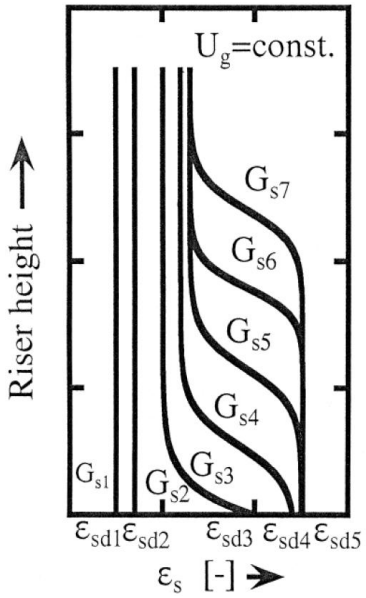

Figure 5.4. Typical axial profiles of solids holdup in circulating fluidized bed risers [147].

Figure 5.4 illustrates the effect of increasing G_S on an ideal axial profile of solids holdup in CFB risers [147]. By increasing G_S, the flow regime changes from pneumatic transport (G_{S1} and G_{S2}) to the core-annular flow regime (G_{S3}). When the solids circulation rate is further increased to the

saturation carrying capacity of the fluid ($G_S^* \approx G_{S4}$), much of the solids begin to accumulate at the bottom of the riser, and a typical S-shaped solids holdup distribution starts to form, indicative of the fast fluidization flow regime (G_{S5} to G_{S7}).

If $V_{CA} < U < V_{mp}$, the riser operates in the core-annular dilute transport flow regime, with no dense bed formation at the bottom of the riser. We then have [146]:

$$V_{CA}\Big/\sqrt{g.d_p} = 21.6Ar^{0.105}\left(\frac{G_s}{\rho_g.V_{CA}}\right)^{0.542} \tag{5.55}$$

$$V_{mp} = 10.1\left(g.d_p\right)^{0.347}\left(G_s/\rho_g\right)^{0.310}\left(d_p/D_{riser}\right)^{-0.139}Ar^{-0.021} \tag{5.56}$$

If we define:

$$\varepsilon_s^{'} = G_s\Big/\left(\rho_p\left(U-u_t\right)\right) \tag{5.57}$$

the solids holdups in the bottom dense zone (ε_{sd}) and top exit (ε_s^*), are considered for two cases:

(i) For $G_S < G_S^*$, profiles are relatively flat with [147]

$$\varepsilon_{sd}/\varepsilon_s^{'} = 1+6.14\times10^{-3}\left(\rho_pU/G_s\right)^{-0.23}\left(\left(\rho_p-\rho_g\right)/\rho_g\right)^{1.21}\left(U/\sqrt{g.D_{riser}}\right)^{-0.383} \tag{5.58}$$

$$\varepsilon_s^* = 4.04\left(\varepsilon_s^{'}\right)^{1.214} \tag{5.59}$$

(ii) For $G_S \geq G_S^*$, there are S-shaped profiles with the limiting holdups given [147] by

$$\varepsilon_{sd}/\varepsilon_s^{'} = 1+0.103\left(\rho_pU/Gs\right)^{1.13}\left(\left(\rho_p-\rho_g\right)/\rho_g\right)^{-0.013} \tag{5.60}$$

$$\varepsilon_s^*/\varepsilon_s^{'} = 1+0.208\sqrt{\rho_pU/Gs}\left(\left(\rho_p-\rho_g\right)/\rho_g\right)^{-0.082} \tag{5.61}$$

For the UBC DFB gasifier, all the fluidizing air is introduced from the bottom of the riser, minimizing the height of the dense bottom zone (if it exists). However, if $Gs \geq Gs^*$, the lower

part of the riser can be modeled as a bubbling or turbulent fluidized bed, with allowance for a splash zone between the lower dense and upper dilute regions.

The axial profile of solids holdup for the core-annulus region can be described by an exponential decay function of height [148]:

$$\frac{\varepsilon_s(z)-\varepsilon_s^*}{\varepsilon_{sd}-\varepsilon_s^*}=\exp\left(-a\left(z-z_0\right)\right) \tag{5.62}$$

where 'a' is the decay constant, estimated from a slightly modified form of Levenspiel [148]:

$$a=3\Big/\left(U-U_{mf}\right) \tag{5.63}$$

The height of the dense bottom region (z_0) is determined from pressure drop measurements. By neglecting frictional pressure losses and particle acceleration and deceleration:

$$\rho_{sand}.\mathrm{g}.\left(z_0.\varepsilon_{sd,ave}+\left(L_{riser}-z_0\right).\varepsilon_{s,ave}\right)=-\left(P\left(z=L_{riser}\right)-P\left(z=0\right)\right) \tag{5.64}$$

where $\varepsilon_{sd,ave}$ and $\varepsilon_{s,ave}$ are the average solid holdup in the dense bottom and core-annular regions of the CFB riser.

Various experimental correlations have been suggested in the literature to estimate the hydrodynamic parameters of the core-annulus regime [149, 150]. Among core radius (R_{core}), annulus voidage (ε_a) and core voidage (ε_c), only two of the parameters are estimated independently, with the third calculated from a solid mass balance at every cross-section of the riser:

$$\left(1-\varepsilon_s\left(z\right)\right).\left(D_{riser}/2\right)^2=\varepsilon_c.\left(R_{core}^2\right)+\varepsilon_a.\left(\left(D_{riser}/2\right)^2-R_{core}^2\right) \tag{5.65}$$

For our simulation purposes, we use the correlations of Kagawa *et al.* [151] and Patience and Chaouki [152] to estimate ε_a and R_{core}, respectively:

$$\varepsilon_a=2.\left(1-\varepsilon_s\left(z\right)\right)-1 \tag{5.66}$$

$$R_{core} = \left(D_{riser}/2\right).\left(1+1.1Fr\left(\frac{G_s}{\rho_p.U}\right)^{0.083Fr}\right)^{-1/2} \tag{5.67}$$

where the dimensionless Froude number is

$$Fr = U\Big/\sqrt{g.D_{riser}} \tag{5.68}$$

To model the core-annular flow regime, we apply the same generic equations for gas mole balances describing two-phase flow, with the core and annulus representing the low and high density phases, respectively. Assuming stagnant gas in the annulus [153], the ordinary differential equations for gas mole balances in the core must be coupled with algebraic equations for gas mole balances in the annulus. The fraction of bed cross-section area occupied by the core:

$$\psi_L = \frac{R_{core}^2}{\left(D_{riser}/2\right)^2} \tag{5.69}$$

The inter-phase volumetric mass transfer coefficient (1/s) is calculated from the correlation of Pugsley *et al.* [154]:

$$a_{I_{L\to H}}.k_{c_{i,L\to H}} = \left(\frac{4.D_i.\varepsilon_a.U}{\pi.L_{riser}}\right)^{1/2}.\left(\frac{2}{R_{core}}\right) \tag{5.70}$$

Assuming that the ratio of char hold-up in adjacent cells of the fluidized bed is the same as the ratio of total solids hold-up of those cells (see equation (5.29)), the net reaction rates for different gaseous species are similar to those for the BFB gasifier, and the total char inventory of the CFB riser (M_{Char}) is determined iteratively. The net reaction rates for different gaseous species are formulated as:

$$Rate_{H_2O,\varphi} = \overbrace{\varepsilon_\varphi.\left(-r_{SMR} - r_{WGS} + r_{H_2,ox} + 2.r_{CH_4,ox}\right)}^{Homogeneous\ reactions} + \overbrace{\left(\frac{1-\varepsilon_\varphi}{1-\varepsilon_{ave}}\right)\left(\frac{M_{Char}/MW_{Char}}{A.L_{bed}}\right).\left(-r_{C2}\right)}^{Heterogeneous\ reactions} \tag{5.71}$$

$$Rate_{O_2,\varphi} = \varepsilon_\varphi.\left(-\tfrac{1}{2} r_{H_2,ox} - \tfrac{1}{2} r_{CO,ox} - \tfrac{3}{2} r_{CH_4,ox}\right) + \left(\frac{1-\varepsilon_\varphi}{1-\varepsilon_{ave}}\right)\left(\frac{M_{Char}/MW_{Char}}{A.L_{bed}}\right).\left(-r_{C,ox}\right) \quad (5.72)$$

$$Rate_{CO,\varphi} = \varepsilon_\varphi.\left(r_{SMR} - r_{WGS} - r_{CO,ox} + r_{CH_4,ox}\right) + \left(\frac{1-\varepsilon_\varphi}{1-\varepsilon_{ave}}\right)\left(\frac{M_{Char}/MW_{Char}}{A.L_{bed}}\right).\left(2.r_{C1} + r_{C2} + \frac{2\eta}{(\eta+2)}.r_{C,ox}\right) \quad (5.73)$$

$$Rate_{CO_2,\varphi} = \varepsilon_\varphi.\left(r_{WGS} + r_{CO,ox}\right) + \left(\frac{1-\varepsilon_\varphi}{1-\varepsilon_{ave}}\right)\left(\frac{M_{Char}/MW_{Char}}{A.L_{bed}}\right).\left(-r_{C1} + \frac{2}{(\eta+2)} r_{C,ox}\right) \quad (5.74)$$

$$Rate_{CH_4,\varphi} = \varepsilon_\varphi.\left(-r_{SMR} - r_{CH_4,ox}\right) + \left(\frac{1-\varepsilon_\varphi}{1-\varepsilon_{ave}}\right)\left(\frac{M_{Char}/MW_{Char}}{A.L_{bed}}\right).\left(r_{C3}\right) \quad (5.75)$$

$$Rate_{H_2,\varphi} = \varepsilon_\varphi.\left(3.r_{SMR} + r_{WGS} - r_{H_2,ox}\right) + \left(\frac{1-\varepsilon_\varphi}{1-\varepsilon_{ave}}\right)\left(\frac{M_{Char}/MW_{Char}}{A.L_{bed}}\right).\left(r_{C2} - 2.r_{C3}\right) \quad (5.76)$$

A modeling approach similar to that for the BFB gasifier is used to account for temperature and pressure variations along the CFB riser. The differential equations for energy and pressure balances together with gas mole balances are coupled and solved with MATLAB ODE solver (ODE45). A description of the algorithm for simulation of the circulating fluidized bed combustor is also provided in Appendix D.

5.4 Boundary conditions

Except for superheated steam that is used as the fluidizing gas, the concentrations of other species at the bottom of the BFB gasifier are equal to zero (assuming no air/gas carryover or leakage). The inlet gas flow is divided into the two phases making use of a split factor:

$$F_{H_2O,H,in} = Split_H.F_{H_2O,in} \quad (5.77)$$

$$F_{H_2O,L,in} = F_{H_2O,in} - F_{H_2O,H,in} \quad (5.78)$$

with the split factor calculated as:

$$Split_H = \left(m.U_{mf}.A.C_{H_2O,in}\right) \Big/ F_{H_2O,in} \quad (5.79)$$

The un-gasified char leaving the gasifier is burnt with excess air in the riser. As the energy gain from char combustion is not sufficient to provide enough heat for the process, natural gas is used as an additional fuel. For simplification of calculations, all the air requirements of the system, including the air for char combustion, natural gas combustion and aeration air for transfer of solids from the gasifier to the combustor, is considered a single stream introduced to the NG burner (air pre-heater) upstream of the combustor (Figure 5.1).

At a given stoichiometric O_2 ratio (λ), the total oxygen flow rate required for complete combustion of natural gas ($CH_4 + 2O_2 \rightarrow CO_2 + 2H_2O$) and char ($C(s) + O_2 \rightarrow CO_2$) is:

$$F_{O_2,total} = \lambda\left(\dot{m}_{Char,in}/12 + 2 \times F_{CH_4,Burner}\right) \tag{5.80}$$

where $F_{CH_4,Burner}$ is the molar flow rate of natural gas to the burner.

Therefore, the CFB riser boundary conditions are determined to be:

$$F_{O_2,\text{in}} = F_{O_2,total} - 2 \times F_{CH_4,Burner} \tag{5.81}$$

$$F_{N_2,\text{in}} = (79/21) \times F_{O_2,total} \tag{5.82}$$

$$F_{H_2O,\text{in}} = 2 \times F_{CH_4,Burner} \tag{5.83}$$

$$F_{CO_2,\text{in}} = F_{CH_4,Burner} \tag{5.84}$$

$$F_{CH_4,\text{in}} = F_{H_2,\text{in}} = F_{CO,\text{in}} = 0 \tag{5.85}$$

In the following paragraphs, energy balances over the two reactors are performed to make first approximations for the riser superficial gas velocity (U) and solid circulation flux (G_S).

5.5 Overall energy balance

Regardless of the reactions included in each reactor, energy balance calculations are only based on total thermodynamic enthalpies of all inlet and outlet streams crossing the system boundaries.

In this manner, the thermodynamic states of streams and the heats of reactions are inherently taken into account. We have:

$$\dot{Q} = \sum_j \dot{m}_j . H_j^* \left(P_j , T_j \right) - \sum_i \dot{m}_i . H_i^* \left(P_i , T_i \right) \tag{5.86}$$

where $\dot{Q}$ is the net input heat (positive for heat sources), $\dot{m}_i$ and $H_i^* \left(P_i , T_i \right)$ are the mass/molar flow rate and total enthalpy of incoming streams at their respective inlet temperatures and pressures, while $\dot{m}_j$ and $H_j^* \left(P_j , T_j \right)$ are the mass/molar flow rate and total enthalpy of exiting streams, respectively.

To describe the thermodynamic states of the streams, substances are divided into four classes, i.e. ideal gases, inorganic solids, organic substances and pure water/steam. Details about energy balance calculations are given in Appendix E. Assuming exit streams are at the same temperature as the reactors, the energy balance for the gasifier is solved for the circulation rate of sand between the two beds:

$$\begin{aligned} &\dot{m}_{fuel} . H_{fuel}^* \left(T_{fuel} \right) + \dot{m}_{moisture} . H_{H_2O}^* \left(P_{fuel} , T_{fuel} \right) + \dot{m}_{steam} . H_{H_2O}^* \left(P_{steam} , T_{steam} \right) + \dot{m}_{sand} . H_{SiO_2}^* \left(T_{comb} \right) \\ &+ \dot{m}_{char,comb} . H_{char}^* \left(T_{comb} \right) - \dot{m}_{sand} . H_{SiO_2}^* \left(T_{gas} \right) - \dot{m}_{char,gas} . H_{char}^* \left(T_{gas} \right) - Q_{loss,gas} - \sum_{i=1}^{Nc} \dot{m}_{i,gasifier} . H_i^* \left(T_{gas} \right) = 0 \end{aligned} \tag{5.87}$$

Thus, the net solids circulation flux for the given riser diameter is estimated to be:

$$G_s = \frac{\dot{m}_{sand}}{\left(\pi . D_{riser}^2 / 4 \right)} \tag{5.88}$$

As a fair initial approximation, we assume complete combustion of char in the riser and complete combustion of natural gas in the NG burner. The energy balance for the combustor, together with NG burner, is then solved for the flow rate of natural gas input to the burner:

$$\dot{m}_{CH_4,Burner}.H^*_{CH_4}(T_{air}) + \dot{m}_{air}.H^*_{air}(T_{air}) + \dot{m}_{sand}.H^*_{SiO_2}(T_{gas}) + \dot{m}_{char,gas}.H^*_{char}(T_{gas}) - \dot{m}_{sand}.H^*_{SiO_2}(T_{comb}) \\ -\dot{m}_{char,riser}.H^*_{char}(T_{comb}) - Q_{loss,riser} - \sum_{i=1}^{Nc} \dot{m}_{i,riser}.H^*_i(T_{riser}) = 0 \quad (5.89)$$

Thus, the riser superficial gas velocity is calculated from CFB riser boundary conditions discussed above and the ideal gas law:

$$U = \frac{R.T_{comb}}{P_{comb}.\left(\pi.D^2_{riser}/4\right)} \sum_{i=1}^{Nc} F_{i,in} \quad (5.90)$$

See Appendix F for the MATLAB code for the dual fluidized bed gasifier.

5.6 Results and discussion

Tables 5.2 and 5.3 summarize the input parameters used for the simulations. The operating conditions are typical of the UBC DFB gasifier.

Table 5.2. Particle and reactor conditions.

Riser diameter	*0.1 m*
Riser height	*6.5 m*
Gasifier diameter	*0.3 m*
Freeboard diameter	*0.66 m*
Gasifier height (with/without freeboard)	*2.43-1.37 m*
Number of holes in distributor plate	*72*
Gasifier bed inventory	*100 kg*
Sand particle diameter	*200 µm*
Sand density	*2650 kg/m^3*
Biomass particle diameter	*790 µm*
Biomass particle density	*570 kg/m^3*

Table 5.3. Operating conditions of DFB gasifier.

Fuel composition	*$CH_{1.47}O_{0.6}$*
Biomass fuel flow rate	*10 kg/h (as received)*
Biomass moisture content	*10 wt% (as received)*
Steam flow rate	*10 kg/h*
T_{fuel} & P_{fuel} (at inlet)	*25°C & 1 atm*
Gasifier temperature	*650-800°C*
T_{steam}	*Same as gasifier*
P_{steam} (at inlet)	*1.2 atm*
Combustor temperature	*900°C*
Excess air	*20%*
T_{air} & P_{air} (at inlet)	*400°C & 1.1 atm*
$Q_{loss,\ combustor}$	*15 % (m_{fuel}* LHV_{fuel})*
$Q_{loss,\ gasifier}$	*15 % (m_{fuel}* LHV_{fuel})*

For the operating conditions of interest, different calculated hydrodynamic parameters for the bubbling fluidized bed gasifier are plotted as functions of height in Figure 5.5. As shown in Figure 5.5 (a), the overall void fraction (ε) and the contribution of bubbles in occupying the bed

cross-sectional area (ψ_L) decrease with increasing height in the reactor. Assuming no solid particles in the bubble phase: $\varepsilon_L=1$ and $\varepsilon_H=\varepsilon_{mf}$. At the bottom of the bed, small bubbles are generated from the distributor, while bubble size increases with height due to coalescence. Larger bubbles rise more quickly and spend less time in any given height interval in the bed. Furthermore, more than 90% of the total gas volumetric flow passes through bubbles. According to Figure 5.5 (b), the bubble rise velocity (u_L) increases with height, whereas the absolute velocity of gas in the emulsion phase slightly decreases. The increase in superficial gas velocity along the dense bubbling bed height is due to the decrease in hydrostatic pressure and increase in gas molar flow resulting from drying and gas-solid reactions (pyrolysis and gasification). Note that the effects of density variation and bulk transfer of gas between the phases are also accounted for in the current model. The decrease in superficial gas velocity with height above the dense bed is due to the temperature drop and the increased cross-sectional area of the freeboard zone. As shown in Figure 5.5 (c), the dense bed, with solids modelled as a perfectly mixed reactor, has a uniform temperature, but from the plug flow model for the gas, a temperature drop of >100K is calculated for the freeboard. As seen in Figure 5.5(d), the pressure drop across the dense bubbling bed is about 14 kPa, while the pressure is predicted to be almost uniform in the freeboard.

The changes in molar fractions of gaseous species in the bubble and emulsion phases along with height are illustrated in Figure 5.6. Dashed curves represent the emulsion phase, whereas the solid curves are for the bubble phase. The heterogeneous reactions of biomass gasification are dominant in the emulsion phase where almost all of the solid char resides. Furthermore, due to the lower gas velocity and higher gas residence time in the emulsion phase, H_2O is consumed more rapidly along the height in the emulsion phase. On the other hand, the H_2 concentration is higher in the emulsion phase than in the bubble phase indicating that more hydrogen is produced in this phase. Due to the Boudouard reaction, the CO concentration is also larger in the emulsion phase than in the bubble phase. Above the two-phase section of the reactor, the homogeneous reactions (i.e. WGS, SMR and tar cracking) generate more H_2. The expanded cross-section of the column in the conical section increases the gas residence time and allows further reactions.

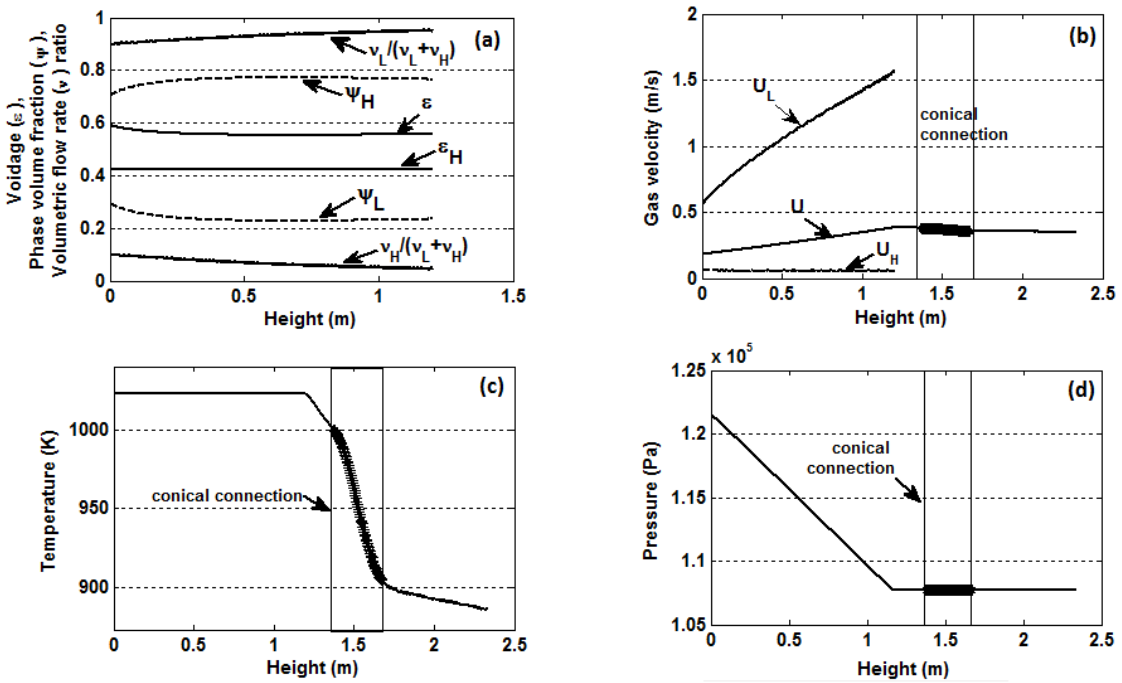

Figure 5.5. Variation of BFB parameters versus height predicted by two-phase model. (a) Emulsion phase voidage and overall dense bed voidage (ε_H, ε), fraction of bed cross-sectional area occupied by each phase (ψ_L, ψ_H), and volumetric flow rate ratios of phases as functions of height in the dense bubbling bed. (b) superficial gas velocity (U) and absolute gas velocities in the bubble and emulsion phases (U_L, U_H), (c) temperature, (d) hydrostatic pressure. Gasifier temperature=750^{o}C, Steam/biomass ratio=1.22. For other operating conditions, see Tables 5.2 and 5.3.

Figure 5.7 illustrates the equilibrium constant of the WGS reaction together with the ratio ($[CO_2].[H_2]$)/($[H_2O].[CO]$) as a function of height in the gasifier. Due to the drop in temperature along the freeboard, the WGS equilibrium varies with height along the reactor. As seen, at the top of the dense bubbling bed, the composition of gas mixture approaches equilibrium and due to the increased gas residence time in the conical section of the reactor, the composition is close to that at equilibrium. However, above the conical section, the gas mixture composition differs substantially from that at equilibrium and almost flattens out due to the low reaction rates at the lower temperatures.

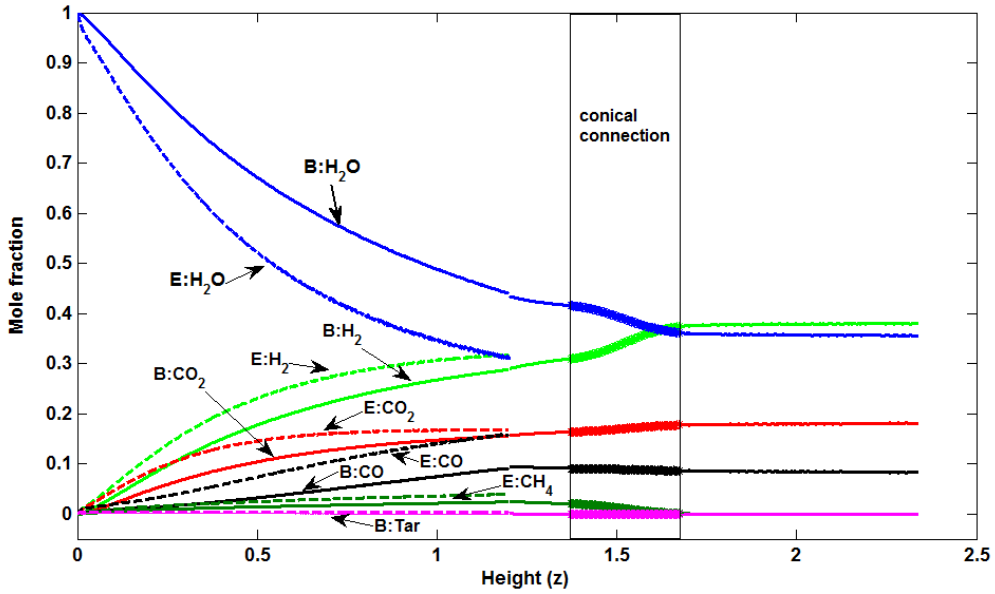

Figure 5.6. Mole fractions of gas species along gasifier height, B: bubble, E: emulsion. Gasifier temperature=750^{o}C, Steam/Biomass mass flow ratio=1.22.

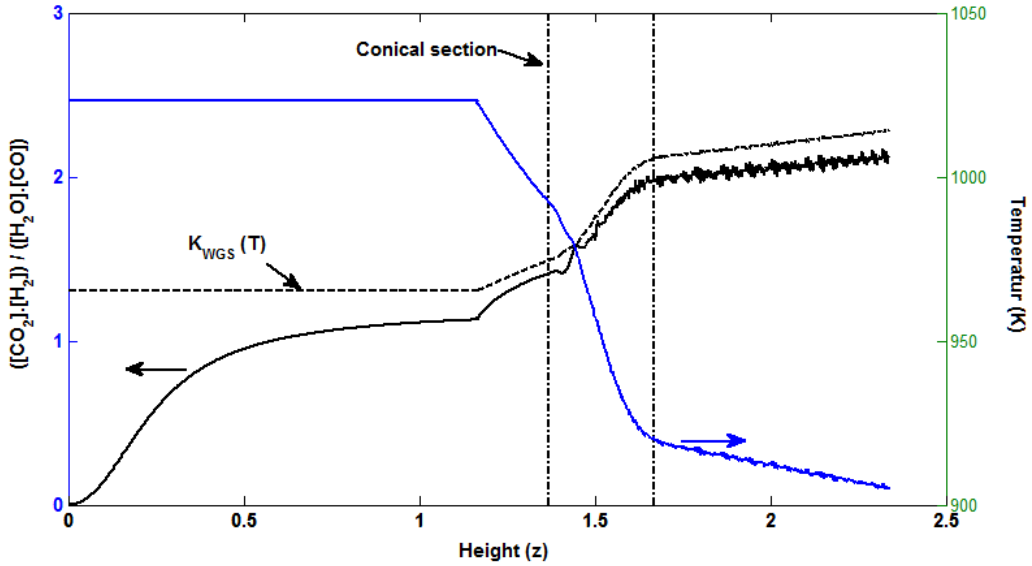

Figure 5.7. Deviation from WGS reaction equilibrium constant (K_{WGS}) as a function of height in the gasifier. Gasifier temperature=750^{o}C, Steam/Biomass mass flow ratio=1.22.

The kinetic model of the gasifier (at temperature 750^{o}C and steam/biomass mass ratio of 1.22) gives a mass flow rate of unreacted char entering the riser of 1.515 kg/h and a solids circulation flux based on riser cross-sectional area of G_s=12.55 kg/m^2.s. Assuming complete combustion of char and methane within the combustor, an energy balance yields a natural gas flow rate, air flow rate and inlet riser superficial gas velocity of 1.64 Nm^3/h, 34.88 Nm^3/h and U=5.55 m/s, respectively. Under these operating conditions, Figure 5.8 predicts that the core-annulus flow regime is encountered in the riser.

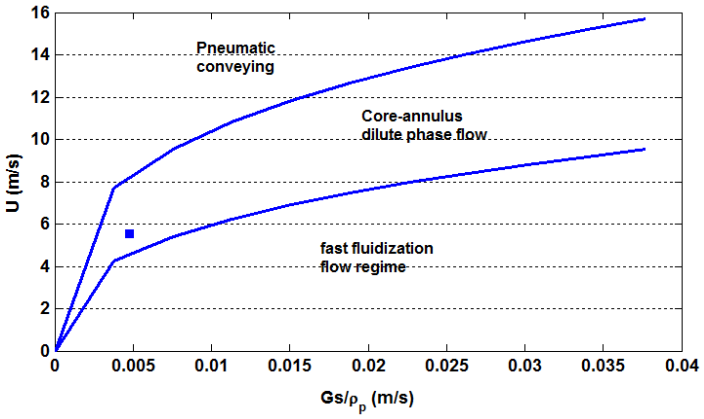

Figure 5.8. Flow regime map for gas-solid upward transport for group B sand particles, d_p=200 µm, ρ_p = 2650 kg/m^3, D_{riser} = 0.1 m.

Figure 5.9 (a) depicts the core-to-column radius ratio (R_{core}/(D_{riser}/2)), core and annulus voidages (ε_c, ε_a) and overall riser voidage (ε) along the riser. In the core-annulus flow regime, the solids hold-up and thus the hydrostatic pressure decrease exponentially with height in the reactor as shown Figure 5.9 (b). Therefore, the overall bed voidage, including the core and annulus voidages, increases with height, with the annulus voidage always less than the core voidage. As observed, the core radius, being only a function of U and G_s, does not change with height. In this model, the temperature variation along the riser is ignored.

Figure 5.10 shows the variation of molar fractions of gaseous species in the core and annulus regions along the riser height. Dashed curves represent the annulus region, whereas unbroken curves denote the core region. The oxygen concentration is lower in the annulus than in the core along the entire reactor height and vice versa for CO_2. The greater char holdup in the annulus

region results in more oxygen consumption and greater CO_2 production than in the core region. However, the changes in concentrations of O_2 and CO_2 with height are sharper in the core region, indicating higher combustion rates in the core region, despite lower char content. This is because of the higher concentration of oxygen in the core region. The difference between the core and annulus gas concentrations decreases with height due to inter-phase mass transfer. Steam concentration is similar for both regions and remains almost constant along the reactor.

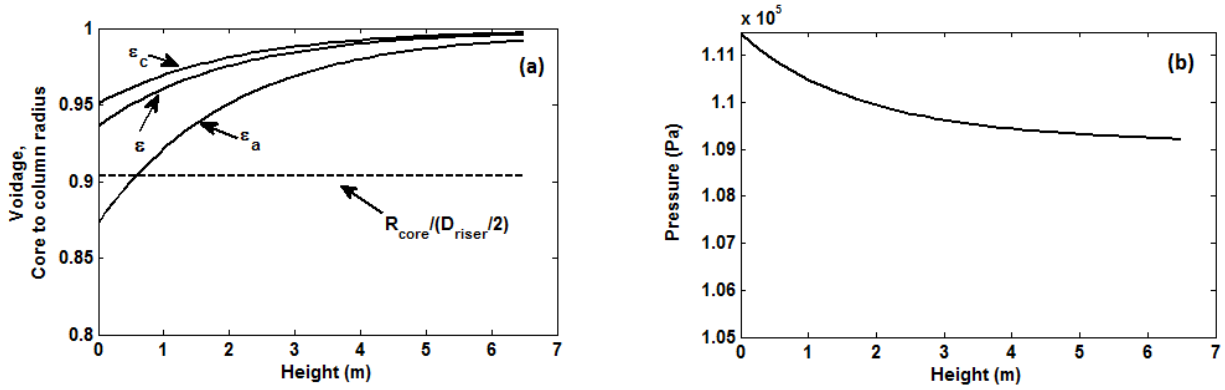

Figure 5.9. Variation of CFB parameters versus height predicted by two-phase model. (a) core-to-column radius ratio ($R_{core}/(D_{riser}/2)$), core and annulus voidages (ε_c, ε_a) and overall riser voidage (ε), (b) hydrostatic pressure as function of riser height. Riser temperature = 900°C, G_S = 12.55 kg/m^2.s, U = 5.55 m/s (at inlet).

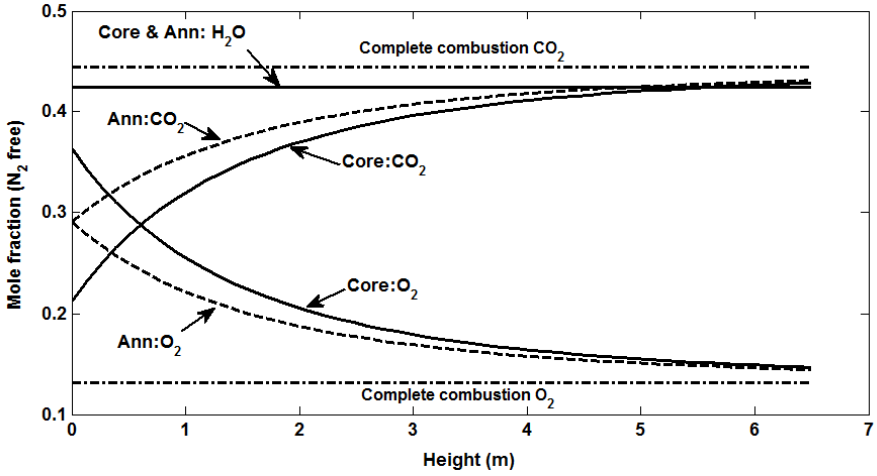

Figure 5.10. Variation of mole fractions of gas species with height. Riser temperature = 900°C, G_S = 12.55 kg/m^2.s, U = 5.55 m/s (at riser inlet).

The predicted dry product gas composition as a function of gasifier temperature is illustrated in Figure 5.11, where unbroken curves are for dry product composition exiting the reactor and dashed curves are for the gas composition just above the dense bubbling bed, respectively. Since the WGS reaction is exothermic, elevating the temperature reverses the reaction towards more CO production and CO_2 consumption. Furthermore, CO and H_2 production are promoted by the endothermic SMR reaction. These trends are consistent with modeling and experimental data from the literature e.g. [61], [155]. The freeboard allows for the homogeneous reactions which enhance the consumption of CH_4 and CO and the production of H_2.

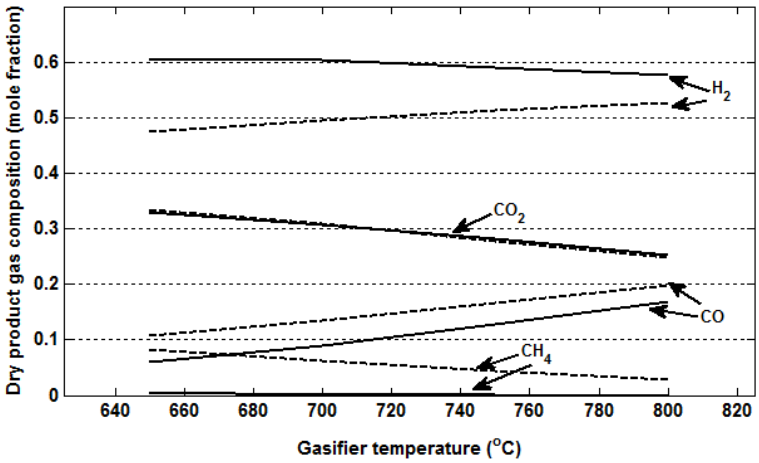

Figure 5.11. Predicted dry product gas composition as a function of dense bed temperature. Unbroken and dashed curves are with and without freeboard. Steam/biomass ratio=1.22. For other operating conditions, see Tables 5.2 and 5.3.

The predicted variations of different performance variables with gasifier temperature are illustrated in Figure 5.12. As gasification is primarily an endothermic process, increasing temperature increases product gas volumetric flow rate (Q_{PG}) at the cost of decreasing the lower heating value (LHV_{PG}). Increasing gasifier temperature at a fixed combustor temperature decreases the temperature difference between the two fluidized beds. In order to provide greater sensible heat transfer, required to maintain the gasifier at higher temperature, the sand circulation rate must increase. Therefore, increasing gasifier temperature increases the solid circulation flux (G_s) and decreases the solids mean residence time (τ_s) in the gasifier. By increasing the gasifier

temperature, the mass flow rate of char transferred to the combustor ($\dot{m}_{char}$) decreases, at the cost of a slight increase in the required natural gas volumetric flow rate (Q_{NG}) input to the combustor.

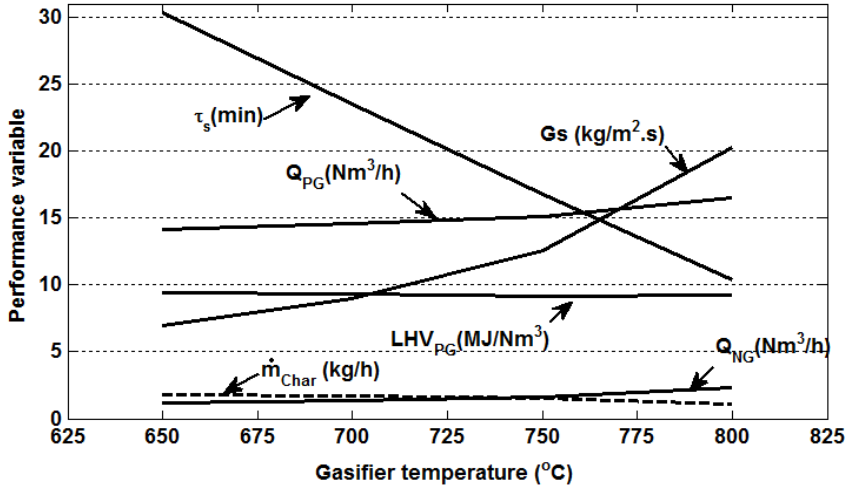

Figure 5.12. Variation of performance variables as a function of gasifier temperature. Steam/biomass ratio =1.22, combustor temperature=900°C.

We define the chemical efficiency of the process as

$$\eta_{chem} = \frac{Q_{PG}.LHV_{PG}}{\dot{m}_{fuel}.LHV_{fuel}} \tag{5.91}$$

Figure 5.13 shows that both the carbon conversion and the chemical efficiency increase noticeably with increasing gasifier temperature, resulting from enhanced gasification reactions which are highly endothermic.

Figure 5.14 shows the predicted dry product gas composition as a function of the S/B ratio, where the unbroken and dashed curves are for the product composition with and without freeboard, respectively. With increased steam, more H_2 and CO_2 are produced at the cost of increased consumption of CO and CH_4 by means of the WGS and SMR reactions. Furthermore, because of the reactions occurring in the freeboard, the consumptions of CH_4 and CO are enhanced and the production of H_2 is increased.

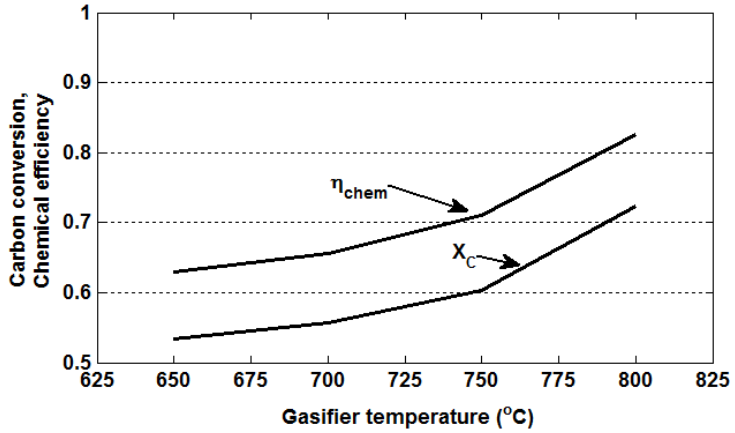

Figure 5.13. Predicted chemical efficiency and carbon conversion as functions of gasifier temperature. Steam/biomass ratio =1.22.

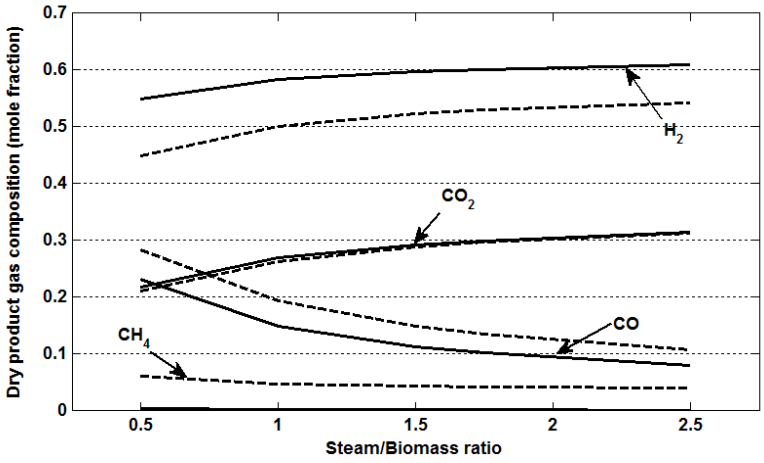

Figure 5.14. Predicted dry product gas composition as a function of S/B ratio. Unbroken and dashed curves are for the composition with and without freeboard. Gasifier temperature=750°C. For other operating conditions, see Tables 5.2 and 5.3.

The variations of different performance variables with steam/biomass ratio are illustrated in Figure 5.15. Increasing the steam/biomass ratio promotes gasification reactions towards increased product gas volumetric flow rate (Q_{PG}). Increasing the steam/biomass ratio decreases the product gas lower heating value (LHV_{PG}), mainly due to increased CO_2 content of the product gas.

As shown in Figure 5.16, the chemical efficiency does not change appreciably with variation of the steam/biomass ratio, whereas the carbon conversion increases slightly with increasing steam/biomass ratio. From Figure 5.16, it seems that there is no justification for S/B ratios higher than 1.5. According to Fig. 5.14, for S/B>1.5, the gas composition does not change much. This is because while increasing S/B ratio initially promotes tar and methane conversion, very high S/B ratio decreases the gas residence time, therefore decreasing tar and methane conversion.

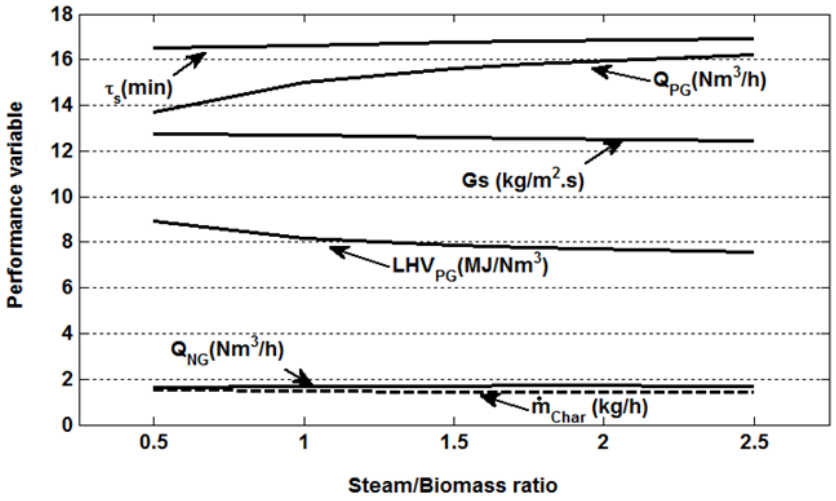

Figure 5.15. Variation of performance variables as a function of S/B ratio. Gasifier temperature=750°C, combustor temperature=900°C. For other operating conditions, see Tables 5.2 and 5.3.

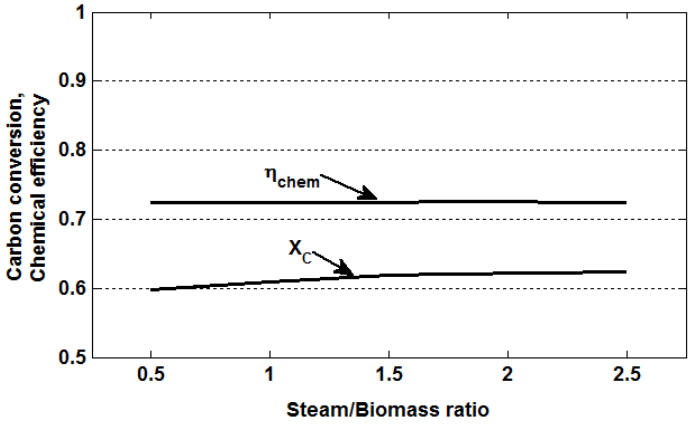

Figure 5.16. Predicted chemical efficiency and carbon conversion as functions of S/B ratio. Gasifier temperature=750°C.

Unlike large plants where process heat integration and comparatively low heat losses lead to higher process efficiencies, for smaller reactors with higher ratio of heat transfer surface area to reactor volumes, heat loss plays an important role in energy balance calculations. Note that the above definition of chemical efficiency does not truly represent the overall process efficiency because it does not take into account the external heating requirements of the process. According to the literature [14, 156], the overall process efficiency can be defined in two ways:

$$\eta_{Overall,I} = \frac{Q_{PG}.LHV_{PG}}{\dot{m}_{fuel}.LHV_{fuel} + Q_{CH_4}.LHV_{CH_4}} \tag{5.92}$$

$$\eta_{Overall,II} = \frac{Q_{PG}.LHV_{PG} - Q_{CH_4}.LHV_{CH_4}}{\dot{m}_{fuel}.LHV_{fuel}} \tag{5.93}$$

The first definition gives the energy obtained in the product gas divided by the total energy input to the system, where the input includes the biomass and any additional fuel such as CH_4. This definition can be generalized by including other energy inputs such as the heat of electric heaters used to preheat the air and to heat the superheated steam to the desired gasifier temperature. The second definition, which gives lower values of process efficiency, is particularly meaningful when one considers the special case of recycling a fraction of product gas to be combusted in the riser.

Figure 5.17 illustrates the effect of heat loss on the mass flow rate of char and volumetric flow rate of natural gas that must be fed to the combustor under stable operating conditions.

Figure 5.18 demonstrates the effect of heat loss on the chemical and overall process efficiencies. The heat loss is taken into account as the fraction of biomass energy input ($\dot{m}_{fuel}.LHV_{fuel}$) to the gasifier. As shown in Figure 5.18, if we assume that the entire heat loss of the dual fluidized bed system occurs from the gasifier, a lower limit for chemical efficiency is obtained. On the other hand, if the entire heat loss is from the combustor, one obtains an upper limit for chemical efficiency which does not change with variation of the heat loss from the combustor. When it comes to overall process efficiency, the distribution of heat losses in the system does not matter, and the overall process efficiency decreases sharply with increasing total heat loss.

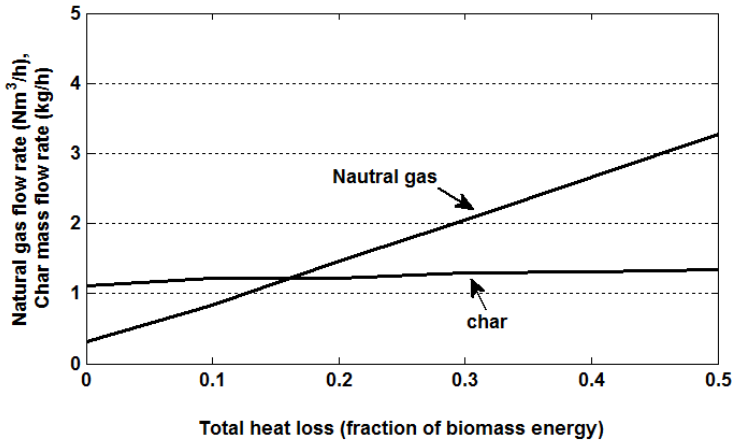

Figure 5.17. Effect of heat loss on char and natural gas flow rates. Gasifier temperature=800°C, Combustor temperature=900°C, steam/biomass ratio=1.22, excess air=20%, solid circulation flux=20 kg.m^{2}s (Fig. 5.12.)

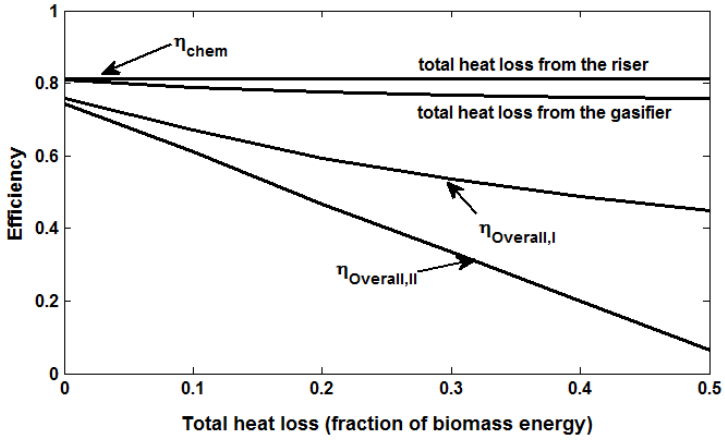

Figure 5.18. Chemical and overall process efficiencies as a function of overall heat loss. Gasifier temperature=800°C, Combustor temperature=900°C, steam/biomass ratio=1.22, excess air=20%.

Figure 5.19 shows a flow regime map for the CFB riser in which a sensitivity analysis has been performed on heat loss from the combustor and/or gasifier of the dual fluidized bed reactor configuration. At one extreme, the total heat loss of the system is considered to occur from the combustor. For a given combustor temperature, the solids circulation rate is not a function of the heat loss from the combustor, and is obtained from the energy balance over the gasifier. From the energy balance over the riser, on the other hand, higher CH_4 flow rates are obtained for higher heat loss. Hence, at higher heat losses from the combustor, greater air flow rates are required in

the riser to provide complete combustion of methane. At the other extreme, if all of the heat losses occurred from the gasifier, G_S would increase and char conversion would decrease. This would lead to introduction of more char to the riser and higher air requirements for complete combustion. As seen from Figure 5.19, greater heat loss from the combustor only increases the superficial gas velocity (U), whereas heat loss from the gasifier increases both U and G_S. In practice, heat losses must be distributed between the gasifier and combustor, with the gasifier having lower operating temperature, and hence a lower driving force, but higher surface area.

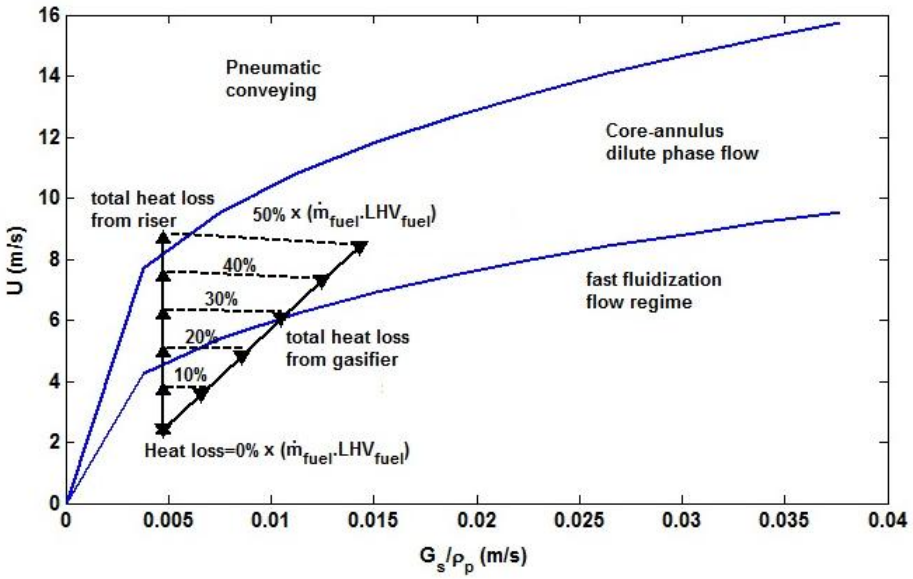

Figure 5.19. Flow regime map for CFB riser including sensitivity analysis on heat loss expressed as percentage of (m_{fuel} . LHV_{fuel}). Gasifier temperature=800°C, Combustor temperature=900°C, steam/biomass ratio=1.22, excess air=20%.

5.7 Summary

The performance of the UBC dual fluidized bed gasifier was simulated with a steady-state predictive kinetic model that uses a generic version of the two-phase fluidized bed reactor model. This model is capable of predicting species concentrations, temperature, pressure, superficial gas velocity and other hydrodynamic parameters such as voidage profiles along each reactor. By integrating the kinetic models of BFB gasifier and CFB riser through mass and energy balances, key operating parameters such as solids circulation rate and natural gas flow rate required for stable operation of the process are predicted. The required solids circulation rate strongly depends on the temperature difference between the two fluidized beds. In order to provide larger

sensible heat transfer required to maintain the gasifier at high temperatures, the circulation rate of sand (inerts) must increase at the cost of decreased mean solids residence time in the gasifier.

Sensitivity analyses over S/B ratio, gasifier temperature and system heat loss are preformed. Since the WGS reaction is exothermic, elevating the temperature reverses the reaction towards more CO production and CO_2 consumption. Furthermore, CO and H_2 production are promoted by the endothermic SMR reaction. The freeboard allows for homogeneous reactions which enhance the consumption of CH_4 and CO and the production of H_2. As gasification is primarily an endothermic process, increasing temperature increases product gas volumetric flow rate at the cost of decreasing the lower heating value of the product gas. By increasing the gasifier temperature, the mass flow rate of char transferred to the combustor decreases, at the cost of a slight increase in the required natural gas volumetric flow rate input to the combustor. With increased steam-to-biomass ratio, more H_2 and CO_2 are produced, at the cost of increased consumption of CO and CH_4 by means of the WGS and SMR reactions. Furthermore, because of the reactions occurring in the freeboard, the consumptions of CH_4 and CO are enhanced and the production of H_2 is increased. Increasing the S/B ratio promotes gasification reactions towards increased product gas volumetric flow rate and decreased product gas lower heating value, mainly due to increased CO_2 content of the product gas.

Studying the distribution of heat losses based on the UBC DFB gasifier shows that the solids circulation rate is strongly affected by the heat loss from the gasifier, whereas additional fuel (natural gas in this study) is required to make up for additional heat loss from the combustor. Selecting operating conditions to minimize heat loss is important, especially for smaller reactors.

Chapter 6: Equilibrium Modeling of Lime-Enhanced Biomass Steam Gasification in a Dual Fluidized Bed Reactor

Among the options for reducing greenhouse gas emissions is gasification of biomass. Steam gasification of biomass coupled with CO_2 capture, is particularly appealing to produce H_2-rich product gas, with a sorbent to capture CO_2 *in situ* [5]. Enhanced hydrogen production from renewable resources (e.g. biomass) with simultaneous CO_2 capture, when integrated with CO_2 sequestration, could result in "negative emissions", i.e. net removal of CO_2 from the atmosphere [10]. Lime (CaO) is able to selectively absorb CO_2 through exothermic gas-solid carbonation and reversibly release the captured CO_2 by endothermic calcination:

$$CaO_{(S)} + CO_2 \leftrightarrow CaCO_{3\,(S)} \qquad \Delta H^{o}_{298} = -178.2\ kJ\ /\ mol \tag{6.1}$$

The importance of this reaction lies in its reversibility, facilitating cyclic calcination/carbonation.

Biomass gasification in the presence of limestone does not date back very far [10, 39, 157]. Integrated biomass steam gasification enhanced by lime-based CO_2 capture has attracted limited attention, particularly with respect to cyclic operation in a dual fluidized bed reactor configuration [36, 41, 158]. Different gasifying agents produce syngas with different calorific values. Steam gasification of biomass produces a medium heating value gas, i.e. 10–18 MJ/Nm^3, attractive compared to N_2-diluted syngas generated from air gasification (4–7 MJ/Nm^3) or the significant power consumption costs and efficiency penalty of an Air Separation Unit required for gasification by O_2-enriched air [8]. Although steam gasification of biofuels has been reported to generate more tar in the product gas than air gasification, the higher H_2-content (30-60% vol. dry), originating from partial conversion of H_2O, is attractive [28].

Steam gasification of biomass is an endothermic process which takes place at high temperatures (typically > 750^{o}C). Due to the reversible nature of key gas phase reactions of biomass gasification, the rate of H_2 production is significantly limited by thermodynamic equilibria. Adding a sorbent capable of *in situ* CO_2 capture can shift the equilibrium reactions of biomass gasification (such as reforming and water-gas shift) towards more H_2 formation, while largely satisfying the heat requirements of the endothermic gasification process. In addition, sorbents

and other particulate materials such as limestone, dolomite, olivine and high-iron solids exhibit some catalytic tar-elimination activity [31].

Despite considerable advancement in both biomass gasification and cyclic lime-based CO_2 capture, these processes have almost always been studied separately. The aim of this chapter is to provide a simple, yet useful, model to assist in integrating these two processes. This model allows identification of the most important operational parameters influencing the performance of biomass steam gasification coupled with cyclic CO_2 capture in a dual fluidized bed reactor. It also helps identify some aspects of the process that require further scrutiny. Unlike the other chapters of this thesis, this chapter utilizes an equilibrium modeling approach for biomass gasification.

6.1 Process description

Figure 6.1 shows a schematic of steam gasification of biomass, coupled with *in situ* CO_2 capture. Calcined lime (CaO) captures CO_2 under desirable operating conditions of the gasifier/carbonator, producing a H_2-rich product gas aided by equilibrium shift, while transporting captured CO_2 in the form of $CaCO_3$ to the regenerator/calciner. A pure $CaCO_3$ sorbent make-up stream is also added to the regenerator where the calcium carbonate particles, accompanied by un-gasified char, contact oxygen. Burning the char particles and additional fuel within the regenerator provides the heat required for sorbent calcination, and thus regenerates lime (CaO) for return to the gasifier. Therefore, the limestone particles have a dual role: heat carrier and selective transporter of CO_2.

Due to the endothermic nature of biomass steam gasification and the heat required for sorbent regeneration in the calciner, direct combustion of unreacted char from the gasifier is usually unable to provide sufficient heat for the process. Indirect heating of the calciner by external heaters or direct burning of char and additional fuel, with an oxygen-enriched air stream could provide a high-purity CO_2 stream from the calciner that contains a high concentration of CO_2 to be sent for sequestration [17]. However, these measures would also increase the concentration of CO_2 within the calciner, thereby promoting sorbent sintering [48, 159]. While oxygen-enriched air would reduce the loss of energy by reducing the amount of hot nitrogen leaving the system,

the energy required to enrich the air would be much higher than the sensible heat loss with nitrogen. Air combustion of unreacted char and/or additional fuel would lower the calcination temperature at the cost of dilution by nitrogen, unsuitable for sequestration. Lowering the CO_2 partial pressure in the calciner by introducing superheated steam could also lower the calcination temperatures, and satisfy the heat requirement of sorbent regeneration [160]. While steam is a desirable diluent because of its easy subsequent removal from the product CO_2 by condensation, its generation would require extra energy, and it could also affect the sorbent structure and integrity [161].

Note that in this chapter, superheated steam is only introduced to the carbonator/gasifier. However, if one introduces steam to the calciner as well, additional heating would be required to increase the steam temperature to the corresponding regeneration temperature (>900^{o}C). In our model, we assume a gasifier whose heat demands are mostly met from the sensible heat of bed materials (sand and/or CaO particles) from the regenerator, where char and natural gas are combusted with air. As before, all the air requirements of the system are considered to be provided by a single stream introduced to a NG burner (air pre-heater) upstream of the combustor (Figure 6.1). To develop the model, mass and energy balances are expanded from previous chapters to include limestone, as well as inert silica sand, as bed materials.

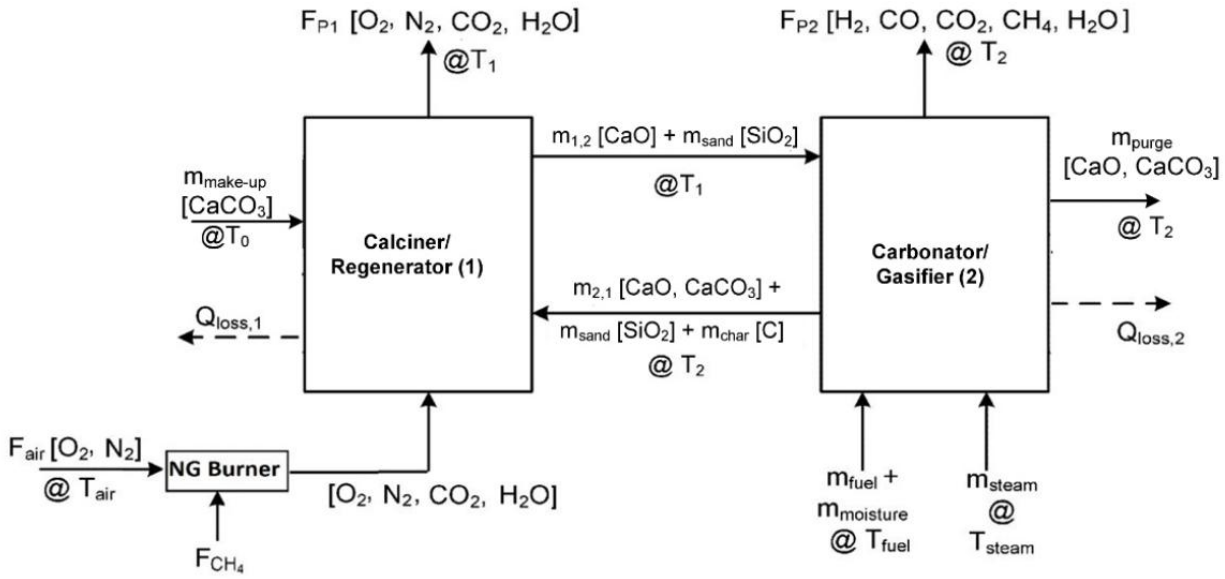

Figure 6.1. Schematic of dual vessel system for lime-enhanced biomass steam gasification. Dashed and solid arrows denote energy and mass flows, respectively.

6.2 Equilibrium model development

6.2.1 Underlying assumptions and methodology

In the present model, complete combustion of unreacted char (modeled as pure carbon) with excess air ($C + O_2 \rightarrow CO_2$) is assumed for the calciner/sorbent regenerator. The assumed complete calcination of sorbent particles leads to a stream of pure CaO (together with accompanying sand) circulating from the calciner to the carbonator. Since perfect mixing of particles is assumed and the volumetric heat capacity of the solids is much higher than that of the gas, the outlet temperature and composition of the solid and gaseous products are the same as within the respective reactors. Although thermodynamic equilibrium may not be fully achieved, models based on thermodynamic equilibrium are used widely, with reasonable success [61, 162, 163]. The equilibrium modeling approach predicts the highest gasification or thermal efficiency that could be attained within the gasifier for a given feedstock, independent of the design of the gasifier [62, 163]. Given the catalytic effects of ash and limestone on biomass gasification reactions, we also assume thermodynamic equilibrium to be achieved for the biomass gasification. We take into account CH_4, CO, CO_2, H_2, and H_2O as the main components coming to thermodynamic equilibrium in the presence of solid carbon. As a simplifying assumption and due to their low contents, nitrogen and sulfur compounds and tars formed during biomass gasification are neglected.

The gasifier product gas composition is predicted by a stoichiometric equilibrium approach where elemental (C, H, O) balances are coupled with stoichiometric equations of three independent reversible chemical reactions). Note that these three heterogeneous reactions are reduced to two when no solid carbon remains at equilibrium. Therefore, the following equilibrium relations describe the biomass gasification [61]:

i. With solid carbon:

$$C_{(S)} + CO_2 \leftrightarrow 2CO \qquad \Delta H^{o}_{298} = 172.5\, kJ / mol \tag{6.2.a}$$

$$C_{(S)} + 2H_2 \leftrightarrow CH_4 \qquad \Delta H^{o}_{298} = -73\, kJ / mol \tag{6.2.b}$$

$$C_{(S)} + H_2O \leftrightarrow CO + H_2 \qquad \Delta H^o_{298} = 131.3\, kJ / mol \tag{6.2.c}$$

ii. Without solid carbon:

$$CO + H_2O \leftrightarrow CO_2 + H_2 \qquad \Delta H^o_{298} = -41.2\, kJ / mol \tag{6.3.a}$$

$$CH_4 + H_2O \leftrightarrow CO + 3H_2 \qquad \Delta H^o_{298} = 206\, kJ / mol \tag{6.3.b}$$

For a dual fluidized bed with high solids circulation rates, it is assumed that the char generated by biomass pyrolysis does not remain in the gasifier long enough to reach complete equilibrium and thus leaves the gasifier almost un-reacted. This is a fair assumption, particularly when we are operating far from the coke formation conditions that are predictable by a non-stoichiometric equilibrium model [62].

Assuming perfect mixing of solids in the bubbling bed gasifier, the rate of char leaving the gasifier is the same as the rate of char generated within the gasifier. The residual char leaving the gasifier is approximated from the two-step pyrolysis kinetic mechanism (see Figure 4.1) :

$$\dot{m}_{char} = \left(k_3 / \left(k_1 + k_2 + k_3\right)\right).\dot{m}_{fuel} \tag{6.4}$$

Starting with elemental mass balances over the complete system, constrained by the above equilibrium gas-phase reactions, we must also account for the enhancement effect of lime. This is achieved by extending the elemental mass balances to account for Ca-containing compounds (i.e. CaO, $CaCO_3$) and performing Ca balances over both reactors. To specify the CO_2 capture efficiency of the gasifier, we need to find the degree of carbonation of CaO particles within the gasifier/carbonator as discussed in the next section.

Corresponding to the streams in Figure 6.1, the system of non-linear algebraic equations consisting of six elemental balances (C and Ca for the calciner and C, H, O and Ca for the carbonator) coupled with two equilibrium equations (6.3.a and 6.3.b) representing biomass gasification, are solved using MATLAB (see Appendix G for the MATLAB code).

We have:

Carbonator / Gasifier :

$$C: \frac{\dot{m}_{fuel} w_C}{MW_C} - \frac{\left(\dot{m}_{purge} + \dot{m}_{2,1}\right) w_{CaCO_3}}{MW_{CaCO_3}} - \frac{\dot{m}_{char}}{MW_C} - F_{P2}\left(y_{CO_2} + y_{CO} + y_{CH_4}\right) = 0 \tag{6.5}$$

$$H: \frac{\dot{m}_{fuel} w_H}{MW_H} + \frac{2 \times \left(\dot{m}_{moisture} + \dot{m}_{steam}\right)}{MW_{H_2O}} - F_{P2}\left(2 \times y_{H_2} + 4 \times y_{CH_4} + 2 \times y_{H_2O}\right) = 0 \tag{6.6}$$

$$O: \left(\begin{array}{l} \dfrac{\dot{m}_{fuel} w_O}{MW_O} + \dfrac{\left(\dot{m}_{moisture} + \dot{m}_{steam}\right)}{MW_{H_2O}} + \dfrac{\dot{m}_{1,2}}{MW_{CaO}} - \left(\dot{m}_{purge} + \dot{m}_{2,1}\right)\left(\dfrac{3 \times w_{CaCO_3}}{MW_{CaCO_3}} + \dfrac{1 - w_{CaCO_3}}{MW_{CaO}} \right) \\ -F_{P2}\left(y_{CO} + 2 \times y_{CO_2} + y_{H_2O}\right) = 0 \end{array} \right) \tag{6.7}$$

$$Ca: \frac{\dot{m}_{1,2}}{MW_{CaO}} - \left(\dot{m}_{purge} + \dot{m}_{2,1}\right)\left(\frac{w_{CaCO_3}}{MW_{CaCO_3}} + \frac{1 - w_{CaCO_3}}{MW_{CaO}} \right) = 0 \tag{6.8}$$

$$y_{H_2O} = 1 - \left(y_{H_2} + y_{CH_4} + y_{CO} + y_{CO_2}\right) \tag{6.9}$$

Equilibrium equations (gasifier) :

$$K_{\mathrm{WGS}} = \frac{y_{CO_2} \times y_{H_2}}{y_{CO} \times y_{H_2O}} = \exp\left(4400/T - 4.036\right) \tag{6.10}$$

$$K_{SMR} = \frac{y_{CO} \times y_{H_2}^3}{y_{CH_4} \times y_{H_2O}} \times \left(P/P_0\right)^2 = \exp\left(-26830/T + 30.114\right) \tag{6.11}$$

Calciner / Regenerator :

$$C: \frac{\dot{m}_{makeup}}{MW_{CaCO_3}} + \frac{\dot{m}_{2,1}.w_{CaCO_3}}{MW_{CaCO_3}} + \frac{\dot{m}_{char}}{MW_C} - F_{P1}.y_{CO_2,P1} = 0 \tag{6.12}$$

$$Ca: \frac{\dot{m}_{makeup}}{MW_{CaCO_3}} + \dot{m}_{2,1}\left(\frac{w_{CaCO_3}}{MW_{CaCO_3}} + \frac{1 - w_{CaCO_3}}{MW_{CaO}} \right) - \frac{\dot{m}_{1,2}}{MW_{CaO}} = 0 \tag{6.13}$$

The energy balance calculations use the general methodology described in Chapter 5 (equation 5.87). Given the limestone fraction of the carbonator bed, the energy balance over the carbonator/gasifier gives the solids circulation rate between the two reactors:

$$\dot{m}_{fuel}.H^*_{fuel}(T_{fuel}) + \dot{m}_{moisture}.H^*_{H_2O}(T_{fuel}, P_{fuel}) + \dot{m}_{steam}.H^*_{steam}(T_{steam}, P_{steam}) + \dot{m}_{1,2}.H^*_{CaO}(T_1) + \dot{m}_{sand}.H^*_{SiO_2}(T_1)$$
$$-\dot{m}_{sand}.H^*_{SiO_2}(T_2) - \dot{m}_{char}.H^*_{char}(T_2) - \left(\dot{m}_{purge} + \dot{m}_{2,1}\right).\left(w_{CaCO_3}.H^*_{CaCO_3}(T_2) + \left(1 - w_{CaCO_3}\right).H^*_{CaO}(T_2)\right) - Q_{loss,gasifier}$$
$$-\left(\sum_{i=1}^{Nc} \dot{m}_{i,gasifier}.H^*_i(T_2)\right) = 0 \tag{6.14}$$

From energy balance over the calciner/combustor, the required additional fuel (i.e. natural gas, assumed to be pure CH_4) is calculated:

$$\dot{m}_{CH_4}.H^*_{CH_4}(T_{air}) + \dot{m}_{air}.H^*_{air}(T_{air}) + \dot{m}_{makeup}.H^*_{CaCO_3}(T_0) + \dot{m}_{Char}.H^*_{Char}(T_2) + \dot{m}_{sand}.H^*_{SiO_2}(T_2) - \dot{m}_{sand}.H^*_{SiO_2}(T_1)$$
$$-Q_{loss,riser} - \dot{m}_{1,2}.H^*_{CaO}(T_1) + \dot{m}_{2,1}.\left(w_{CaCO_3}.H^*_{CaCO_3}(T_2) + \left(1 - w_{CaCO_3}\right).H^*_{CaO}(T_2)\right) - \left(\sum_{i=1}^{Nc} \dot{m}_{i,riser}.H^*_i(T_1)\right) = 0 \tag{6.15}$$

To describe the thermodynamic states of the streams, substances are divided into four classes, i.e. ideal gases, inorganic solids, organic substances and pure water/steam [164]. NASA-polynomials are used to calculate isobaric heat capacities of ideal gases and inorganic solid species [165]. The empirical correlations of Boie [164] and Merrick [166] are applied to calculate the lower heating value of dry and ash-free biomass (LHV_{fuel}) and the enthalpy and heat capacity of char as a function of temperature, respectively. IAPWS-IF97 [167, 168] is used to estimate the enthalpy of sub-cooled liquid water (i.e. biomass moisture content) and superheated steam.

6.2.2 Finding the average carbonation conversion

For the current model, the effects of attrition, entrainment, coke formation and pore blockage by $CaSO_4$ are neglected, but loss of reactivity due to sintering is taken into account. Sintering, the main contributor to the decrease in CO_2 carrying capacity of the sorbent, occurs mostly during calcination [169]. SEM images demonstrate sorbent particles going through multiple capture and release cycles, decreasing in micro-porosity and increasing in meso-porosity, leading to loss of surface area available for CO_2 capture [170]. In addition, previous research [46, 47, 171]

shows that a fast, chemically controlled, initial carbonation stage is followed by a second slower reaction stage controlled by diffusion through the $CaCO_3$ layer. Transition between the fast and slow stages takes place quite abruptly. The maximum achievable degree of carbonation of sorbent particles at the end of the fast carbonation period decreases with each cycle; eventually a decay asymptote is reached. This limiting conversion determines the overall reactor performance, with gas-solid contact sufficient to ensure that most sorbent particles complete the fast reaction stage [171]. To maintain steady-state operation of the system and keep the average carbonation conversion constant, it is essential to compensate for the reactivity loss of the sorbent by replacing some "old" particles with fresh sorbent particles. As discussed by Rodriguez *et al.* [172] and Grasa *et al.* [53], the fraction of particles which have experienced a number of complete carbonation–calcination cycles can be expressed as a function of the actual carbonation and calcination levels in each reactor. By averaging over the reactivity of different groups of particles entering the carbonator from N=1 (freshly added) to $N=\infty$ (aged to their residual reactivity), we account for the loss of sorbent reactivity during cyclic operation due to sintering. To find the maximum achievable average carbonation conversion of a CaO population over N carbonation-calcination cycles, we write:

$$X_{ave} = \sum_{N=1}^{\infty} \alpha_N . X_N \tag{6.16}$$

where X_N is the maximum utilization efficiency of CaO particles at the end of the fast carbonation period after the N^{th} cycle and α_N is the fraction of sorbent particles that have experienced N sorption–desorption cycles. X_N is often expressed as a function of the cycle number [47, 171]. Grasa *et al.* [171] fitted experimental results up to 500 cycles and a wide range of operating conditions by

$$X_N = \frac{1}{1/(1-X_r) + k_d . N} + X_r \tag{6.17}$$

where k_d and X_r are a fitted deactivation constant and the residual conversion, respectively, both depending on the sorbent characteristics. These constants would be modified if the negative effect of sulfation is taken into account [173]. Note that equation (6.17) only considers the fast

(kinetically-controlled) stage of carbonation where solid conversion under the diffusion-controlled regime is not yet important. This approach is limited to carbonation times less than about 5 min, carbonation temperature of about 650^{o}C and average CO_2 partial pressures less than 0.1 bar [174].

During steady-state operation, particles of different ages are continuously fed to the carbonator. The proportion of these particles ranges from α_1 (for particles freshly introduced to the system from the make-up stream) to α_∞ (for particles not yet purged which have remained in the system for many cycles). To determine the population distribution of these particles, the fraction of particles entering the carbonator that have circulated N times, α_N, is calculated from a succession of mole balances over Ca [175]:

$$\alpha_1 \equiv \frac{\text{Ca introduced from make-up stream}}{\text{Total Ca in the stream entering the carbonator}} \tag{6.18}$$

$$\alpha_2 = \alpha_1\left(1-\alpha_1\right) \tag{6.19}$$

$$\alpha_N = \alpha_1\left(1-\alpha_1\right)^{N-1} \tag{6.20}$$

Substituting equations (6.17) and (6.20) into equation (6.16) gives

$$X_{ave} = \sum_{N=1}^{\infty}\alpha_1\left(1-\alpha_1\right)^{N-1}.\left(\frac{1}{1/\left(1-X_r\right)+k_d.N}+X_r\right) \tag{6.21}$$

While it is reasonable to assume that the calciner is sufficiently large, or the calcination rate fast enough, to allow all particles to convert fully from $CaCO_3$ to CaO within the calciner, several issues remain to be addressed for the carbonator. Owing to factors other than sintering, such as non-uniform residence time distribution and chemical kinetic limitations, sorbent particles do not carbonate completely within the reactor. In most fluidized bed reactors, the mean residence time of particles is much larger than their turnover time, and perfect mixing of solid particles is then a reasonable approximation. Because of the distribution of residence times for particles entering the carbonator, CaO particles have unequal chances of being carbonated. Previous studies [52,

53] demonstrate that during carbonation, a $CaCO_3$ product layer forms on the outer surface of particles, causing resistance to further CO_2 diffusion to the unreacted CaO core. To account for the mixing and the kinetic limitation of the carbonation reaction, we consider the Residence Time Distribution (RTD) of solid material in the carbonator, combined with a suitable model for the carbonation rate of CaO particles as a function of cycle number (N). With the assumptions of uniform CO_2 concentration and perfect mixing of sorbent particles, the conversion of CaO in individual particles depends on the duration of their stay within the reactor. Different particles, despite belonging to the same cycle number, experience different reaction times within the carbonator. Hence, in addition to our earlier classification of entering particles to the carbonator based on the number of cycles previously experienced (α_N), we also need to account for their distribution of residence times within the carbonator. For a mean residence time of τ_s, the perfect mixing RTD function is:

$$E(t) = \exp\left(-t/\tau_s\right)\Big/\tau_s \tag{6.22}$$

The representative average carbonation conversion of the N^{th} group of particles is estimated by:

$$\overline{X}_N = \int_0^\infty X_N(t).E(t)\,dt \tag{6.23}$$

Here $X_N(t)$ is the conversion of CaO to $CaCO_3$ both as a function of reaction time and number of cycles (N) experienced by CaO particles. To find the overall average carbonation conversion for all CaO particles, we need to replace X_N from equation (6.16) (in which only the effect of sorbent sintering is taken into account) by:

$$X_{ave} = \sum_{N=1}^{\infty} \alpha_N . \overline{X}_N \tag{6.24}$$

Substituting equation (6.23) into (6.24), the overall average carbonation conversion is then

$$X_{ave} = \sum_{N=1}^{\infty} \alpha_N . \left(\int_0^\infty X_N(t).E(t)\,dt \right) \tag{6.25}$$

Various approaches have been suggested to simulate the carbonation rate of limestone particles, ranging from simple Homogeneous Grain models to Shrinking Core and Pore models. However, most of these expressions require several fitted parameters that limit their applicability to a specific set of experimental conditions and/or a specific sorbent. Grasa *et al.* [176] suggested that a simple first order kinetic model is sufficient to describe the carbonation of highly cycled particles during the fast reaction phase usually encountered in industrial applications. Although they neglected the effects of intra-particle and transport resistances, the wide range of reaction conditions, particle sizes and sorbents used to find the curve-fitting parameters give credibility to this approach. The first-order carbonation rate expression is then:

$$dX_N(t)/dt = K_S S_N \left(1 - X_N(t)\right)^{2/3} \left(C_{CO2} - C_{CO2,eq}\right) \tag{6.26}$$

where K_S is an intrinsic kinetic constant, S_N the specific surface area available for reaction in a particle which has experienced N carbonation-calcination cycles, and C_{CO2} and $C_{CO2,eq}$ are the actual and equilibrium CO_2 concentrations. With the dependence of the equilibrium partial pressure of CO_2 on the decomposition temperature of $CaCO_3$ based on a semi-empirical correlation proposed by Baker [177] and ideal gas law behaviour, $C_{CO2,eq}$ is given as a function of carbonation temperature:

$$C_{CO2,eq}\left(mol/m^3\right) = 10^{\left(-8308/T\right)+9.079}\ (kPa)/RT \tag{6.27}$$

From equation (6.26), the dependence of the carbonation rate of particles on the cycle number is seen through particle available surface area, which in turn is proportional to the maximum carbonation degree at the end of the fast carbonation period (X_N):

$$S_N = \rho_{CaO}\left(VM_{CaCO_3}\, X_N / MW_{CaO}\, h\right) \tag{6.28}$$

Here VM_{CaCO3} is the molar volume of $CaCO_3$, MW_{CaO} and ρ_{CaO} are the molecular mass and density of CaO, respectively, and h is the thickness of the $CaCO_3$ product layer, found to be about 50 nm and almost constant during cycling [178]. Table 6.1 gives the parameters used in this study to calculate the sorbent conversion.

Table 6.1. Parameters used to calculate sorbent conversion [179].

K_S (m^4/mol/s)	VM_{CaCO3} (m^3/mol)	ρ_{CaO} (kg/m^3)	h (m)	k_d (-)	X_r (-)
6.05×10^{-10}	36.9×10^{-6}	3320	50×10^{-9}	0.52	0.075

Upon integration of equation (6.26), the carbonation degree of a CaO-based particle can be expressed explicitly by:

$$X_N(t) = 1 - \left(1 - \left(K_S S_N \left(C_{CO2} - C_{CO2,eq}\right) \Big/ 3\right) t\right)^3 \qquad for\ t \le \tau_N \tag{6.29}$$

where τ_N is the time required for a particle to reach a conversion of X_N:

$$\tau_N = 3\left(1 - \left(1 - X_N\right)^{1/3}\right) \Big/ K_S S_N \left(C_{CO2} - C_{CO2,eq}\right) \tag{6.30}$$

As noted above, sintering imposes an upper limit on the maximum achievable conversion of particles that have experienced N calcination-carbonation cycles at a given temperature and time of carbonation. Hence, for $t > \tau_N$, $X_N(t)$ remains constant. The conversion of sorbent particles is plotted versus time in Figure 6.2, for different cycle numbers and CO_2 concentrations, with the parameters reported in Table 6.1 [179].

Overall, equation (6.25) can be rewritten to find the overall average carbonation conversion:

$$X_{ave} = \sum_{N=1}^{\infty} \alpha_N \cdot \left(\int_0^{\tau_N} X_N(t).E(t)\,dt + X_N \int_{\tau_N}^{\infty} E(t)\,dt \right) \tag{6.31}$$

From equation (6.31), the average carbonation conversion of CaO particles within the carbonator is related not only to the carbonator operating conditions (e.g. temperature, CO_2 partial pressure and mean residence time of sorbent particles), but also restricted by the degree of sintering during cyclic operation.

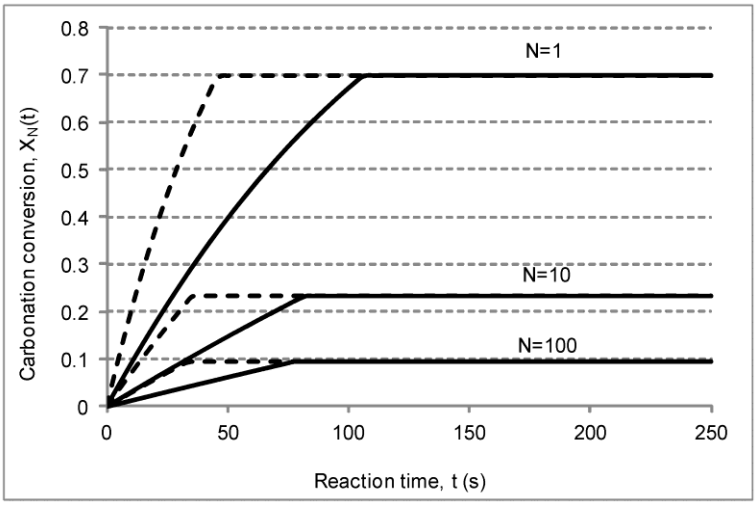

Figure 6.2. Sorbent conversion *vs* time for particles with different number of carbonation cycles, exposed to different CO_2 concentrations (Dashed lines: P_{CO2} = 10 kPa; solid lines: P_{CO2} = 5 kPa) at atmospheric pressure and carbonation temperature of 650°C (adapted from Romano [179]).

6.3 Results and discussion

The properties of biomass (pine sawdust), as well as process operating conditions used in the simulations, are summarized in Tables 6.2 and 6.3, respectively.

Table 6.2. Biomass properties.

LHV (MJ/kg)		*18.8*
Moisture content		*10*
Ash content (wt %)		*1.2*
Dry bulk density (kg/m^3)		*570*
Particle diameter (µm)		*500*
Ultimate analysis (wt%, dry and ash-free)	*C*	*42.5*
	H	*6.3*
	O	*51.0*
	N	*0.15*

Table 6.3. Constant process parameters for simulation.

Biomass flow rate	*10 kg/h (as received)*
Steam flow rate	*10 kg/h*
Gasifier Bed inventory	*100 kg*
T_{fuel} & P_{fuel} (at inlet)	*25°C & 1 atm*
Gasifier temperature	*650-700 °C*
Gasifier pressure	*1 atm*
Combustor temperature	*900 °C*
Combustor Excess air	*20%*
T_{air} & P_{air} (at inlet)	*400°C & 1 atm*
T_{steam} & P_{steam}	*Same as gasifier*
$Q_{loss,\ gasifier}$	*15 % (m_{fuel}* LHV_{fuel})*
$Q_{loss,\ combustor}$	*15 % (m_{fuel}* LHV_{fuel})*

The predicted dry product gas composition as a function of the weight fraction of limestone in the gasifier is depicted in Figure 6.3. As seen, by increasing the sorbent availability in the gasifier (i.e. increasing sorbent circulation rate), more CO_2 is captured from the product gas shifting the water-gas shift reaction towards more H_2 production and more CO consumption.

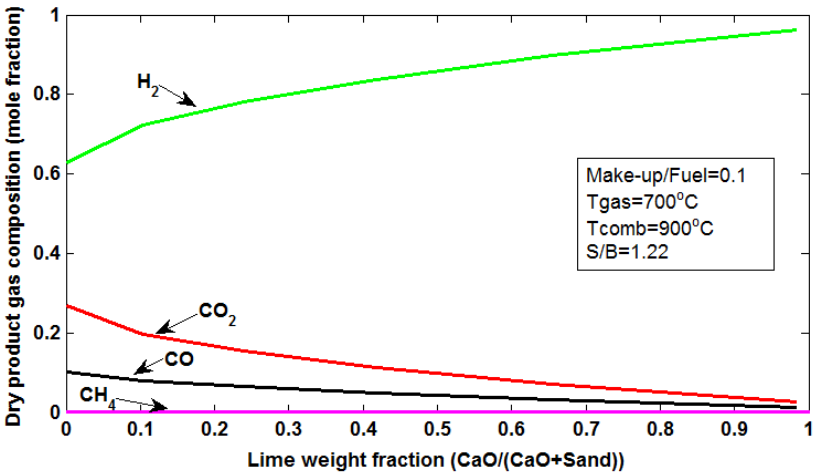

Figure 6.3. Predicted dry product gas composition versus weight fraction of limestone in the gasifier.

As observed in Figure 6.4, because of increased CO_2 capture, the produced product gas volumetric flow rate decreases, whereas its Lower Heating Value increases with increasing limestone weight fraction. Furthermore, the increase of limestone weight fraction of the bed does not impose significant energy penalty on the system, so that it could be operated with only a small increase in the natural gas input to the combustor.

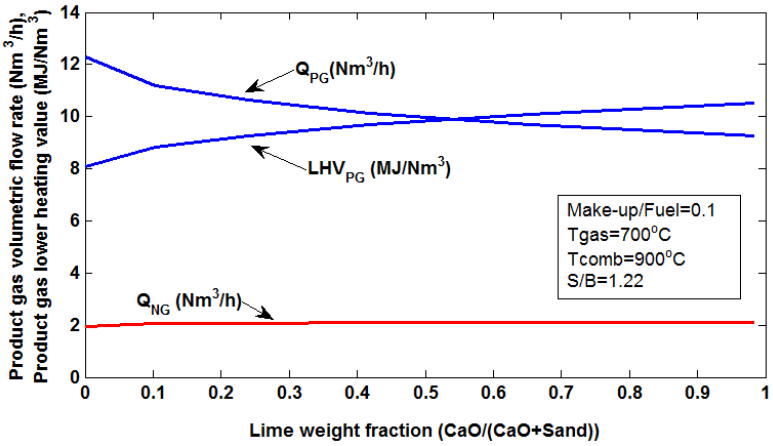

Figure 6.4. Predicted dry product gas volumetric flow rate, LHV and natural gas volumetric flow rate versus weight fraction of limestone in the gasifier.

Optimizing the solid circulation rate between the two reactors is of paramount importance for effective CO_2 capture and heat delivery. Figure 6.5 illustrates solids circulation mass flow rates as a function of the weight fraction of limestone in the gasifier. For lime-enhanced gasification, due to the *in situ* heat generated by the exothermic carbonation reaction within the gasifier, the dependence on the sensible heat transfer by solids circulation is reduced, and the total solids circulation rate is predicted to decrease considerably with increasing limestone weight fraction of bed (or sorbent circulation rate). Therefore, the mean solids residence time increases with increasing lime weight fraction (dashed curve).

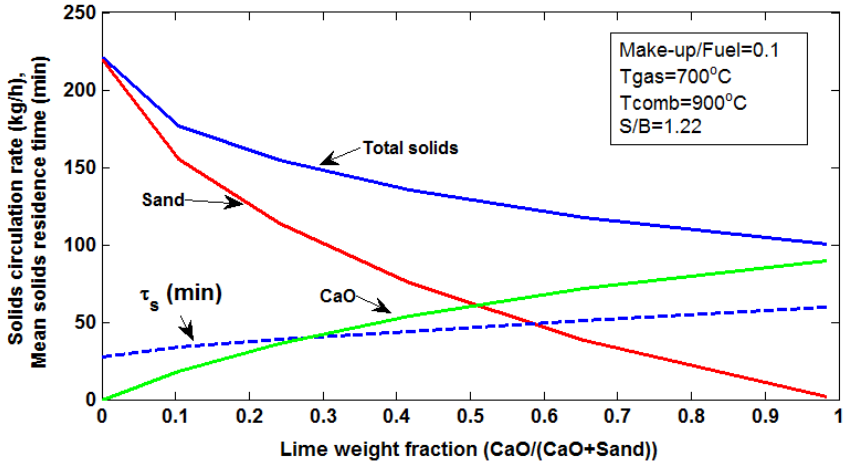

Figure 6.5. Predicted solids circulation rate and mean solids residence time versus weight fraction of limestone in the gasifier.

For lime-enhanced steam biomass gasification, it is of interest to see how the CO_2 capture ratio, η_{CO2}, defined as the ratio of the CO_2 captured by the lime to all carbon converted to CO_2 within the gasifier, is affected by the operating conditions. Furthermore, a useful criterion to evaluate the gasification performance is the "cold gas efficiency", which indicates the proportion of the fuel heating value retained by the product gas [162]. Consistent with [61], we define the cold gas efficiency as

$$\eta_{Overall} = \frac{F_{PG}.LHV_{PG} - F_{CH_4}.LHV_{CH_4}}{\dot{m}_{fuel}.LHV_{fuel}} \tag{6.32}$$

As discussed in Chapter 5, another way to compare the results with and without lime is to define

the overall process efficiency as the ratio of the energy output from the H_2 produced, discounting the heat necessary to drive the reaction process, to the energy input from the biomass [10]:

$$\eta_{H2} = \frac{F_{H2}.LHV_{H2} - F_{CH_4}.LHV_{CH_4}}{\dot{m}_{fuel}.LHV_{fuel}} \tag{6.33}$$

Figure 6.6 shows the CO_2 capture ratio, cold gas efficiency, and H_2 production efficiency as functions of the weight fraction of limestone in the gasifier. Increasing the weight fraction of limestone in the gasifier increases the surface area available for CO_2 capture, and hence the CO_2 capture ratio, η_{CO2}. For similar operating conditions, the cold gas efficiency of lime-enhanced steam gasification is slightly less than for non-enhanced gasification because of the additional external heating requirements for sorbent calcination within the regenerator. Finally, lime-enhanced biomass gasification is predicted to have slightly better performance in terms of the H_2 production efficiency. Therefore, using limestone or other sorbents in fluidized bed gasifiers for high-temperature CO_2 capture is particularly advantageous if the production of H_2-rich product gas is a major objective. Note that the above definitions of cold gas efficiency and H_2 production efficiency (i.e. subtracting methane consumption from the numerator instead of adding it to the denominator) leads to low values. Another reason for the low process efficiencies is the 30% heat loss assumed for the relatively small UBC DFB gasifier, which needs to be compensated by methane combustion.

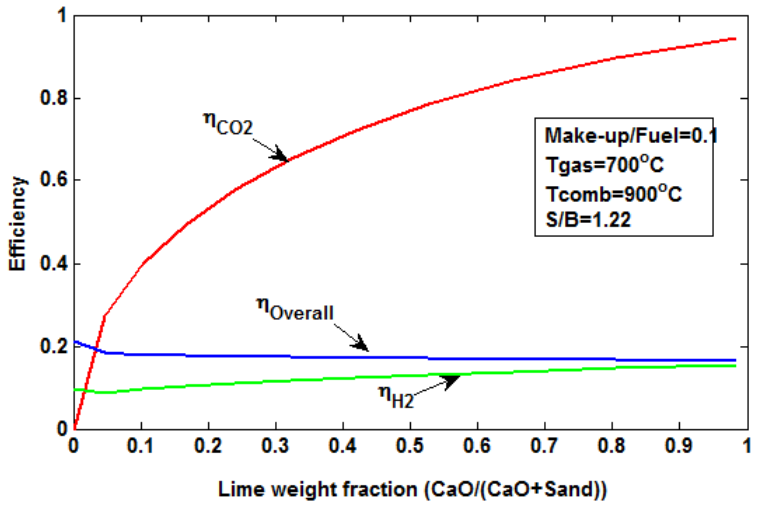

Figure 6.6. Predicted CO_2 capture ratio, cold gas efficiency, and H_2 production efficiency.

Figure 6.7 compares the dry product gas composition, volumetric flow rate and Lower Heating Value generated from non-enhanced (solid curves) and lime-enhanced (dashed curves) biomass gasification *vs* gasifier temperature at 50 wt% limestone in the gasifier. Hydrogen production is observed to be enhanced up to a gasifier temperature of 750^{o}C at atmospheric pressure. Beyond this temperature, the partial pressure of CO_2 in the gasifier falls below its equilibrium pressure and carbonation no longer occurs.

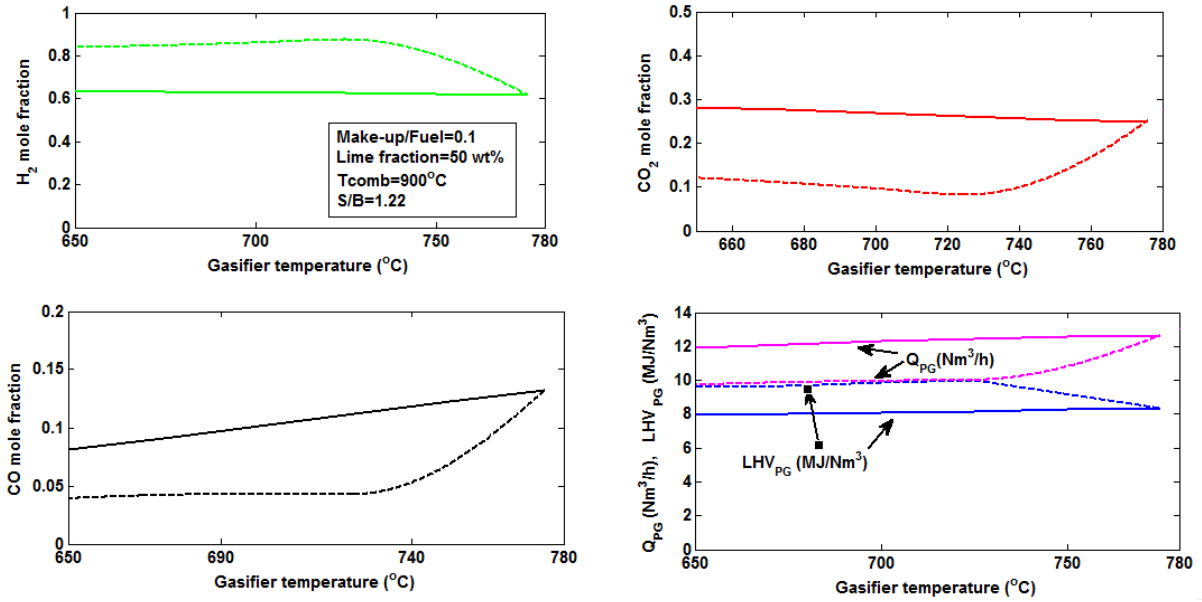

Figure 6.7. Predicted dry product gas composition, volumetric flow rate and LHV versus gasifier temperature. Solid and dashed curves are for non-enhanced and lime-enhanced biomass gasification, respectively.

6.4 Summary

A relatively simple model is developed to capture the essence of integrated biomass gasification with cyclic CO_2 capture in a dual fluidized bed reactor, with limestone particles constituting all, or a fraction of the bed material. Conversion of solid biomass particles to major gaseous products (H_2, CO, CH_4 and CO_2) is first modeled by a simple stoichiometric equilibrium model.

By adopting an empirical kinetic model for the carbonation rate of limestone particles from the literature, not only is the effect of sorbent reactivity loss due to sintering during cyclic operation taken into account, but the dependencies of the average carbonation conversion of CaO particles on operating parameters such as carbonation temperature, CO_2 partial pressure and mean

residence time of sorbent particles within the carbonator are also clarified. Although there is considerable scope for refining the model in the future work, the model provides a basic tool to describe the general trends of the process and to identify the effects of key operating variables. Although the developed model is not tested with experimental data, it offers a starting point for experimental design and for kinetic modeling as carried out in next chapter.

Chapter 7: Kinetic Modeling of Lime-Enhanced Biomass Steam Gasification in a Dual Fluidized Bed Reactor

In this chapter, we develop a steady-state kinetic model for lime-enhanced biomass steam gasification in the UBC dual fluidized bed reactor. This is achieved by extending the two-phase kinetic model of bubbling fluidized bed gasifier, developed in Chapter 5, to also account for *in situ* sorbent carbonation under steady-state Ca-looping operation. For simplification, we mainly focus on modelling the bubbling fluidized bed gasifier/carbonator, while assuming complete char combustion and complete sorbent calcination in the circulating fluidized bed riser.

7.1 Methodology

Based on our discussion in Chapter 6, we first approximate the average carbonation rate of perfectly-mixed limestone particles in the BFB gasifier of dual fluidized bed reactor operating under steady-state operation. We should modify the net reaction rate in CO_2 mole balance in the generic two-phase kinetic model developed in Chapter 5 to account for selective CO_2 capture during cyclic operation. Furthermore, the consumption rate of CaO is calculated by performing a Calcium balance over the BFB at steady-state.

Using equation (6.26), the first-order carbonation rate for the average sorbent particle is approximated as:

$$r_{Carb}\left(s^{-1}\right) = K_S S_{ave}\left(1 - X_{ave}\right)^{2/3}\left(C_{CO2} - C_{CO2,eq}\right) \tag{7.1}$$

where K_S is an intrinsic kinetic constant, S_{ave} is the average sorbent specific surface area available for reaction, X_{ave} is the average carbonation conversion of sorbent particles in the BFB reactor during cyclic operation, C_{CO2} is CO_2 concentration that changes with height in the BFB reactor, and $C_{CO2,eq}$ is the equilibrium CO_2 concentration at BFB temperature. The average sorbent particle available surface area is approximated from equation (6.28) [176]:

$$S_{ave} = \rho_{CaO}\left(VM_{CaCO_3}\, X_{ave} / MW_{CaO}\, h\right) \tag{7.2}$$

Here VM_{CaCO3} is the molar volume of $CaCO_3$, MW_{CaO} and ρ_{CaO} are the molecular mass and density of CaO, respectively, h is the thickness of the $CaCO_3$ product layer, and the average carbonation conversion over N carbonation-calcination cycles is estimated from equation (6.16):

$$X_{ave} = \sum_{N=1}^{\infty} \alpha_N . X_N \tag{7.3}$$

See Chapter 6, for kinetic parameters and further details with regards to finding the average carbonation conversion.

To approximate the distribution of reacting sorbent hold-up in the BFB reactor, we follow the approach used to model the distribution of char hold-up introduced in Chapter 5. Given the perfect mixing assumption for solids in the BFB, we assume that the local hold-up ratio of calcined lime (m_{CaO}) in adjacent cells of the fluidized bed is the same as the hold-up ratio of total solids in adjacent cells. With Δz being the equal cell height, we have:

$$\frac{m_{CaO}(z+\Delta z)}{m_{CaO}(z)} = \frac{(1-\varepsilon(z+\Delta z)).A.\Delta z}{(1-\varepsilon(z)).A.\Delta z} \tag{7.4}$$

If M_{CaO} is the total reacting sorbent hold-up in bed, L_{bed} the expanded dense bed height and ε_{ave} the average bed voidage, the local calcined lime hold-up in every cell can be calculated as:

$$\frac{m_{CaO}(z)}{M_{CaO}} = \frac{(1-\varepsilon(z)).A.\Delta z}{(1-\varepsilon_{ave})A.L_{bed}} \tag{7.5}$$

We now modify the net reaction rate in CO_2 mole balance in the generic two-phase kinetic model developed in Chapter 5 to also account for selective CO_2 capture during cyclic operation. According to equations (5.35) and (5.37), CO_2 is generated/consumed from three sources including:

I. Biomass pyrolysis occurring uniformly along the dense bed height:

$$Rate_{CO_2,\varphi,pyrolysis} = \left(\frac{1-\varepsilon_{\varphi}}{1-\varepsilon_{ave}}\right).\frac{\bar{Y}_{G,pyro}.\left(\dot{m}_{B,in}+\dot{m}_{M,in}\right).\left(w_{CO_2,pyro}/MW_{CO_2}\right)}{A.L_{bed}} \quad (7.6)$$

II. Homogeneous thermal tar cracking:

$$Rate_{CO_2,\varphi,tar\ cracking} = \varepsilon_{\varphi}.\left(k_4.\left(1-\gamma_{Tar_{inert}}\right).C_{Tar,\varphi}\right).MW_{Tar}.\left(w_{CO_2,\text{tar cracking}}/MW_{CO_2}\right) \quad (7.7)$$

III. Homogeneous and heterogeneous gasification reactions (WGS and Boudouard):

$$Rate_{CO_2,\varphi,gasification} = \varepsilon_{\varphi}.\left(r_{WGS}\right)+\left(\frac{1-\varepsilon_{\varphi}}{1-\varepsilon_{ave}}\right)\left(\frac{M_{Char}/MW_{Char}}{A.L_{bed}}\right).\left(-r_{C1}\right) \quad (7.8)$$

For kinetic parameters and further details with regards to formulation, see Chapter 5.

On the other hand, CO_2 is selectively consumed because of sorbent carbonation:

$$Rate_{CO_2,\varphi,carbonation} = \left(\frac{1-\varepsilon_{\varphi}}{1-\varepsilon_{ave}}\right)\left(\frac{M_{CaO}/MW_{CaO}}{A.L_{bed}}\right).\left(-r_{Carb}\right) \quad (7.9)$$

Combining equations (7.6) to (7.9), the net reaction rate for CO_2 mole balance is:

$$Rate_{CO_2,\varphi} = Rate_{CO_2,\varphi,pyrolysis} + Rate_{CO_2,\varphi,tar\ cracking} + Rate_{CO_2,\varphi,gasification} + Rate_{CO_2,\varphi,carbonation} \quad (7.10)$$

As with the char hold-up of the bed, the reacting sorbent hold-up (M_{CaO}) in the dense bubbling bed is determined iteratively. Performing a CaO balance over the dense bubbling bed at steady-state, the consumption rate of CaO in the carbonator/ gasifier is:

$$\dot{m}_{CaO,cons} = \dot{m}_{CaO,in} - \dot{m}_{CaO,out} = \dot{m}_{CaO,in}.X_{ave} \quad (7.11)$$

Assuming solid-free bubbles, from the axial partial pressure profile of CO_2 in the emulsion phase of dense bed, the carbonation rate is approximated from equation (7.1) along the reactor. We also have:

$$\dot{m}_{CaO,cons} = \int_0^{L_{bed}} \left(d\dot{m}_{CaO,carbonation}/dz\right).dz = \int_0^{L_{bed}} \left(r_{Carb,H}\left(z\right)\right).\left(M_{CaO}/L_{bed}\right).dz \quad (7.12)$$

Combining equations (7.11) and (7.12), the reacting sorbent hold-up in the bed is updated:

$$M_{CaO} = \dot{m}_{CaO,in}.X_{ave} \Big/ \left(\int_0^{L_{bed}} \left(r_{Carb,H}(z).dz \right) \Big/ L_{bed} \right) \tag{7.13}$$

Note that in the above calculations, we have neglected the catalytic effect of lime on the reaction network of biomass gasification and assumed that carbonation is an independent reaction occurring in parallel to other reactions.

7.2 Results and discussion

With the operating conditions summarized in Tables 5.2 and 5.3, Figure 7.1 illustrates the predictions of the kinetic model for dry product gas composition versus height in the gasifier of UBC DFB reactor. Unbroken and dashed curves are for non-enhanced and lime-enhanced biomass gasification, respectively. As observed, for lime-enhanced gasification, CO_2 capture along the reactor results in more hydrogen being produced and more CO being consumed according to the WGS reaction. However, the CH_4 content of gas is not affected by the presence of sorbent.

Figure 7.2 illustrates the dry product gas composition at the freeboard exit as a function of gasifier temperature. The results for the non-enhanced (unbroken curves) and lime-enhanced (dashed curves) biomass gasification are obtained from the models developed in Chapter 5 and this chapter, respectively. For the non-enhanced gasification, elevating the temperature reverses the exothermic WGS reaction toward more CO production, H_2 consumption and CO_2 consumption. For the lime-enhanced gasification, elevating the temperature reverses the exothermic carbonation leading to the enhancement effect of limestone only up to gasifier temperature of 750-760^{o}C. Beyond this temperature, the partial pressure of CO_2 in the gasifier falls below its equilibrium pressure and carbonation no longer occurs. For temperatures less than 700^{o}C, the H_2 content of dry product gas for the none-enhanced and lime-enhanced biomass gasification are ~60 mole % and ~75 mole %, respectively.

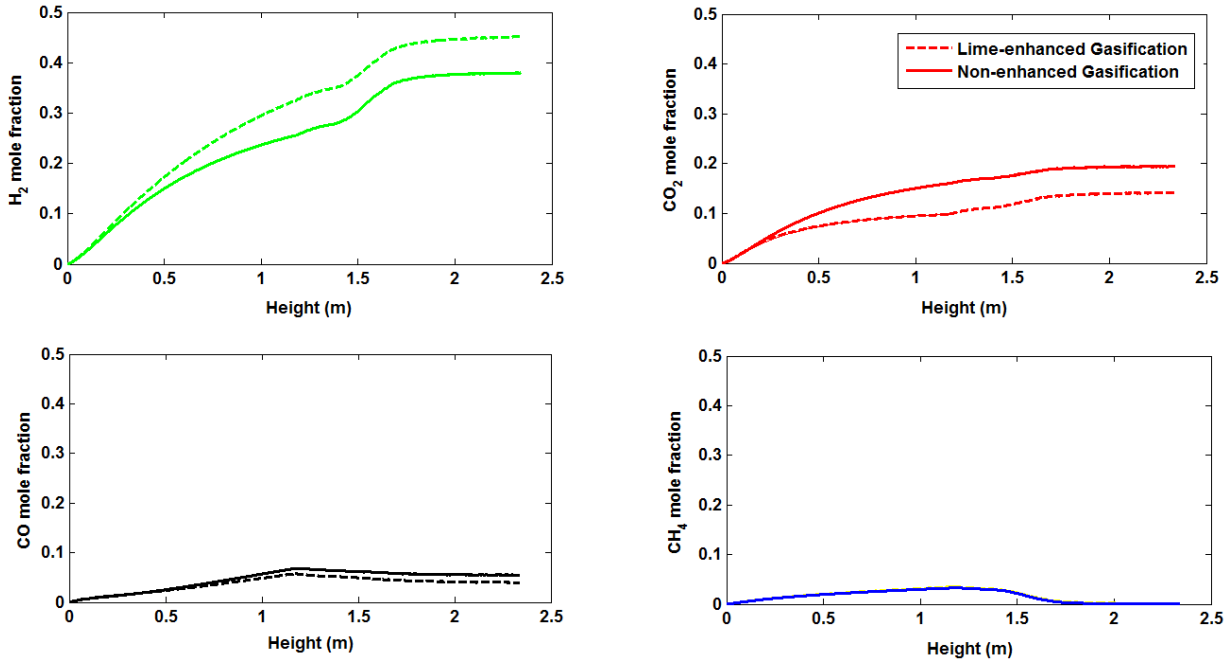

Figure 7.1. Predicted product gas composition *vs* height in the gasifier. Unbroken and dashed curves are for non-enhanced and lime-enhanced biomass gasification, respectively. Gasifier temperature=700°C, Combustor temperature=900°C, steam/biomass ratio=1.22, sorbent make-up mass flow rate/biomass ratio=0.1. Sorbent circulation mass flow rate/biomass ratio = 5. For other operating conditions, see Tables 5.2 and 5.3.

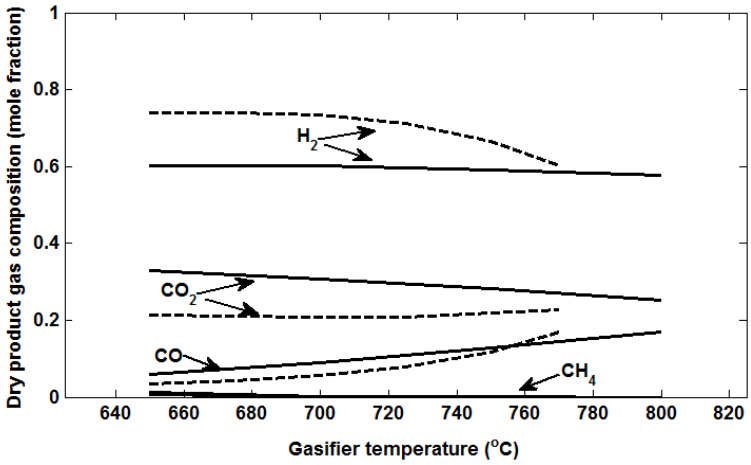

Figure 7.2. Predicted dry product gas composition as a function of gasifier temperature. Unbroken and dashed curves are for non-enhanced and lime-enhanced biomass gasification, respectively. Combustor temperature = 900°C, steam/biomass feed ratio = 1.22, sorbent make-up mass flow rate/biomass feed ratio=0.1. Sorbent circulation mass flow rate/biomass feed ratio = 5. For other operating conditions, see Tables 5.2 and 5.3.

Comparing Figure 6.7 and Figure 7.2, good agreement is observed between the predictions of the equilibrium and kinetic models of lime-enhanced biomass gasification. Although the CH_4 content of the product gas is under-predicted by both the kinetic and thermodynamic equilibrium models, the kinetic model gives better predictions of CH_4 that are closer to the experimental data. Most models developed for lime-enhanced biomass gasification in the literature are thermodynamic equilibrium models. Our findings suggest that thermodynamic equilibrium models provide convenient tools to make predictions for lime-enhanced biomass gasification systems.

7.3 Summary

A steady-state kinetic model for lime-enhanced biomass steam gasification was developed by extending the two-phase kinetic model of bubbling fluidized bed gasifier to account for selective CO_2 capture under steady-state Ca-looping operation. By adopting an empirical kinetic model for the carbonation rate of limestone particles, the effect of sorbent loss of reactivity due to sintering during cyclic operation was taken into account. *In situ* CO_2 capture versus height in the gasifier clearly shows the sorbent enhancement effect on shifting the water-gas shift reaction towards more H_2 production and CO consumption. Enhanced hydrogen production is observed up to a gasifier temperature of 750°C at atmospheric pressure. Good agreement is observed between the predictions of the equilibrium and kinetic models of lime-enhanced biomass gasification.

Chapter 8: Conclusions and Recommendations

Emissions of large amounts of greenhouse gases (largely CO_2) to the atmosphere, mostly as a by-product of burning fossil fuels in man-made processes, are contributing to climate change. The need to move towards a sustainable energy future is motivating a search for new technologies to address the ever-growing world energy demand. As a result, the share of biomass as a renewable and carbon-neutral source of energy has substantially increased in recent years. Through gasification, a variety of biomass feedstocks can be converted to diverse end products such as hydrogen, methanol, ethanol, transportation fuel and power. Lime-enhanced biomass gasification is among the promising technologies being developed for sustainable production of hydrogen. When integrated with CO_2 sequestration, this novel process could potentially result in the net removal of CO_2 from the atmosphere, i.e. negative greenhouse gas emissions.

In this thesis, a comprehensive model for steam gasification of biomass integrated with Ca-looping in a dual fluidized bed reactor was developed. Integration of a single particle model to fluidized bed reactor model is among the unique features of this model. By constraining the coupled single particle and reactor model with CHO elemental balances, biomass drying and pyrolysis products yield, as well as the composition of principal components in the pyrolysis gas are predicted as functions of the key operating parameters such as reactor temperature and feed particle size distribution. To address the uncertainties in tar measurement and analysis, we treat tar as a mixture of carbon, hydrogen and oxygen. Unlike previous models, this is a predictive model that bridges the different phenomena biomass particles go through upon entrance to a fluidized bed reactor. Based on a step-by-step approach, biomass drying, pyrolysis and gasification have been studied as a continuous process so that better predictions of the overall process are achieved. The predictions of the models developed in each step are compared with literature experimental data in the process of developing a comprehensive reactor model. Another novel contribution of this thesis is to integrate Ca-looping with biomass steam gasification in a dual fluidized bed reactor using both equilibrium and kinetic modeling. Our modeling study provides a basic tool describing the general trends of the process and predicting the effects of key operating variables, as well as identifying promising operating conditions. The developed model offers a starting point for experimental design.

8.1 Conclusions

The main conclusions of this thesis are summarized as follows:

1) The time required for complete conversion and heat-up of a biomass particle to the reactor temperature is predicted to decrease strongly with increasing reactor temperature and decreasing biomass particle size. Due to evolution and accumulation of water vapour and volatiles, a negative pressure gradient forms inside the porous structure of biomass particle which disappears over time as the water vapor and volatiles are released at the particle surface. For larger particles, the greater observed accumulation of pyrolysis products is predicted due to increased internal mass transfer resistances. The time required for complete gasification of a single char particle is virtually independent of its initial size, but decreases noticeably with increasing gasification temperature. Whereas biomass drying and pyrolysis are completed within seconds, the time required for complete gasification of char particles is of the order of hours.

2) Our coupled particle and reactor model of biomass drying and pyrolysis in a bubbling fluidized bed (BFB) reactor addresses an existing gap of knowledge in predicting the proportions of major compounds in the pyrolysis gas based on a few simplifying assumptions and CHO elemental balances. With organic tar and char elemental compositions as model input parameters, elemental balances lead to predictions of the composition of pyrolysis gas at the reactor exit as a function of process operating parameters. The model gives reasonable predictions of the composition of pyrolysis gas at temperatures above 400°C. With increasing the reactor temperature, CO and CH_4 mass fractions in dry-nitrogen-free non-condensable gas increase, whereas the CO_2 mass fraction decreases. Limitations of the current model in predicting the pyrolysis product distribution can be largely attributed to inaccurate kinetics or incomplete pyrolysis mechanism proposed for different types of biomass with varying properties.

3) The coupled particle and reactor model of biomass drying and pyrolysis in a BFB reactor was extended to steam gasification of biomass in a BFB gasifier, and its accuracy was tested by comparing predictions with independent experimental data from the literature. The

effects of steam-to-biomass ratio and reactor temperature on the distribution of products generated from steam gasification of pine sawdust were analyzed. As observed experimentally, the yields of gas increase, while tar and char yields decrease, with increasing steam-to-biomass (S/B) ratio or reactor temperature. Comparison of the model predictions with experimental data indicates that the char and tar yields are reasonably captured, whereas the product gas yield is always over-predicted. This discrepancy may be attributed to the temperature drop in the freeboard and downstream components such as the cyclone, exit gas line and heat exchanger that are externally heated and insulated.

4) The effect of S/B ratio on dry and N_2-free product gas composition for steam gasification of pine sawdust in a BFB reactor at a temperature of 750°C showed that the H_2 mole fraction in the product gas increases with increasing S/B ratio because of the water-gas, steam methane reforming and water-gas shift reactions. The CO_2 mole fraction also increases with increasing S/B ratio, probably due to the water gas shift reaction becoming dominant at high gasifier temperatures. Increasing the S/B ratio causes the mole fractions of CO and CH_4 to decrease due to enhanced WGS and steam methane reforming (SMR) reactions. Furthermore, the predicted product gas composition for steam gasification of pine sawdust shows that at higher reactor temperatures, H_2 and CO production are promoted by the endothermic Boudouard, water-gas and steam methane reforming reactions. Elevating the temperature also reverses the exothermic WGS reaction towards more CO production and CO_2 consumption. The product gas composition from steam gasification of pine wood chips [128], shows good agreement with the model predictions.

5) The performance of the UBC dual fluidized bed gasifier was simulated with steady-state predictive kinetic model that uses a generic version of the two-phase fluidized bed reactor model. This model is capable of predicting species concentrations, temperature, pressure, superficial gas velocity and other hydrodynamic parameters such as voidage profiles along each reactor. By integrating the kinetic models of BFB gasifier and CFB riser through mass and energy balances, key operating parameters such as solids circulation rate and natural gas flow rate required for stable operation of the process are predicted. The required solids circulation rate strongly depends on the temperature difference between the two fluidized beds. In order to provide larger sensible heat transfer required to maintain the gasifier at high

temperatures, the circulation rate of sand (inerts) must increase at the cost of decreased mean solids residence time in the gasifier.

Sensitivity analyses over S/B ratio, gasifier temperature and system heat loss are preformed. Unlike large commercial reactors where process heat integration and comparatively low heat losses lead to higher process efficiencies, for small scale reactors with high ratio of heat transfer surface area to reactor volumes, heat loss plays an important role in energy balance calculations. Studying the distribution of heat losses based on the UBC DFB gasifier shows that the solids circulation rate is strongly affected by the heat loss from the gasifier, whereas additional fuel (natural gas in this study) is required to make up for additional heat loss from the combustor. Hence, at higher heat losses from the combustor, greater air flow rates are required in the riser to ensure complete combustion of methane.

6) A relatively simple model was developed to capture the essence of biomass gasification integrated with cyclic CO_2 capture in a dual fluidized bed reactor, where limestone sorbent particles constitute a major fraction of the bed material. Conversion of solid biomass particles to dominant gaseous products (H_2, CO, CH_4 and CO_2) is modeled by a simple stoichiometric equilibrium model. By adopting an empirical kinetic model for the carbonation rate of limestone particles from the literature [176], not only is the effect of sorbent loss of reactivity due to sintering during cyclic operation taken into account, but the dependencies of the average carbonation conversion of CaO particles on operating parameters such as carbonation temperature, CO_2 partial pressure and mean residence time of sorbent particles within the carbonator are also clarified.

By increasing the sorbent availability in the gasifier (i.e. increasing the sorbent circulation rate), more CO_2 is captured from the product gas, shifting the water-gas shift reaction towards more H_2 production and CO consumption. Because of increased CO_2 capture, the product gas volumetric flow rate decreases, whereas its Lower Heating Value increases at greater limestone mass fractions.

For lime-enhanced gasification, due to the *in situ* heat generated by the exothermic carbonation reaction within the gasifier, the dependence on the sensible heat transfer by solids circulation

is reduced, and the total solids circulation rate is predicted to decrease considerably with increasing sorbent circulation rate or limestone mass fraction in the bed.

Enhanced hydrogen production is observed up to a gasifier temperature of 750°C at atmospheric pressure. Beyond this temperature, the partial pressure of CO_2 in the gasifier falls below its equilibrium pressure and carbonation no longer proceeds.

8.2 Recommendations for future work

There is considerable scope for refining the model in the future work, including:

1) For the single particle model, the effect of particle volume shrinkage due to pyrolysis (especially for larger particles) should be taken into consideration.

2) The assumption of constant heats of reaction in the two-step biomass pyrolysis kinetic model should be replaced by more accurately formulated functions of temperature. To obtain a dynamic heat of pyrolysis as a function of pyrolysis conversion, the HHV, LHV and heat of formation of the remaining char should be calculated based on its instantaneous elemental composition. Furthermore, the activation energies of pyrolysis reactions should be correlated with the CHO elemental composition of the remaining solid, rather than versus conversion.

3) The catalytic effects of metal components present in biomass ash (e.g. Ca, Na and K), as well as the catalytic influence of limestone on biomass gasification reaction kinetics, should if possible be incorporated into the model.

4) A more elaborate and accurate kinetic model for tar cracking and reforming should be adopted to increase the accuracy of the model predictions.

5) To account for changes in Particle Size Distribution (PSD), as well as the entrainment of fine particles from the system, a population balance model should be developed to cover biomass particles.

6) A global pressure balance over the two interconnected fluidized bed reactors should be performed to find the solids circulation rate required to meet the hydrodynamic constraints of the system for both cold and hot test runs.

7) Dispersion terms should be included in the one-dimensional gas mole balances of the generic two-phase reactor model.

8) To couple differential equations describing energy balance with differential equations of gas mole balances and hydrostatic pressure along the fluidized beds, accurate temperature and pressure measurements are needed along the BFB gasifier and its freeboard, and the CFB riser of the UBC dual bed gasifier facility.

9) Accurate measurements of solids circulation rate and heat losses under steady-state operational condition of the UBC DFB reactor would be very helpful in testing the model.

10) Accurate tar and char ultimate and proximate analyses are needed for each successful test run.

11) Future work should also take into account what nitrogen and sulfur compounds are formed during biomass gasification.

12) For lime-enhanced biomass gasification, in addition to the loss of specific area due to sintering, the loss of effectiveness of limestone particles due to sulfation (pore blockage by $CaSO_4$) should be addressed.

13) Since Ca-looping leads to changes in the density of the sorbent particles which are also subject to a continuous change in Particle Size Distribution (PSD) due to attrition and elutriation, developing a population balance model over limestone particles would be an important contribution, allowing the entrainment and loss of fine particles to be estimated.

14) To consider the effect of sorbent coking, the general non-stoichiometric equilibrium model of Li [62] can be adapted to represent the gasifier as a C-H-O ternary diagram. From this model, the maximum carbon conversion that is thermodynamically possible within the gasifier and the suitable operational conditions to avoid coke formation could be predicted.

15) To accommodate Ca-looping in the UBC experimental dual fluidized bed, it is recommended to make the necessary modifications to the reactor design and operation. For instance, an efficient way of recycling the fine sorbent particles (as well as other bed material) back to system should be found, and an extra hopper should be installed for sorbent make-up.

16) Studying the complicated hydrodynamics of a DFB reactor using Computational Fluid Dynamics (CFD) software packages, is also recommended. Ultimately, CFD models need to be integrated with reactor modeling.

17) In order to apply the kinetic models developed in this thesis to industrial reactors, the models should be extended to accommodate a broad range of fuel-related parameters (e.g. molecular composition, elemental composition, moisture content, particle size, shape and density of the fuel particles) as well as process-related parameters (e.g. reactor temperature and pressure).

References

[1] Intergovernmental Panel on Climate Change (IPCC) Special Report on Renewable Energy Sources and Climate Change Mitigation, Ed. Edenhofer O, Pichs-Madruga O, Sokona Y, Seyboth K, Matschoss P, Kadner S, Zwickel T, Eickemeier P, Hansen G, Schlömer S, von Stechow C, Cambridge University Press, Cambridge, UK and New York, NY, USA, 2011.

[2] Vakkilainen E, Kuparinen K, Heinimö J. Large industrial users of energy biomass, IEA Bioenergy Task 40: Sustainable International Bio Trade, 2013.

[3] Corella J, Toledo JM, Molina G. A review on dual fluidized-bed biomass gasifiers. Ind Eng Chem Res 2007; 46:6831–9.

[4] Dayton D. A review of the literature on catalytic biomass tar destruction. National Renewable Energy Laboratory Technical Report, NREL/TP-510-32815, 2002.

[5] Corella J, Toledo JM, Molina G. Biomass gasification with pure steam in fluidized bed: Twelve variables that affect the effectiveness of the biomass gasifier. Int J Oil, Gas Coal Technol 2008;1:194–207.

[6] Devi L, Ptasinski KJ, Janssen FJJG. Review of the primary measures for tar elimination in biomass gasification processes, Biomass Bioenergy 2003;24:125–140.

[7] Ahmed TY, Ahmad MM, Yusup S, Inayat A, Khan Z. Mathematical and computational approaches for design of biomass gasification for hydrogen production: A review. Renewable Sustainable Energy Rev 2012;16:2304–15.

[8] LV PM, Xiong ZH, Chang J, Wu CZ, Chen Y, Zhu JX. An experimental study on biomass air–steam gasification in a fluidized bed. Bioresour Technol 2004;95:95–101.

[9] Gil J, Corella J, Aznar MP, Caballero MA. Biomass gasification in atmospheric and bubbling fluidized bed: effect of the type of gasifying agent on the product distribution. Biomass Bioenergy 1999; 17:389–403.

[10] Florin NH, Harris AT. Enhanced hydrogen production from biomass with *in situ* carbon dioxide capture using calcium oxide sorbents. Chem Eng Sci 2008; 63:287–316.

[11] Ammendola P, Chirone R, Miccio F, Ruoppolo G, Scala F. Devolatilization and attrition behavior of fuel pellets during fluidized-bed gasification. Energy Fuels 2011; 25:1260–66.

[12] Mahecha-Botero A, Grace JR, Elnashaie SSEH, Lim CJ. Advances in modeling of fluidized-bed catalytic reactors: A comprehensive review. Chem Eng Commun 2009; 196:1375–1405.

[13] Gómez-Barea A, Leckner B. Modeling of biomass gasification in fluidized bed. Prog Energy Combust Sci 2010; 36:444–509.

[14] Pfeifer C, Rauch R, Hofbauer H. In-bed catalytic tar reduction in a dual fluidized bed biomass steam gasifier. Ind Eng Chem Res 2004; 43:1634–40.

[15] Milne TA, Abatzoglou N, Evans RJ. Biomass gasifier "tars": their nature, formation, and conversion, National Renewable Energy Laboratory Technical Report, NREL/TP-570-25357, 1998.

[16] Dean CC, Blamey J, Florin NH, Al-Jeboori MJ, Fennell PS. The calcium looping cycle for CO_2 capture from power generation, cement manufacture and hydrogen production. Chem Eng Res Des 2011; 89:836–855.

[17] Intergovernmental Panel on Climate Change (IPCC) Special Report on Carbon Dioxide Capture and Storage (pp. 442), Ed. Metz B, Davidson O, de Coninck HC, Loos M, Meyer L, Cambridge University Press, Cambridge, United Kingdom and New York, NY, USA, 2005.

[18] Abanades JC, Arias B, Lyngfelt A, Mattisson T, Wiley DE, Li H, Ho MT, Mangano E, Brandani S. Emerging CO_2 capture systems. Int. J. Greenh. Gas Control 2015; 40:126–66.

[19] Boot-Handford ME, Abanades JC, Anthony EJ, Blunt MJ, Brandani S, MacDowell N, Fernandez JR, Ferrari MC, Gross R, Hallett JP, Haszeldine RS, Heptonstall P, Lyngfelt, Makuch Z, Mangano E, Porter RTJ, Pourkashanian M, Rochelle GT, Shah N, Yao JG, Fennell PS. Carbon capture and storage update. Energy Environ Sci 2014; 7:130–189.

[20] Anthony EJ, Fennell PS, Carbon Capture Technology: Status and Future Prospects, in Handbook of Sustainable Energy (Ch. 17, pp. 357–374), Ed. Galarraga I, González-Eguino M, Markandya A, Edward Elgar Publishing, Inc., USA, 2011.

[21] Grace JR, Avidan A, Knowlton TM. Circulating Fluidized Beds (Ch.1). Blackie Academic & Professional, London, UK 1997.

[22] Shimizu T, Hirama T, Hosoda H, Kitano K, Inagaki M, Tejima K. A twin fluid-bed reactor for removal of CO_2 from combustion processes. Chem Eng Res Des 1999; 77:62–68.

[23] Rubin ES, Short C, Booras G, Davison J, Ekstrom C, Matuszewski M, Mccoy S. A proposed methodology for CO_2 capture and storage cost estimates. Int J Greenh Gas Control 2013; 17, 488–503.

[24] Mantripragada HC, Rubin ES. Calcium looping cycle for $_{CO2}$ capture: performance: cost and feasibility analysis. Energy Procedia 2014; 63, 2199–2206.

[25] Read P, Lermit J. Bio-energy with carbon storage (BECS): A sequential decision approach to the threat of abrupt climate change. Energy 2005; 30: 2654.

[26] Gough C, Upham P. Biomass energy with carbon capture and storage (BECCS): a review. Tyndall Centre for Climate Change Research, Working Paper 147, 2010.

[27] Kemper J. Biomass and carbon dioxide capture and storage: A review. Int J Greenh Gas Control 2015; 40: 401–430.

[28] Corella J, Toledo JM, Molina G. Steam gasification of coal at low-medium (600-800^oC) temperature with simultaneous CO_2 capture in fluidized bed at atmospheric pressure: The effect of inorganic species. 1. Literature review and comments. Ind Eng Chem Res 2006; 45:6137–46.

[29] Florin NH, Harris AT. Hydrogen production from biomass coupled with carbon dioxide capture: The implications of thermodynamic equilibrium. Fuel Cells 2007; 32:4119–34.

[30] Butler J. Limestone as a sorbent for CO_2 capture and its application in enhanced biomass gasification. PhD Thesis, University of British Columbia, 2013.

[31] Corella J, Toledo JM, Molina G. Calculation of the conditions to get less than 2 g tar/Nm^3 in a fluidized bed biomass gasifier. Fuel Process Technol 2006; 87:841–46.

[32] Li Y., Wu Z. Effects of catalytic cracking conditions on biomass tar cracking. J Tsinghua Univ 2009; 49, 253–256.

[33] Corella J, Toledo JM, Molina G. Performance of CaO and MgO for the hot gas clean up in gasification of a chlorine-containing (RDF) feedstock, Bioresour Technol 2008; 99, 7539–7544.

[34] Delgado J, Aznar MP, Corella J. Calcined dolomite, magnesite, and calcite for cleaning hot gas from a fluidized bed biomass gasifier with steam: life and usefulness. Ind Eng Chem Res 1996; 35, 3637–3643.

[35] Delgado J, Aznar MP, Corella J. Biomass gasification with steam in fluidized bed: Effectiveness of CaO, MgO, and CaO-MgO for hot raw gas cleaning. Ind Eng Chem Res 1997; 36, 1535–1543.

[36] Alonso M, Diego ME, Pérez C, Chamberlain JR, Abanades JC. Biomass combustion with in situ CO_2 capture by CaO in a 300kWth circulating fluidized bed facility. Int J Greenh Gas Control 2014; 29,142–152.

[37] Kremer J, Galloy A, Ströhle J, Epple B. Continuous CO_2 capture in a 1-MWth carbonate looping pilot plant. Chem Eng Technol 2013; 36, 1518–1524.

[38] Chang MH, Chen WC, Huang CM, Liu WH, Chou YC, Chang WC, Chen W, Cheng JY, Huang KE, Hsu HW. Design and experimental testing of a 1.9 MWth calcium looping pilot plant. Energy Procedia 2014; 63, 2100–2108.

[39] Curran GP, Fink CE, Gorin E. CO_2 acceptor gasification process – studies of acceptor properties. Adv Chem Ser 1967; 69:141–65.

[40] European Commission, 2010a. Community Research and Development Information Service (CORDIS), 6th Framework Programme (FP6). From http://cordis.europa. eu/fetch?CALLER=FP6_PROJ&ACTION=D&DOC=1&CAT=PROJ&QUERY=1202995 103012&RCN=75092.N.

[41] Pfeifer C, Puchner B, Hofbauer H. *In situ* CO_2-absorption in a dual fluidised bed biomass steam gasifier to produce a hydrogen rich syngas. Int J Chem Reactor Eng 2007; 5:A9.

[42] Proell T, Hofbauer H. H_2 rich syngas by selective CO_2 removal from biomass gasification in a dual fluidized bed system—process modeling approach. Fuel Process Technol 2008; 89: 1207–17.

[43] Koppatz S, Pfeifer G, Rauch R, Hofbauer H, Marquard-Moellenstedt T, Specht M. H_2 rich product gas by steam gasification of biomass with *in situ* CO_2 absorption in a dual fluidized bed system of 8 MW fuel input. Fuel Process Technol 2009; 90:914–21.

[44] Lin S, Harada M, Suzuki Y, Hatano H. Developing an innovative method, HyPr-RING, to produce hydrogen from hydrocarbons. Energy Conv & Management 2004a; 43:1283–90.

[45] Lin S, Suzuki Y, Hatano H, Harada M. Continuous experiment regarding hydrogen production by coal/CaO reaction with steam (I) gas products. Fuel 2004b; 83:869–74.

[46] Sun P, Lim CJ, Grace JR. Cyclic CO_2 capture by limestone-derived sorbent during prolonged calcination/carbonation cycling. AIChE J 2008; 54: 1668–77.

[47] Abanades JC, Alvarez D. Conversion limits in the reaction of CO_2 with lime. Energy Fuels 2003; 17:308–15.

[48] Lu DY, Hughes RW, Anthony EJ, Manovic V. Sintering and reactivity of $CaCO_3$-based sorbents for *in situ* CO_2 capture in fluidized beds under realistic calcination conditions. J Environ Eng 2009; 135:404–10.

[49] Sun P, Grace JR, Lim CJ, Anthony EJ. Co-capture of H_2S and CO_2 in a pressurized-gasifier-based process. Energy Fuels 2007; 21, 836–844.

[50] Chauk SS, Agnihotri R, Jadhav RA, Misro SK, Fan L-S. Kinetics of high-pressure removal of hydrogen sulfide using calcium oxide powder. AIChE J 2000; 46, 1157–1167.

[51] Zevenhoven CAP, Yrjas KP, Hupa MM. Product layer development during sulfation and sulfidation of uncalcined limestone particles at elevated pressures. Ind Eng Chem Res 1998; 37, 2639–2646.

[52] Johnsen K, Grace JR, Elnashaie SSEH, Eriksen D. Modeling of sorption-enhanced steam reforming in a dual fluidized bubbling bed reactor. Ind Eng Chem Res 2006; 45:4133–44.

[53] Grasa G, Abanades JC, Anthony EJ. Effect of partial carbonation on the cyclic CaO carbonation reaction. Ind Eng Chem Res 2009; 48:9090–96.

[54] Chen Z, Grace JR, Lim CJ. Limestone particle attrition and size distribution in a small circulating fluidized bed. Fuel 2008; 87:1360–71.

[55] González B, Alonso M, Abanades CJ. Sorbent attrition in a carbonation/calcination pilot plant for capturing CO_2 from flue gases. Fuel 2010; 89:2918–24.

[56] Weimer T, Berger R, Hawthrone C, Abanades CJ. Lime enhanced gasification of solid fuels: Examination of a process for simultaneous hydrogen production and CO_2 capture. Fuel 2008; 87:1678–86.

[57] Corella J, Toledo JM, Molina G. Steam gasification of coal at low-medium (600-800^oC) temperature with simultaneous CO_2 capture in a bubbling fluidized bed at atmospheric pressure. 2. Results and recommendations for scaling up. Ind Eng Chem Res 2008; 47:1798–1811.

[58] Aihara M, Nagai T, Matushita J, Negishi Y, Ohya H. Development of porous solid reactant for thermal-energy storage and temperature upgrade using carbonation/decarbonation reaction. Appl Energy 2001; 69, 225–238.

[59] Feng B, Liu W, Li X, An H. Overcoming the problem of loss in capacity of calcium oxide in CO_2 capture. Energy Fuels 2006; 20, 2417–2420.

[60] Li ZS, Cai NS, Huang YY, Han HJ. Synthesis, experimental studies, and analysis of a new calcium based carbon dioxide absorbent. Energy Fuels 2005; 19, 1447–1452.

[61] Schuster G, Loffler G, Weigl K, Hofbauer H. Biomass steam gasification – an extensive parametric modeling study. Bioresour Technol 2001; 77:71–9.

[62] Li X. Biomass Gasification in a circulating fluidized bed. PhD Thesis, University of British Columbia, 2002.

[63] Corella J, Sanz A. Modeling circulating fluidized bed biomass gasifiers: A pseudo-rigorous model for stationary state. Fuel Proc. Technol. 2005; 86:1021–53.

[64] Radmanesh R, Chaouki J, Guy C. Biomass gasification in a bubbling fluidized bed reactor: experiments and modeling. AlChE J 2006; 52:4258–72.

[65] Lü P, Kong X, Wu C, Yuan Z, Ma L, Chang J. Modeling and simulation of biomass air-steam gasification in a fluidized bed. Front Chem Eng Chin 2008; 2:209–213

[66] Kaushal P, Abedi J, Mahinpey N. A comprehensive mathematical model for biomass gasification in a bubbling fluidized bed reactor. Fuel 2010; 89:3650–61.

[67] Kaushal P, Proell T, Hofbauer H. Model for biomass char combustion in the riser of a dual fluidized bed gasification unit: Part 1 – model development and sensitivity analysis. Fuel Process Technol 2008; 89:651–9.

[68] Hamel S, Krumm W. Mathematical modelling and simulation of bubbling fluidised bed gasifiers. Powder Technol 2001; 120:105–12.

[69] Fiaschi D, Michelini M. A two-phase one-dimensional biomass gasification kinetics model. Biomass Bioenergy 2001; 21:121–32.

[70] Masnadi MS. Biomass/fossil fuel co-gasification with and without integrated CO_2 capture. PhD Thesis, University of British Columbia, 2014.

[71] Ahmad MM, Chiew CK, Inayat A, Yusup S. Simulation of integrated pressurized steam gasification of biomass for hydrogen production using Icon. J Appl Sci 2011; 11:3593–9.

[72] Inayat A, Ahmad MM, Mutalib MIA, Yusup S. Flowsheet development and modeling of hydrogen production from empty fruit bunch via steam gasification. Chem Eng Trans 2010; 21:427–32.

[73] Basu P, Kaushal P. Modeling of pyrolysis and gasification of biomass in fluidized beds: a review. Chem Prod Process Model 2009; 4:1–45.

[74] Sadaka S, Ghaly AE, Sabbah MA. Two phase biomass air–steam gasification model for fluidized bed reactors: Part I – model development. Biomass Bioenergy 2002; 22:439–62.

[75] Petersen I, Werther J. Experimental investigation and modeling of gasification of sewage sludge in the circulating fluidized bed. Chem Eng Process 2005; 44:717–36.

[76] Petersen I, Werther J. Three-dimensional modeling of a circulating fluidized bed gasifier for sewage sludge. Chem Eng Sci 2005; 60:4469–84.

[77] Gordillo ED, Belghit A. A two phase model of high temperature steam-only gasification of biomass char in bubbling fluidized bed reactors using nuclear heat. Int J Hydrogen Energy 2011; 36:374–81.

[78] Yan L, Lim CJ, Yue G, He B, Grace JR. One-dimensional modeling of a dual fluidized bed for biomass steam gasification. Energy Conv & Management 2016; 127:612-622.

[79] Babu BV, Chaurasia AS. Heat transfer and kinetics in the pyrolysis of shrinking biomass particle. Chem Eng Sci 2004; 59:1999–2012.

[80] Sharma AK, Pareek V, Wanga S, Zhang Z, Yang H, Zhang D. A phenomenological model of the mechanisms of lignocellulosic biomass pyrolysis processes. Comput Chem Eng 2014; 60:231–241.

[81] Shafizadeh F, Chin PPS. Wood Technology: Chemical Aspects (pp. 57–81), Ed. Goldstein IS, American Chemical Society Symposium Series 1977; 43.

[82] Chan WCR, Kelbon M, Krieger BB. Modelling and experimental verification of physical and chemical processes during pyrolysis of a large biomass particle. Fuel 1985; 64:1505–1513.

[83] Di Blasi C, Branca C. Kinetics of primary product formation from wood pyrolysis. Ind Eng Chem Res 2001; 40:5547–5556.

[84] Liden AG, Berruti F, Scott DS. A kinetic model for the production of liquids from the flash pyrolysis of biomass. Chem Eng Comm 1988; 65:207–221.

[85] Park WC, Atreya A, Baum HR. Experimental and theoretical investigation of heat and mass transfer processes during wood pyrolysis. Comb Flame 2010; 157:481–494.

[86] Di Blasi C. Analysis of convection and secondary reaction effects within porous solid fuels undergoing pyrolysis. Comb Sc and Tech 1993a; 90:315–340.

[87] Bryden KM, Hagge MJ. Modeling the combined impact of moisture and char shrinkage on the pyrolysis of a biomass particle. Fuel 2003; 82:1633–1644.

[88] Haseli Y, van Oijen JA, de Goey LPH. Modeling biomass particle pyrolysis with temperature-dependent heat of reactions. J Anal Appl Pyrol 2011; 90:140–154.

[89] Wang X, Kersten SRA, Prins W, van Swaaij WPM. Biomass pyrolysis in a fluidized bed reactor. part 2: experimental validation of model results. Ind Eng Chem Res 2005; 44: 8786–8795.

[90] Mochulski D. Multiple reaction solid state kinetic parameter determination and its application to woody biomass. MSc Thesis, University of British Columbia, 2015.

[91] Wagenaar BM, Prins W, van Swaaij WPM. Pyrolysis of biomass in the rotating cone reactor: modelling and experimental justification. Chem Eng Sc 1994; 49:5109–26.

[92] Kumar S, Jain VK. Diffusion through wood. Diffusion of boric acid. Holzvertwert 1973; 25:21–24.

[93] Janse AMC, Westerhout RWJ, Prins W. Modelling of flash pyrolysis of a single wood particle. Chem Eng Proc 2000; 39:239–252.

[94] Grønli MG, Melaaen MC. Mathematical model for wood pyrolysis: comparison of experimental measurements with model predictions. Energy Fuels 2000; 14:791–800.

[95] Di Blasi C. Physico-chemical processes occurring inside a degrading two-dimensional anisotropic porous medium. Int J Heat Mass Transfer 1998; 41:4139–4150.

[96] Ranz WE, Marshall WR. Evaporation from drops, Parts 1 & 2. Chem Eng Prog 1952; 48: 141–146 & 173–180.

[97] Agarwal PK, Genetti WE, Lee YY. Models for devolatilization of coal particles in fluidized beds. Fuel 1984; 63:1157–65.

[98] Frössling N. Gerlands beitr. Geophys 1938; 52:170–175.

[99] Koch P. Specific heat of oven-dry spruce pine wood and bark. Wood Sci 1969; 1:203–214.

[100] Raznjevik K. Handbook of Thermodynamic Tables and Charts. Hemisphere Publishing Corporation, McGraw-Hill, 1976.

[101] Barrio M, Hustad JE. CO_2 gasification of birch char and the effect of CO inhibition on the calculation of chemical kinetics, Progress in Themochemical Biomass Conversion (pp. 47–60), Ed. Bridgwater AV, Blackwell Science Ltd., 2001.

[102] Barrio M, Gobel B, Risnes H, Henriksen U, Hustad JE, Sorensen LH. Steam gasification of wood char and the effect of hydrogen inhibition on the chemical kinetics, Progress in Themochemical Biomass Conversion (pp. 32–46), Ed. Bridgwater AV, Blackwell Science Ltd., 2001.

[103] Babu B, Sheth P. Modeling and simulation of reduction zone of downdraft biomass gasifier: effect of char reactivity factor. Energy Conv & Management 2006;47:2602–11.

[104] Wurzenberger JC, Wallner S, Raupenstrauch H, Khinast JG. Thermal conversion of biomass: comprehensive reactor and particle modeling. AIChE J 2002; 48, 2398–2411.

[105] Ergudenler A, Ghaly AE, Hamdullahpur F, Al-Taweel AM Mathematical modeling of a fluidized bed gasifier. Part I – model development. Energy Source 1997; 19:1065–84.

[106] Buekens AG, Schoeters JG. Modelling of biomass gasification. Fundamentals of Thermochemical Biomass Conversion (Ch. 35, pp. 619–89), Ed. Overend RP, Milne TA, Mudge LK, Elsevier Applied Science Publishers, London, 1985.

[107] Ji P, Feng W, Chen B. Comprehensive simulation of an intensified process for H_2 production from steam gasification of biomass. Ind Eng Chem Res 2009; 48:3909–20.

[108] Jiang H, Morey RV. A numerical model of fluidized bed biomass gasifier. Biomass Bioenergy 1992; 3:431–47.

[109] Thunman H, Niklasson F, Johnsson F, Leckner B. Composition of volatile gases and thermo-chemical properties of wood for modeling of fixed or fluidized beds. Energy Fuels 2001; 15:1488–97.

[110] Di Blasi C. Dynamic behaviour of stratified downdraft gasifiers. Chem Eng Sci 2000; 55: 2931–44.

[111] Fagbemi L, Khezami L, Capart R. Pyrolysis products from different biomasses: application to the thermal cracking of tar. Appl Energy 2001; 69:293–306.

[112] Neves D, Thunman H, Matos A, Tarelho L, Gómez-Barea A. Characterization and prediction of biomass pyrolysis products. PECS 2011; 37:611–630.

[113] Kaushal P, Abedi J. A simplified model for biomass pyrolysis in a fluidized bed reactor. JIEC 2010; 16:748–755.

[114] Gerun L, Paraschiv M, Vijeu R, Bellettre J, Tazerout M, Gøbel B, Henriksen U. Numerical investigation of the partial oxidation in a two-stage downdraft gasifier. Fuel 2008; 87: 1383–93.

[115] El-Rub ZA. Biomass char as an in-situ catalyst for tar removal in gasification systems. PhD Thesis, University of Twente, 2008.

[116] Levenspiel O. Chemical Reaction Engineering (3rd ed.). John Wiley and Sons, New York, 1999.

[117] Clift R, Grace JR. Continuous bubbling and slugging, in Fluidization (Ch. 3, pp. 73–132), Ed. Davidson JF, Clift R, Harrison D, Academic Press, London, 1985.

[118] Darton RC, Lanauze RD, Davidson JF, Harrison D. Bubble growth due to coalescence in fluidized-beds. Trans Inst Chem Eng 1977; 55:274–280.

[119] Di Blasi C. Modeling wood gasification in a countercurrent fixed-bed reactor. AIChE J 2004; 50:2306–19.

[120] Oasmaa A, Meier D. Fast Pyrolysis of Biomass: A Handbook (p. 23), Ed. Bridgwater AV, CPL Press, Newbury, UK, 2002.

[121] Boroson ML, Howard JB, Longwell JP, Peters WA. Product yields and kinetics from the vapor phase cracking of wood pyrolysis tars. AIChE J 1989b; 35:120–128.

[122] Westerhof RJM. Refining fast pyrolysis of biomass. PhD Thesis, University of Twente, 2011.

[123] Rapagnà S, Jand N, Kiennemann A, Foscolo PU. Steam-gasification of biomass in a fluidized-bed of olivine particles. Biomass Bioenergy 2000; 19:187–97.

[124] Sutton D, Kelleher B, Ross JRH. Review of literature on catalysts for biomass gasification. Fuel Process Technol 2001; 73:155–73.

[125] Gómez-Barea A, Leckner B. Estimation of gas composition and char conversion in a fluidized bed biomass gasifier. Fuel 2013; 107:419–43.

[126] Biba V, Macak J, Klose E, Malecha J. Mathematical modeling for the gasification of coal under pressure. Ind Eng Chem Process Des Dev 1978; 17:92–98.

[127] Parent JD, Katz S. Equilibrium compositions and enthalpy changes for the reaction of carbon, oxygen, and steam. IGT-Inst Gas Tech, Research Bulletin 2, 1948.

[128] Herguido J, Corella J, González-Saiz J. Steam gasification of lignocellulosic residues in a fluidized bed at a small pilot scale. Effect of the type of feedstock. Ind Eng Chem Res 1992; 31:1274–82.

[129] Asadi-Saghandi H, Sheikhi A, Sotudeh-Gharebagh R. Sequence-based process modeling of fluidized bed biomass gasification. ACS Sustain Chem Eng 2015; 3:2640–51.

[130] Li YH, Watkinson AP *et al.* A novel dual bed gasifier, to be published.

[131] Di Blasi C, Buonanno F, Branca C. Reactivities of some biomass chars in air. Carbon 1999; 37:1227.

[132] Monson CR, Germane GJ, Blackham AU, Smoot LD. Char oxidation at elevated pressures. Combust and Flame 1995; 100:669.

[133] Dd Vilienskii TV, Hezmalian DM. Dynamics of the combustion of pulverized fuel. Energia (Moscow) 1978; 11:246–251.

[134] Howard JB, Williams GC, Fine DH. Kinetics of carbon monoxide oxidation in post flame gases. 14th Symposium (International) on Combustion, The Combustion Institute, Pittsburgh 1973, 975–986.

[135] Jensen A, Johnsson JE, Andries J, Laughli K, Read G, Mayer M. Formation and reduction of NOx in pressurized fluidized bed combustion of coal. Fuel 1995; 74:1555–69.

[136] Abba IA, Grace JR, Bi HT, Thompson ML. Spanning the flow regimes: Generic fluidized bed reactor model. AIChE J 2003; 49:1838–48.

[137] Mahecha-Botero A. Comprehensive modeling and its application to simulation of fluidized-bed reactors for efficient production of hydrogen and other hydrocarbon processes. PhD Thesis, University of British Columbia, 2009.

[138] Sit SP, Grace JR. Effect of bubble interaction on interphase mass transfer in gas fluidized beds. Chem Eng Sci 1981; 36:327–335.

[139] Grace JR. Fluidized-bed hydrodynamics, in Handbook of Multiphase Systems (Ch. 8, pp. 5–64), Ed. Hetsroni G., Hemisphere, Washington, 1982.

[140] Davidson JF, Harrison D. Fluidised Particles. Cambridge. Cambridge University Press, 1962.

[141] Wilke CR. Dusional properties of muticomponent gases. Chem Eng Prog 1950; 46:95–104.

[142] Cussler EL. Diffusion: Mass Transfer in Fluid Systems (2nd ed.). Cambridge University Press, New York, 1997.

[143] Hirschfelder J, Curtiss CF, Bird RB. Molecular Theory of Gases and Liquids. Wiley, New York, 1954.

[144] Turek DG, Sopko SJ, Jansesen K. A generic circulating fluidized bed for cogenerating steam, electricity and hot air. In proceedings of 8th International Conference on Fluidized Bed Combustion 1985; 1:395–405.

[145] Holman JP. Heat Transfer (10^{th} ed.). McGraw Hill, New York, 2010.

[146] Bi X, Grace JR. Flow regime diagrams for gas solid fluidization and upward transport. Int J Multiphase Flow 1995; 21:1229–36.

[147] Bai D, Kato K. Quantitative estimation of solids holdups at dense and dilute regions of circulating fluidized beds. Powder Technol 1999; 101:183–190.

[148] Kunii D, Levenspiel O. Circulating fluidized bed reactors. Chem Eng Sc 1997; 52:2471.

[149] Basava Rao VV, Bala Narsaiaha T, Reddy BV. Prediction of falling solids film thickness near the wall in circulating fluidized bed risers. Int J Chem Eng 2011; 2:84–90.

[150] Löffler G, Kaiser S, Bosch K, Hofbauer H. Hydrodynamics of a dual fluidized-bed gasifier—Part I: simulation of a riser with gas injection and diffuser. Chem Eng Sc 2003; 58:4197–4213.

[151] Kagawa H, Mineo H, Yamazaki R, Yoshida K. A gas-solid contacting model for fast-fluidized bed, in Circulating Fluidized Bed Technology III, Ed. Basu P, Horio M, Hasatani M, Pergamon, Oxford, 1991, pp. 551–556.

[152] Patience GS, Chaouki J. Gas phase hydrodynamics in the riser of a circulating fluidized bed. Chem Eng Sci 1993; 48:3195–3205.

[153] Berruti F, Kalogerakis N. Modelling the internal flow structure of circulating fluidized beds. Can J Chem Eng 1989; 67:1010–14.

[154] Pugsley TS, Patience GS, Berruti F, Chaouki J. Modeling the catalytic oxidation of n-butane to maleic anhydride using a circulating fluidized bed reactor. Ind Eng Chem Res 1992; 31:2652.

[155] Hofbauer H, Rauch R. Stoichiometric water consumption of steam gasification by the FICFB-gasification process, Progress in Thermochemical Biomass Conversion, Innsbruck, Austria, 2000.

[156] Higman C, van der Burgt M. Gasification. Gulf Professional Publishing. USA, 2003.

[157] Hanaoka T, Yoshida T, Fujimoto S, Kamei K, Harada M, Suzuki Y. Hydrogen production from woody biomass by steam gasification using a CO_2 sorbent. Biomass Bioenergy 2005; 28:63–8.

[158] Pfeifer C, Puchner B, Pröll T, Hofbauer H. H_2-rich syngas from renewable sources by dual fluidized bed steam gasification of solid biomass, in Fluidization XII, ed. X. Bi, F. Berruti and T. Pugsley, Engng. Conf. Intern., 2007, pp. 889-896.

[159] Sakadjian BB, Iyer MV, Gupta H, Fan LS. Kinetics and structural characterization of calcium-based sorbents calcined under subatmospheric conditions for the high-temperature CO_2 capture process. Ind Eng Chem Res 2007; 46:35–42.

[160] Hughes RW, Lu DY, Anthony EJ, Macchi A. Design, process simulation and construction of an atmospheric dual fluidized bed combustion system for *in situ* CO_2 capture using high-temperature sorbents. Fuel Process Technol 2005; 86:1523–31.

[161] Donat F, Florin NH, Anthony EJ, Fenell PS. The influence of high-temperature steam on the reactivity of CaO sorbent for CO_2 capture. Environ Sci Technol 2012; 46:1262–9.

[162] Li XT, Grace JR, Lim CJ, Watkinson AP, Chen HP, Kim JR. Biomass gasification in a circulating fluidized bed. Biomass Bioenergy 2004; 26:171–93.

[163] Watkinson AP, Lucas JP, Lim CJ. A prediction of performance of commercial coal gasifiers. Fuel 1991; 70:519–27.

[164] Pröll T, Hofbauer H. Development and application of a simulation tool for biomass gasification based processes. Int J Chem Reactor Eng 2008; 6:A89.

[165] McBride BJ, Gordon S, Reno MA. Coefficients for calculating thermodynamic and transport properties of individual species. NASA Technical Memorandum 4513, NASA, 1993.

[166] Merrick D. Mathematical models of the thermal decomposition of coal– Parts 1–6. Fuel 1988; 62: 534–70.

[167] Dooley B. Release on the IAPWS industrial formulation 1997 for the thermodynamic properties of water and steam. IAPWS Secretariat, EPRI, Palo Alto CA, 1997.

[168] Burcat A, McBride B. Ideal gas thermodynamic data for combustion and air pollution use, Report No. TAE 804, Technion Israel Institute of Technology, Aerospace Engineering, 1997.

[169] Sun P, Grace JR, Lim CJ, Anthony EJ. The effect of CaO sintering on cyclic CO_2 capture in energy systems. AIChE J 2007; 53:2432–42.

[170] Symonds RT, Lu DY, Hughes RW, Anthony EJ, Macchi A. CO_2 capture from simulated syngas via cyclic carbonation/calcination for a naturally occurring limestone: pilot-plant testing. Ind Eng Chem Res 2009; 48:8431–40.

[171] Grasa GS, Abanades JC. CO_2 capture capacity of CaO in long series of carbonation/calcination cycles. Ind Eng Chem Res 2006; 45:8846–51.

[172] Rodriguez N, Alonso M, Abanades JC. Average activity of CaO particles in a calcium looping system. Chem Eng J 2010; 156:388–94.

[173] Grasa GS, Alonso M, Abanades JC. Sulfation of CaO particles in a carbonation/calcination loop to capture CO_2. Ind Eng Chem Res 2008; 47:1630–5.

[174] Ariasa B, Abanades JC, Grasa GS. An analysis of the effect of carbonation conditions on CaO deactivation curves. Chem Eng J 2011; 167:255–61.

[175] Abanades JC. The maximum capture efficiency of CO_2 using a carbonation/calcination cycle of $CaO/CaCO_3$. Chem Eng J 2002;90:303–6.

[176] Grasa GS, Abanades JC, Alonso M, Gonzales B. Reactivity of highly cycled particles of CaO in a carbonation/calcination loop. Chem Eng J 2008; 137:561–7.

[177] Baker EH. The calcium oxide-carbon dioxide system in the pressure range 1-300 atm. J Chem Soc 1962:464–70.

[178] Alvarez D, Abanades JC. Determination of the critical product layer thickness in the reaction of CaO with CO_2. Ind Eng Chem Res 2005; 44:5608–15.

[179] Romano MC. Modelling the carbonator of a Ca-looping process for CO_2 capture from power plant flue gas. Chem Eng Sci 2012; 69:257–69.

Appendices

Appendix A Schematic and description of UBC pilot scale dual fluidized bed gasifier

A schematic of the dual fluidized bed (DFB) gasification system in the UBC Pulp and Paper Centre is presented in Figure A.1. The DFB is composed of a Bubbling Fluidized Bed (BFB) gasifier, typically operating in the temperature range 750-800°C, fluidized by steam at modest superficial gas velocities (0.5-1 m/s), and a Circulating Fluidized Bed (CFB) combustor which operates at higher temperature (850-900°C) and superficial gas velocities (8-10 m/s), with air as the fluidizing agent. The system operates at atmospheric pressure. Superheated steam (600-800°C) is supplied through a steam superheater to the BFB at ~10 kg/h. A CFB-natural gas main air preheater is used to preheat the air to ~400°C. A biomass screw feeder is used to feed the biomass to the BFB at a rate of ~ 10-15 kg/h for steam gasification. Typical biomass feedstocks used for the DFB experiments are similar to those for the six woody biomass species (Cypress, Hemlock, SPF (spruce, pine and fir mixture), Cedar, PS (50 wt% pine bark + 50 wt% spruce whitewood mix) and mixed sawdust) investigated by Li [62]. The average properties of the biomass feed material is summarized in Table A.1.

The bottoms of the two columns are connected by a J-valve, aerated by air, to circulate bed material, accompanied by unreacted char, resulting from biomass gasification, from the gasifier to the combustor. External cyclones are provided at the top of each fluidized bed for gas-solid separation. The combustion flue gas is exhausted from the combustor cyclone, sent to downstream cooling and cleaning devices before being vented. Similarly, the product gas leaving the gasifier cyclone (syngas) is sent to a downstream cooler and a particulate filter before being incinerated in an afterburner. In addition to a hot flow of solids that is continuously directed from the top of the combustor to the gasifier through a standpipe/return leg, the solid stream exiting the gasifier cyclone is recycled back to the gasifier. There are two natural gas burners installed for the system preheating and to provide for heat losses during operation.

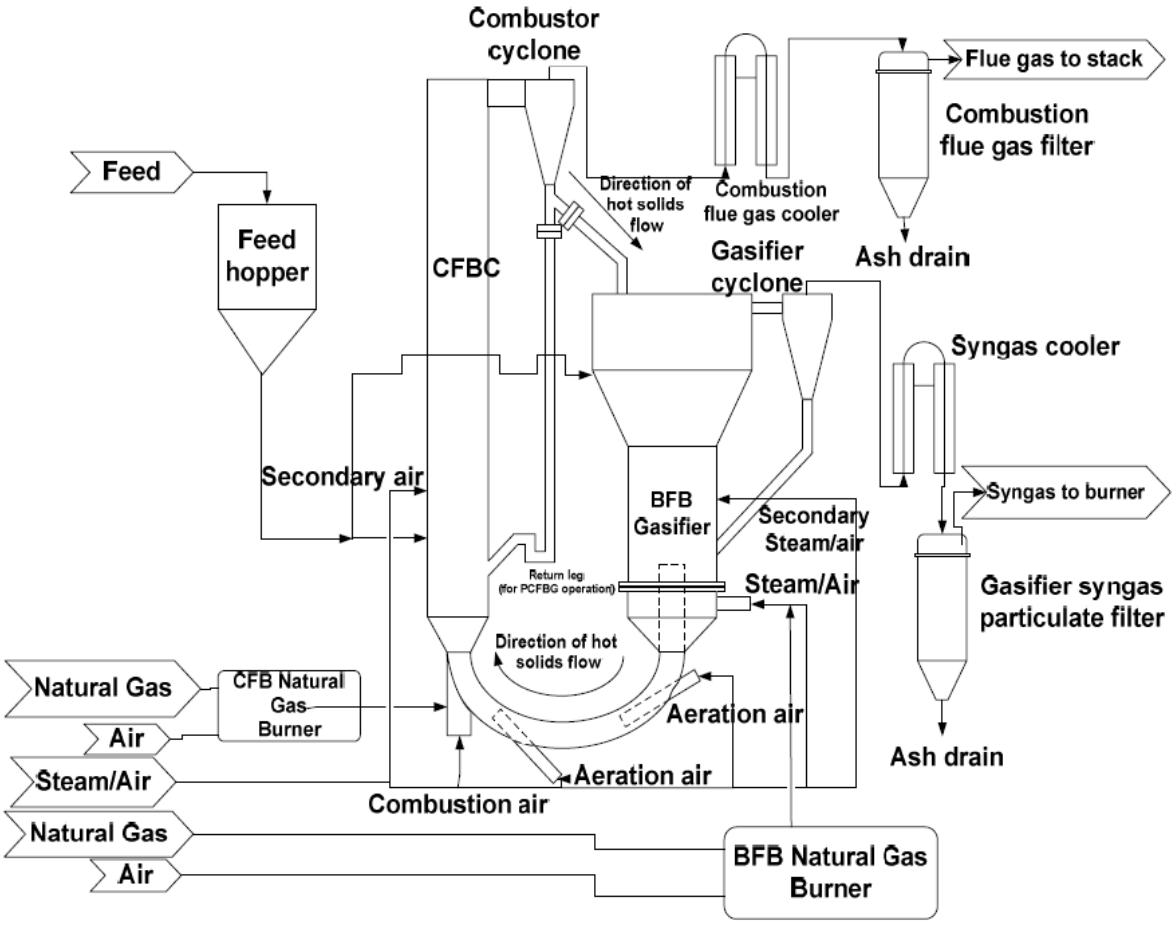

Figure A.1 Schematic of dual fluidized bed gasification system at UBC.

Table A.1 Average properties of biomass feed [62].

Proximate analysis and other properties		**Ultimate analysis (wt%, dry and ash-free)**	
HHV (MJ/kg)	20.6	C	51.5
Moisture content	15	H	6.7
Ash content (wt %)	1.14	O	41.0
Dry bulk density (kg/m^3)	220	N	0.52
Particle diameter (mm)	0.79	S	0.34

Appendix B MATLAB code for single particle model of biomass drying and pyrolsysis.

Appendix B develops a single-particle model to study biomass drying and pyrolysis. A Progressive Conversion Model is used to describe the drying and pyrolysis of a single non-shrinking biomass particle, taking into account the transport phenomena in a porous medium and the change in particle thermo-physical properties during release of volatiles from particles and the heat-up to the reactor temperature.

```
function PCM_Pyrolysis
%Progressive Conversion Model for biomass drying and pyrolysis without shrinkage
clear all
global Rho_Bio0 Rho_Cf Rho_M0 Epsi_Bio0 Epsi_Char Betta_Bio0 Betta_Char Tgas Tw Pgas
R dp Dmix Taw k_Bio0 k_Char k_Vol sigma_rad dpore_Char dpore_Bio0 Emissivity_Char
Emissivity_Bio0 g alpha Ug MW_Gas MW_Tar MW_N2 MW_Vap DH_rxn1 DH_rxn2 DH_rxn3
DH_rxn4 DH_rxn5 DH_vap k01 k02 k03 k04 k05 k0vap E1 E2 E3 E4 E5 Evap
clc
g=9.81;
R=8.314;
 dp=1000*10^-6;                          %Initial biomass particle diameter (m)
Rho_Bio0=570;                            %Dry bulk density of biomass (kg/m3)
Rho_M0=10/(100-10)*Rho_Bio0;             %Biomass moisture density for 10 wt% moisture a.r.
Ug=0.1;                                  %Sweep gas (N2) velocity relative to particle (m/s)
Epsi_Bio0=0.4;                           %Biomass porosity
Epsi_Char=0.91;                          %Char porosity
Betta_Bio0=(10^(-14)+10^(-11))/2;        % Biomass permeability (m2)
Betta_Char=(5*10^(-12)+5*10^(-11))/2;    % Char permeability (m2)
k_Bio0=1/2*(10.46*10^-2+25.5*10^-2);     %Biomass thermal conductivity (W/m.K)
k_Char=1/2*(7.1*10^-2+10.5*10^-2);       %Char thermal conductivity (W/m.K)
k_Vol=25.77*10^-3;                       %Volatiles thermal conductivity (W/m.K)
dpore_Bio0=5*10^-5;                      %Pore diameter in biomass (m)
dpore_Char=10^-4;                        %Pore diameter in char (m)
Emissivity_Bio0=0.6;                     %Biomass emissivity
Emissivity_Char=1;                       %Char emissivity
sigma_rad=5.67*10^-8;                    % Stefan-Boltzmann constant (W/m2.K4)
Taw=1;                                   % Tortuosity
Dmix=10^-6;                              % Gas-phase Molecular diffusivity (m2/s)
MW_Gas=38;                               % Molecular weight of pyrolysis gas (g/mol)
MW_Tar=94;                               % Molecular weight of bio-oil (g/mol)
MW_N2=28;
MW_Vap=18;
 %Reaction network of biomass drying and pyrolysis:
%Biomass--k1-->Gas1
%Biomass--k2-->Tar1
%Biomass--k3-->Char
```

```
 %Tar1--k4-->(1-alpha)Gas2+(alpha)Tar2
%Tar1--k5-->Char
%Moisture--kvap-->Vapour
 alpha=0.78;
%Di Blasi
k01=4.38*10^9;    %1/s
k02=1.08*10^10;
k03=3.27*10^6;
E1=1.527*10^5;     %J/mole
E2=1.48*10^5;
E3=1.117*10^5;
DH_rxn1=64*1000;     %J/kg
DH_rxn2=64*1000;     %J/kg
DH_rxn3=64*1000;     %J/kg
DH_rxn4=-42*1000;    %J/kg
DH_rxn5=-42*1000;    %J/kg
DH_vap=2440*1000;    %J/kg
%Chan
% k01=1.3*10^8;    %1/s
% k02=2.0*10^8;
% k03=1.10*10^7;
% E1=140.3*1000;     %J/mole
% E2=133.1*1000;
% E3=121.3*1000;
% DH_rxn1=150*1000;     %J/kg
% DH_rxn2=150*1000;     %J/kg
% DH_rxn3=150*1000;     %J/kg
% DH_rxn4=-42*1000;    %J/kg
% DH_rxn5=-42*1000;    %J/kg
% Boronson (500-800 C)
% k04=1*10^4.98;
% E4=93.37*1000;
% Liden
k04=4.28*10^6;
E4=108*1000;
%Di Blasi
k05=1*10^5;
E5=108*1000;
% Bryden
k0vap=5.13*10^10;
Evap=88000;

Rho_Cf=100;                          %Initial guess for final char bulk density (kg/m3)
Pgas=1.01325*10^5;                   %Reactor pressure (Pa)
```

```
Tgas=650+273.15;                        %Reactor temperature (K)
Tw=Tgas-10;                             %Initial guess for reactor wall temperature (K)

Vp0=4/3*pi()*(dp/2)^3;                  % Initial particle volume
MBio0=Rho_Bio0*4/3*pi()*(dp/2)^3;       % Mass of dry biomass in the particle
MMoist0=Rho_M0*4/3*pi()*(dp/2)^3;       % Mass of moisture in the particle
MP0=MBio0+MMoist0;

 bol=0;                                 % Logical variable that singnals complete conversion
RhoC_temp=0;
tend=60;                                % Initial guess for required time for complete conversion(s)
%Fixing final char density with a while loop
while or(abs(RhoC_temp-Rho_Cf)>1,bol==0)
   RhoC_temp=Rho_Cf;
   mCf=Rho_Cf*Vp0;

   m=2;                % Particle shape parameter, 2 for spherical particles
   Nx=21;              % Number of radial grids along particle radius
   x=linspace(0,dp/2,Nx);
   A_r=4*pi().*x.^2;

   Nt=25000;           % Number of temporal grids should be chosen appropriately
   t=linspace(0,tend,Nt);

   % Vectors for saving instantaneous mass of different species
   MP=zeros(Nt,1);
   MBio=zeros(Nt,1);
   MChar=zeros(Nt,1);
   MMoist=zeros(Nt,1);
   MVpore=zeros(Nt,1);
   MG1pore=zeros(Nt,1);
   MG2pore=zeros(Nt,1);
   MT1pore=zeros(Nt,1);
   MT2pore=zeros(Nt,1);
   MTpore=zeros(Nt,1);
   MVol=zeros(Nt,1);
   MVap=zeros(Nt,1);
   MGas1=zeros(Nt,1);
   MGas2=zeros(Nt,1);
   MGas=zeros(Nt,1);
   MTar1=zeros(Nt,1);
   MTar2=zeros(Nt,1);
   MTar=zeros(Nt,1);
   MN2=zeros(Nt,1);
```

```
    dMVol_dt=zeros(Nt,1);
    dMVap_dt=zeros(Nt,1);
    dMGas1_dt=zeros(Nt,1);
    dMGas2_dt=zeros(Nt,1);
    dMTar1_dt=zeros(Nt,1);
    dMTar2_dt=zeros(Nt,1);
    dMN2_dt=zeros(Nt,1);

    sol=pdepe(m,@pdex1pde,@pdex1ic,@pdex1bc,x,t);
    RhoBio=sol(:,:,1);     %Rho(t,x)
    RhoChar=sol(:,:,2);
    RhoM=sol(:,:,3);
    RhoVap=sol(:,:,4);
    RhoGas1=sol(:,:,5);     %Gas=CO+CO2+H2+CH4
    RhoGas2=sol(:,:,6);
    RhoTar1=sol(:,:,7);
    RhoTar2=sol(:,:,8);
    RhoN2=0*sol(:,:,9);
    T=sol(:,:,10);          %T(t,x)
    P=sol(:,:,11);
    U_Vol=sol(:,:,12);

    XBio=(Rho_Bio0-(RhoBio+RhoChar))/(Rho_Bio0-Rho_Cf);
    Epsi_p=Epsi_Bio0+XBio*(Epsi_Char-Epsi_Bio0);
    RhoVol=RhoVap+RhoGas1+RhoGas2+RhoTar1+RhoTar2+RhoN2;
    Rhop=RhoBio+RhoM+RhoChar+Epsi_p.*(RhoVol);

    for i=1:Nt
        MBio(i)=trapz(x,RhoBio(i,:).*A_r);
        MChar(i)=trapz(x,RhoChar(i,:).*A_r);
        MMoist(i)=trapz(x,RhoM(i,:).*A_r);
    end
    XBio_ave=((MBio0+MMoist0)-(MBio+MMoist+MChar))./((MBio0+MMoist0)-mCf);

    for i=1:Nt
        if XBio_ave(i)>0.99
            tend=ceil(t(i));
            bol=1;
            break
        end
    end
    mCf=MChar(Nt);
    Rho_Cf=mCf/Vp0;
end
```

```
MP(1)=MP0;
MBio(1)=MBio0;
MMoist(1)=MMoist0;
for i=2:Nt
   %inside particle
   MP(i)=trapz(x,Rhop(i,:).*A_r);
   MBio(i)=trapz(x,RhoBio(i,:).*A_r);
   MChar(i)=trapz(x,RhoChar(i,:).*A_r);
   MMoist(i)=trapz(x,RhoM(i,:).*A_r);
   MVpore(i)=trapz(x,Epsi_p(i,:).*RhoVap(i,:).*A_r);
   MG1pore(i)=trapz(x,Epsi_p(i,:).*RhoGas1(i,:).*A_r);
   MG2pore(i)=trapz(x,Epsi_p(i,:).*RhoGas2(i,:).*A_r);
   MT1pore(i)=trapz(x,Epsi_p(i,:).*RhoTar1(i,:).*A_r);
   MT2pore(i)=trapz(x,Epsi_p(i,:).*RhoTar2(i,:).*A_r);
   MTpore(i)=MT1pore(i)+MT2pore(i);
   %Volatiles realease rates at the particle surface
   dMVol_dt(i)=4*pi()*(dp/2)^2*(Epsi_p(i,Nx).*U_Vol(i,Nx).*RhoVol(i,Nx));
   dMVap_dt(i)=4*pi()*(dp/2)^2*(Epsi_p(i,Nx).*U_Vol(i,Nx).*RhoVap(i,Nx));
   dMGas1_dt(i)=4*pi()*(dp/2)^2*(Epsi_p(i,Nx).*U_Vol(i,Nx).*RhoGas1(i,Nx));
   dMGas2_dt(i)=4*pi()*(dp/2)^2*(Epsi_p(i,Nx).*U_Vol(i,Nx).*RhoGas2(i,Nx));
   dMTar1_dt(i)=4*pi()*(dp/2)^2*(Epsi_p(i,Nx).*U_Vol(i,Nx).*RhoTar1(i,Nx));
   dMTar2_dt(i)=4*pi()*(dp/2)^2*(Epsi_p(i,Nx).*U_Vol(i,Nx).*RhoTar2(i,Nx));
   dMN2_dt(i)=4*pi()*(dp/2)^2*(Epsi_p(i,Nx).*U_Vol(i,Nx).*RhoN2(i,Nx));
   %Cumulative volatile released from particle surface
   MVol(i)=trapz(t(1:i),dMVol_dt(1:i));
   MVap(i)=trapz(t(1:i),dMVap_dt(1:i));
   MGas1(i)=trapz(t(1:i),dMGas1_dt(1:i));
   MGas2(i)=trapz(t(1:i),dMGas2_dt(1:i));
   MGas(i)=MGas1(i)+MGas2(i);
   MTar1(i)=trapz(t(1:i),dMTar1_dt(1:i));
   MTar2(i)=trapz(t(1:i),dMTar2_dt(1:i));
   MTar(i)=MTar1(i)+MTar2(i);
   MN2(i)=trapz(t(1:i),dMN2_dt(1:i));
end

figure
plot(t,MP/MP0)
hold on
plot(t,(MBio+MChar+MMoist+MVpore+MG1pore+MG2pore+MT1pore+MT2pore)/MP0,'--m')
hold on
plot(t,MChar/MP0,'k')
hold on
plot(t,MVap/MP0)
```

```
hold on
plot(t,MTar/MP0,'r')
hold on
plot(t,MGas/MP0,'g')
hold on
plot(t,MVol/MP0,'m')    %Vol=Gas+Tar+Vap
hold on
plot(t,(ones(Nt,1)*MP0-MP)/MP0,'.m')
hold on
plot(t,(MP+MVol)/MP0,'.b')

%*******3D plots*************************************************************
figure
subplot(1,2,1)
surf(x/(dp/2),t,T-273.15)
az = 85;
el = 15;
view(az, el);
xlabel('r/Rp')
ylabel('Time (sec)')
zlabel('Particle Temperature (^oC)')

subplot(1,2,2)
surf(x/(dp/2),t,XBio)
az = 85;
el = 15;
view(az, el);
xlabel('r/Rp')
ylabel('Time (sec)')
zlabel('Particle Conversion')


figure
subplot(1,2,1)
surf(x/(dp/2),t,Rhop)
az = 100;
el = 15;
view(az, el);
xlabel('r/Rp')
ylabel('Time (sec)')
zlabel('Particle Density (kg/m^3)')

subplot(1,2,2)
surf(x/(dp/2),t,RhoVol)
```

```
az = 100;
el = 15;
view(az, el);
xlabel('r/Rp')
ylabel('Time (sec)')
zlabel('Volatiles Density (kg/m^3)')

figure
surf(x/(dp/2),t,Epsi_p)
az = 100;
el = 30;
view(az, el);
xlabel('Time (sec)')
ylabel('r/Rp')
zlabel('Particle Voidage')

end             %function "PCM_Pyrolysis"

function [c,f,s]=pdex1pde(x,t,u,DuDx)
global Rho_Bio0 Rho_M0 Rho_Cf Epsi_Bio0 Epsi_Char Betta_Bio0 Betta_Char R sigma_rad
k_Bio0 k_Char dpore_Char dpore_Bio0 k_Vol Emissivity_Char Emissivity_Bio0 epsi_rad Betta
keff MW_Gas MW_Tar MW_N2 MW_Vap DH_rxn1 DH_rxn2 DH_rxn3 DH_rxn4 DH_rxn5
DH_vap Taw Dmix k01 k02 k03 k04 k05 k0vap E1 E2 E3 E4 E5 Evap alpha
 %   Biomass--k1-->Gas1
%   Biomass--k2-->Tar1
%   Biomass--k3-->Char
%   Tar1--k4-->(1-alpha)Gas2+(alpha)Tar2
%   Tar1--k5-->Char
%   Moisture--kvap-->Vapour

Rho_Bio=u(1);
Rho_Char=u(2);
Rho_M=u(3);      %Moisture
Rho_Vap=u(4);    %Vapour
Rho_Gas1=u(5);   %Gas1
Rho_Gas2=u(6);   %Gas2
Rho_Tar1=u(7);   %bio-oil (includes pyrolytic water)
Rho_Tar2=u(8);
Rho_N2=u(9);
T=u(10);
P=u(11);
U_Vol=u(12);

dRhoVol_dr=0;
```

```
Rho_Vol=0;
for i=4:9
   Rho_Vol=Rho_Vol+u(i);
   dRhoVol_dr=dRhoVol_dr+DuDx(i);
end
MW_mix=Rho_Vol/((Rho_Gas1+Rho_Gas2)/MW_Gas+(Rho_Tar1+Rho_Tar2)/MW_Tar+Rho_N2/MW
_N2+Rho_Vap/MW_Vap);

Mu_Gas=7.85*10^-6+3.18*10^-8*T;          %Vicosity (kg/m.s)
Mu_Tar=-3.73*10^-7+2.62*10^-8*T;
Mu_N2=-1.47*10^-6+3.78*10^-8*T;
Mu_Vap=9.12*10^-6+3.27*10^-8*T;
Mu_mix=(Rho_Gas1+Rho_Gas2)/Rho_Vol*Mu_Gas+(Rho_Tar1+Rho_Tar2)/Rho_Vol*Mu_Tar+Rho_
N2/Rho_Vol*Mu_N2+Rho_Vap/Rho_Vol*Mu_Vap;   %kg/m.s

Cp_Bio0=1500+T;                    %Heat capacity (J/kg.K)  (spruce)
Cp_Bio0=-91.2+4.4*T;                %J/kg.K  (pine)
Cp_Char=420+2.09*T-6.85*10^-4*T^2;       %J/kg.K
Cp_M=4180;                         %J/kg.K
Cp_Gas=770+0.629*T-1.91*10^-4*T^2;       %J/kg.K
Cp_Tar=-100+4.4*T-1.57*10^-3*T^2;        %J/kg.K
Cp_Vap=1670+0.64*T;                 %J/kg.K
Cp_N2=950+0.188*T;                  %J/kg.K

X_Bio=((Rho_Bio0+Rho_M0)-(Rho_Bio+Rho_M+Rho_Char))/((Rho_Bio0+Rho_M0)-Rho_Cf);
X_B=(Rho_Bio0-(Rho_Bio+Rho_Char))/(Rho_Bio0-Rho_Cf);
Epsi_p=Epsi_Bio0+X_B*(Epsi_Char-Epsi_Bio0);
d_pore=dpore_Bio0+X_B*(dpore_Char-dpore_Bio0);
Betta=Betta_Bio0+X_B*(Betta_Char-Betta_Bio0);
epsi_rad=Emissivity_Bio0+X_B*(Emissivity_Char-Emissivity_Bio0);
ks=k_Bio0+X_B*(k_Char-k_Bio0);
kcond=ks+Epsi_p*k_Vol;
krad=4*epsi_rad*Epsi_p*sigma_rad*T^3*d_pore/(1-Epsi_p);
keff=kcond+krad;         %W/m.K
Deff=Epsi_p*Dmix/Taw;

k1=k01*exp(-E1/R/T);   %1/s
k2=k02*exp(-E2/R/T);
k3=k03*exp(-E3/R/T);
k4=k04*exp(-E4/R/T);
k5=k05*exp(-E5/R/T);
kvap=k0vap*exp(-Evap/R/T);
```

```
dEpsi_p_dt=(Epsi_Char-Epsi_Bio0)/(Rho_Bio0+Rho_M0-
Rho_Cf)*((k1+k2+k3)*Rho_Bio+kvap*Rho_M-k3*Rho_Bio-k5*Epsi_p*Rho_Tar1);
c=[1;1;1;Epsi_p;Epsi_p;Epsi_p;Epsi_p;Epsi_p;Epsi_p;(Rho_Bio*Cp_Bio0+Rho_Char*Cp_Char+Rho_M
*Cp_M+Epsi_p*((Rho_Gas1+Rho_Gas2)*Cp_Gas+(Rho_Tar1+Rho_Tar2)*Cp_Tar+Rho_N2*Cp_N2+
Rho_Vap*Cp_Vap));Epsi_p/T;0];

f=[0;
  0;
  0;
  Epsi_p*Deff*DuDx(4)-Epsi_p*Rho_Vap*U_Vol;
  Epsi_p*Deff*DuDx(5)-Epsi_p*Rho_Gas1*U_Vol;
  Epsi_p*Deff*DuDx(6)-Epsi_p*Rho_Gas2*U_Vol;
  Epsi_p*Deff*DuDx(7)-Epsi_p*Rho_Tar1*U_Vol;
  Epsi_p*Deff*DuDx(8)-Epsi_p*Rho_Tar2*U_Vol;
  Epsi_p*Deff*DuDx(9)-Epsi_p*Rho_N2*U_Vol;
  keff*DuDx(10)-
Epsi_p*U_Vol*((Rho_Gas1+Rho_Gas2)*Cp_Gas+(Rho_Tar1+Rho_Tar2)*Cp_Tar+Rho_N2*Cp_N2+R
ho_Vap*Cp_Vap)*T;
  -Epsi_p*U_Vol*P/T;
  0];

s=[-(k1+k2+k3)*Rho_Bio;
  +k3*Rho_Bio+k5*(Epsi_p*Rho_Tar1);
  -kvap*Rho_M;
  +kvap*Rho_M-(Rho_Vap*dEpsi_p_dt);
  +k1*Rho_Bio-(Rho_Gas1*dEpsi_p_dt);
  +(1-alpha)*k4*(Epsi_p*Rho_Tar1)-(Rho_Gas2*dEpsi_p_dt);
  +k2*Rho_Bio-k4*(Epsi_p*Rho_Tar1)-k5*(Epsi_p*Rho_Tar1)-(Rho_Tar1*dEpsi_p_dt);
  +alpha*k4*(Epsi_p*Rho_Tar1)-(Rho_Tar2*dEpsi_p_dt);
  0-Rho_N2*dEpsi_p_dt;
  -((k1*DH_rxn1+k2*DH_rxn2+k3*DH_rxn3)*Rho_Bio+k4*(Epsi_p*Rho_Tar1)*DH_rxn4+...
  k5*(Epsi_p*Rho_Tar1)*DH_rxn5+kvap*Rho_M*DH_vap);
  (R/MW_mix*1000)*((k1+k2)*Rho_Bio-k5*(Epsi_p*Rho_Tar1)+kvap*Rho_M)-(P/T)*dEpsi_p_dt;
  -(Mu_mix/Betta*U_Vol+R/MW_mix*1000*(T*dRhoVol_dr+DuDx(10)*Rho_Vol))];

      % Last line of s is the expansion of -(Mu_mix/Betta*U_Vol+DuDx(11))=0
end                %function "pdex1pde"

function u0=pdex1ic(x)
global R  Rho_Bio0  Rho_M0

T0=25+273.15;
P0=1.01325*10^5;
Rho_N2=P0*28/(R*T0)/1000;        %kg/m3
```

```
u0=[Rho_Bio0;0;Rho_M0;0;0;0;0;0;Rho_N2;T0;P0;0];

end      %function pdex1ic

function [pl,ql,pr,qr]=pdex1bc(xl,ul,xr,ur,t)
global Rho_Bio0 Ug Rho_Cf Epsi_Char Epsi_Bio0 epsi_rad sigma_rad Tgas Pgas Dmix Taw
Rhog dp Rep k_Vol Tw R

qfu=0;
Cp_N2=950+0.188*Tgas;                %J/kg.K
Mu_N2=-1.47*10^-6+3.78*10^-8*Tgas;
Rhog=Pgas*28/(R*Tgas)/1000;          %kg/m3
Rep=Rhog*Ug*dp/Mu_N2;
Pr=Mu_N2*Cp_N2/k_Vol;
hconv=k_Vol/dp*(2+0.6*Rep^(1/2)*Pr^(1/3));   %W/m2.K
X_B=(Rho_Bio0-(ur(1)+ur(2)))/(Rho_Bio0-Rho_Cf);
Epsi_pr=Epsi_Bio0+X_B*(Epsi_Char-Epsi_Bio0);
Deff=Epsi_pr*Dmix/Taw;
Sc=Mu_N2/Rhog./Deff;
hmass=Deff./dp.*(2+0.6*Rep.^(1/2).*Sc.^(1/3));    %m/s

pl=[0;0;0;0;0;0;0;0;0;0;0;0];
ql=[1;1;1;1;1;1;1;1;1;1;1;1];
pr=[0;0;0;-Epsi_pr*hmass*(0-ur(4));-Epsi_pr*hmass*(0-ur(5));-Epsi_pr*hmass*(0-ur(6));-
Epsi_pr*hmass*(0-ur(7));-Epsi_pr*hmass*(0-ur(8));-Epsi_pr*hmass*(Rhog-ur(9));-hconv*(Tgas-ur(10))-
sigma_rad*epsi_rad*(Tw^4-ur(10)^4)-qfu;ur(11)-Pgas;ur(12)-hmass];
qr=[1;1;1;1;1;1;1;1;0;1;0;0];

end       %function "pdex1bc"
```

Appendix C MATLAB code for coupled particle and reactor model of biomass pyrolysis

In Appendix C, the comprehensive single particle model of biomass drying and pyrolysis from the previous chapter is coupled with an ideal reactor model for a bubbling fluidized bed, with nitrogen as the fluidizing agent. The resulting predictive model provides a useful tool to relate biomass pyrolysis products yield and composition to process operating parameters (e.g. biomass ultimate analysis, reactor temperature, gas residence time, mean solids residence time, biomass particle size and moisture content). The model predicts the composition of major compounds in pyrolysis gas, based on simplifying assumptions and CHO elemental balances.

```
function Coupled_particle_reactor_model
clear all
global Tgas Pgas R m_N2 A dp dp_sand Rho_sand Y_V Y_G1 Y_G2 Y_T1 Y_T2 m_Bin
m_Min L_bed g Epsi_mf yH2O MW_Gas MW_Tar MW_N2 MW_Vap

clc
g=9.81;
R=8.314;
ID=0.1;                          %BFB inside diameter (m)
A=pi()*ID^2/4;                   %Reactor cross-section
Rho_sand=2600;                   %Sand particle density (kg/m3)
dp_sand=250*10^-6;               %Sand particle size (m)
sphericity=0.95;                 %Sand particle sphericity
Epsi_mf=(14*sphericity)^(-1/3);  %Voidage at minimum fluidization
m_N2=1/3600;                     % N2 mass flowrate (kg/s)
m_Bin=1/3600;                    % Biomass feeding rate (kg/s)
m_Min=10/(100-10)*m_Bin;         %Moisture content=10 wt% on "as-received" basis

%Biomass ultimate analysis(daf): Pine from Westerhof [100]
wC_B=46.58/100;
wH_B=6.34/100;
wO_B=46.98/100+0.1/100;
wN_B=0;
wS_B=0;

dp=1000*10^-6;                   %Initial biomass particle diameter (m)
Pgas=1.01325*10^5;               %Reactor pressure (Pa)
Tgas=650+273.15;                 %Reactor temperature (K)
%*************************************************************************
% For certain process operating conditions such as reactor temperature and pressure, biomass particle size
and moisture content, etc. , the single particle model developed in script "PCM_Pyrolysis" is first run and
then coupled with the ideal reactor model of BFB as follows:

Taw_S=25*60;                     %Mean solids residence time(s) from Westerhof [100]
```

```
E_t=1/Taw_S.*exp(-t'./Taw_S);          %RTD for perfectly-mixed solids
 %Yields of species inside average particle leaving the reactor
Y_B=(trapz(t,MBio.*E_t)+MBio(end)*exp(-tend/Taw_S))/MP0;
Y_M=(trapz(t,MMoist.*E_t)+MMoist(end)*exp(-tend/Taw_S))/MP0;
Y_C=(trapz(t,MChar.*E_t)+MChar(end)*exp(-tend/Taw_S))/MP0;
Y_Vpore=(trapz(t,MVpore.*E_t)+MVpore(end)*exp(-tend/Taw_S))/MP0;
Y_G1pore=(trapz(t,MG1pore.*E_t)+MG1pore(end)*exp(-tend/Taw_S))/MP0;
Y_G2pore=(trapz(t,MG2pore.*E_t)+MG2pore(end)*exp(-tend/Taw_S))/MP0;
Y_T1pore=(trapz(t,MT1pore.*E_t)+MT1pore(end)*exp(-tend/Taw_S))/MP0;
Y_T2pore=(trapz(t,MT2pore.*E_t)+MT2pore(end)*exp(-tend/Taw_S))/MP0;
Y_P=Y_B+Y_M+Y_C+Y_Vpore+Y_G1pore+Y_G2pore+Y_T1pore+Y_T2pore;
%Yields of volatiles released from average particle surface inside the reactor
Y_V=(trapz(t,MVap.*E_t)+MVap(end)*exp(-tend/Taw_S))/MP0;
Y_G1=(trapz(t,MGas1.*E_t)+MGas1(end)*exp(-tend/Taw_S))/MP0;    %dry gas
Y_G2=(trapz(t,MGas2.*E_t)+MGas2(end)*exp(-tend/Taw_S))/MP0;
Y_G=Y_G1+Y_G2;
Y_T1=(trapz(t,MTar1.*E_t)+MTar1(end)*exp(-tend/Taw_S))/MP0;   %includes pyrolytic water
Y_T2=(trapz(t,MTar2.*E_t)+MTar2(end)*exp(-tend/Taw_S))/MP0;
Y_T=Y_T1+Y_T2;
%Elemental balances on average particle inside the reactor
%Mositure/vapor
wC_H2O=0;
wH_H2O=2/18;
wO_H2O=16/18;
%Char=CH0.2526O0.0236
wH_C=0.2526/(12+0.2526+0.0236*16);
wC_C=12/(12+0.2526+0.0236*16);
wO_C=0.0236*16/(12+0.2526+0.0236*16);
%Tar elemental composition from Neves et al.
wC_Tdry=1.14*wC_B;
wH_Tdry=1.13*wH_B;
wO_Tdry=1-(wC_Tdry+wH_Tdry);
 %Finding average gas composition released from the average particle surface
N=0;     %Counter of acceptable answers
for i=1:10001
   wH_T(i)=0.0001*(i-1);
   wC_T(i)=wC_Tdry+(wC_H2O-wC_Tdry)*(wH_T(i)-wH_Tdry)/(wH_H2O-wH_Tdry);
   wO_T(i)=wO_Tdry+(wO_H2O-wO_Tdry)*(wH_T(i)-wH_Tdry)/(wH_H2O-wH_Tdry);
   %Pyrolytic water yield
   yH2O(i)=(wC_T(i)-wC_Tdry)/(wC_H2O-wC_Tdry)*Y_T;
   %Elemental balances on average particle surface
   wC_g(i)=((MBio0/MP0-Y_B)*wC_B+(MMoist0/MP0-Y_M-Y_V)*wC_H2O-Y_C*wC_C-
        Y_T*wC_T(i))/Y_G;
```

```
   wH_g(i)=((MBio0/MP0-Y_B)*wH_B+(MMoist0/MP0-Y_M-Y_V)*wH_H2O-Y_C*wH_C-
       Y_T*wH_T(i))/Y_G;
   wO_g(i)=((MBio0/MP0-Y_B)*wO_B+(MMoist0/MP0-Y_M-Y_V)*wO_H2O-Y_C*wO_C-
       Y_T*wO_T(i))/Y_G;
   %Assuming non-condensable gas is only composed of CO, CO2 and CH4
   AA=[12/28,12/44,12/16;0,0,4/16;16/28,32/44,0];
   BB=[wC_g(i);wH_g(i);wO_g(i)];
   CC=AA\BB;
   wCO_g(i)=CC(1);
   wCO2_g(i)=CC(2);
   wCH4_g(i)=CC(3);
   %Saving all acceptable answers
   if and(yH2O(i)>=0,yH2O(i)<=1)
      if and(wC_T(i)>=0,wC_T(i)<=1)
         if and(wO_T(i)>=0,wO_T(i)<=1)
            if and(wCO_g(i)>=0,wCO_g(i)<=1)
               if and(wCO2_g(i)>=0,wCO2_g(i)<=1)
                  if and(wCH4_g(i)>=0,wCH4_g(i)<=1)
                     if and(wH_g(i)>=0,wH_g(i)<=1)
                        if and(wC_g(i)>=0,wC_g(i)<=1)
                           if and(wO_g(i)>=0,wO_g(i)<=1)
                              N=N+1;
                              wH_TAR(N,1)=wH_T(i);
                              wC_TAR(N,1)=wC_T(i);
                              wO_TAR(N,1)=wO_T(i);
                              YH2O(N,1)=yH2O(i);
                              wC_GAS(N,1)=wC_g(i);
                              wH_GAS(N,1)=wH_g(i);
                              wO_GAS(N,1)=wO_g(i);
                              wCO_GAS(N,1)=wCO_g(i);
                              wCO2_GAS(N,1)=wCO2_g(i);
                              wCH4_GAS(N,1)=wCH4_g(i);
                           end
                        end
                     end
                  end
               end
            end
         end
      end
   end
end

wH_Gmean=mean(nonzeros(wH_GAS(:)));
```

```
wC_Gmean=mean(nonzeros(wC_GAS(:)));
wO_Gmean=mean(nonzeros(wO_GAS(:)));

AA=[12/28,12/44,12/16;0,0,4/16;16/28,32/44,0];
BB=[wC_Gmean;wH_Gmean;wO_Gmean];
CC=AA\BB;
wCO_Gmean=CC(1);
wCO2_Gmean=CC(2);
wCH4_Gmean=CC(3);

wH_Oilmean=mean(nonzeros(wH_TAR(:)));
wC_Oilmean=mean(nonzeros(wC_TAR(:)));
wO_Oilmean=mean(nonzeros(wO_TAR(:)));
YH2Omean=mean(nonzeros(YH2O(:)));

%Reactor model: Perfectly-mixed solids and plug flow of gases
M=20;                          % Number of cells along the dense bed height
U=zeros(1,M+1);                % Superficial gas velocity
Epsi=zeros(1,M+1);             % Voidage
db=zeros(1,M+1);               % Bubble diameter
L_bed=0.25;                    % Dense bed height from Westerhof [100]

zspan=linspace(0,L_bed,M+1);
[z,Sol]=ode45('dM_dz',zspan,[0 0 0 0 0]);
m_Vap=Sol(:,1);                % Mass flow rate of vapour (excludes pyrolytic water)
m_Gas1=Sol(:,2);               % Mass flow rate of dry primary gas
m_Gas2=Sol(:,3);               % Mass flow rate of dry secondary gas
m_Tar1=Sol(:,4);               % Mass flow rate of primary tar (includes pyrolytic water)
m_Tar2=Sol(:,5);               % Mass flow rate of primary tar
m_gas=m_N2+m_Vap+m_Gas1+m_Gas2+m_Tar1+m_Tar2;

for J=1:M+1
    U(J)=(R*Tgas/Pgas/A)*(m_N2/MW_N2+m_Vap(J)/MW_Vap+(m_Gas1(J)+m_Gas2(J))/MW_Gas+(
    m_Tar1(J)+m_Tar2(J))/MW_Tar)*1000;    %m/s

    MWgas=(m_N2+m_Vap(J)+m_Gas1(J)+m_Gas2(J)+m_Tar1(J)+m_Tar2(J))/...
    (m_N2/MW_N2+m_Vap(J)/MW_Vap+(m_Gas1(J)+m_Gas2(J))/MW_Gas+(m_Tar1(J)+m_Tar2(J))/
    MW_Tar);

    Rhogas=Pgas*MWgas/(R*Tgas)/1000;          %Gas mixture density (kg/m^3)
    %Assuming released volatiles are at the reactor temperature
    Mu_Gas=7.85*10^-6+3.18*10^-8*Tgas;        %Viscosity (kg/m.s)
    Mu_Tar=-3.73*10^-7+2.62*10^-8*Tgas;
    Mu_N2=-1.47*10^-6+3.78*10^-8*Tgas;
```

```
    Mu_Vap=9.12*10^-6+3.27*10^-8*Tgas;
    Mu_mix=(m_Gas1(J)+m_Gas2(J))/m_gas(J)*Mu_Gas+(m_Tar1(J)+m_Tar2(J))/...
    m_gas(J)*Mu_Tar+m_N2/m_gas(J)*Mu_N2+m_Vap(J)/m_gas(J)*Mu_Vap;   %kg/m.s

    Ar=g*Rhogas*(Rho_sand-Rhogas)*dp_sand^3/Mu_mix^2;
    Umf=Mu_mix/Rhogas/dp_sand*(sqrt(27.2^2+0.0408*Ar)-27.2);

    Nor=72;           %Number of holes in distributor
    db(J)=0.54*g^(-0.2)*(U(J)-Umf)^0.4*(z(J)+4*sqrt(A/Nor))^0.8;
    Epsi(J)=1-(1-Epsi_mf)/(1+(U(J)-Umf)/(0.711*sqrt(g*db(J))));
end
Epsi_ave=trapz(z,Epsi)/L_bed;
Y_Tout=(m_Tar1(M+1)+m_Tar2(M+1))/(m_Bin+m_Min);
Y_Gout=(m_Gas1(M+1)+m_Gas2(M+1))/(m_Bin+m_Min);

 %Elemental balance over entire reactor
%Secondary gas composition from Boroson et al.
wCO_G2=0.5633/0.78;
wCO2_G2=0.1109/0.78;
wCH4_G2=0.0884/0.78;
wH2_G2=0.0173/0.78;

wC_G2=12/28*wCO_G2+12/44*wCO2_G2+12/16*wCH4_G2;
wH_G2=wH2_G2+4/16*wCH4_G2;
wO_G2=16/28*wCO_G2+32/44*wCO2_G2;
%Bio-oil (tar) elemental composition at the reactor exit
wH_OR=(Y_T*wH_Oilmean-(Y_T-Y_Tout)*wH_G2)/Y_Tout;
wC_OR=(Y_T*wC_Oilmean-(Y_T-Y_Tout)*wC_G2)/Y_Tout;
wO_OR=(Y_T*wO_Oilmean-(Y_T-Y_Tout)*wO_G2)/Y_Tout;
%Dry gas elemental composition at the reactor exit
wH_GR=((Y_Gout-Y_G)*wH_G2+Y_G*wH_Gmean)/Y_Gout;
wC_GR=((Y_Gout-Y_G)*wC_G2+Y_G*wC_Gmean)/Y_Gout;
wO_GR=((Y_Gout-Y_G)*wO_G2+Y_G*wO_Gmean)/Y_Gout;

wH2_GR=(Y_Gout-Y_G)*wH2_G2/Y_Gout;
%Composition of dry gas at the reactor exit
AA=[12/28,12/44,12/16;0,0,4/16;16/28,32/44,0];
BB=[wC_GR;wH_GR-wH2_GR;wO_GR];
CC=AA\BB;
wCO_GR=CC(1);
wCO2_GR=CC(2);
wCH4_GR=CC(3);

end         %function "Coupled_particle_reactor_model"
```

```
function Vdot=dM_dz(z,V)
global m_Bin m_Min L_bed m_N2 Y_V Y_G1 Y_G2 Y_T1 Y_T2 MW_Gas MW_Tar MW_N2
MW_Vap dp_sand Rho_sand Pgas Tgas R A Umf Epsi_mf g k04 E4

mdot_Vap=V(1);
mdot_Gas1=V(2);
mdot_Gas2=V(3);
mdot_Tar1=V(4);
mdot_Tar2=V(5);

mdot_gas=m_N2+mdot_Vap+mdot_Gas1+mdot_Gas2+mdot_Tar1+mdot_Tar2;

U=(R*Tgas/Pgas/A)*(m_N2/MW_N2+mdot_Vap/MW_Vap+(mdot_Gas1+mdot_Gas2)/MW_Gas+(mdo
t_Tar1+mdot_Tar2)/MW_Tar)*1000;    %m/s

MW_mix=(m_N2+mdot_Vap+mdot_Gas1+mdot_Gas2+mdot_Tar1+mdot_Tar2)/...
(m_N2/MW_N2+mdot_Vap/MW_Vap+(mdot_Gas1+mdot_Gas2)/MW_Gas+(mdot_Tar1+mdot_Tar2)/
MW_Tar);

Rhogas=Pgas*MW_mix/(R*Tgas)/1000;                    %Mixture density (kg/m3)
%Assuming released volatiles are at the reactor temperature
Mu_Gas=7.85*10^-6+3.18*10^-8*Tgas;                   %Viscosity of non-condensable gas (kg/m.s)
Mu_Tar=-3.73*10^-7+2.62*10^-8*Tgas;
Mu_N2=-1.47*10^-6+3.78*10^-8*Tgas;
Mu_Vap=9.12*10^-6+3.27*10^-8*Tgas;
Mu_mix=(mdot_Gas1+mdot_Gas2)/mdot_gas*Mu_Gas+(mdot_Tar1+mdot_Tar2)/mdot_gas*Mu_Tar+m
_N2/mdot_gas*Mu_N2+mdot_Vap/mdot_gas*Mu_Vap;   %kg/m.s

Ar=g*Rhogas*(Rho_sand-Rhogas)*dp_sand^3/Mu_mix^2;
Umf=Mu_mix/Rhogas/dp_sand*(sqrt(27.2^2+0.0408*Ar)-27.2);
Nor=72;
db=0.54*g^(-0.2)*(U-Umf)^0.4*(z+4*sqrt(A/Nor))^0.8;
Epsi=1-(1-Epsi_mf)/(1+(U-Umf)/(0.711*sqrt(g*db)));

k4=k04*exp(-E4/R/Tgas);   %Bio-oil cracking
%Water vapour and volatiles released from the average particle to the  reactor are uniformly distributed
Vdot(1)=Y_V*(m_Bin+m_Min)/L_bed;
Vdot(2)=Y_G1*(m_Bin+m_Min)/L_bed;
Vdot(3)=Y_G2*(m_Bin+m_Min)/L_bed+k4*mdot_Tar1*(Epsi/U);
Vdot(4)=Y_T1*(m_Bin+m_Min)/L_bed-k4*mdot_Tar1*(Epsi/U);
Vdot(5)=Y_T2*(m_Bin+m_Min)/L_bed;
Vdot=Vdot';
end                %function "dM_dz
```

Appendix D Algorithm for simulation of dual fluidized bed biomass gasifier

D.1 Algorithm for simulation of BFB gasifier

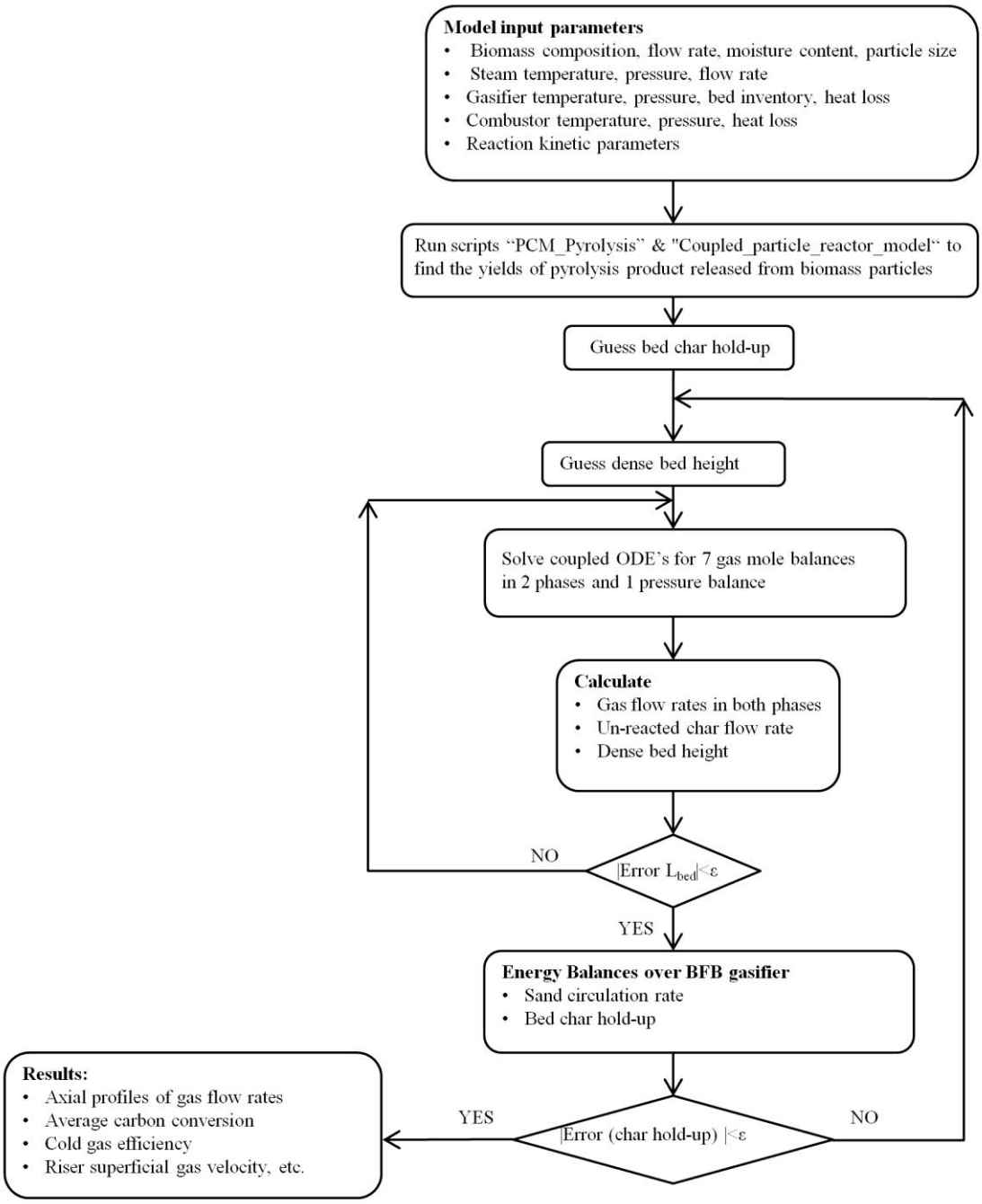

D.2 Algorithm for simulation of CFB combustor

This algorithm is an iterative one. As an initial guess, complete char combustion is assumed in the riser to estimate U and G_s from energy balance calculations (see section 5.5). After determining the combustor flow regime, the combustor kinetic model is solved for carbon conversion in the combustor. Finally, the unreacted char leaving the combustor is updated in the energy balance calculations until convergence is achieved.

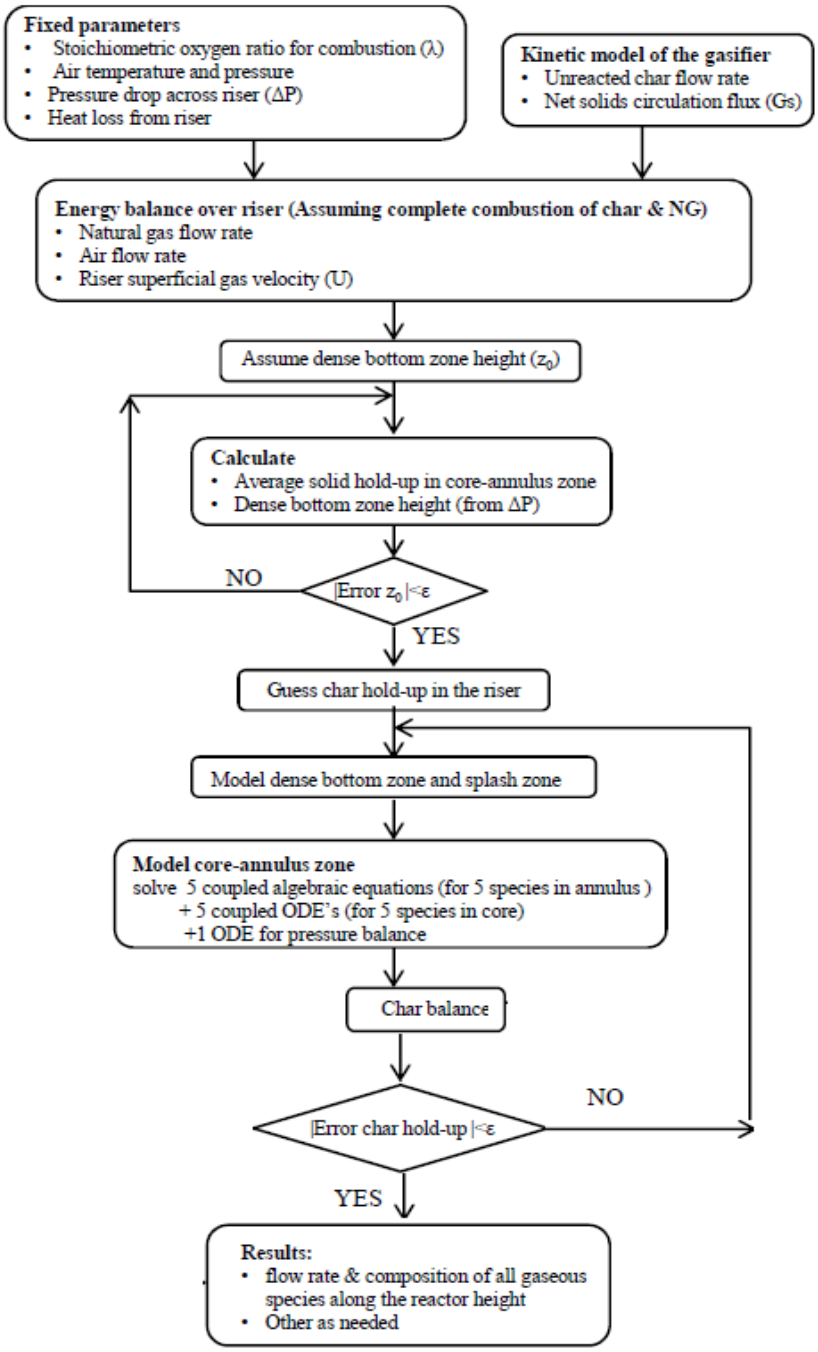

Appendix E Thermodynamic calculations

To describe the thermodynamic states of the streams involved in the process, the total enthalpy for four different classes of substances are calculated as follows:

I. **Ideal gases**: The gasifier product gas (except for steam), combustor flue gas and the air stream are all assumed to be ideal gas mixtures, with enthalpies independent of pressure and calculated as linear combinations of the component molar enthalpies, i.e.

$$H_{ig}^{*}(T) = \sum_{i} y_i H_i^{*}(T) \tag{E.1}$$

where the total enthalpy of a single species is calculated from:

$$H_i^{*}(T) = \Delta H_{f,298,i}^{0} + \int_{298.15\,K}^{T} C_{P,i}(T).dT \tag{E.2}$$

with $C_{P,i}(T)$, described by a 5-coefficient polynomial [165]:

$$\frac{C_{P,i}(T)}{R} = a_{1,i} + a_{2,i}.T + a_{3,i}.T^2 + a_{4,i}.T^3 + a_{5,i}.T^4 \tag{E.3}$$

which after incorporation in the integral of equation (E.2) gives:

$$\frac{H_i^{*}(T)}{R.T} = a_{1,i} + \frac{a_{2,i}}{2}.T + \frac{a_{3,i}}{3}.T^2 + \frac{a_{4,i}}{4}.T^3 + \frac{a_{5,i}}{5}.T^4 + \frac{a_{6,i}}{T} \tag{E.4}$$

With known $\Delta H_{f,298,i}^{0}$ at standard temperature, the integration constants $a_{6,i}$ are determined. For the gas components of interest, two sets of coefficients $a_{1,i}$,…, $a_{6,i}$ are reported in Table E.1 for low (≤1000 K) and high (≥1000 K) temperature ranges. The molecular weights, heats of formation and lower heating values of gaseous species are included in Table E.2.

II. **Inorganic solids:** Inorganic solids (silica sand, limestone, etc.) are also treated as physical mixtures of chemically defined species. The mass specific total enthalpies of solid mixtures are obtained from:

$$H^*_{solid}(T) = \sum_i w_i \frac{H^*_i(T)}{M_i} \tag{E.5}$$

where w_i and M_i are the weight fraction and molecular weight, respectively, of species i in a mixture. The temperature dependency of a single species enthalpy is formulated in the same way as in equations (E.2) to (E.4) for ideal gases. Two sets of coefficients for two ranges of temperatures for different inorganic solid species are reported in Table E.3 according to NASA polynomials. The molecular weights and standard heats of formation of these solids are also listed in Table E.4.

III. **Organic substances:** Organic components like biomass, char, tar, etc. are not clearly defined on a molecular basis. Their descriptions are therefore based on ultimate analyses. For mass specific total enthalpy:

$$H^*_{org}(T) = \Delta H^0_{f,298} + \int_{298.15\,K}^{T} C_P(T).dT \tag{E.6}$$

where the enthalpies of formation of solid and liquid organic fuels are calculated based on their Lower Heating Values (LHV_{fuel}) and elementary composition:

$$\Delta H^0_{f,298} = LHV + \frac{w_C}{M_C}.\Delta H^0_{f,298,CO_2} + \frac{w_H}{2.M_H}.\Delta H^0_{f,298,H_2O_{(g)}} + \frac{w_S}{M_S}.\Delta H^0_{f,298,SO_2} \tag{E.7}$$

The empirical correlation of Boie [164] is applied to calculate LHV_{fuel} (in kJ/kg):

$$LHV_{fuel} = 34835.w_C + 93870.w_H - 10800.w_O + 6280.w_N + 10465.w_S \tag{E.8}$$

where M_C, M_H and M_S are atomic weights, and w_C, w_H, w_O, w_N and w_S denote mass fractions of respective elements, measured by ultimate analysis on a moisture-free, ash-free basis. To calculate the specific heat capacity for an organic substance, a simple two-constant linear correlation was applied by Pröll *et al.* [164]:

$$C_P(T) = k.T + d \tag{E.9}$$

where k and d are empirical constants. Note that in this study biomass is assumed to be introduced to the system at 25°C and therefore equation (E.9) is not used. For char, the empirical correlation of Merrick [166] is applied to calculate the enthalpy and heat capacity as functions of temperature:

$$C_p(T) = \frac{R}{M_{waf}} \cdot \left\{ \exp\left(\frac{380}{T}\right) \cdot \left[\frac{\exp\left(\frac{380}{T}\right) - 1}{\frac{380}{T}} \right]^{-2} + 2 \cdot \exp\left(\frac{1800}{T}\right) \cdot \left[\frac{\exp\left(\frac{1800}{T}\right) - 1}{\frac{1800}{T}} \right]^{-2} \right\} \quad \text{(E.10)}$$

$$h(T) = \frac{R}{M_{waf}} \cdot \left[\frac{380}{\exp\left(\frac{380}{T}\right) - 1} + \frac{21800}{\exp\left(\frac{1800}{T}\right) - 1} \right] \quad \text{(E.11)}$$

where R is the ideal gas constant, and M_{waf} represents the mean atomic mass of the char from its elementary analysis:

$$M_{waf} = \left[\sum_i \left(\frac{w_i}{M_i} \right) \right]^{-1} \quad \text{(E.12)}$$

The total enthalpy is estimated as:

$$H^*_{char}(T) = \Delta H^0_{f,298} + h(T) - h(298.15) \quad \text{(E.13)}$$

where the enthalpy of formation follows again from the LHV and ultimate analysis of char (assumed here to be pure carbon).

IV. **Pure water/steam:** The water/steam thermodynamic properties are based on the "IAPWS Industrial Formulation 1997 for the Thermodynamic Properties of Water and Steam", recommended for industrial use [167]. To be consistent with the other species above, the total enthalpy of water/steam is calculated as:

$$H^*_{H2O}(P,T) = \frac{\Delta H^0_{f,298,H_2O_{(l)}}}{M_{H_2O}} + \left[H_{IAPWS}(P,T) - H_{IAPWS,0} \right] \quad \text{(E.14)}$$

where $\Delta H^0_{f,298,H_2O_{(l)}} = -285.83\,kJ/mol$ [168], and $H_{IAPWS,0}=104.928\ kJ/kg$ is the enthalpy of water at standard conditions, $P_0=1\ bar$, $T_0=298.15\ K$.

The entire range of validity for IAPWS-IF97 is divided into five regions as shown in Fig. E.1. Since we are dealing with fuel moisture content (stable single-phase liquid, Region 1) and superheated steam (stable single-phase vapor, Region 2), the formulations for calculating $H_{IAPWS}\ (P,T)$ for these two regions are summarized in Table E.5.

Table E.1 Coefficients for calculation of isobaric heat capacity of ideal gases according to NASA-polynomials [165].

Species	Temperature range	a_1	a_2 [K^{-1}]	a_3 [K^{-2}]	a_4 [K^{-3}]	a_5 [K^{-4}]	a_6 [K]
CO_2	T>=1000 K	4.63659493E+00	2.74131991E-03	-9.95828531E-07	1.60373011E-10	-9.16103468E-15	-4.90249341E+04
	T<=1000 K	2.35677352E+00	8.98459677E-03	-7.12356269E-06	2.45919022E-09	-1.43699548E-13	-4.83719697E+04
CO	T>=1000 K	3.04848583E+00	1.35172818E-03	-4.85794075E-07	7.88536486E-11	-4.69807489E-15	-1.42661171E+04
	T<=1000 K	3.57953347E+00	-6.10353680E-04	1.01681433E-06	9.07005884E-10	-9.04424499E-13	-1.43440860E+04
CH_4	T>=1000 K	1.63552643E+00	1.00842795E-02	-3.36916254E-06	5.34958667E-10	-3.15518833E-14	-1.00056455E+04
	T<=1000 K	5.14987613E+00	-1.36709788E-02	4.91800599E-05	-4.84743026E-08	1.66693956E-11	-1.02466476E+04
H_2	T>=1000 K	2.93286579E+00	8.26607967E-04	-1.46402335E-07	1.54100359E-11	-6.88804432E-16	-8.13065597E+02
	T<=1000 K	2.34433112E+00	7.98052075E-03	-1.94781510E-05	2.01572094E-08	-7.37611761E-12	-9.17935173E+02
H_2S	T>=1000 K	2.74521990E+00	4.04346070E-03	-1.53845100E-06	2.75202490E-10	-1.85920950E-14	-3.41994440E+03
	T<=1000 K	3.93234760E+00	-5.02609050E-04	4.59284730E-06	-3.18072140E-09	6.64975610E-13	-3.65053590E+03
NH_3	T>=1000 K	2.71709692E+00	5.56856338E-03	-1.76886396E-06	2.67417260E-10	-1.52731419E-14	-6.58451989E+03
	T<=1000 K	4.30177808E+00	-4.77127330E-03	2.19341619E-05	-2.29856489E-08	8.28992268E-12	-6.74806394E+03
O_2	T>=1000 K	3.66096083E+00	6.56365523E-04	-1.41149485E-07	2.05797658E-11	-1.29913248E-15	-1.21597725E+03
	T<=1000 K	3.78245636E+00	-2.99673415E-03	9.84730200E-06	-9.68129508E-09	3.24372836E-12	-1.06394356E+03
N_2	T>=1000 K	2.95257626E+00	1.39690057E-03	-4.92631691E-07	7.86010367E-11	-4.60755321E-15	-9.23948645E+02
	T<=1000 K	3.53100528E+00	-1.23660987E-04	-5.02999437E-07	2.43530612E-09	-1.40881235E-12	-1.04697628E+03

Table E.2 Properties of ideal gas species [164].

Gas species	M (kg/kmol)	$\Delta H^0_{298,f}$ (kJ/mol)	LHV (kJ/mol)	LHV[a] (MJ/Nm^3)
CO_2	44.010	-393.51	0.00	0.00
CO	28.010	-110.53	282.98	12.625
CH_4	16.043	-74.89	802.27	35.793
H_2	2.016	0.00	241.83	10.789
H_2S	34.082	-20.60	518.06	23.113
NH_3	17.031	-45.94	316.80	14.134
O_2	31.999	0.00	0.00	0.00
N_2	28.013	0.00	0.00	0.00
H_2O (g)	18.015	-241.83	0.00	0.00
SO_2	64.065	-296.84	0.00	0.00

[a]The normal ideal gas volume at 1.01325 bar and 273.15 K (DIN, 1999).

Table E.3 Coefficients for calculation of heat capacity of inorganic solids according to NASA-polynomials [164].

Species	T_{min} [K]	T_{max} [K]	a_1 [K]	a_2 [K^{-1}]	a_3 [K^{-2}]	a_4 [K^{-3}]	a_5 [K^{-4}]	a_6 [K]
K_2O	298.15	700	5.26630120E+00	2.01572960E-02	-3.39640300E-05	2.89076170E-08	-9.24878980E-12	-4.56980980E+04
	700	1013	7.47592960E+00	8.35280880E-03	-1.04300450E-05	8.17177000E-09	-2.44222740E-12	-4.60275840E+04
SiO_2	298.15	1000	6.86099160E+00	-2.47320880E-02	9.59213240E-05	-1.11018800E-07	4.13248490E-11	-1.11098590E+05
	1000	1700	5.59194200E+01	-1.44862260E-01	1.61961260E-04	-7.89418770E-08	1.42797310E-11	-1.24715460E+05
Mg_2SiO_4	298.15	1000	3.36224340E-01	7.35156580E-02	-1.11995600E-04	8.18567720E-08	-2.27243190E-11	-2.64357040E+05
	1000	2171	1.06183750E+01	2.08719300E-02	-1.57573220E-05	6.18279530E-09	-9.27043690E-13	-2.65837710E+05
Fe_2SiO_4	298.15	1000	1.39525940E+00	8.03129630E-02	-1.34331000E-04	1.07686640E-07	-3.22993640E-11	-1.80986120E+05
	1000	1490	-2.52502650E+01	1.47449290E-01	-1.75866840E-04	9.59314330E-08	-1.94991190E-11	-1.73684730E+05
MgO	298.15	1000	3.04696230E-01	2.21970220E-02	-3.43804890E-05	2.47560000E-08	-6.72578250E-12	-7.31324670E+04
	1000	3015	4.57618720E+00	2.70768510E-03	-1.54142500E-06	4.59917420E-10	-5.09186860E-14	-7.38665970E+04
CaO	298.15	1000	1.57835230E+00	1.88151540E-02	-2.97951290E-05	2.18940890E-08	-6.03660530E-12	-7.74680640E+04
	1000	3200	5.14514060E+00	2.11373130E-03	-1.09159190E-06	3.24128320E-10	-3.55478970E-14	-7.80597080E+04
$CaCO_3$	298.15	700	-5.04743680E+00	9.37488070E-02	-1.96914510E-04	1.97711220E-07	-7.56953080E-11	-1.46438360E+05
	700	1200	3.78466800E+00	3.22493500E-02	-4.14936350E-05	2.71805430E-08	-6.75192900E-12	-1.47404610E+05
$CaMg(CO_3)_2$	298.15	700	1.81788330E+00	1.01170670E-01	-1.99730920E-04	2.01189990E-07	-7.72506640E-11	-2.83429820E+05
	700	1200	1.06856700E+01	3.89926030E-02	-4.18386240E-05	2.73367810E-08	-6.77466170E-12	-2.84389430E+05
$CaSO_4$	298.15	1000	4.66181040E+00	4.02700680E-02	-7.40710520E-05	8.02095240E-08	-3.06884100E-11	-1.75158440E+05
	1000	1635	2.77486750E+01	-8.59493760E-02	1.66066090E-04	-1.13753890E-07	2.62704400E-11	-1.78082210E+05
$Ca(OH)_2$	298.15	700	-5.67483770E+00	1.09340740E-01	-2.58889670E-04	2.84635960E-07	-1.17960970E-10	-1.19987930E+05

Table E.4 Properties of inorganic solid species [164].

Solid species	M (kg/kmol)	$\Delta H^0_{298,f}$ (kJ/mol)
K_2O	94.195	-361.50
SiO_2	60.084	-910.86
Mg_2SiO_4	140.693	-2176.94
Fe_2SiO_4	203.777	-1479.90
MgO	40.304	-601.24
CaO	56.077	-635.09
$CaCO_3$	100.087	-1206.92
$CaMg(CO_3)_2$	184.401	-2326.30
$CaSO_4$	136.142	-1434.11
$Ca(OH)_2$	74.093	-986.09

Table E.5 Enthalpy formulation for sub-cooled liquid water and superheated steam according to IAPWS-IF97[a] [167].

stable single-phase liquid	stable single-phase vapour
Basic Equation for Region 1: $\frac{g(P,T)}{RT} = \gamma(\pi,\tau) = \sum_{i=1}^{34} n_i (7.1-\pi)^{I_i} (\tau - 1.222)^{J_i}$ $where: \begin{pmatrix} R = 0.461526\left[kJkg^{-1}K^{-1}\right] \\ \pi = \frac{P}{P^*} = \frac{P\left[MPa\right]}{16.53} \\ \tau = \frac{T^*}{T} = \frac{1386\left[K\right]}{T} \end{pmatrix}$ Enthalpy Calculation from Basic Equation: $h = g - T\left(\frac{\partial g}{\partial T}\right)_p \Rightarrow \frac{h(\pi,\tau)}{RT} = \tau.\gamma_\tau$ $where: \gamma_\tau = \left(\frac{\partial \gamma}{\partial \tau}\right)_\pi = \sum_{i=1}^{34} n_i (7.1-\pi)^{I_i} J_i (\tau - 1.222)^{J_i - 1}$ $\frac{H_{IAPWS}(P,T)}{RT} = \tau.\sum_{i=1}^{34} n_i (7.1-\pi)^{I_i} J_i (\tau - 1.222)^{J_i - 1}$	Basic Equation for Region 2: $\frac{g(P,T)}{RT} = \gamma(\pi,\tau) = \gamma^0(\pi,\tau) + \gamma^r(\pi,\tau)$ Ideal gas part: $\gamma^0(\pi,\tau) = \ln\pi + \sum_{i=1}^{9} n_i^0 \tau^{J_i^0}$ Residual part: $\gamma^r(\pi,\tau) = \sum_{i=1}^{43} n_i \pi^{I_i} (\tau - 0.5)^{J_i}$ $where: \begin{pmatrix} R = 0.461526\left[kJkg^{-1}K^{-1}\right] \\ \pi = \frac{P}{P^*} = \frac{P\left[MPa\right]}{1} \\ \tau = \frac{T^*}{T} = \frac{540\left[K\right]}{T} \end{pmatrix}$ Enthalpy Calculation from Basic Equation: $h = g - T\left(\frac{\partial g}{\partial T}\right)_p \Rightarrow \frac{h(\pi,\tau)}{RT} = \tau.\left(\gamma_\tau^0 + \gamma_\tau^r\right)$ $where: \gamma_\tau^0 = \left(\frac{\partial \gamma^0}{\partial \tau}\right)_\pi = 0 + \sum_{i=1}^{9} n_i^0 J_i^0 \tau^{J_i^0 - 1}$ $\gamma_\tau^r = \left(\frac{\partial \gamma^r}{\partial \tau}\right)_\pi = \sum_{i=1}^{43} n_i \pi^{I_i} J_i (\tau - 0.5)^{J_i - 1}$ $\frac{H_{IAPWS}(P,T)}{RT} = \tau.\left(\sum_{i=1}^{9} n_i^0 J_i^0 \tau^{J_i^0 - 1} + \sum_{i=1}^{43} n_i \pi^{I_i} J_i (\tau - 0.5)^{J_i - 1}\right)$

[a] For coefficients (I_i , J_i ,n_i ; i=1,…,34 for single-phase liquid) and (J_{i0} and n_{i0}; i=1,…,9 and I_i, J_i , n_i; i=1,…,43 for single-phase vapor) refer to IAPWS-IF97 [167].

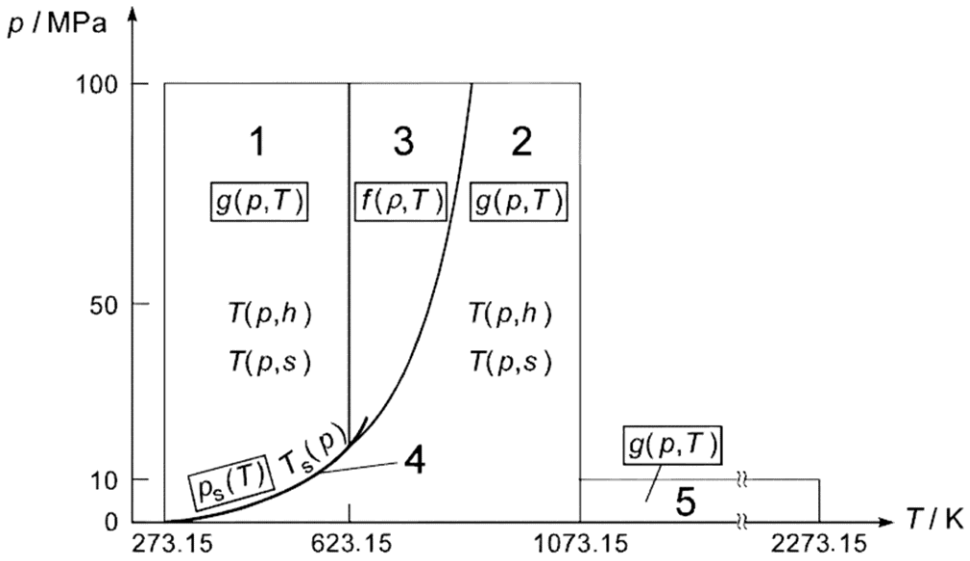

Figure E.1 Regions and equations of IAPWS-IF97 [167].

Appendix F MATLAB code for dual fluidized bed biomass gasifier

In Appendix F, the kinetic gasifier model from the previous chapter evolves into a comprehensive version of two-phase kinetic model of a bubbling fluidized bed gasifier. By incorporating reaction kinetics and reactor hydrodynamics, the two kinetic models of biomass steam gasification in the BFB and char (and natural gas) combustion with air in the CFB riser of the UBC DFB reactor are developed and integrated by performing mass and energy balances over both reactors. These models are capable of predicting species concentrations, solids hold-up, temperature, pressure and superficial gas velocity profiles along the height of each reactor, as well as key operating parameters such as solids circulation rate and natural gas flow rate required for stable operation.

```
function DFB_Gasifier
% Two-phase model for UBC DFB gasifier
clear all
global LHV_Bio Epsi_ave L_total Lfb Rho_Bio0 Tgas Pgas R Y_G A dp dp_sand Rho_sand m_Bin m_Min L_bed g Epsi_mf m_Steam Y_H2 Y_CO Y_CO2 Y_CH4 MC Y_C ID M Y_H2O m_N2 Uriser Qair_N QCH4_N QPG_N LHV_PG Etta_CHEM Etta_CGE1 Etta_CGE2

clc
g=9.81;
R=8.314;
L_total=1.37;                 %Total BFB height w/o freeboard (m)
ID=0.3;                       %Gasifier inside diameter(m)
A=pi()*ID^2/4;                %Gasifier cross-sectional area (m^2)

ID_riser=0.1;                 %Riser inside diameter (m)
A_riser=(pi()*ID_riser^2/4);  %Riser cross-sectional area (m^2)

M_sand=100;                   %Sand inventory of BFB (kg)
Rho_sand=2650;                %Sand particle density (kg/m^3)
dp_sand=200*10^-6;
sphericity=0.95;
Epsi_mf=(14*sphericity)^(-1/3);

T0=25+273.15;
P0=1.01325*10^5;
Tfuel=25+273;                 %Fuel inlet temperature (K)
Pfuel=P0;                     % Fuel inlet temperature (Pa)
Tgas=750+273.15;              %Gasifier temperature (K)
Pgas=1.01325*10^5;            %Inlet gas pressure (Pa)
Tsteam=Tgas;                  %Superheated steam inlet temperature (K)
Psteam=P0;                    %Superheated steam inlet pressure (Pa)
Tair=400+273.15;              %Combustor air inlet temperature (K)
Pair=P0;                      %Combustor air inlet pressure (Pa)
```

```
Tcomb=900+273.15;                  %Combustor temperature (K)
MWH2O=18;

dp=790*10^-6;                      %Biomass particle size (m)
LHV_Bio=18.8*1000;                 %Biomass heating value (kJ/kg)
Rho_Bio0=570;                      %Biomass dry bulk density (kg/m^3)

m_Bin=10/3600*(100-10)/100;        %Dry biomass feeding flow rate (kg/s)
m_Min=10/(100-10)*m_Bin;           %Moisture content=10 wt%, on "as-received" basis
m_Steam=10/3600;                   %Superheated steam flow rate (kg/s)
% S_B=(m_Steam+m_Min)/m_Bin;

m_N2=0;                                                    %Nitrogen mass flow rate  (kg/s)
U0=(m_N2/28+m_Steam/18)*(R*Tgas)/(Pgas*A)*1000;            %Inlet superficial gas velocity (m/s)

Qloss_gas=15/100*(m_Bin*LHV_Bio);                          %Gasifier heat loss (kW)
Qloss_comb=15/100*(m_Bin*LHV_Bio);                         %Combustor heat loss (kW)
%*************************************************************************
% From elemental balances over the coupled particle and reactor model (with steam as fluidization
medium), the yields of pyrolysis product are  obtained as discussed "Coupled_particle_reactor_model"
and used in the gasifier model.
%Tar yields released from average particle surface inside the reactor is:
% Y_T=(trapz(t,MTar2.*E_t)+MTar2(end)*exp(-tend/Taw_S))/MP0;
%Pyrolytic water yield yields released from average particle surface inside the reactor
Y_H2O=yH2Omean
% Dry gas species yields released from average particle surface inside the reactor
Y_H2=0*Y_G;
Y_CO=wCO_gmean*Y_G;
Y_CO2=wCO2_gmean*Y_G;
Y_CH4=wCH4_gmean*Y_G;


MC=0.5;                            %Initial guess for char hold-up of dense bubbling bed (kg)
MChar_temp=0;
%Fixing char hold-up with a while loop
while abs(MC-MChar_temp)>0.01
   MChar_temp=MC;
   Epsi_ave=0.5;
   L_bed=1;                        % Initial guess for expanded dense bed height(m)
   L_temp=0;
   %Fixing dense bed height with a while loop
   while abs(L_temp-L_bed)>10^-2
      L_temp=L_bed;
```

```
M=1000;                                          %Number of cells along dense bed height
zspan=linspace(0,L_bed,M+1);
Uvec=zeros(1,M+1);                               %Superficial gas velocity (m/s)
Epsi=zeros(1,M+1);                               %Bed voidage
db=zeros(1,M+1);                                 %Bubble diameter (m)

Rhogas=Pgas*18/(R*Tgas)/1000;                    % Inlet steam density (kg/m3)
Mu_Vap=9.12*10^-6+3.27*10^-8*Tgas;               % Steam viscosity (kg/m.s)
Ar=g*Rhogas*(Rho_sand-Rhogas)*dp_sand^3/Mu_Vap^2;
Umf=Mu_Vap/Rhogas/dp_sand*(sqrt(27.2^2+0.0408*Ar)-27.2);  %Min fluidization velocity (m/s)
m=1;                                             %Parameter for modified two-phase theory
Split_H=m*Umf/U0;                                %H-phase flow split factor at inlet
% 15 Boundary conditions: Molar flow rates of 7 species (H2,CO2,CO, H2O,CH4,Tar,N2)
% in two phases (L and H)  and one hydrostatic pressure
BC=[0 0 0 (1-Split_H)*m_Steam/18 0 0 (1-Split_H)*m_N2/28 0 0 0 Split_H*m_Steam/18 0 0
      Split_H*m_N2/28 Pgas];

[z,Vol]=ode45('dFi_dz',zspan,BC);
FLH2=Vol(:,1);                          %Molar flow rate of H2 in L-phase (kmol/s)
FLCO2=Vol(:,2);
FLCO=Vol(:,3);
FLH2O=Vol(:,4);
FLCH4=Vol(:,5);
FLTar=Vol(:,6);
FLN2=Vol(:,7);

FHH2=Vol(:,8);                          %Molar flow rate of H2 in H-phase (kmol/s)
FHCO2=Vol(:,9);
FHCO=Vol(:,10);
FHH2O=Vol(:,11);
FHCH4=Vol(:,12);
FHTar=Vol(:,13);
FHN2=Vol(:,14);

Press=Vol(:,15);                        %Hydrostatic pressure (Pa)

RCcons=0;                               %Overall char consumption rate along BFB (1/s)
for I=1:M+1
   comp=zeros(1,7);
   Fi=zeros(1,7);
   Fsum=0;
   for i=1:7
      Fi(i)=Vol(i)+Vol(I,i+7);
      Fsum=Fsum+Fi(i);
```

```
    end

    % i=1 H2, i=2 CO2, i=3 CO, i=4 H2O, i=5 CH4 i=6 Tar, i=7 N2
    MW(1)=2;    MW(2)=44;    MW(3)=28;       MW(4)=18;
    MW(5)=16;   MW(6)=94;    MW(7)=28;
    MW_mix=0;
    for i=1:7
       comp(i)=Fi(i)./Fsum;
       MW_mix=MW_mix+comp(i)*MW(i);
    end

    Mu_Vap=9.12*10^-6+3.27*10^-8*Tgas;
    Mu_mix=Mu_Vap;
    Rhog=Press(I)*MW_mix/(R*Tgas)/1000;   %kg/m3
    Ar=g*Rhog*(Rho_sand-Rhog)*dp_sand^3/Mu_mix^2;
    Umf=Mu_mix/Rhog/dp_sand*(sqrt(27.2^2+0.0408*Ar)-27.2);

    QL=0;
    QH=0;
    for i=1:7
       QL=QL+R*Tgas/Press(I)*1000*Vol(I,i);              %m3/s
       QH=QH+R*Tgas/Press(I)*1000*Vol(I,i+7);            %m3/s
    end
    Uvec(I)=(QL+QH)/A;

    Nor=72;
    db(I)=0.54*g^(-0.2)*(Uvec(I)-Umf).^0.4*(z(I)+4*sqrt(A/Nor)).^0.8;
    Epsi(I)=1-(1-Epsi_mf)/(1+(Uvec(I)-Umf)/(0.711*sqrt(g*db(I))));

   [ Ratei, Rchar_consH]=  Rxn_Rate(1, 2, Uvec(I), FHH2(I), FHCO2(I), FHCO(I), FHH2O(I),
    FHCH4(I), FHTar(I), Tgas);
    RCcons=RCcons+Rchar_consH;    %1/s
  end

  Epsi_ave=trapz(z,Epsi)/L_bed;
  L_bed=M_sand/(Rho_sand*A*(1-Epsi_ave));
end

%**************Char balance  Over the BFB gasifier**********************************
mdotC_out=Y_C*(m_Bin+m_Min)-RCcons*(MC/M);    %Un-reacted char mass flow rate (kg/s)

%Molar gas flow rates leaving dense bed
FH2_dense=FLH2(M+1)+FHH2(M+1);
FCO2_dense=FLCO2(M+1)+FHCO2(M+1);
```

```
   FCO_dense=FLCO(M+1)+FHCO(M+1);
   FH2O_dense=FLH2O(M+1)+FHH2O(M+1);
   FCH4_dense=FLCH4(M+1)+FHCH4(M+1);
   FTar_dense=FLTar(M+1)+FHTar(M+1);
   FN2_dense=FLN2(M+1)+FHN2(M+1);
    %****Energy balance for the BFB gasifier(m:kg/s, F:kmole/s,  H:kJ/kg or kJ/kmol, Q:kJ/s)******
   H_moisture=-285.83/18*1000+(H_IAPWS(1,Pfuel,Tfuel)-H_IAPWS(1,P0,T0));          %kJ/kg
   H_steamIN=-285.83/18*1000+(H_IAPWS(2,Psteam,Tsteam)-H_IAPWS(1,P0,T0));         %kJ/kg
   H_steamOUT=-285.83/18*1000+(H_IAPWS(2,P0,Tgas)-H_IAPWS(1,P0,T0));              %kJ/kg

    m_sand=1/(H_sand(Tgas)-H_sand(Tcomb))*
    (FN2_dense*H_N2(Tair)+m_Bin*H_fuel(Tfuel)+m_Min*H_moisture+m_Steam*H_steamIN-
    mdotC_out*H_char(Tgas)-Qloss_gas-
    (FH2_dense*H_H2(Tgas)+FCO_dense*H_CO(Tgas)+FCO2_dense*H_CO2(Tgas)+FCH4_dense*
    H_CH4(Tgas)+FTar_dense*H_Tar(Tgas)+FN2_dense*H_N2(Tgas)+FH2O_dense*MWH2O*
    H_steamOUT));

   Taw_S=M_sand/m_sand;                  %Mean solids residence time in the gasifier (s)
   MC=(mdotC_out*Taw_S);
end          %While MC

%Freeboard with expanded cross-sectional area
Lfb=L_total-L_bed;                       %Reactor length above dense bed
Mfb=200;                                 %Number of cells along freeboard
zspan=linspace(L_bed,2.34,Mfb+1);
% 7 Boundary conditions: Molar flow rates of 7 species and one freeboard temperature
[zfb,Volfb]=ode45('dFifb_dz',zspan,[FH2_dense FCO2_dense FCO_dense FH2O_dense FCH4_dense
FTar_dense  FN2_dense  Tgas]);

FH2_fb=Volfb(:,1);
FCO2_fb=Volfb(:,2);
FCO_fb=Volfb(:,3);
FH2O_fb=Volfb(:,4);
FCH4_fb=Volfb(:,5);
FTar_fb=Volfb(:,6);
FN2_fb=Volfb(:,7);
Tgas_fb=Volfb(:,8);


%*****Energy balance for the riser************************************************
H_steamOUT2=-285.83/18*1000+(H_IAPWS(2,P0,Tcomb)-H_IAPWS(1,P0,T0));

% FCH4_in*H_CH4(Tair)+FO2_in*H_O2(Tair)+FN2*H_N2(Tair)+m_charG*H_char(Tgas)+m_sand*
H_sand(Tgas)-m_charC*H_char(Tcomb)-m_sand*H_sand(Tcomb)-Qloss_comb-
```

```
(FN2*H_N2(Tcomb)+FO2_comb*H_O2(Tcomb)+FH2_comb*H_H2(Tcomb)+FCO_comb*H_CO(Tco
mb)+FCO2_comb*H_CO2(Tcomb)+FH2O_comb*MWH2O*H_steamOUT2)=0

% Assuming complete combustion of  NG and Char
Landa=1.2;      %Soichiometric O2 ratio (20% excess air)
%     FO2_in=Landa*(2*FCH4_in+m_charG/12);   %kmol/s
%     FN2=79/21*FO2_in;
%     FO2_comb=FO2_in-2*FCH4_in-m_charG/12;
%     FO2_comb=(Landa-1)*(2*FCH4_in+m_charG/12);
%     FCO2_comb=FCH4_in+m_charG/12;
%     FH2O_comb=2*FCH4_in;
%     FH2_comb=0;
%     FCO_comb=0;

%Upon substitution of the above equations in combustor energy balance and solving for natural gas molar
flow rate
FCH4_in=-(Landa*(m_charG/12)*H_O2(Tair)+79/21*Landa*(m_charG/12)*H_N2(Tair)+m_charG*
H_char(Tgas)+m_sand*H_sand(Tgas)-m_charC*H_char(Tcomb)-m_sand*H_sand(Tcomb) -
Qloss_comb-(79/21*Landa*(m_charG/12)*H_N2(Tcomb)+(Landa-1)* (m_charG/12)*H_O2(Tcomb)
+FH2_comb*H_H2(Tcomb)+FCO_comb*H_CO(Tcomb)+(m_charG/12)*H_CO2(Tcomb)))/
(H_CH4(Tair)+Landa*2*H_O2(Tair)+79/21*Landa*2*H_N2(Tair)-79/21*Landa*2*H_N2(Tcomb)-
2*(Landa-1)*H_O2(Tcomb)-H_CO2(Tcomb)- 2*MWH2O*H_steamOUT2);

FO2_in=Landa*(2*FCH4_in+m_charG/12);                %Input oxygen flow rate (kmol/s)
F_total=100/21*FO2_in+FCH4_in;
Uriser=F_total*R*Tcomb/(P0*A_riser)*1000;           %Riser superficial gas velocity (m/s)
Qair_N=100/21*FO2_in*R*273.15*1000/Pair*3600;       %Air flow rate (Nm^3/h)
QCH4_N=FCH4_in*R*273.15*1000/Pair*3600;             % Required NG flow rate (Nm^3/h)

%Syngas leaving freeboard
gas_yield=(FH2_fb(Mfb+1)+FCO2_fb(Mfb+1)+FCO_fb(Mfb+1)+FCH4_fb(Mfb+1))*1000*R/1.01325/1
0^5*(0+273.15);                                     %Product gas volumetric flow rate (Nm^3/s)
QPG_N(Itemp,1)=gas_yield*3600;                      % Product gas volumetric flow rate (Nm^3/h)

LHV_PG=(FH2_fb(Mfb+1)*10.789+FCO_fb(Mfb+1)*12.625+FCH4_fb(Mfb+1)*35.793)/(FH2_fb(Mfb
+1)+FCO2_fb(Mfb+1)+FCO_fb(Mfb+1)+FCH4_fb(Mfb+1));     %Product gas heating value (MJ/Nm^3)
%Chemical and cold gas efficiency
Etta_CHEM=(gas_yield*LHV_PG*1000)/(m_Bin*LHV_Bio);
Etta_CGE1=(gas_yield*LHV_PG*1000)/(m_Bin*LHV_Bio+QCH4_N/3600*35.793*1000);
Etta_CGE2=(gas_yield*LHV_PGfb*1000-QCH4_N/3600*35.793*1000)/(m_Bin*LHV_Bio);

Gs=m_sand/A_riser;                                  %Solid circulation flux (kg/m^2.s)

end                         %function "DFB_Gasifier"
```

```
function Vdot=dFi_dz(z,V)
global L_bed SaiL SaiH Epsi Epsi_L UL Epsi_H UH M dp_sand Rho_sand Tgas R A Epsi_mf
g
%V(1) to V(7): Molar flow rates of (H2,CO2,CO,H2O,CH4,Tar,N2) in L-phase (kmol/s)
%V(8) to V(14): Molar flow rates of (H2,CO2,CO,H2O,CH4,Tar,N2) in H-phase (kmol/s)

Press=V(15);

QL=0;      %Volumetric flow rate of phase L (m3/s)
QH=0;      %Volumetric flow rate of phase H (m3/s)
for i=1:7
   QL=QL+R*Tgas/Press*1000*V(i);
   QH=QH+R*Tgas/Press*1000*V(i+7);
end
U=(QL+QH)/A;                    %Superficial gas velocity (m/s)

y=zeros(1,7);                   %Molar fraction
F=zeros(1,7);                   %Molar flow rate (kmol/s)

Fsum=0;
for i=1:7
   F(i)=V(i)+V(i+7);
   Fsum=Fsum+F(i);
end

for i=1:7
   y(i)=F(i)/Fsum;
end
%Assume MWtar=94 g/mol
MW_mix=y(1)*2+y(2)*44+y(3)*28+y(4)*18+y(5)*16+y(6)*94+y(7)*28;              %Mixture MW
Rhogas=Press*MW_mix/(R*Tgas)/1000;              %Density of gas phase(kg/m3)
Mu_Vap=9.12*10^-6+3.27*10^-8*Tgas;              %Viscosity of gas phase (approximated by steam)

Ar=g*Rhogas*(Rho_sand-Rhogas)*dp_sand^3/Mu_Vap^2;                    %Archimedes number
Umf=Mu_Vap/Rhogas/dp_sand*(sqrt(27.2^2+0.0408*Ar)-27.2);
Umb=Umf*4.125*10^4*Mu_Vap^0.9*Rhogas^0.1/((Rho_sand-Rhogas)*g*dp_sand);    %Geldart 1978
Uc=Mu_Vap/Rhogas/dp_sand*(0.57*Ar^0.46);
Use=Mu_Vap/Rhogas/dp_sand*(1.53*Ar^0.5);

% if U<Umb
%     input('bubble-free expansion')
% elseif (U>=Uc && U<=Use)
%     input('turbulent regime')
```

```
% elseif U>Use
%     input('fast fluidization regime')
% end
% if U<4*Umf
%     input('Segregation')                %Herguido et al.
% end

Nor=72;
db=0.54*g^(-0.2)*(U-Umf)^0.4*(z+4*sqrt(A/Nor))^0.8;
Epsi=1-(1-Epsi_mf)/(1+(U-Umf)/(0.711*sqrt(g*db)));
Epsi_L=1;   %Solid-free bubble
SaiL=(Epsi-Epsi_mf)/(Epsi_L-Epsi_mf);
SaiH=1-SaiL;
Epsi_H=(Epsi-SaiL*Epsi_L)/SaiH;

Ubr=(U-Umf)*(1+0.711/U*sqrt(g*db));    %Bubble rise velocity (m/s) Davidson & Harrison
UL=QL/(SaiL*Epsi_L*A);     %Convective gas velocity of phase L (m/s)
UH=QH/(SaiH*Epsi_H*A);     %Convective gas velocity of phase H (m/s)

%*****Molecular diffusivity: Chapman–Enskog theory **********************
% i=1 H2, i=2 CO2, i=3 CO, i=4 H2O, i=5 CH4 i=6 Tar, i=7 N2
sigma(1)=2.827;
sigma(2)=3.941;
sigma(3)=3.690;
sigma(4)=2.641;
sigma(5)=3.758;
sigma(6)=5.349;
sigma(7)=3.758;

Epsi_K(1)=59.7;
Epsi_K(2)=195.2;
Epsi_K(3)=91.7;
Epsi_K(4)=809.1;
Epsi_K(5)=148.6;
Epsi_K(6)=412.3;
Epsi_K(7)=148.6;

MW(1)=2;
MW(2)=44;
MW(3)=28;
MW(4)=18;
MW(5)=16;
MW(6)=94;
MW(7)=28;
```

```
Diff=zeros(7,7);

for i=1:7
   for j=1:7
      Ts=Tgas/(Epsi_K(i)*Epsi_K(j))^(1/2);
      GammaD=1.06036/Ts^0.15610+0.19300/exp(0.47635*Ts)+1.03587/exp(1.52996*Ts)+1.76474/exp(
      3.89411*Ts);

      Diff(i,j)=1.858*10^-3*Tgas^(3/2)*((MW(i)+MW(j))/MW(i)/MW(j))^(1/2)/...
      (Press/1.01325/10^5*(1/2*(sigma(i)+sigma(j)))^2*GammaD)*10^-4;
   end
end
 Dmix=zeros(1,7);
for i=1:7
   sum=0;
   for j=1:7
      if j~=i
         sum=sum+y(j)/Diff(i,j);
      end
   end
   if y(i)==1
      Dmix(i)=Diff(i,i);
   else
      Dmix(i)=(1-y(i))/sum;
   end
end

%Inter-phase volumetric mass transfer coefficient (1/s) Sit & Grace
for i=1:7
   K(i)=(Umf/3+2*(Dmix(i)*Epsi_mf*Ubr/(pi()*db))^(1/2))*6/db;
end

%Convective (bulk) mass transfer between phases
m=1;
if QH>=(m*Umf*A)
%    input('forming bubbles')
   Qbulk_LH=0;
   Qbulk_HL=(QH-m*Umf*A)/(SaiH*A*L_bed/M);
else
%    input('avoid defluidization')
   Qbulk_LH=(m*Umf*A-QH)/(SaiH*A*L_bed/M);
   Qbulk_HL=0;
end
```

```
% Rxn_Rate is defined as a sub-routine in which the first and second arguments are species number
(i=1:7) and phase number (L-phase=1, H-phase=2)
%Mole balances for bubble phase (i=1 H2, i=2 CO2, i=3 CO, i=4 H2O, i=5 CH4 i=6 Tar, i=7 N2)

Vdot(1)=-K(1)*SaiL*(V(1)/(SaiL* Epsi_L*UL)-V(8)/(SaiH*Epsi_H*UH))-Qbulk_LH*(V(1)/( Epsi_L*
UL))+Qbulk_HL*(V(8)/(Epsi_H*UH))+SaiL*A*Rxn_Rate(1,1,U,V(1),V(2),V(3),V(4),V(5),V(6),Tgas);

Vdot(2)=-K(2)*SaiL*(V(2)/(SaiL* Epsi_L*UL)-V(9)/(SaiH*Epsi_H*UH))-Qbulk_LH*(V(2)/( Epsi_L*
UL))+Qbulk_HL*(V(9)/(Epsi_H*UH))+SaiL*A*Rxn_Rate(2,1,U,V(1),V(2),V(3),V(4),V(5),V(6),Tgas);

Vdot(3)=-K(3)*SaiL*(V(3)/(SaiL* Epsi_L*UL)-V(10)/(SaiH*Epsi_H*UH))-Qbulk_LH*(V(3)/( Epsi_L*
UL))+Qbulk_HL*(V(10)/(Epsi_H*UH))+SaiL*A*Rxn_Rate(3,1,U,V(1),V(2),V(3),V(4),V(5),V(6),Tgas)

Vdot(4)=-K(4)*SaiL*(V(4)/(SaiL* Epsi_L*UL)-V(11)/(SaiH*Epsi_H*UH))-Qbulk_LH*(V(4)/( Epsi_L*
UL))+Qbulk_HL*(V(11)/(Epsi_H*UH))+SaiL*A*Rxn_Rate(4,1,U,V(1),V(2),V(3),V(4),V(5),V(6),Tgas)

Vdot(5)=-K(5)*SaiL*(V(5)/(SaiL* Epsi_L*UL)-V(12)/(SaiH*Epsi_H*UH))-Qbulk_LH*(V(5)/( Epsi_L*
UL))+Qbulk_HL*(V(12)/(Epsi_H*UH))+SaiL*A*Rxn_Rate(5,1,U,V(1),V(2),V(3),V(4),V(5),V(6),Tgas)

Vdot(6)=-K(6)*SaiL*(V(6)/(SaiL* Epsi_L*UL)-V(13)/(SaiH*Epsi_H*UH))-Qbulk_LH*(V(6)/( Epsi_L*
UL))+Qbulk_HL*(V(13)/(Epsi_H*UH))+SaiL*A*Rxn_Rate(6,1,U,V(1),V(2),V(3),V(4),V(5),V(6),Tgas)

Vdot(7)=-K(7)*SaiL*(V(7)/(SaiL* Epsi_L*UL)-V(14)/(SaiH*Epsi_H*UH))-Qbulk_LH*(V(7)/( Epsi_L*
UL))+Qbulk_HL*(V(14)/(Epsi_H*UH))+0;
%Mole balances for emulsion phase (i=8 H2, i=9 CO2, i=10 CO, i=11 H2O, i=12 CH4 i=13 Tar, i=14
N2)
Vdot(8)=-K(1)*SaiL*(V(8)/(SaiH*Epsi_H*UH)-V(1)/(SaiL* Epsi_L*UL))+...
Qbulk_LH*(V(1)/( Epsi_L*UL))-Qbulk_HL*(V(8)/(Epsi_H*UH))+SaiH*A*...
Rxn_Rate(1,2,U,V(8),V(9),V(10),V(11),V(12),V(13),Tgas);

Vdot(9)=-K(2)*SaiL*(V(9)/(SaiH*Epsi_H*UH)-V(2)/(SaiL* Epsi_L*UL))+...
Qbulk_LH*(V(2)/( Epsi_L*UL))-Qbulk_HL*(V(9)/(Epsi_H*UH))+SaiH*A*...
Rxn_Rate(2,2,U,V(8),V(9),V(10),V(11),V(12),V(13),Tgas);

Vdot(10)=-K(3)*SaiL*(V(10)/(SaiH*Epsi_H*UH)-V(3)/(SaiL* Epsi_L*UL))+...
Qbulk_LH*(V(3)/( Epsi_L*UL))-Qbulk_HL*(V(10)/(Epsi_H*UH))+SaiH*A*...
Rxn_Rate(3,2,U,V(8),V(9),V(10),V(11),V(12),V(13),Tgas);

Vdot(11)=-K(4)*SaiL*(V(11)/(SaiH*Epsi_H*UH)-V(4)/(SaiL* Epsi_L*UL))+...
Qbulk_LH*(V(4)/( Epsi_L*UL))-Qbulk_HL*(V(11)/(Epsi_H*UH))+SaiH*A*...
Rxn_Rate(4,2,U,V(8),V(9),V(10),V(11),V(12),V(13),Tgas);

Vdot(12)=-K(5)*SaiL*(V(12)/(SaiH*Epsi_H*UH)-V(5)/(SaiL* Epsi_L*UL))+...
```

```
Qbulk_LH*(V(5)/( Epsi_L*UL))-Qbulk_HL*(V(12)/(Epsi_H*UH))+SaiH*A*...
Rxn_Rate(5,2,U,V(8),V(9),V(10),V(11),V(12),V(13),Tgas);

Vdot(13)=-K(6)*SaiL*(V(13)/(SaiH*Epsi_H*UH)-V(6)/(SaiL* Epsi_L*UL))+...
Qbulk_LH*(V(6)/( Epsi_L*UL))-Qbulk_HL*(V(13)/(Epsi_H*UH))+SaiH*A*...
Rxn_Rate(6,2,U,V(8),V(9),V(10),V(11),V(12),V(13),Tgas);

Vdot(14)=-K(7)*SaiL*(V(14)/(SaiH*Epsi_H*UH)-V(7)/(SaiL* Epsi_L*UL))+...
Qbulk_LH*(V(7)/( Epsi_L*UL))-Qbulk_HL*(V(14)/(Epsi_H*UH))+0;
%**************Hydrostatic pressure*****************************************************
Vdot(15)=-Rho_sand*g*(1-Epsi);
Vdot=Vdot';
end                %function "dFi_dz"

function Vdot=dFifb_dz(z,V)
global L_bed  g  A  R  Lfb  Pfb  k04  E4

Temp=V(8);
% i=1 H2, i=2 CO2, i=3 CO, i=4 H2O, i=5 CH4 i=6 Tar, i=7 N2, i=8 Temp
%Freeboard cross-sectional area with varying diameter
if (z>=L_bed && z<1.37)
   Dt=0.3;
   Lt=1.37;
elseif (z>=1.37 && z<=1.67)
   Dt=1.2*(z-1.12);
   Lt=1.67-1.37;
elseif (z>1.67 && z<=2.34)
   Dt=0.66;
   Lt=2.34-1.67;
end
At=pi()*Dt^2/4;

FT=V(1)+V(2)+V(3)+V(4)+V(5)+V(6)+V(7);
MW_mix=V(1)/FT*2+V(2)/FT*44+V(3)/FT*28+V(4)/FT*18+V(5)/FT*16+V(6)/FT*94+V(7)/FT*28;
Rhogas=Pfb*MW_mix/(R* Temp)/1000;
U=FT*R* Temp/(Pfb*At)*1000;

Mu_Vap=9.12*10^-6+3.27*10^-8* Temp;    %Steam viscosity (kg/m.s)
Cp_g=(0.0006599* Temp+1.632)*1000;     %Steam heat capacity (J/kg.K)
kg=0.1077;                          %Steam thermal conductivity (W/m.K)
Re=Rhogas*U*Dt/Mu_Vap;
Pr=Mu_Vap*Cp_g/kg;

Tcool=25+273.15;                %Ambient air temperature
```

```
Tsurf= Temp;                %Initial guess for reactor external surface temperature
Twall= Temp;                %Initial guess for reactor internal wall temperature
OD=Dt+2*12.5/100;           %Wall thickness=12.5 mm
k_wall=2.5;                 %Reactor wall thermal conductivity (W/m.K)
Mu_w=9.12*10^-6+3.27*10^-8*Twall;
h_wall=kg/Dt*0.023*Re^0.8*Pr^0.33*(Mu_Vap/Mu_w)^0.14 ;  %Dittus_Bolter
Rho_air=1.12;   %kg/m3
Cp_air=950+0.188*Tcool;   %J/kg.K
Mu_air=9.12*10^-6+3.27*10^-8*Tcool;  %kg/m.s
k_air=0.025;   %J/m.s.K
Gr_Pr=(Lt^3*Rho_air^2*g*Cp_air*(Tsurf-Tcool)/(0.5*(Tsurf+Tcool)))/(Mu_air*k_air);


if Gr_Pr<10^9
   h_air=1.42*((Tsurf-Tcool)/Lt)^(1/4);
else
   h_air=1.31*(Tsurf-Tcool)^(1/3);
end
h=1/((OD/Dt)*1/h_wall+OD/2/k_wall*log(OD/Dt)+1/h_air);

As=(pi()*Dt*Lfb)/(pi()*Dt^2/4*Lfb);
% i=1 H2, i=2 CO2, i=3 CO, i=4 H2O, i=5 CH4 i=6 Tar, i=7 N2
CH2=V(1)*1000/(U*A);
CCO2=V(2)*1000/(U*A);   %mole/m3,g
CCO=V(3)*1000/(U*A);
CH2O=V(4)*1000/(U*A);
CCH4=V(5)*1000/(U*A);
CTar=V(6)*1000/(U*A);

%   Rxn 1: C+CO2<-->2CO
%   Rxn 2: C+H2O<-->CO+H2
%   Rxn 3: C+2H2<-->CH4
%   Rxn 4: CH4+H2O<-->CO+3H2
%   Rxn 5: CO+H2O<-->CO2+H2
%   Rxn 6: Tar1-->alpha*G2+(1-alpha)*T2

%Only homogeneous reactions occur in freeboard
rate(1)=0;
rate(2)=0;
rate(3)=0;
rate(4)=3*10^5*exp(-125000/R/ Temp)*CCH4*CH2O;          %SMR reaction rate (mole/m3,g/s)
Keq=0.0265*exp(3968/ Temp);
rate(5)=2.78*exp(-1510/ Temp)*(CH2O*CCO-CH2*CCO2/Keq);  %WGS reaction rate (mole/m3,g/s)
```

```
rate(6)=k04*exp(-E4/R/ Temp)*CTar;
 %Heats of reaction are expresssed in integrated forms

if Temp>=1000
    Heat_of_rxn(1)=172.44*1000+(23461*Temp)/25000 - 8400956030975999/(17179869184*Temp) -
    (140407*Temp^2)/25000000 + (58892632407867613*Temp^3)/8854437155380584775680000 -
    (35379552610251659*Temp^4)/773712524553362671811952640 0 -
    (632354825417847759*Temp^5)/158456325028528675187087900672000 0 +
    257078157742470800030976232994768282863091/13833979939014124571997713203200000000;

    Heat_of_rxn(2)=131.3*1000-(19834229022357117157987 5*Temp^6 -
    43383925515129803489601600 00*Temp^5 + 38767961718716207050045521920000*Temp^4 +
    51779170312184118764694341802786816*Temp^3 -
    20234619374093472461171669559033200 6400*Temp^2 +
    18387615117565359445134147666308580975136*Temp +
    10823705904284649776741229412032184320000000)/(22134367902422599315196341125120000
    000*Temp);

    Heat_of_rxn(3)=-74.52*1000-(22246430488538756764091 25*Temp^6 -
    46392736468140931100104320000*Temp^5 + 37761957648800152677787893760 0000*Temp^4 -
    13130116778838962817394714062020935 68*Temp^3 +
    20489819782261244062236157293669384192 00*Temp^2 -
    57627080035241545166969658169571954769 6928*Temp +
    21647411808569299553482458824064368640000000)/(44268735804845198630392682250240000
    000*Temp);

    Heat_of_rxn(4)=205.82*1000+((Temp - 298)*(16357570187084862042 5*Temp^4 -
    33262836457744755139933 50*Temp^3 + 25861890789046375216542544900*Temp^2 -
    11905557430846726915807525135 6504*Temp +
    18408961475835808313738566641993 2048))/396140812571321687967719751 6800000;

    Heat_of_rxn(5)=-41.14*1000+((Temp - 298)*(- 25437460906847732979375*Temp^4 +
    58833995552497928094494625 0*Temp^3 - 52260388270310253908792892175 00*Temp^2 +
    81786991477774896438879805288094 48*Temp +
    26809657383163230237417388831796543504))/29710560942849126597578981376 00000000;

     Heat_of_rxn(6)=-42*94;   %Di Blasi
elseif  Temp<=1000
    Heat_of_rxn(1)=172.44*1000+(17942*Temp)/625 - 8400956030975999/(17179869184*Temp) -
    (239257*Temp^2)/5000000 + (44954709404672071459*Temp^3)/17708874310761169551360 00 -
    (12985903969444631871*Temp^4)/96714065569170333976494080 00 -
    (34252553043466872087*Temp^5)/12379400392853802748991242240000 -
    71744495503840732317340675215427206247/21615593654709569643746426880000000;
```

```
    Heat_of_rxn(2)=131.3*1000-(158798355853364837763043 75*Temp^6 -
    505757619657920629750036000 00*Temp^5 + 590413973959878938869825536000 00*Temp^4 -
    221896922938620394685810725869322 24*Temp^3 -
    996378571127553308173563295747276800 0*Temp^2 +
    184709629830184464968059274385561722409 6*Temp +
    563734682514825509205272365210009600000000)/(11528316615845103809998094336000000000
    *Temp);

    Heat_of_rxn(3)=-74.52*1000+(2705380301236406261*Temp^3)/1106804644422573096960 0 -
    8400956030975999/(17179869184*Temp) - (6437331*Temp^2)/50000000 - (364621*Temp)/50000
    - (27922960112316835931*Temp^4)/151115727451828646838272000 +
    (10118552046531962003*Temp^5)/193428131138340667952988160000 +
    17078030362516169336216501438415889583/16887182542741851284176896000000000;
    Heat_of_rxn(4)=205.82*1000+((Temp - 298)*(- 153395447884564383854062 5*Temp^4 +
    485015217075301976548569375 0*Temp^3 - 541700133031858621228915446250 0*Temp^2 +
    182089210326677128277579353675983 2*Temp +
    912506082548953847790936741080189936))/232113757366008801543585792000000 00;

    Heat_of_rxn(5)=-41.14*1000-((Temp - 298)*(638761740763270032543 75*Temp^4 -
    243332425556210239745096250*Temp^3 + 37198277088759235214661731750 0*Temp^2 -
    278516422522177409499680625213352*Temp +
    33432223693240074893770155639957104))/58028439341502200385896448000000 00;

    Heat_of_rxn(6)=-42*94;   %Di Blasi
end

Rxn_Heat=0;
for k=1:6
   Rxn_Heat=Rxn_Heat+rate(k)*Heat_of_rxn(k);   %(mol/m3.s)(J/mol)=W/m3
end

% i=1 H2, i=2 CO2, i=3 CO, i=4 H2O, i=5 CH4 i=6 Tar, i=7 N2, i=8 Temp
Vdot(1)=At*Rxn_Rate(1,3,U,V(1),V(2),V(3),V(4),V(5),V(6), Temp);
Vdot(2)=At*Rxn_Rate(2,3,U,V(1),V(2),V(3),V(4),V(5),V(6), Temp);
Vdot(3)=At*Rxn_Rate(3,3,U,V(1),V(2),V(3),V(4),V(5),V(6), Temp);
Vdot(4)=At*Rxn_Rate(4,3,U,V(1),V(2),V(3),V(4),V(5),V(6), Temp);
Vdot(5)=At*Rxn_Rate(5,3,U,V(1),V(2),V(3),V(4),V(5),V(6), Temp);
Vdot(6)=At*Rxn_Rate(6,3,U,V(1),V(2),V(3),V(4),V(5),V(6), Temp);
Vdot(7)=0;
Vdot(8)=double(1/(Cp_g*Rhogas*U)*(-Rxn_Heat-h*As*( Temp -Tcool)));

Vdot=Vdot';

end             %function " dFifb_dz "
```

```
function [Ratei,Rchar_cons] = Rxn_Rate(i,phase,U,FH2,FCO2,FCO,FH2O,FCH4,FTar,T1)
global A R m_Bin m_Min Epsi_ave SaiL SaiH L_bed Epsi_L Epsi_H UL UH MW_Tar alpha
wCO_G2 wCO2_G2 wCH4_G2 wH2_G2 MC k04 E4 Y_T Y_V Y_H2 Y_CO Y_CO2 Y_CH4

   % phase=1-->L   & phase=2-->H,  phase=3-->Freeboard
   if phase==1
      CCO2=FCO2*1000/(SaiL*Epsi_L*UL*A);          %Concentartion (mol/m^3,g)
      CH2=FH2*1000/(SaiL*Epsi_L*UL*A);
      CCO=FCO*1000/(SaiL*Epsi_L*UL*A);
      CH2O=FH2O*1000/(SaiL*Epsi_L*UL*A);
      CCH4=FCH4*1000/(SaiL*Epsi_L*UL*A);
      CTar=FTar*1000/(SaiL*Epsi_L*UL*A);
   elseif phase==2
      CCO2=FCO2*1000/(SaiH*Epsi_H*UH*A);          % Concentartion (mol/m^3,g)
      CH2=FH2*1000/(SaiH*Epsi_H*UH*A);
      CCO=FCO*1000/(SaiH*Epsi_H*UH*A);
      CH2O=FH2O*1000/(SaiH*Epsi_H*UH*A);
      CCH4=FCH4*1000/(SaiH*Epsi_H*UH*A);
      CTar=FTar*1000/(SaiH*Epsi_H*UH*A);
   elseif phase==3
      CCO2=FCO2*1000/(U*A);                       %Concentartion (mol/m^3,g)
      CH2=FH2*1000/(U*A);
      CCO=FCO*1000/(U*A);
      CH2O=FH2O*1000/(U*A);
      CCH4=FCH4*1000/(U*A);
      CTar=FTar*1000/(U*A);
   end

   PCO2=CCO2*(R*T1);                              %Partial pressure (Pa)
   PH2=CH2*(R*T1);
   PH2O=CH2O*(R*T1);

   % Biomass dying & pyrolysis product  yields
   % Biomass--> Tar (Bio-oil)
   Ftar_pyro=Y_T*(m_Bin+m_Min)/MW_Tar*1000;       %mol/s
   % Biomass--> Gas (H2,CO,CO2,CH4)
   FH2_pyro=Y_H2*(m_Bin+m_Min)/2*1000;            %mol/s
   FCO_pyro=Y_CO*(m_Bin+m_Min)/28*1000;           %mol/s
   FCO2_pyro=Y_CO2*(m_Bin+m_Min)/44*1000;         %mol/s
   FCH4_pyro=Y_CH4*(m_Bin+m_Min)/16*1000;         %mol/s
   %Moisture-->Vapour
   FH2O_pyro=Y_V*(m_Bin+m_Min)/18*1000;           %mol/s

   %Gasification reaction
```

```
% Boudourd: C+CO2<-->2CO
rC1=3.1*10^6*exp(-215000/R/T1)*(PCO2/10^5)^0.38;                %1/s   (Barrio et al.)

% Water_Gas:C+H2O<-->CO+H2
rC2=2.62*10^8*exp(-237000/R/T1)*(PH2O/10^5)^0.57;               %1/s    (Barrio et al.)

% Methanation:C+2H2<-->CH4
rC3=16.4*exp(-94800/R/T1)*(PH2/10^6)^0.93;                      %1/s

%Overall char consumption rate in emulsion phase (1/s)
if phase==2
   Rchar_cons=(rC1+rC2+rC3);
else
   Rchar_cons=0;
end

% SMR:CH4+H2O<-->CO+3H2
rSMR=3*10^5*exp(-125000/R/T1)*CCH4*CH2O;                        %mole/m3,g/s (Gomez et al.)

% WGS:CO+H2O<-->CO2+H2
Keq=0.0265*exp(3968/T1);
rWGS=2.78*exp(-1510/T1)*(CH2O*CCO-CH2*CCO2/Keq);                %mole/m3,g/s   (Biba et al.)

% Tar cracking:Tar1-->alpha*G2+(1-alpha)*T2
rtar_crack=k04*exp(-E4/R/T1)*CTar;                              %mol/m3,g/s     (Boronson or Liden)
% From Boroson et al, aplha=0.78 and sencondary gas (G2=CO,CO2,H2,CH4)
wCO_G2=0.5633/0.78;
wCO2_G2=0.1109/0.78;
wCH4_G2=0.0884/0.78;
wH2_G2=0.0173/0.78;

if phase==1
   %No biomass pyrolysis in the solid-free bubble phase
   rtar_pyro=0;                    %mole/m3,L-phase/s
   rH2_pyro=0;
   rH2O_pyro=0;
   rCO_pyro=0;
   rCO2_pyro=0;
   rCH4_pyro=0;
   rC1=rC1*(1-Epsi_L)*(MC/MWchar*1000)/((1-Epsi_ave)*(A*L_bed));
   rC2=rC2*(1-Epsi_L)*(MC/MWchar*1000)/((1-Epsi_ave)*(A*L_bed));
   rC3=rC3*(1-Epsi_L)*(MC/MWchar*1000)/((1-Epsi_ave)*(A*L_bed));
   rSMR=rSMR*Epsi_L;
   rWGS=rWGS*Epsi_L;
```

```
   rtar_crack=rtar_crack*Epsi_L;
elseif phase==2
   %Biomass pyrolysis products are uniformly released to the emulsion phase
   rtar_pyro=Ftar_pyro/(SaiH*A*L_bed);          %mole/m3,H-phase/s
   rH2_pyro=FH2_pyro/(SaiH*A*L_bed);
   rH2O_pyro=FH2O_pyro/(SaiH*A*L_bed);
   rCO_pyro=FCO_pyro/(SaiH*A*L_bed);
   rCO2_pyro=FCO2_pyro/(SaiH*A*L_bed);
   rCH4_pyro=FCH4_pyro/(SaiH*A*L_bed);
   rC1=rC1*(1-Epsi_H)*(MC/MWchar*1000)/((1-Epsi_ave)*(A*L_bed));
   rC2=rC2*(1-Epsi_H)*(MC/MWchar*1000)/((1-Epsi_ave)*(A*L_bed));
   rC3=rC3*(1-Epsi_H)*(MC/MWchar*1000)/((1-Epsi_ave)*(A*L_bed));
   rSMR=rSMR*Epsi_H;
   rWGS=rWGS*Epsi_H;
   rtar_crack=rtar_crack*Epsi_H;
elseif phase==3
   %No biomass pyrolysis in the solid-free freeboard
   rtar_pyro=0;
   rH2_pyro=0;
   rH2O_pyro=0;                    %mole/s
   rCO_pyro=0;                     %mole/s
   rCO2_pyro=0;                    %mole/s
   rCH4_pyro=0;                    %mole/s
   rC1=0;
   rC2=0;
   rC3=0;
   rSMR=rSMR*1;
   rWGS=rWGS*1;
   rtar_crack=rtar_crack*1;    %tar cracking in freeboard
end

%Net reaction rate of species (kmol/m^3,phase/s)
if i==1      %H2
   Ratei=(rH2_pyro+rC2-2*rC3+3*rSMR+rWGS+(1-alpha)*wH2_G2*(MW_Tar/2)*rtar_crack)/1000;
end
if i==2      %CO2
   Ratei=(rCO2_pyro-rC1+rWGS+(1-alpha)*wCO2_G2*(MW_Tar/44)*rtar_crack)/1000;
end
if i==3      %CO
   Ratei=(rCO_pyro+2*rC1+rC2+rSMR-rWGS+(1-alpha)*wCO_G2*(MW_Tar/28)*rtar_crack)/1000;
end
if i==4      %H2O
   Ratei=(rH2O_pyro-rC2-rSMR-rWGS)/1000;
end
```

```
   if i==5       %CH4
      Ratei=(rCH4_pyro+rC3-rSMR+(1-alpha)*wCH4_G2*(MW_Tar/16)*rtar_crack)/1000;
   end
   if i==6       %CTar
      Ratei=(rtar_pyro-(1-alpha)*rtar_crack)/1000;
   end

end              %function "Rxn_Rate "

function H2_Enthalpy=H_H2(T)
   if (T>=1000)
      a1=2.93286579E+00;  a2=8.26607967E-04;  a3=-1.46402335E-07; a4=1.54100359E-11;
      a5=-6.88804432E-16; a6=-8.13065597E+02;
   end
   if (T<=1000)
      a1=2.34433112E+00;  a2=7.98052075E-03;  a3=-1.94781510E-05; a4=2.01572094E-08;
      a5=-7.37611761E-12; a6=-9.17935173E+02;
   end
   H2_Enthalpy=(8.314*T)*(a1+a2/2*T+a3/3*T^2+a4/4*T^3+a5/5*T^4+a6/T);   %(kJ/kmol)
end

function CO_Enthalpy=H_CO(T)
   if T>=1000
      a1=3.04848583E+00;  a2=1.35172818E-03;  a3=-4.85794075E-07; a4=7.88536486E-11;
      a5=-4.69807489E-15; a6=-1.42661171E+04;
   end
   if T<=1000
      a1=3.57953347E+00;  a2=-6.10353680E-04; a3=1.01681433E-06;  a4=9.07005884E-10;
      a5=-9.04424499E-13; a6=-1.43440860E+04;
   end
   CO_Enthalpy=(8.314*T)*(a1+a2/2*T+a3/3*T^2+a4/4*T^3+a5/5*T^4+a6/T);   %(kJ/kmol)
end

function CO2_Enthalpy=H_CO2(T)
   if T>=1000
      a1=4.63659493E+00;  a2=2.74131991E-03;  a3=-9.95828531E-07; a4=1.60373011E-10;
      a5=-9.16103468E-15; a6=-4.90249341E+04;
   end
   if T<=1000
      a1=2.35677352E+00;  a2=8.98459677E-03;  a3=-7.12356269E-06; a4=2.45919022E-09;
      a5=-1.43699548E-13; a6=-4.83719697E+04;
   end
   CO2_Enthalpy=(8.314*T)*(a1+a2/2*T+a3/3*T^2+a4/4*T^3+a5/5*T^4+a6/T);   %(kJ/kmol)
end
```

```
 function CH4_Enthalpy=H_CH4(T)
   if T>=1000
      a1=1.63552643E+00;  a2=1.00842795E-02;  a3=-3.36916254E-06; a4=5.34958667E-10;
      a5=-3.15518833E-14; a6=-1.00056455E+04;
   end


   if T<=1000
      a1=5.14987613E+00;  a2=-1.36709788E-02; a3=4.91800599E-05;  a4=-4.84743026E-08;
      a5=1.66693956E-11;  a6=-1.02466476E+04;
   end
   CH4_Enthalpy=(8.314*T)*(a1+a2/2*T+a3/3*T^2+a4/4*T^3+a5/5*T^4+a6/T);   %(kJ/kmol)
end

function O2_Enthalpy=H_O2(T)
   if T>=1000
      a1=3.66096083E+00;  a2=6.56365523E-04;  a3=-1.41149485E-07; a4=2.05797658E-11;
      a5=-1.29913248E-15; a6=-1.21597725E+03;
   end
   if T<=1000
      a1=3.78245636E+00;  a2=-2.99673415E-03; a3=9.84730200E-06;  a4=-9.68129508E-09;
      a5=3.24372836E-12;  a6=-1.06394356E+03;
   end
   O2_Enthalpy=(8.314*T)*(a1+a2/2*T+a3/3*T^2+a4/4*T^3+a5/5*T^4+a6/T);   %(kJ/kmol)
end

function N2_Enthalpy=H_N2(T)
   if T>=1000
      a1=2.95257626E+00;  a2=1.39690057E-03;  a3=-4.92631691E-07; a4=7.86010367E-11;
      a5=-4.60755321E-15; a6=-9.23948645E+02;
   end
   if T<=1000
      a1=3.53100528E+00;  a2=-1.23660987E-04; a3=-5.02999437E-07; a4=2.43530612E-09;
      a5=-1.40881235E-12; a6=-1.04697628E+03;
   end
   N2_Enthalpy=(8.314*T)*(a1+a2/2*T+a3/3*T^2+a4/4*T^3+a5/5*T^4+a6/T);   %(kJ/kmol)
end

function Sand_Enthalpy=H_sand(T)
   if (T>298.15 && T<1000)
      a1=6.86099160E+00; a2=-2.47320880E-02;  a3=9.59213240E-05;  a4=-1.11018800E-07;
      a5=4.13248490E-11;  a6=-1.11098590E+05;
   end
   if (T>1000 && T<1700)
```

```
      a1=5.59194200E+01; a2=-1.44862260E-01;  a3=1.61961260E-04;  a4=-7.89418770E-08;
      a5=1.42797310E-11;  a6=-1.24715460E+05;
   end
   MWSiO2=60.084;
   Sand_Enthalpy=(8.314*T/MWSiO2)*(a1+a2/2*T+a3/3*T^2+a4/4*T^3+a5/5*T^4+a6/T);
%(kJ/kmol)/(kg/kmol)
end

function CaO_Enthalpy=H_CaO(T)
   if (T>298.15 && T<1000)
      a1=1.57835230E+00;  a2=1.88151540E-02;  a3=-2.97951290E-05; a4=2.18940890E-08;
      a5=-6.03660530E-12; a6=-7.74680640E+04;
   end
   if (T>1000 && T<3200)
      a1=5.14514060E+00;  a2=2.11373130E-03;  a3=-1.09159190E-06; a4=3.24128320E-10;
      a5=-3.55478970E-14; a6=-7.80597080E+04;
   end
   MWCaO=56;
   CaO_Enthalpy=(8.314*T/MWCaO)*(a1+a2/2*T+a3/3*T^2+a4/4*T^3+a5/5*T^4+a6/T);
%(kJ/kmol)/(kg/kmol)
end

function CaCO3_Enthalpy=H_CaCO3(T)
   if (T>=298.15 && T<700)
      a1=-5.04743680E+00; a2=9.37488070E-02;  a3=-1.96914510E-04; a4=1.97711220E-07;
      a5=-7.56953080E-11; a6=-1.46438360E+05;
   end
   if (T>700 && T<1200)
      a1=3.78466800E+00;  a2=3.22493500E-02;  a3=-4.14936350E-05; a4=2.71805430E-08;
      a5=-6.75192900E-12; a6=-1.47404610E+05;
   end
   MWCaCO3=100;
   CaCO3_Enthalpy=(8.314*T/MWCaCO3)*(a1+a2/2*T+a3/3*T^2+a4/4*T^3+a5/5*T^4+a6/T);
%(kJ/kmol)/(kg/kmol)
end

function Fuel_Enthalpy=H_fuel(T)
   wC=0.425;
   wH=0.063;
   wO=0.512;
   wN=0;
   wS=0;
   LHV=34835*wC+93870*wH-10800*wO+6280*wN+10465*wS;   %kJ/kg
   DeltaH298_CO2=-393.51;
```

```
    DeltaH298_H2O=-241.83;
    DeltaH298_SO2=-296.84;   %kJ/mol

     DeltaH298_fuel=LHV+(wC/12*DeltaH298_CO2+wH/2*DeltaH298_H2O+wS/32*DeltaH298_SO2)*
     1000;
    Fuel_Enthalpy=DeltaH298_fuel+0;   %kJ/kg
end

function Tar_Enthalpy=H_Tar(T)
   %Approximating Tar=C6H6O
    wC=(6*12)/94;
    wH=(6*1)/94;
    wO=(1*16)/94;
    wN=0;
    wS=0;
    LHV_Tar=34835*wC+93870*wH-10800*wO+6280*wN+10465*wS;   %kJ/kg
    DeltaH298_CO2=-393.51;
    DeltaH298_H2O=-241.83;
    DeltaH298_SO2=-296.84;   %kJ/mol

     DeltaH298_Tar=LHV_Tar+(wC/12*DeltaH298_CO2+wH/2*DeltaH298_H2O+wS/32*DeltaH298_S
     O2)*1000;

       Cp_Tar=-100+4.4*T-1.57*10^-3*T^2;         %J/kg.K

     Tar_Enthalpy=DeltaH298_Tar+(-100*T+4.4*1/2*T^2-1.57*10^-3*1/3*T^3)/1000-
     (-100*298+4.4*1/2*298^2-1.57*10^-3*1/3*298^3)/1000;   %kJ/kg
    Tar_Enthalpy=Tar_Enthalpy*78;  %kJ/kg*kg/kmol
end

function Char_Enthalpy=H_char(T)
%Assuming Char=pure carbon
    wC=1;
    wH=0;
    wO=0;
    wN=0;
    wS=0;
    LHV=34835*wC+93870*wH-10800*wO+6280*wN+10465*wS;   %kJ/kg
    DeltaH298_CO2=-393.51;
    DeltaH298_H2O=-241.83;
    DeltaH298_SO2=-296.84;   %kJ/mol

     DeltaH298_char=LHV+(wC/12*DeltaH298_CO2+wH/2*DeltaH298_H2O+wS/32*DeltaH298_SO2)
     *1000;
```

```
    Char_Enthalpy=DeltaH298_char+8.314/12*(380/(exp(380/T)-1)+21800/(exp(1800/T)-1))-
    8.314/12*(380/(exp(380/298.15)-1)+21800/(exp(1800/298.15)-1));   %kJ/kg
end

function   H_H2O=H_IAPWS(region,P,T)   %P:Pa, T:K, H:kJ/kg
   if region==1
      Rr=0.461526;  %kJ/kg/K
      Pi=P/10^6/16.53;
      Taw=1386/T;

      i=1; I(i)=0; J(i)=-2; n(i)=0.14632971213167;
      i=2; I(i)=0; J(i)=-1; n(i)=-0.84548187169114;
      i=3; I(i)=0; J(i)=0; n(i)=-0.37563603672040*10^1;
      i=4; I(i)=0; J(i)=1; n(i)=0.33855169168385*10^1;
      i=5; I(i)=0; J(i)=2; n(i)=-0.95791963387872;
      i=6; I(i)=0; J(i)=3; n(i)=0.15772038513228;
      i=7; I(i)=0; J(i)=4; n(i)=-0.16616417199501*10^-1;
      i=8; I(i)=0; J(i)=5; n(i)=0.81214629983568*10^-3;
      i=9; I(i)=1; J(i)=-9; n(i)=0.28319080123804*10^-3;
      i=10; I(i)=1; J(i)=-7; n(i)=-0.60706301565874*10^-3;
      i=11; I(i)=1; J(i)=-1; n(i)=-0.18990068218419*10^-1;
      i=12; I(i)=1; J(i)=0; n(i)=-0.32529748770505*10^-1;
      i=13; I(i)=1; J(i)=1; n(i)=-0.21841717175414*10^-1;
      i=14; I(i)=1; J(i)=3; n(i)=-0.52838357969930*10^-4;
      i=15; I(i)=2; J(i)=-3; n(i)=-0.47184321073267*10^-3;
      i=16; I(i)=2; J(i)=0; n(i)=-0.30001780793026*10^-3;
      i=17; I(i)=2; J(i)=1; n(i)=0.47661393906987*10^-4;
      i=18; I(i)=2; J(i)=3; n(i)=-0.44141845330846*10^-5;
      i=19; I(i)=2; J(i)=17; n(i)=-0.72694996297594*10^-15;
      i=20; I(i)=3; J(i)=-4; n(i)=-0.31679644845054*10^-4;
      i=21; I(i)=3; J(i)=0; n(i)=-0.28270797985312*10^-5;
      i=22; I(i)=3; J(i)=6; n(i)=-0.85205128120103*10^-9;
      i=23; I(i)=4; J(i)=-5; n(i)=-0.22425281908000*10^-5;
      i=24; I(i)=4; J(i)=-2; n(i)=-0.65171222895601*10^-6;
      i=25; I(i)=4; J(i)=10; n(i)=-0.14341729937924*10^-12;
      i=26; I(i)=5; J(i)=-8; n(i)=-0.40516996860117*10^-6;
      i=27; I(i)=8; J(i)=-11; n(i)=-0.12734301741641*10^-8;
      i=28; I(i)=8; J(i)=-6; n(i)=-0.17424871230634*10^-9;
      i=29; I(i)=21; J(i)=-29; n(i)=-0.68762131295531*10^-18;
      i=30; I(i)=23; J(i)=-31; n(i)=0.14478307828521*10^-19;
      i=31; I(i)=29; J(i)=-38; n(i)=0.26335781662795*10^-22;
      i=32; I(i)=30; J(i)=-39; n(i)=-0.11947622640071*10^-22;
      i=33; I(i)=31; J(i)=-40; n(i)=0.18228094581404*10^-23;
      i=34; I(i)=32; J(i)=-41; n(i)=-0.93537087292458*10^-25;
```

```
    Sum=0;
    for i=1:34
       Sum=Sum+n(i)*(7.1-Pi)^I(i)*J(i)*(Taw-1.222)^(J(i)-1);
    end
    H_H2O=Rr*T*Taw*Sum;
elseif region==2
    Rr=0.461526;  %kJ/kg/K
    Pi=P/10^6/1;
    Taw=540/T;

    i=1;  J0(i)=0;  n0(i)=-0.96927686500217*10^1;
    i=2;  J0(i)=1;  n0(i)=0.10086655968018*10^2;
    i=3;  J0(i)=-5; n0(i)=-0.56087911283020*10^-2;
    i=4;  J0(i)=-4; n0(i)=0.71452738081455*10^-1;
    i=5;  J0(i)=-3; n0(i)=-0.40710498223928;
    i=6;  J0(i)=-2; n0(i)=0.14240819171444*10^1;
    i=7;  J0(i)=-1; n0(i)=-0.43839511319450*10^1;
    i=8;  J0(i)=2;  n0(i)=-0.28408632460772;
    i=9;  J0(i)=3;  n0(i)=0.21268463753307*10^-1;

    i=1; I(i)=1;  J(i)=0; n(i)=-0.17731742473213*10^-2;
    i=2; I(i)=1;  J(i)=1; n(i)=-0.17834862292358*10^-1;
    i=3; I(i)=1;  J(i)=2; n(i)=-0.45996013696365*10^-1;
    i=4; I(i)=1;  J(i)=3; n(i)=-0.57581259083432*10^-1;
    i=5; I(i)=1;  J(i)=6; n(i)=-0.50325278727930*10^-1;
    i=6; I(i)=2;  J(i)=1; n(i)=-0.33032641670203*10^-4;
    i=7; I(i)=2;  J(i)=2; n(i)=-0.18948987516315*10^-3;
    i=8; I(i)=2;  J(i)=4; n(i)=-0.39392777243355*10^-2;
    i=9; I(i)=2;  J(i)=7; n(i)=-0.43797295650573*10^-1;
    i=10; I(i)=2; J(i)=36; n(i)=-0.26674547914087*10^-4;
    i=11; I(i)=3;  J(i)=0; n(i)=0.20481737692309*10^-7;
    i=12; I(i)=3;  J(i)=1; n(i)=0.43870667284435*10^-6;
    i=13; I(i)=3;  J(i)=3; n(i)=-0.32277677238570*10^-4;
    i=14; I(i)=3;  J(i)=6; n(i)=-0.15033924542148*10^-2;
    i=15; I(i)=3; J(i)=35; n(i)=-0.40668253562649*10^-1;
    i=16; I(i)=4;  J(i)=1; n(i)=-0.78847309559367*10^-9;
    i=17; I(i)=4;  J(i)=2; n(i)=0.12790717852285*10^-7;
    i=18; I(i)=4;  J(i)=3; n(i)=0.48225372718507*10^-6;
    i=19; I(i)=5;  J(i)=7; n(i)=0.22922076337661*10^-5;
    i=20; I(i)=6;  J(i)=3; n(i)=-0.16714766451061*10^-10;
    i=21; I(i)=6; J(i)=16; n(i)=-0.21171472321355*10^-2;
    i=22; I(i)=6; J(i)=35; n(i)=-0.23895741934104*10^2;
    i=23; I(i)=7;  J(i)=0; n(i)=-0.59059564324270*10^-17;
    i=24; I(i)=7; J(i)=11; n(i)=-0.12621808899101*10^-5;
```

```
        i=25; I(i)=7; J(i)=25; n(i)=-0.38946842435739*10^-1;
        i=26; I(i)=8;  J(i)=8; n(i)=0.11256211360459*10^-10;
        i=27; I(i)=8; J(i)=36; n(i)=-0.82311340897998*10^1;
        i=28; I(i)=9; J(i)=13; n(i)=0.19809712802088*10^-7;
        i=29; I(i)=10; J(i)=4; n(i)=0.10406965210174*10^-18;
        i=30; I(i)=10; J(i)=10; n(i)=-0.10234747095929*10^-12;
        i=31; I(i)=10; J(i)=14; n(i)=-0.10018179379511*10^-8;
        i=32; I(i)=16; J(i)=29; n(i)=-0.80882908646985*10^-10;
        i=33; I(i)=16; J(i)=50; n(i)=0.10693031879409;
        i=34; I(i)=18; J(i)=57; n(i)=-0.33662250574171;
        i=35; I(i)=20; J(i)=20; n(i)=0.89185845355421*10^-24;
        i=36; I(i)=20; J(i)=35; n(i)=0.30629316876232*10^-12;
        i=37; I(i)=20; J(i)=48; n(i)=-0.42002467698208*10^-5;
        i=38; I(i)=21; J(i)=21; n(i)=-0.59056029685639*10^-25;
        i=39; I(i)=22; J(i)=53; n(i)=0.37826947613457*10^-5;
        i=40; I(i)=23; J(i)=39; n(i)=-0.12768608934681*10^-14;
        i=41; I(i)=24; J(i)=26; n(i)=0.73087610595061*10^-28;
        i=42; I(i)=24; J(i)=40; n(i)=0.55414715350778*10^-16;
        i=43; I(i)=24; J(i)=58; n(i)=-0.94369707241210*10^-6;

        Sum1=0;
        for i=1:9
           Sum1=Sum1+n0(i)*J0(i)*Taw^(J0(i)-1);
        end
        Sum2=0;
        for i=1:43
           Sum2=Sum2+n(i)*Pi^I(i)*J(i)*(Taw-0.5)^(J(i)-1);
        end
        H_H2O=Rr*T*Taw*(Sum1+Sum2);
    end
end             %function " H_IAPWS "
```

Appendix G MATLAB code for lime-enhance biomass gasification

A model is developed in this appendix to capture the essence of integrated biomass gasification with cyclic CO_2 capture in a dual fluidized bed reactor, with limestone particles constituting all or a fraction of the bed material. Conversion of solid biomass particles to the dominant gaseous products (H_2, CO, CH_4 and CO_2) is modeled by a simple stoichiometric equilibrium model. By adopting an empirical kinetic model for the carbonation rate of limestone particles from the literature, the effect of sorbent loss of reactivity due to sintering during cyclic operation is also taken into account.

```
function Lime_Enhanced_Equilibrium_Gasification
clc
R=8.314;
T0=25+273.15;
P0=10^5;
 %Biomass fuel ultimate analysis
wC_F=0.425;
wH_F=0.063;
wO_F=0.512;
wN_F=0;
wS_F=0;
LHV_F=34835*wC_F+93870*wH_F-10800*wO_F+6280*wN_F+10465*wS_F;          % (kJ/kg)
Tfuel=25+273.15;
Pfuel=1.01325*10^5;                          %Pa
Tcarb=700+273.15;                            %Gasifier/carbonator temperature (K)
Tgas=Tcarb;
Tsteam=Tgas;                                 %Superheated steam temperature
Pcarb=101.325;                               %Carbonator pressure (kPa)
Tcomb=900+273.15;                            %Combustor temperature (K)
Psteam=1.01325*10^5;
Tair=400+273.15;
Landa=1.2;                                   %Stoichiometric O2 ratio (20% excess)
W_bed=100;                                   %Gasifier inventory (kg)
A_riser=pi()*0.1^2/4;                        %Riser cross-sectional area (m2)
Wet_Fuel=10;                                 %Wet biomass feeding rate (kg/h)
Moisture=0.10*Wet_Fuel;                      %10% biomass moisture content
Fuel=Wet_Fuel-Moisture;                      %Dry biomass feeding rate (kg/h)
Steam=10;                                    %Superheated steam flo rate (kg/h)
S_B=(Moisture+Steam)/Fuel;                   %Steam to biomass ratio
Qloss_gas=15/100*(Fuel*LHV_F);               %Heat loss from the gasifier (kJ/h)
Qloss_comb=15/100*(Fuel*LHV_F);              %Heat loss from the combustor (kJ/h)

k0_char=1.08*10^7;                           %(1/s)
```

```
E_char=121000;                          %(J/mol)
k_char=k0_char*exp(-E_char/R/Tgas);

k0_gas=1.3*10^8;
E_gas=140000;
k_gas=k0_gas*exp(-E_gas/R/Tgas);

k0_tar=2*10^8;
E_tar=133000;
k_tar=k0_tar*exp(-E_tar/R/Tgas);

Char_frac=k_char/(k_char+k_gas+k_tar);
Char=Char_frac*Fuel;                    %Char mass flow rate (kg/h)

%Definition of variables
m_fuel = sym('m_fuel');                 %Biomass feed flow rate (kg/h)
m_char = sym('m_char');                 %Char mass flow rate leaving the gasifier (kg/h)
m_makeup = sym('m_makeup');             %Sorbent make-up flow rate enetering the calciner (kg/h)
m_moisture = sym('m_moisture');         %Biomass moisture flow rate(kg/h)
m_steam = sym('m_steam');               %Superheated steam flow rate entering the gasifier(kg/h)
m_purge = sym('m_purge');               %Sorbent purge flow rate exiting the gasifier (kg/h)
m12 = sym('m12');                       %Sorbent mass flow rate from calciner to carbonator (kg/h)
m21=sym('m21');                         %Sorbent mass flow rate from carbonator to calciner (kg/h)
wCaCO3 = sym('wCaCO3');                 %Weight fraction of CaCO3 in sorbent streams exiting the gasifier
(kg/h)
FCO2_Cal= sym('FCO2_Cal');              %Molar flow rate of CO2 released from sorbent calcination (kmol/h)
Fp2 = sym('Fp2');                       %Molar flow rate of product gas leaving the carbonator (kmol/h)
P=sym('P');                             %Gasifier pressure (atm)
yCO2= sym('yCO2');                      %CO2 mole fraction in product gas
yCO= sym('yCO');                        %CO mole fraction in product gas
yCH4= sym('yCH4');                      %CH4 mole fraction in product gas
yH2O= sym('yH2O');                      %H2O mole fraction in product gas
yH2= sym('yH2');                        %H2 mole fraction in product gas
wC=sym('wC');                           %Elemental carbon mass fraction in dry-ash-free biomass
wO=sym('wO');                           %Elemental oxygen mass fraction in dry-ash-free biomass
wH=sym('wH');                           %Elemental hydrogen mass fraction in dry-ash-free biomass
kWGS=sym('kWGS');                       %Equilibrium constant for WGS
kSMR=sym('kSMR');                       %Equilibrium constant for SMR
%**************Solving system of algebraic equations for non-enhanced gasification***************
L=solve(subs(m_fuel*wC/12-m_char/12-Fp2*(yCO2+yCO+yCH4),
            {m_fuel,wC,m_char},{Fuel,wC_F,Char}),...
        subs(m_fuel*wH/1+(m_moisture+m_steam)*2/18-Fp2*(yH2*2+yH2O*2+yCH4*4),
            {m_fuel,wH,m_moisture,m_steam},{Fuel,wH_F,Moisture,Steam}),...
        subs(m_fuel*wO/16+(m_moisture+m_steam)/18-Fp2*(yH2O+yCO+yCO2*2),
```

```
            {m_fuel,wO,m_moisture,m_steam},{Fuel,wO_F,Moisture,Steam}),...
        subs(yCO2+yCO+yCH4+yH2O+yH2-1),...
        subs(kWGS-yCO2*yH2/(yCO*yH2O),{kWGS},{exp(4400/Tcarb-4.036)}),...
        subs(kSMR-yCO*yH2^3/(yCH4*yH2O)*P^2,
            {kSMR,P},{exp(-26830/Tcarb+30.114),Pcarb/10^2}));

%Selecting acceptable (non-imaginary) answers
j1=0;
sol=0;
for i=1:8
   if double(L.yCO2(i))>0 && double(L.yCO2(i))<1
      if double(L.yCO(i))>0 && double(L.yCO(i))<1
         if double(L.yCH4(i))>0 && double(L.yCH4(i))<1
            if double(L.yH2O(i))>0 && double(L.yH2O(i))<1
               if double(L.yH2(i))>0 && double(L.yH2(i))<1
                  sol=sol+1;
                  j1=i;
               end
            end
         end
      end
   end
end
if sol>1
   input('Non-enhanced gasification: multiple answers!')
end

YCO2=double(L.yCO2(j1));
YCO=double(L.yCO(j1));
YCH4=double(L.yCH4(j1));
YH2O=double(L.yH2O(j1));
YH2=double(L.yH2(j1));
FPG=double(L.Fp2(j1));     %Product gas flow rate (kmol/h)

%******Energy balance for the gasifier: Non-enhanced**************************************
%Formulation and enthalpies are discussed in script "DFB_Gasifier"
m_sand=(Fuel*H_fuel(Tfuel)+Moisture*H_moisture+Steam*H_steamIN-Char*H_char(Tgas)-Qloss_gas
-FPG*(YH2*H_H2(Tgas)+YCO*H_CO(Tgas)+YCO2*H_CO2(Tgas)+YCH4*H_CH4(Tgas)+
YH2O*MWH2O*H_steamOUT))/(H_sand(Tgas)-H_sand(Tcomb));

Gs=(m_sand+Char)/3600/A_riser;          %Solids mass flux per riser cross-section (kg/m^2/s)
TawS=W_bed/((m_sand+Char)/3600);        %Mean solids residence time in gasifier (s)
Wsand=m_sand/(m_sand+Char);             %Sand weight fraction in gasifier
Wchar=Char/(m_sand+Char);               %Char weight fraction in gasifier
```

```
%******Energy balance for the riser: complete combustion ************************************
% FCH4_in*H_CH4(Tair)+FO2_in*H_O2(Tair)+FN2*H_N2(Tair)+Char*H_char(Tgas)+
m_sand*H_sand(Tgas)-m_sand*H_sand(Tcomb)-(FN2*H_N2(Tcomb)+FO2_comb*H_O2(Tcomb)
+FCO2_comb*H_CO2(Tcomb)+FH2O_comb*MWH2O*H_steamOUT2)-Qloss_comb=0

% FO2_in=Landa*(2*FCH4_in+Char/12)   %kmol/hr
% FN2=79/21*FO2_in
% FO2_comb=FO2_in-2*FCH4_in-Char/12
% FO2_comb=(Landa-1)*(2*FCH4_in+Char/12)
% FCO2_comb=FCH4_in+Char/12
% FH2O_comb=2*FCH4_in
%Upon rearrangement (Refer to script "DFB_Gasifier")
FCH4_in=-(Landa*(Char/12)*H_O2(Tair)+79/21*Landa*(Char/12)*H_N2(Tair)+Char*H_char(Tgas)
+m_sand*H_sand(Tgas)+ -m_sand*H_sand(Tcomb)-(79/21*Landa*(Char/12)*H_N2(Tcomb)
+(Landa-1)*(Char/12)*H_O2(Tcomb)+(Char/12)*H_CO2(Tcomb))-Qloss_comb)/
(H_CH4(Tair)+Landa*2*H_O2(Tair)+79/21*Landa*2*H_N2(Tair)-79/21*Landa*2*H_N2(Tcomb)-
(Landa-1)*2*H_O2(Tcomb)-H_CO2(Tcomb)-2*MWH2O*H_steamOUT2);

FO2_in=Landa*(2*FCH4_in+Char/12);                    %kmol/hr
FN2=79/21*FO2_in;
FO2_comb=(Landa-1)*(2*FCH4_in+Char/12) ;
FCO2_comb=FCH4_in+Char/12;
FH2O_comb=2*FCH4_in;
F_total=100/21*FO2_in+FCH4_in;

Uriser=F_total*R*Tcomb/(P0*A_riser)*1000/3600;       %Superficial gas velocity in riser (m/s)
QairN=100/21*FO2_in*R*273.15*1000/P0;                %Required air flow rate in riser (Nm3/hr)
QCH4N=FCH4_in*R*273.15*1000/P0 ;                     %Required NG flow rate in riser (Nm3/hr)

LHVPG=(YH2*10.789+YCO*12.625+YCH4*35.793)/(YH2+YCO2+YCO+YCH4);     % (MJ/NM3)
QPGN=(YH2+YCO2+YCO+YCH4)*FPG*R*273.15*1000/P0;       %Product gas flow rate (NM3/hr)
QH2N=YH2*FPG*R*273.15*1000/P0;                       %Generated H2 flow rate (NM3/hr)
EttaCGE=(QPGN*LHVPG*1000-QCH4N*35.793*1000)/(Fuel*LHV_F);         %Cold gas efficiency
EttaH2=(QH2N*10.789*1000-QCH4N*35.793*1000)/(Fuel*LHV_F);         %H2 efficiency

 %***********Lime-enhanced biomass gasification*****************************
PCO2=Pcarb*double(L.yCO2(j1));         %CO2 partial pressure in the gasifier (kPa)
PCO2_eq=10^(-8308/Tcarb+9.079);        %Equilibrium CO2 partial pressure(kPa)

Makeup=0.1*Fuel;              %Sorbent make-up flow rate enetering the calciner (kg/h)
CR=4;                         %The ratio of sorbent circulation flow rate to biomass feed rate (m12/m_fuel)

if PCO2<=PCO2_eq
   input('Partial pressure of CO2 is lower than equilibrium: Carbonation cannot occur!')
```

```
   Xave=0;                        %Average carbonation conversion
else
%input('Partial pressure of CO2 is higher than equilibrium: Carbonation can occur!')
   % While loop for convergence to avarage carbonation conversion
   N=0;
   Xave=0;
   Xave0=0.5;
   while abs(Xave0-Xave)>10^-6
      Xave0=Xave;
      N=N+1;
      Xr=0.075;
      k=0.52;
      X(N)=1/(1/(1-Xr)+k*N)+Xr;
      alpha1=(Makeup/100)/(CR*Fuel/56);
      alpha(N)=alpha1*(1-alpha1)^(N-1);
      Xave=Xave+alpha(N)*X(N);
   end
end

WCaCO3=100*Xave/(44*Xave+56);       %Weight fraction of CaCO3 in (m21+m_purge) (kg/h)
%**************Solving system of algebraic equations for Lime-enhanced gasification**********
I=solve(subs(m_makeup/100+m21*(wCaCO3/100+(1-wCaCO3)/56)-m12/56,
                {m_makeup,m12,wCaCO3},{Makeup,CR*Fuel,WCaCO3}),...
            subs(m_makeup/100+m21*wCaCO3/100-FCO2_Cal,
                {m_makeup,m_char,wCaCO3},{Makeup,Char,WCaCO3}),...
            subs(m12/56-(m_purge+m21)*(wCaCO3/100+(1-wCaCO3)/56),
                {m12,m_makeup,wCaCO3},{CR*Fuel,Makeup,WCaCO3}),...
            subs(m_fuel*wC/12-(m_purge+m21)*wCaCO3/100-m_char/12-Fp2*(yCO2+yCO+yCH4),
                {m_fuel,wC,m_char,wCaCO3},{Fuel,wC_F,Char,WCaCO3}),...
            subs(m_fuel*wH/1+(m_moisture+m_steam)*2/18-Fp2*(yH2*2+yH2O*2+yCH4*4),
                {m_fuel,wH,m_moisture,m_steam},{Fuel,wH_F,Moisture,Steam}),...
           subs(m_fuel*wO/16+m12/56+(m_moisture+m_steam)/18-Fp2*(yH2O+yCO+yCO2*2)-
                (m_purge+m21)*(wCaCO3/100*3+(1-wCaCO3)/56),
                {m_fuel,wO,m12,m_moisture,m_steam,wCaCO3},
                        {Fuel,wO_F,CR*Fuel,Moisture,Steam,WCaCO3}),...
              subs(yCO2+yCO+yCH4+yH2O+yH2-1),...
             subs(kWGS-yCO2*yH2/(yCO*yH2O),{kWGS},{exp(4400/Tcarb-4.036)}),...
             subs(kSMR-yCO*yH2^3/(yCH4*yH2O)*P^2,
                  {kSMR,P},{exp(-26830/Tcarb+30.114),Pcarb/10^2}));

%Selecting acceptable (non-imaginary) answers
j2=0;
sol=0;
```

```
for j=1:7
   if double(I.yCO2(j))>0 && double(I.yCO2(j))<1
      if double(I.yCO(j))>0 && double(I.yCO(j))<1
         if double(I.yCH4(j))>0 && double(I.yCH4(j))<1
            if double(I.yH2O(j))>0 && double(I.yH2O(j))<1
               if double(I.yH2(j))>0 && double(I.yH2(j))<1
                  sol=sol+1;
                  j2=j;
               end
            end
         end
      end
   end
end
if sol>1
   input('Lime-enhanced gasification: multiple answers!')
end

YCO2_Lime=double(I.yCO2(j2));
YCO_Lime=double(I.yCO(j2));
YCH4_Lime=double(I.yCH4(j2));
YH2O_Lime=double(I.yH2O(j2));
YH2_Lime=double(I.yH2(j2));
FPG_Lime=double(I.Fp2(j2));     %Product gas flow rate (kmol/h)
%******Energy balance for the gasifier: Lime-enahnced ********************
%Formulation and enthalpies are discussed in script "DFB_Gasifier"
m_sand=(Fuel*H_fuel(Tfuel)+Moisture*H_moisture+Steam*H_steamIN-Char*H_char(Tgas) -
(double(I.m21(j2))+double(I.m_purge(j2)))*(WCaCO3*H_CaCO3(Tgas)+(1-WCaCO3)*H_CaO(Tgas))-
Qloss_gas+(CR*Fuel)*H_CaO(Tcomb) -
FPG_Lime*(YH2_Lime*H_H2(Tgas)+YCO_Lime*H_CO(Tgas)+YCO2_Lime*H_CO2(Tgas)+YCH4_
Lime*H_CH4(Tgas)+YH2O_Lime*MWH2O*H_steamOUT))/(H_sand(Tgas)-H_sand(Tcomb));

Gs_Lime=(m_sand+double(I.m21(j2))+Char)/3600/A_riser ;              %Solids mass flux (kg/m^2/s)
TawS_Lime=W_bed/((m_sand+double(I.m21(j2))+Char))*3600;          %Mean solids residence time (s)
Wsand_Lime=m_sand/(m_sand+double(I.m21(j2))+double(I.m_purge(j2))+Char);
Wsorbent=(double(I.m21(j2))+double(I.m_purge(j2)))/...
            (m_sand+double(I.m21(j2))+double(I.m_purge(j2))+Char);          %Sorbent weight fraction
Wchar_Lime=Char/(m_sand+double(I.m21(j2))+double(I.m_purge(j2))+Char);    %Char weight fraction
Etta_CO2=(CR*Fuel/56*Xave)/(CR*Fuel/56*Xave+FPG_Lime*double(I.yCO2(j2)));     %CO2 capture
%******Energy balance for the riser/calciner: complete combustion ******************************
% FCH4_in*H_CH4(Tair)+FO2_in*H_O2(Tair)+FN2*H_N2(Tair)+Makeup*H_CaCO3(Tfuel)+
Char*H_char(Tgas)+m_sand*H_sand(Tgas) -m_sand*H_sand(Tcomb)-(CR*Fuel)*H_CaO(Tcomb)
+(double(I.m21(j2)))*(W*H_CaCO3(Tgas)+(1-W)*H_CaO(Tgas))-(FN2*H_N2(Tcomb)+
```

```
FO2_comb*H_O2(Tcomb)+FCO2_comb*H_CO2(Tcomb)+FH2O_comb*MWH2O*H_steamOUT2)-
Qloss_comb=0

% FO2_in=Landa*(2*FCH4_in+Char/12)   %kmol/hr
% FN2=79/21*FO2_in
% FO2_comb=FO2_in-2*FCH4_in-Char/12
% FO2_comb=(Landa-1)*(2*FCH4_in+Char/12)
% FCO2_comb=FCH4_in+Char/12+double(I.FCO2_Cal(j2))
% FH2O_comb=2*FCH4_in

FCH4_in=-(Landa*(Char/12)*H_O2(Tair)+79/21*Landa*(Char/12)*H_N2(Tair)+
Makeup*H_CaCO3(Tfuel)+Char*H_char(Tgas)+m_sand*H_sand(Tgas) -m_sand*H_sand(Tcomb)-
(CR*Fuel)*H_CaO(Tcomb)+(double(I.m21(j2)))*(WCaCO3*H_CaCO3(Tgas)+(1-
WCaCO3)*H_CaO(Tgas)) -(79/21*Landa*(Char/12)*H_N2(Tcomb)+
(Landa-1)*(Char/12)*H_O2(Tcomb)+(Char/12+double(I.FCO2_Cal(j2)))*H_CO2(Tcomb))-
Qloss_comb)/ (H_CH4(Tair)+Landa*2*H_O2(Tair)+79/21*Landa*2*H_N2(Tair)-
79/21*Landa*2*H_N2(Tcomb)-(Landa-1)*2*H_O2(Tcomb)-H_CO2(Tcomb)-
2*MWH2O*H_steamOUT2);

FO2_in=Landa*(2*FCH4_in+Char/12);   %kmol/hr
FN2=79/21*FO2_in;
FO2_comb=(Landa-1)*(2*FCH4_in+Char/12);
FCO2_comb=FCH4_in+Char/12+double(I.FCO2_Cal(j2));
FH2O_comb=2*FCH4_in;
F_total=100/21*FO2_in+FCH4_in;

Uriser_Lime=F_total*R*Tcomb/(P0*A_riser)*1000/3600;    %Superficial gas velocity in riser (m/s)
QairN_Lime=100/21*FO2_in*R*273.15*1000/P0;             %Required air flow rate in riser (Nm3/hr)
QCH4N_Lime=FCH4_in*R*273.15*1000/P0;                   %Required NG flow rate in riser (Nm3/hr)

LHVPG_Lime=(YH2_Lime*10.789+YCO_Lime*12.625+YCH4_Lime*35.793)/(YH2_Lime+YCO2_Li
me+YCO_Lime+YCH4_Lime);                %MJ/Nm^3
QPGN_Lime=(YH2_Lime+YCO2_Lime+YCO_Lime+YCH4_Lime)*FPG_Lime*R*273.15*1000/P0;
QH2N_Lime=YH2_Lime*FPG_Lime*R*273.15*1000/P0;                    %Nm^3/h
EttaCGE_Lime=(QPGN_Lime*LHVPG_Lime*1000-QCH4N_Lime*35.793*1000)/(Fuel*LHV_F);
EttaH2_Lime=(QH2N_Lime*10.789*1000-QCH4N_Lime*35.793*1000)/(Fuel*LHV_F);

end          %function " Lime_Enhanced_Equilibrium_Gasification "
```